Offshore Wind Energy: Wind and Sea Surface Temperature from Satellite Observations

Karagali, Ioanna

Publication date:
2012

Document Version
Publisher's PDF, also known as Version of record

Offshore Wind Energy: Wind and Sea Surface Temperature from Satellite Observations

DTU Wind Energy - PhD

Ioanna Karagali
DTU Wind Energy - PhD - 003 (EN)
February 2012

DTU Wind Energy
Department of Wind Energy

Offshore Wind Energy: Wind and Sea Surface Temperature from Satellite Observations

Ioanna Karagali

Roskilde 2012
DTU Wind Energy-PhD-003(EN)

Author: Ioanna Karagali
Title: Offshore Wind Energy: Wind and Sea Surface Temperature from Satellite Observations
Division: DTU Wind Energy

DTU Wind Energy-PhD-003(EN)
February 2012

Abstract:

As the land space suitable for wind turbine installations becomes saturated, there is a growing interest for offshore locations. There, available measurements of various environmental parameters are limited and the physical environment is still not well understood. Thus, there is a need for readily available wind speed and direction observations over the ocean and for a better understanding of the marine atmospheric boundary layer (MABL). The sea surface temperature (SST) has a direct impact on the marine atmospheric boundary layer, as the top few meters of the ocean have the same heat capacity as the entire atmosphere above. Under conditions of light winds and strong solar insolation, warming of the upper oceanic layer may occur.
In this PhD study, remote sensing from satellites is used to obtain information for the near-surface ocean wind and the sea surface temperature over the North Sea and the Baltic Sea. The aim is to evaluate their potential use and demonstrate their applicability within the context of offshore wind energy; for the quantification of the wind resources and for the identification of diurnal warming of the sea surface temperature.
Space-borne observations of wind are obtained from scatterometers and Synthetic Aperture Radars (SAR); active microwave radars that relate radiation backscattered from the sea surface to wind. Scatterometers are characterized by global spatial coverage and long temporal availability, while their resolution is ∼25 km. SARs are characterized by very high resolution, ∼600 m, and infrequent temporal and spatial coverage.
Twice daily wind speed and direction measurements from scatterometers are used in the present study for an evaluation of the wind resources. The spatial spectral properties of wind fields from scatterometers and SARs, evaluated in this study, demonstrate that wind information from SAR is more appropriate when small scale local features are of interest, not resolved by scatterometers.
Hourly satellite observations of the sea surface temperature, from a thermal infra-red sensor, are used to identify and quantify the daily variability of the sea surface temperature. This is found to occur from April to August mostly in the Baltic Sea and the eastern North Sea. Finally, as very often information on the daily variability of sea surface temperature is not available from measurements, three models that predict this variability are applied and compared with the observed warming patterns from the satellite observations.

The thesis is submitted to the Danish Technical University in partial fulfilment of the requirements for the PhD degree.

ISBN 978-87-92896-02-5

Sponsorship:
NORSEWInD

Pages:235
References:93

Information Service Department
DTU Wind Energy
Risø Campus
Technical University of Denmark
P.O.Box 49
DK-4000 Roskilde
Denmark
Telephone +45 46774005
bibl@risoe.dtu.dk
Fax +45 46774013
www.vindenergi.dtu.dk

Forfatter: Ioanna Karagali

Titel: Offshore vindenergi: vind og overfladetemperatur fra satellit observationer

Division: DTU Vind Energi

Dansk Resumé:

Efterhånden som passende steder til vindmøller på landjorden er blevet udnyttet stiger interessen for offshore området. Tilgængelige målinger af en række miljG'Eparametre offshore er begrænsede og de fysiske processer er fortsat ikke fuldt ud afklarede. Derfor er der bruger for tilgængelig vindhastighed og vindretnings observationer over havet og for en forbedret forståelse af det marine atmosfæriske grænselag (MABL). Havets overfladetemperatur (SST) har direkte betydning for det marine grænselag, idet de øverste få meter af havet har samme varmekapacitet som hele atmosfæren derover. I tilfælde af let vind og stor solar indstråling vil opvarmning af det øvre lag af havet ske.
I indeværende PhD studie er telemålingsdata fra satellitter blevet anvendt til at få information om vinden nær havets overflade og havets overfladetemperatur i Nordsøen og Østersøen. Formålet er at evaluere disse telemålings-observationers mulige brug samt at demonstrere deres anvendelser indenfor emnet offshore vindenergi; for at kvantificere vindressourcerne og for at identificere den daglige opvarmning af havet.
Satellit observationer af vinden over havet fås fra scatterometer og fra Syntetisk Apertur Radar (SAR). Begge er aktive mikrobølge radarer hvor der er relation mellem den tilbagespredte stråling fra havets overflade og overfladevinden. Scatterometere er karakteristiske ved at give global dækning gennem mange år og deres rumlige opløsning er 25 km. SAR er karakteristiske ved meget høj rumlig opløsning, 600 m, men mindre hyppig temporal og rumlig dækning. I indeværende studie er vindhastighed og vindretning målt to gange om dagen fra scatterometer blevet anvendt til evaluering af vind ressourcerne. Den rumlige spektrale analyse af vindfelter målt fra både scatterometer og SAR demonstrerer at SAR er bedst egnet til at opløse lokale vindfænomener.
Satellit observationer af havets overfladetemperatur fra termisk infra-rød sensor målt hver time er anvendt til at identificere og kvantificere den daglige variation i opvarmningen af havets overflade. Der er især fundet episoder mellem april og august måned i det meste af Østersøen og i den østlige del af Nordsøen. Ofte mangler der information om den daglige variation af overfladetemperaturen målt fra satellit, og der er derfor anvendt tre forskellige modeller som kan forudsige variabiliteten. Resultaterne fra disse modeller er blevet sammenlignet med de opvarmningsmønstre som er kortlagt fra satellit observationerne.

Συγγραφέας: Ιωάννα Καράγαλη
Τίτλος: Υπεράκτια Αιολική ενέργεια: Δορυφορικές μετρήσεις ανέμου και επιφανειακής θερμοκρασίας της θάλασσας
Τμήμα: Πολυτεχνείο Δανίας - Τμήμα Αιολικής Ενέργειας
Περίληψη:

Καθώς ο διαθέσιμος χερσαίος χώρος, κατάλληλος για την εγκατάσταση ανεμογεννητριών τείνει να κορεστεί, η τάση για εξάπλωση στο θαλάσσιο χώρο συνεχώς αυξάνεται. Εκεί οι διαθέσιμες μετρήσεις διαφόρων περιβαλλοντικών παραμέτρων είναι περιορισμένες και το φυσικό περιβάλλον δεν είναι ακόμα απολύτως κατανοητό. Υπάρχει λοιπόν μια αυξανόμενη ανάγκη για διαθέσιμες μετρήσεις της ταχύτητας και διεύθυνσης του ανέμου και για μια καλύτερη κατανόηση του θαλάσσιου οριακού ατμοσφαιρικού στρώματος. Η θερμοκρασία της επιφάνειας της θάλασσας έχει άμεση επίδραση στο θαλάσσιο οριακό ατμοσφαιρικό στρώμα καθώς τα πρώτα μέτρα της υδάτινης στήλης έχουν την ίδια θερμοχωρητικότητα με ολόκληρη την υπερκείμενη ατμόσφαιρα. Υπό συνθήκες λιγοστού ανέμου και αυξημένης ηλιακής ακτινοβολίας, θέρμανση του ανώτερου θαλάσσιου στρώματος μπορεί να λάβει χώρα. Στην παρούσα διδακτορική διατριβή, δορυφορικά δεδομένα χρησιμοποιούνται για την περιγραφή και ποσοτικοποίηση του αιολικού δυναμικού και την ταυτοποίηση συνθηκών ημερήσιας αύξησης της θερμοκρασίας της επιφάνειας της θάλασσας, στη Βόρεια Θάλασσα και την Βαλτική. Κύριος στόχος είναι η αξιολόγηση των δορυφορικών δεδομένων για την πιθανή χρήση τους στο πλαίσιο των μελετών αιολικού δυναμικού.
Δορυφορικά δεδομένα για τον άνεμο λαμβάνονται με τη χρήση σκατερόμετρων και ραντάρ συνθετικού διαφράγματος (Synthetic Aperture Radar, SAR). Αυτά είναι ενεργά ραντάρ μικροκυμάτων που μετρούν την ακτινοβολία που ανακλάται από την επιφάνεια της θάλασσας και η οποία μπορεί να συσχετιστεί με τον άνεμο. Τα σκατερόμετρα χαρακτηρίζονται από εκτεταμένη χωρική κάλυψη (σχεδόν 90% του παγκόσμιου ωκεανού ημερισίως) κα μακροχρόνια διαθεσιμότητα, ενώ η χωρική τους ανάλυση είναι 25 χλμ. Τα SAR χαρακτηρίζονται από πολύ υψηλή ανάλυση, της τάξης των 600 μέτρων, αλλά πάσχουν από μη συστηματική χωρική και χρονική κάλυψη.
Μετρήσεις ταχύτητας και διεύθυνσης του ανέμου από σκατερόμετρα, χρησιμοποιούνται στην παρούσα μελέτη για την εκτίμηση του υπεράκτιου αιολικού δυναμικού. Τα χωρικά φασματικά χαρακτηριστικά του αιολικού πεδίου από σκατερόμετρα και SAR, καταδεικνύουν πώς η χωρική πληροφορία από τα SAR είναι πιο ακριβής για την περιγραφή χαρακτηριστικών μικρής κλίμακας, τα οποία δεν επιλύονται από τα σκατερόμετρα.
Ωριαίες δορυφορικές μετρήσεις της θερμοκρασίας της επιφάνειας της θάλασσας από έναν αισθητήρα υπερύθρων χρησιμοποιούνται για την ταυτοποίηση και ποσοτικοποίηση της ημερήσιας αύξησης της θαλάσσιας επιφανειακής θερμοκρασίας. Αυτή η αύξηση λαμβάνει χώρα κυρίως από τον Απρίλιο εώς και τον Αύγουστο στη Βαλτική και την ανατολική Βόρεια Θάλασσα. Πολύ συχνά μετρήσεις που αντι-

κατοπτρίζουν την ημερήσια μεταβολή της θαλάσσιας επιφανειακής θερμοκρασίας δεν είναι διαθέσιμες. Σε αυτό το πλαίσιο, τρία μοντέλα που προβλέπουν αυτήν την μεταβολή αξιολογούνται και συγκρίνονται με τις παρατηρούμενες δορυφορικές μετρήσεις.

Acknowledgements

I am deeply grateful for the wonderful collaboration with Charlotte B. Hasager, Jacob L. Høyer and Merete Badger. I feel extremely lucky to have had three supervisors that cared so much during these 3 years, for the fruitful discussions, the outstanding understanding and support they kindly provided. Thank you very much! It has been great!

Many thanks to my officemates; old and new. Special thanks to Claire Louise Vincent, Rozenn Wagner and Caroline Draxl for being there when I arrived and helping me get introduced to the PhD world. Many thanks to Joachim Refslund for transmitting to me the Ubuntu bug. Warm thanks to Alfredo Peña for the help he offered all these years (and for *Dexter*). Special thanks to Eleni Markou for just being there and being who she is.

Many thanks to Risø, now DTU Wind Energy for providing the grounds for this study to happen. Special thanks to everyone at the MET group, for creating a pleasant environment to work and socialize. Many warm thanks to Pierre Le Borgne at CMS, for his interest and support.

Ze, Leonardo, Maria, Guillermo, Claire and Thanos have been around these years, for the fun moments and the not-so-fun moments, for dinners and movies and lots of discussions on life, the universe and everything. Thank you all for that, and for tolerating me.

Many thanks to Panos and Themis, for being there and for helping me to get my mind off things. Kostas gets special merit for being a good friend and for the CFD course.

Special thanks to my B.Sc. thesis supervisor Takvor Soukissian for "watering" the seed of research in my head and motivating me to apply for an M.Sc. at DTU. The rest just followed.

My parents are especially thanked. They have always motivated me to keep on with my studies. They have never shown any reserve from expressing their admiration and pride to me.

Efrén, thank you for everything. For being there, for the support, the understanding, the interest, the questions, the spectral analyses discussions. For the trips, the driving, the music, the jokes and especially, for your overwhelming interest in my existence.

Financial Support and Data Resources

The EU-NORSEWInD project has supported financially the conduction of the present study.

Remote Sensing Systems provided the QuikSCAT data and especially, many thanks to Deborah K. Smith, that has been very helpful with the user support.

The European Space Agency (ESA) is acknowledged for the ENVISAT ASAR data.

SEVIRI data were processed by the Centre de Météorolgie Spatiale, Météo France for the EUMETSAT OSI-SAF project.

HIRLAM and $K_{d(490)}$ data obtained from the Danish Meteorological Institute (DMI).

Data from the MARNET Monitoring Network are obtained from Bundesamt Für Seeschifffahrt und Hydrographie (BSH), Germany.

Data from Horns Rev (M2) were provided by Vattenfall and DONG Energy.

FINO-1 meteorological data were obtained from DEWI (Deutsches Windenergie Institut, German Wind Energy Institute), oceanographic data from BSH, all through the NORSEWInD project. Greater Gabbard data are provided by SSE Renewables.

Contents

List of Figures

Acronyms

AATSR Advanced ATSR. 52

ADEOS Advanced Earth Observing Satellite. 18

ALOS Advanced Land Observing Satellite. 24

AMI Advanced Microwave Imager. 18, 24

AMSR-E Advanced Microwave Scanning Radiometer-EOS. 10

ANSWRS APL/NOAA SAR Wind Retrieval System. 24

ASAR Advanced SAR. 24, 25

ASCAT Advanced Scatterometer. 18, 19, 75

ATSR Along Track Scanning Radiometer. 52

AVHRR Advanced Very High Resolution Radiometer. 52

CLS Collecte Localisation Satellites. 25

CMS Centre de Météorologie Spatiale. 54, 55

DMI Danish Meteorological Institute. 58, 67, 111

ECMWF European Centre for Medium-Range Weather Forecasting. 19

ENVISAT ENVironmental SATtelite. 24, 25, 52

ENW Equivalent Neutral Wind. 19, 29, 30

ERS European Remote Sensing. 18, 24, 52

ESA European Space Agency. 18, 24, 52, 53

EUMETSAT European Organisation for the Exploitation of Meteorological Satellites. 52, 53

GHRSST Group for High Resolution SST. 50

GlobCol ESA Global Colour Project. 67

GMF Geophysical Model Function. 15, 16, 19, 20, 22, 26, 74, 78

GOES Geostationary Operational Environmental Satellite. 52

GWEC Global Wind Energy Council. 2

HIRLAM High Resolution Limited Area Model. 62, 84

IOVWST International Ocean Vector Winds Science Team. 79

ISRO Indian Space Research Organization. 18

JERS Japanese Earth Remote Sensing. 24

JHU/APL Johns Hopkins University Applied Physics Laboratory. 24

JPL Jet Propulsion Laboratory. 20, 27

KNMI Koninklijk Nederlands Meteorologisch Instituut. 22

L1 Level 1. 22

L2B Level 2B. 22, 28

L3 Level 3. 22, 27, 99, 101, 102

MFG Meteosat First Generation. 52

MODIS Moderate Resolution Imaging Spectroradiometer. 52

MSG Meteosat Second Generation. 52, 53

MVIRI Meteosat Visible and Infra-Red Imager. 52

NASA National Aeronautics and Space Administration. 18, 52

NASDA National Space Development Agency of Japan. 18

NCAR National Center for Atmospheric Research. 36

NN Neural Network. 62

NOAA National Oceanic and Atmospheric Administration. 20, 52

NOGAPS Navy Operational Global Atmospheric Prediction System. 25

NRT Near-Real-Time. 20

NSCAT NASA Scatterometer. 18

NWP Numerical Weather Prediction. 1, 3, 9, 12, 30, 36, 41, 62, 63, 69, 76, 78, 83

OI Optimal Interpolation. 58, 111

OSI SAF Ocean & Sea Ice Satellite Application Facility. 22, 54

PALSAR Phased Array L-band Synthetic Aperture Radar. 24

PO.DAAC Physical Oceanography Distributed Active Archive. 20

POES Polar-orbiting Operational Environmental Satellites. 52

RSS Remote Sensing Systems. 21, 22, 27, 29

SAF Satellite Application Facilities. 53

SAR Synthetic Aperture Radar. 10, 12, 18, 23–25, 41, 75, 82, 84

SASS Seasat Scatterometer. 18

SDIS Stability Dependent In Situ. 30

SEVIRI Spinning Enhanced Visible Infrared Imager. 52, 53

SOPRANO SAR Ocean Products Demonstration. 25

SSI Surface Solar Irradiance. 67, 84, 115, 116, 119, 120

SSM/I Special Sensor Microwave/Imager. 10, 19

SST Sea Surface Temperature. 1, 4, 47–49, 52, 54, 55, 58, 78

TanDEM-X TerraSAR-X Add-oN for Digital Elevation Measurement. 24

TMI TRMM Microwave Imager. 10

TOGA-COARE Tropical Ocean-Global Atmosphere – Coupled Ocean-Atmosphere Response Experiment. 62

WRF Weather Reasearch & Forecasting. 30, 36, 39, 83, 105

WVC Wind Vector Cell. 16, 20, 22, 41

Symbols

A scale parameter. 5, 29, 34

B radiance. 48

E wind power density. 5

K degrees Kelvin. 32, 54, 55, 57–59, 63, 65, 67, 71, 77, 112

$K_{d(490)}$ diffuse attenuation coefficient. 67–69, 84, 115, 116, 119, 120, 123, 124

Q integrated net heat flux. 62, 67, 84, 115, 116, 119, 120, 123

R^2 coefficient of determination, the correlation coefficient r squared. 37, 57

SSI' integrated Surface Solar Irradiance. 67

T absolute temperature of black body. 48

T_λ brightness temperature. 48

$Tair$ air temperature. 7

U mean wind speed estimated from the Weibull fit. 5

Γ gamma function. 5

Ψ_M stability function. 4

κ von Kármán constant. 4

λ wavelength. 48

ρ air density. 5

σ standard deviation. 37, 55, 57

σ_0 normalized radar cross section. 15–17, 19, 20, 22, 24, 41, 44, 74

θ incidence angle of the radar signal. 16

θ_{sat} satellite zenith angle. 54

ξ azimuth angle. 16

c speed of light. 48

d diurnal free layer depth. 62

$dSST$ daytime temperature anomaly. 62, 63, 65, 67, 115, 116, 119, 120, 123

f frequency of the radar signal. 16

$f(u)$ frequency distribution of wind speed. 5

g gravitational acceleration. 8

h Planck constant. 48

k shape parameter. 5, 29, 34

k_B Boltzman constant. 48

pol polarization of radar signal. 16

u_* friction velocity. 4, 7

z measurement height. 4

z_0 surface roughness. 4, 8

u wind speed. 4, 5, 7, 27, 67, 84, 101, 102, 115, 116, 119, 120, 123

Chapter 1

Introduction

As siting of wind farms moves from land to coastal and offshore locations, there is an increased need for long, continuous, readily available observations of the wind over the ocean. The North Sea and the Baltic Sea have, currently, the highest concentration of operating offshore wind farms in Europe with more under construction and in the planning phase. In situ measurements, typically preferred for wind resource assessment studies, are scarce and even when existing may be private or bounded by confidentiality issues.

The strength of space-borne observations can help overcome issues related with the lack of observations. Previous studies exist (Christiansen et al., 2006; Hasager et al., 2005, 2006, 2008, 2011), that demonstrate the applicability of satellite wind fields for resource assessment. Space-borne instruments provide wind fields at 10 m above the sea surface, relevant for describing the wind characteristics, validating Numerical Weather Prediction (NWP) models and for wind resource assessment at this height.

To obtain information at higher levels, comparable to the offshore wind turbine hub heights of approximately 100 m, extrapolation of the wind speed is required and knowledge of the atmospheric stratification is fundamental. Over the ocean, stratification can be influenced by the diurnal variability of the Sea Surface Temperature (SST), but often this is neglected. Due to the increased heat capacity of the ocean, the top 2-3 m of the water column have the same heat capacity as the atmosphere above. In addition, ∼50% of the solar radiation penetrating the ocean surface is absorbed within the first 0.5 m (Soloviev & Lukas, 2006).

Light winds and high insolation may cause the trapping of heat in the upper few meters of the water column, leading to an increase of the temperature that follows the daily solar cycle, with a time-lag of ∼2-3 hours. Therefore, the temperature of the sea surface can vary during the course of a day, complicating the interactions between the atmosphere and ocean. There is a need to increase the availability of observations over the ocean and quantify the occurrence of warming events in order to better understand the interactions between the sea surface and the atmosphere and their impact on offshore wind energy.

Thus, the aim of the present study is to demonstrate the applicability of satellite observations of the near-surface ocean winds for wind resource assessment and to improve our understanding of the marine environment by quantifying the diurnal variability of SST, for large offshore areas where in situ measurements are scarce.

1.1 Offshore Wind Energy

Acknowledging the anthropogenic contribution to the recent increase in concentrations of atmospheric greenhouse gases, mainly through the consumption of fossil fuel for energy production, has led in a shift towards more environmental friendly sources of energy. In addition, the realization that fossil fuel is limited and deposits will eventually be exhausted, is the driving force behind policies that support sustainable energy sources, that meet today's energy consumption needs without compromising the future generations' resources. Renewable energy is extracted from natural resources such as the sun, the wind, the tides and waves that are naturally restored. Wind energy is currently one of the fastest growing sources of renewable energy.

The Global Wind Energy Council (GWEC) in its global wind report states than in 2010 the global installed wind power capacity increased by 24.1% (GWEC, 2010). Moreover, during 2010 in the EU the annual offshore market increased by approximately 51% compared to 2009 and accounted for 9.5% of all the capacity additions. Archer & Jacobson (2005) showed that offshore stations experience mean wind speeds at 80 m above the sea surface that are, on average, 90% higher than over land. Northern Europe is one of the leading regions in operating offshore wind farms, having currently more than 25 in operation mode, more than 10 under construction and many under the planning stage. For an overview of the locations, see Figure 1.1. For more details see http://www.4coffshore.com/offshorewind.

Planning an offshore wind farm requires finding the optimal location that satisfies different requirements.

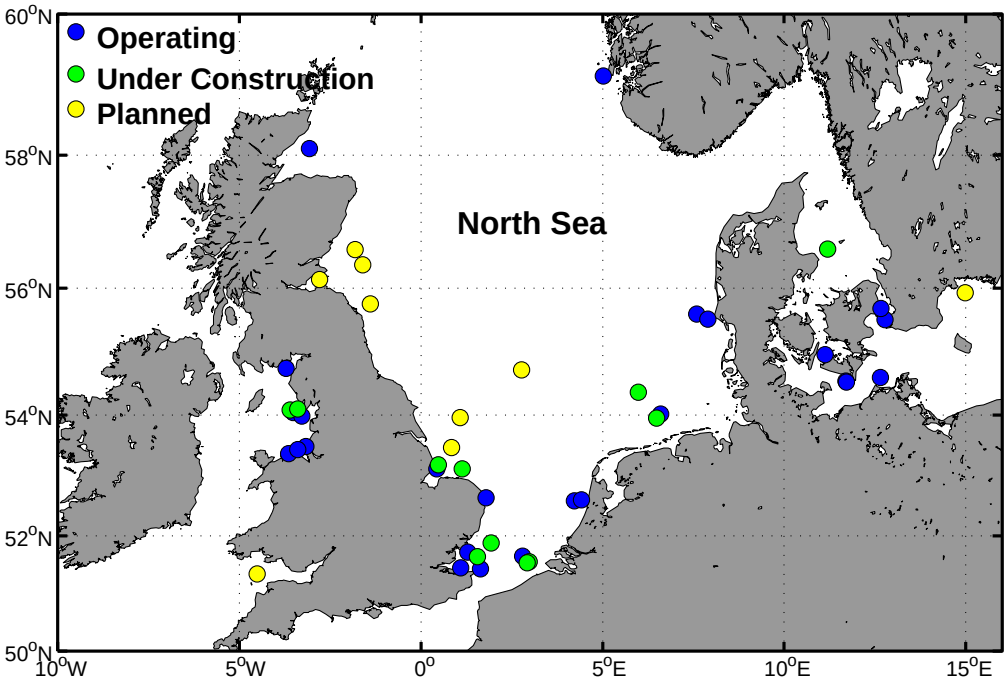

Figure 1.1: Map of the largest offshore wind farms operating, under construction and in the planning phase in North Europe. A list of the wind farms and their co-ordinates and operating status is available in Appendix A.

- Suitable wind resources are essential and they are evaluated with the use of a wind atlas. Such an atlas examines wind speeds at various heights, including turbine hub heights according to the current and near-future technology.
- Water depths are required to be within some range that permits bankable foundation costs.
- Accessibility to and cost-effective grid connection.
- Finally, no preservable natural or cultural heritage value as in this case no permission will be granted.

After the permission is granted, monitoring of the wind resource during the construction and operation phases usually takes place. Moreover, short term forecasting is performed with the use of NWP models, to estimate the energy production in a day-to-day basis.

1.2 Wind Resource Assessment

The wind resources are evaluated through an assessment study that will result in the composition of a wind resource map or a wind atlas, with detailed information on prospective sites for the installation of wind farms. Typically, such maps are based on in situ measurements of wind speed and direction. Over the ocean, such measurements are available at limited locations due to inflated costs for installation and maintenance of the in situ instrumentation. Depending on the accuracy of the measurements and their spatial extend, the wind resource maps can be of low or high detail. Low accuracy maps are mainly used for an initial evaluation of the wind climate and to highlight areas or locations that may show a high potential and where more accurate measurements should be obtained, in order to make a detailed wind resource assessment. In situ observations are usually acquired with the installation of meteorological towers, also known as masts or met. masts, that are equipped with various instruments at multiple heights.

Parameters to be measured for an accurate wind resource assessment are the wind speed and direction. Modern wind turbines have hub heights of more than 80 m and rotor diameters of 90 m or more. In situ measurements are very rarely available at multiple heights or exceeding 60 m as met. masts are not cost effective above a certain height. Knowledge of the vertical wind profile is of extreme interest as it describes the wind speed at various heights relevant for the wind turbine. Such profiles are usually acquired by extrapolating measurements from heights with available measuring instrumentation to other levels, a process that also requires air temperature, pressure and humidity measurements.

Extrapolation can be performed with the implementation of the diabatic wind profile expression (Stull, 1988) (Eq. 1.1).

$$u = \frac{u_*}{\kappa}\left[\ln\left(\frac{z}{z_0}\right) - \Psi_M\right], \tag{1.1}$$

In this formulation, u is the wind speed at some height z, u_* is the friction velocity, κ the von Kármán constant ($\sim$0.4) and z_0 is the surface roughness. The term Ψ_M accounts for atmospheric stratification, i.e. the stability of the atmosphere between the two heights of interest. For the offshore sites, water temperature measurements at some depth are also acquired and are used for the extrapolation of measurements when aiming to obtain a detailed vertical wind profile.

But it is the top of the water column that is in contact with the atmosphere. The temperature there, namely the SST, holds a fundamental role in the stratification

of the lower atmospheric levels. Low winds and strong solar heating are favourable conditions for warming of the very top layer of the sea surface. Such conditions can cause rapid increase of the SST even within a few hours and may have an impact on the stratification of the overlying atmosphere. This increase may occur in just the first few top meters of the water column and is very often not "felt" by temperature sensors at some depth, e.g. ∼3 or 4 m. More detail on the impact of SST on stratification and the vertical wind profile follows shortly.

For wind resource assessment, the wind speed frequency distribution is of interest. At least one year of site specific, frequent - typically 10 minute- measurements are required in order to calculate an accurate annual wind speed frequency distribution $f(u)$. This may also be sufficiently described by the Weibull distribution (Troen & Petersen, 1989). The two parameter Weibull function (Equation 1.2) is fitted to measurements through the estimation of the scale (A) and shape (k) parameters that provide the best fit. The scale parameter is associated with the mean wind speed while the shape parameter is an indicator of the width of the distribution. Very narrow distributions show that the wind speed is mostly contained within a narrow range.

$$f(u) = \frac{k}{A}\left(\frac{u}{A}\right)^{k-1} \exp\left[-\left(\frac{u}{A}\right)^{k}\right] \tag{1.2}$$

The mean wind speed U (Equation 1.3) and the wind power density E (Equation 1.4) can be also estimated from the Weibull function with known A and k parameters.

$$u = A\Gamma\left(1 + \frac{1}{k}\right) \tag{1.3}$$

$$E = \frac{1}{2}\rho A^3 \Gamma\left(1 + \frac{3}{k}\right) \tag{1.4}$$

Where ρ is the air density (assumed to be constant and ∼1.225 kg m^{-3} at 10 ℃), u is the wind speed and Γ is the gamma function. Especially the wind power density, is a measure of the energy that can be extracted from the wind and it can also be estimated directly from the time-series of wind speed observations, as in Equation 1.5.

$$E = \frac{1}{2}\rho\overline{u^3} \tag{1.5}$$

The wind speed frequency distribution allows to identify the frequency of occurrence of different wind speed thresholds and this is important as wind turbines operate within certain wind speed ranges. The cut in speed is defined as the threshold, usually in the range between 3 and 4.5 m s^{-1}, below which no power will be produced. The rated speed is that at which the maximum possible power is produced (11-16 m s^{-1}). A cut-out speed is also established, above which the turbine must be stopped from turning (20-36 m s^{-1}).

The final product of the wind resource assessment is the wind atlas, containing wind resource maps but also time series of wind speed and direction observations and wind speed frequency distributions. Atlases are typically provided for various atmospheric levels, relevant for wind turbines, often between 30 m and 100 m. Climatological wind atlases are composed of averages over longer periods, of few decades and they are typically estimated for a standard height of 10 m above the surface.

Offshore measurements: how can satellites help?

While the installation of met. masts on land is a rather common practise, such structures become very expensive to install and maintain at offshore sites. Thus, wind speed and direction measurements offshore are difficult to obtain. Satellite observations of near surface wind are expected to help mitigate this issue, as nowadays there exist relatively long and continuous records that are typically available twice every day. Such datasets can be useful for the initial wind resource maps, as information is available over extended areas. Wind speed frequency distributions and time series can be extracted from satellite wind records, aiding the prospective site selection process. Moreover, satellite observations can be used to create or validate the climatological wind atlases and to examine the spatial variability of the wind field in relation to various wind speed thresholds of interest.

As the reference height is standardised to 10 m above the surface, space-borne observations of wind can not be very helpful to determine the vertical wind profile. For this, in situ observations of temperature, pressure and humidity are required so extrapolation to higher levels can be performed. For the implementation of extrapolation techniques, SST observations from space can be used when water temperatures are required to accurately describe the temperature of the surface in contact with the atmosphere. Often, short term forecasting is performed for the large offshore wind farms. Satellite observations of wind can be used to test various model set-ups. Finally, both wind and SST observations from space can be assimilated in the NWP models.

SST and the vertical wind profile

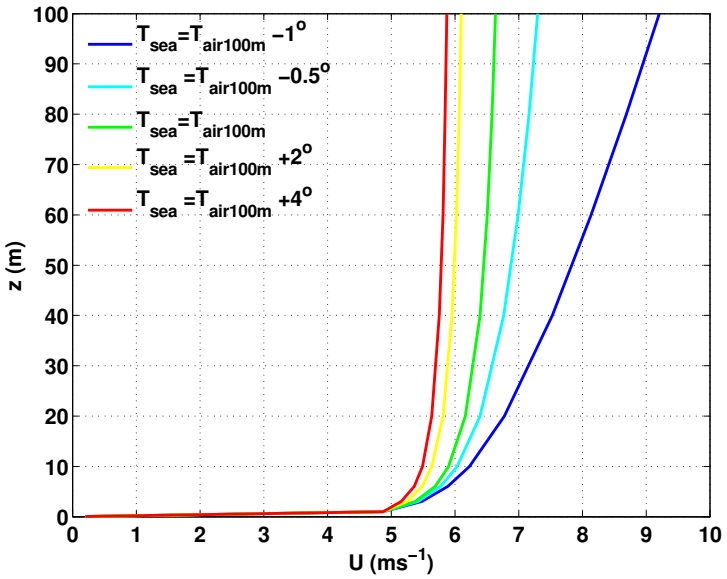

Figure 1.2: The shape of the diabatic wind profile for different stability cases, i.e. different air-sea temperature differences.

Using the formulation for the diabatic wind profile one can visualize the impact of the varying SST on the wind speed at 100 m. Considering a constant air temperature at 100 m ($Tair$) and a constant friction velocity u_*, SST is allowed to range from 1° lower to 4° higher than the $Tair$. Using Equation 1.1, the wind speeds u at 1 m, 3 m, 6 m, 10 m, 20 m, 40 m, 60 m, 80 m and 100 m above the surface are estimated. Figure 1.2 shows the wind profiles for the different SSTs. When the SST is lower than the $Tair$ (stable stratification), u at 100 m is higher than when the SST is equal (neutral) or higher (unstable) than $Tair$.

Assuming that the conditions are neutral, which is very often the case over the sea, an increase of the SST of 2° will cause an 8% decrease of the u_{100m} while a 4° SST increase will drive an 11.5% decrease of the $u_{100\ m}$, when compared to the neutral case. If the wind power density is estimated from Eq. 1.5 for using just 1 value for u instead of an average, then there will be a 22% and 30% decrease in the estimates for an SST increase of 2° and 4°.

Example: Using SST and bulk sea temperature when extrapolating wind speed measurements

In the following, extrapolation of the available 15 m wind speed measurements from a cup anemometer to a height of 100 m, typical for offshore wind turbine

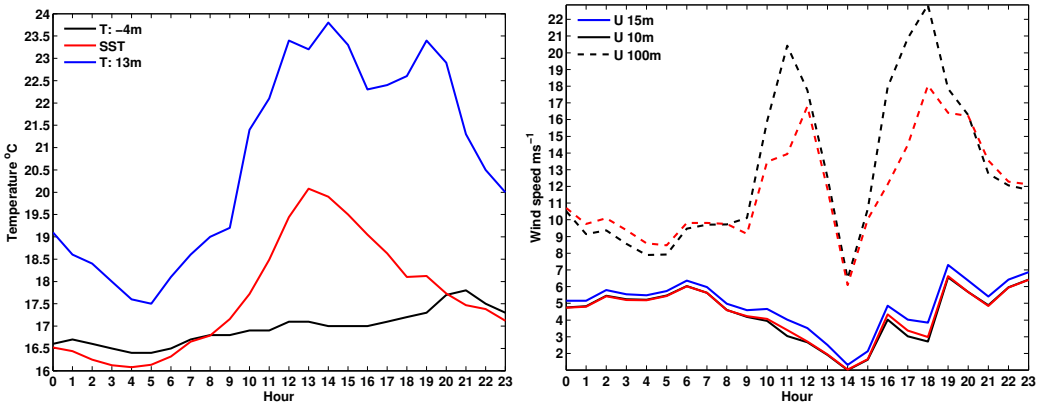

(a) (b)

Figure 1.3: a) Measured air and sea temperatures at Horns Rev on the 04/07/2006. SST refers to satellite derived temperatures and T -4 m is the temperature from a sensor located at that depth. T 13 m is the air temperature from a sensor at that height. b) Measured wind speed at 15 m (blue) and extrapolated wind speeds at 10 m (solid) and 100 m (dashed), always using the T 13 m for the air temperature and either the T -4 m (black) or the SST (red) for the sea temperature.

hub heights, is performed. It illustrates the impact of SST versus bulk water temperatures. Air temperature measurements are available at 13 m, while water temperature measurements are available at -4 m and at the surface (SST). The surface roughness parameter z_0 is described from Charnock (1955) ($z_0 = 0.015\frac{u_*^2}{g}$), where g is the gravitational acceleration. A value for z_0 equal to 0.0144 is assumed, according to Sathe et al. (2011). The extrapolation is performed using Equation 1.1.

Figure 1.3a shows the daily variability of the sea temperature at the surface (red line) and at -4 m (black). Moreover, in combination with Figure 1.3b, it illustrates the impact of low wind on the diurnal warming of SST. The measured wind speed at 15 m (Figure 1.3b, blue line) shows a decrease from 6 o'clock, at which time the SST starts to increase. As the wind speed constantly decreases, SST increases 3.7 ℃ from its 6 o'clock value. The wind speed minimum observed at 14:00 is followed by an increase forcing the SST to decrease due to mixing.

Figure 1.3b illustrates the impact of i) using the sea surface temperature instead of a depth temperature and ii) properly resolving the diurnal cycle of SST, when extrapolating wind speed measurements to various heights. The black curves show the temporal variability of wind speed at 10 m (solid) and 100 m (dashed) when the

extrapolation from the 15 m measurement is performed using the sea temperature at -4 m. To the contrary, if the SST is considered instead of the temperature at a depth, the extrapolated wind speeds at 10 m and 100 m are reproduced by the red lines.

One can immediately see that there are differences between the extrapolated wind speeds at both the 10 m and 100 m level. Especially for the warming period between 09:00 and 14:00, the maximum differences at 10 m is less than 0.1 m s^{-1} but it reaches to 6.5 m s^{-1} at the height of 100 m. While the air temperature and the SST significantly increase during the daytime, the -4 m temperature varies by less than 1°Cwithin the course of a full day.

This drives a very large air-sea temperature difference when the -4 m temperature is considered. This is unrealistic, as the surface is decoupled from the water below, while it is the SST that drives the atmospheric stratification. The biases are small close to the surface and to the measurement height of 15 m but they become large at turbine hub-heights.

The example above demonstrates the interaction between the lower atmosphere and the upper ocean. With persistently low enough winds, the mixing that distributes heat in the upper water column is blocked. That forces an increase of the sea surface temperature, the peak of which is time-aligned with the wind minima. Immediately after that, the wind starts to increase and the temperature decreases.

Moreover it highlights the importance of properly resolving the daily SST cycle in the context of extrapolating wind speeds from measurement heights to different atmospheric levels. This can be achieved either through frequent SST measurements or with the implementation of simple models that can predict diurnal warming. The temperature predictions from such models can be superimposed on bulk water temperature measurements, if SST observations are not available. Moreover, these models can be implemented in NWP models that use bulk temperature fields in order to resolve the daily cycle.

This example also shows the occurrence of diurnal warming which forces the decoupling of the upper few meters of the sea surface from the water below. Finally, it allows the identification of a near surface wind speed threshold of 5 m s^{-1} (note that this is above the cut in threshold for wind turbines) below which warming of the sea surface starts under clear sky conditions, due to the lack of vertical mixing. The aforementioned phenomena are explored and quantified in the present study for the Northern European Seas, with the use of satellite observations.

1.3 Satellite Data

Remote sensing from space provides frequent, high resolution observations of various environmental parameters on a global scale. The parameters under investigation are derived through the intensity and the frequency distribution of the radiation received by the satellite sensor. The radiation received by the sensor has three basic sources, the reflected solar radiation, the emitted blackbody radiation and the energy emitted from satellite radars and backscattered from the surface. Satellite data are being used in many applications ranging from weather prediction, storm tracking and aerosol measurements to ship route monitoring.

Radiation from the ocean is received in three bands of the electromagnetic spectrum; the infra-red, visible and microwave bands. In the infra-red band, blackbody radiation is emitted from the top few micrometers of the sea surface (Martin, 2004). In the microwave band, observations are divided in passive and active observations. In passive observations, the reflected solar radiation and blackbody radiation are received by the sensor. Active microwave observations originate from active radars that send pulses towards the Earth's surface and measure the backscattered signal.

Both passive and active microwave observations are used to derive ocean near-surface winds. Passive instruments include the Special Sensor Microwave/Imager (SSM/I), the TRMM Microwave Imager (TMI) and Advanced Microwave Scanning Radiometer-EOS (AMSR-E) that provide wind speed. Wind vector, i.e. wind speed and direction, information from satellites is currently provided by active radars, known as scatterometers. The main principle of function is to transmit radiation towards the ocean surface and measure the signal backscattered due to the small scale waves (in the order of 2 cm). Extended studies have related the backscattered signal to the surface stress and developed algorithms to related this to wind speed (for more information see Chapter 2.1). In addition, with a similar principle of function as the scatterometer, Synthetic Aperture Radars (SARs) are active radars that measure the backscattered signal but only wind speed measurements can be retrieved.

SST is measured from space with the use of microwave and infra-red radiometers. The operating principle is based on measuring the brightness temperature, i.e. the equivalent blackbody temperature, in the microwave and thermal infra-red bands of the electromagnetic spectrum. The signals registered from the detectors are electronically processed and a variety of surface and atmospheric parameters are estimated, including SST.

Due to the relatively long time period of available observations; up to 10 years for the twice daily surface winds from scatterometers and 7 years for the hourly

SST fields from an infra-red sensor, and the extended spatial coverage, satellite observations are considered a valuable source of information for the description of the wind and SST over large areas. For this reason, they are chosen in the present study to describe the wind field characteristics and quantify the diurnal warming of SST in the North Sea and the Baltic Sea.

Studies using satellite observations have attempted to explain the mechanisms by which near surface wind and SST interact, mainly in the Tropics. The increase of wind over an area with warm SST has been attributed by many to the buoyancy instability and the mixing. Chelton et al. (2001) have found observational evidence of ocean-atmosphere coupling in the eastern Tropical Pacific.

Chelton et al. (2004) used satellite observations of winds and SST to examine small scale features in ocean winds. They attribute much of the small-scale variability in the wind stress field to SST modification of the low-level winds, through air-sea heat fluxes. Recently, large horizontal variations in surface wind speed near meandering SST fronts, have been noted by O'Neill et al. (2010) in the mid-latitudes. Stronger wind speeds were recorded over warmer water and weaker wind speeds over cooler water.

Sweet et al. (1981) suggested that the observed wind variability across the SST front of the Gulf Stream was due to increased turbulent mixing driven by the stability change forced by the SST change across the front. Jury (1993) observed increased wind stress and surface heat fluxes across an SST front. Xie (2004) discussed the local and shallow atmospheric response on the vicinity of varying SST over the cool oceanic part.

In the North Sea and the Baltic Sea, the diurnal warming of the sea surface may give rise to situations mentioned in the studies above, where a warm SST anomaly may give rise to instability that will force increased near surface wind speeds. The present study will focus on quantifying the involved parameters, i.e. ocean surface winds for wind resource assessment and the diurnal SST cycle with the use of satellite observations and it is structured as follows.

1.4 Structure

The thesis consists of two parts. The synopsis is a collection of information that will guide the reader through the main applications of satellite near surface winds over the sea and SST. The second part is a collection of manuscripts published and submitted to scientific journals, where the reader will be referred to, for all

the background information.

Twice daily satellite observations of surface winds at 10 m from the QuikSCAT scatterometer over the period 1999-2009, are compared with available in situ observations from meteorological masts erected for wind energy related purposes. The scatterometer wind fields are then used to describe the average wind field, to evaluate the seasonal and spatial wind variability and for comparisons with re-analysis fields from NWP models. SAR wind retrievals are processed with various resolutions and are spectrally compared with the QuickSCAT wind product. The aim is to evaluate the different spatial resolutions of the satellite wind products and describe their spectral properties. The relevant results are presented in Chapter 2.

In Chapter 3 hourly satellite observations of SST over the period 2004-2009, are validated against in situ measurements. They are then used to demonstrate that diurnal variability does occur in the Northern European Seas and evaluate its amplitude and occurrence. Finally, various parametrization models for the diurnal cycle of SST are applied and compared with the satellite observations.

Discussion related with the applicability of scatterometer winds for offshore wind energy purposes and the identification of diurnal warming events in the North Sea and the Baltic Sea can be found Chapter 4. A short summary of the study and the main conclusions are presented in Chapter 5. Finally, recommendations for future investigations that have emerged from the analyses performed during the present study are available in Chapter 6.

Results related to the objectives of this PhD study have been collected in the form of manuscripts. These are referenced in the first part of the thesis and attached at the end of the synopsis. The first three manuscripts listed below are related to the applicability of scatterometer winds for wind resource assessment purposes and the latter two, with the diurnal variability of SST through hourly satellite observations and modelling.

1. “Wind characteristics in the North and Baltic Seas” submitted to Wind Energy.
2. “Spatial and temporal variability of winds in the Northern European Seas”, draft manuscript, to be submitted to Renewable Energy.
3. “Spectral properties of QuikSCAT and ENVISAT ASAR wind fields in the North Sea”, draft manuscript, to be submitted to Geophysical Research Letters.

4. "SST diurnal variability in the North Sea and the Baltic Sea" accepted in Remote Sensing of Environment, in press.

5. "Observations and modelling of the diurnal SST cycle in the North and Baltic Seas", draft manuscript, to be submitted to Remote Sensing of Environment.

During the PhD study, manuscripts appearing in journals or in Proceedings, but not referenced in the study are:

1. Hasager, Charlotte Bay; Badger, Merete; Astrup, Poul; **Karagali, Ioanna** (2012): Satellite Remote Sensing in Offshore Wind Energy. In: Handbook of Wind Power Systems, Springer, in press.

2. Høeyer, Jacob L.; **Karagali, Ioanna**; Dybkjær, Gorm; & Tonboe, Rasmus (2012): Multi sensor validation and error characteristics of Arctic satellite sea surface temperature observations. In: Remote Sensing of Environment, in press.

3. **Karagali, Ioanna**; Høyer, Jacob L. (2011): Diurnal warming in the Northern European shelf seas: Observations vs. modelling. In: Proceedings (p. 225-229). Presented at: GHRSST XII Science Team Meeting, Edinburgh (GB), 27 Jun - 1 Jul GHRSST

4. **Karagali, Ioanna**; Sempreviva, Anna Maria; Hasager, Charlotte Bay (2011): Analysis of 10 years of wind vector information from quikSCAT for the North Sea: Preliminary results from the OREC-CA project. In: Proceedings (p. 6 pages), Presented at: EWEA Annual Event 2011, Brussels (BE), 14-17 Mar EWEA

5. Hasager, Charlotte Bay; Badger, Merete; Badger, Jake; Bingöl, Ferhat; Clausen, Niels-Erik; Hahmann, Andrea N.; **Karagali, Ioanna**; Peña Diaz, Alfredo (2011): Combining satellite wind maps and mesoscale modelling for a wind atlas of the South Baltic Sea. In: Proceedings EWEA, Presented at: EWEA Annual Event 2011, Brussels (BE), 14-17 Mar

6. **Karagali, Ioanna**; Høyer, Jacob L. (2010): SEVIRI SST Diurnal warming and QuikSCAT ocean Winds in the North Sea and the Baltic Sea. In: Proceedings. Presented at: 2010 EUMETSAT Meteorological Satellite Conference, Cordoba (ES), 20-24 Sep EUMETSAT

7. **Karagali, Ioanna**; Badger, Merete; Sørensen, Lise Lotte (2010): MERIS Ocean Colour Data for the Estimation of Surface Water pCO_2: The Case Studies of Peru and Namibia. In: Lacoste-Francis,H. (Ed.), Proceedings.

Presented at: ESA Living Planet Symposium, Bergen (NO), 28 Jun - 2 Jul European Space Agency, ESA

8. Hasager, Charlotte Bay; **Karagali, Ioanna**; Astrup, Poul; Badger, Merete; Mouche, Alexis; Stoffelen, Ad (2010): Offshore Wind Atlas for Northern European Seas. In: Lacoste-Francis,H. (Ed.), Proceedings. Presented at: ESA Living Planet Symposium, Bergen (NO), 28 Jun - 2 Jul European Space Agency, ESA

9. **Karagali, Ioanna**; Høyer, Jacob L. (2010): Diurnal warming in the North Sea and Baltic Sea. In: Proceedings. Presented at: 11th GHRSST Science Team Meeting, Lima (PE), 21-25 June The Group for High-Resolution Sea Surface Temperature

Chapter 2

Near-surface Ocean Wind

2.1 Scatterometry from Space

Scatterometry is the technique by which a microwave radar pulse is transmitted towards the Earth's surface and the reflected energy is measured. The backscattered signal is then determined by subtracting the noise signal (arising from the instrument noise and the natural emisivity of the atmosphere-earth system at the frequency of the radar pulse) from the total measured reflected energy to finally estimate the normalized radar cross section σ_0. Currently, radar scatterometers are most widely used to obtain near-surface wind vector information over the ocean from space-borne platforms.

The small scale waves generated by the wind on the ocean surface are assumed to be the driving force for the scattering of the radar signal over the ocean. Thus the fraction of the radar signal backscattered to the instrument is a function of the near-surface ocean wind velocity, relative to the orientation of the instrument. To derive information about the wind velocity from the normalized radar cross section, the relationship between the two, also known as Geophysical Model Function (GMF) must be known. GMFs have an empirical form and during the decades of scatterometer applications, several GMFs have been developed and are constantly modified to improve the accuracy of the retrieved winds.

The empirical form of the GMFs has been relying on the correlation of the mea-

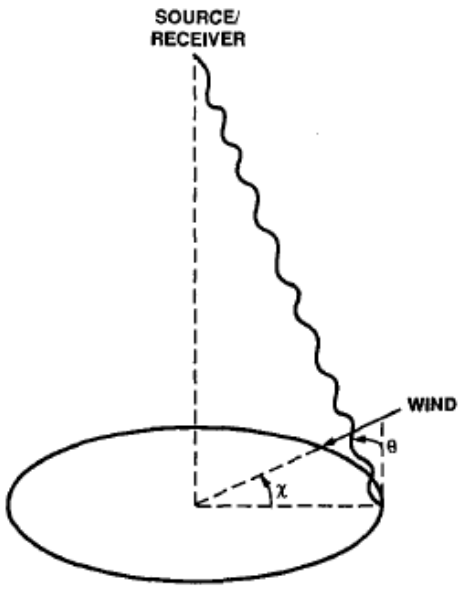

Figure 2.1: Scattering geometry sketch from Naderi et al. (1991).

sured σ_0 at a location with in situ wind velocity observations. The general form of GMFs, as given in Naderi et al. (1991) is

$$\sigma_0 = f\left(|u|, \xi, ...; \theta, f, pol\right) \tag{2.1}$$

where $|u|$ is the wind speed, ξ the azimuth angle between the wind vector and the incident radar pulse (χ in Figure 2.1), θ is the incidence angle of the radar signal measured in the vertical plane, f is the frequency of the radar signal and *pol* its polarization. The term ... accounts for non-wind variables such as long waves, stratification and temperature, the effects of which are considered small (Naderi et al., 1991).

A single σ_0 measurement is not sufficient to determine both the wind speed and direction, thus more measurements are required from different azimuth angles. To obtain these multiple σ_0 measurements, more than one beams are required. Each σ_0 measurement, also known as "footprint" corresponds to a cell of geometry depending on the scatterometer characteristics. Multiple nearly-simultaneous, space-collocated σ_0 measurements are averaged in cells called Wind Vector Cell (WVC) with dimensions depending on the mission specifications.

Thus, for a given area of the ocean surface multiple radar backscatter signals are obtained. Using a maximum-likelihood estimation (MLE) to determine the set of wind speed and direction that maximize the probability of the measured σ_0, the

wind velocity can then be determined, during what is called the wind inversion process. Typically, this results in more than one solutions with extreme MLE values, referred to as "ambiguities", that correspond to almost the same wind speed but different wind directions. The extreme of the extrema is then chosen as the "best" estimate.

Sources of error

Some of the physical parameters known to affect the backscattered signal are rain, currents, sea surface temperature and the atmospheric stratification. Hilburn et al. (2006) stated that rain changes the ocean surface roughness, backscatters the radar pulse and reduces its transmission through the atmosphere. Ku-band instruments are more sensitive to rain than the C-band ones.

SST influences the viscosity of the upper water layer, in contact with the atmosphere, where the wind stress is applied. Higher (lower) SST results in lower (higher) viscosity, which for a certain wind speed causes more (less) wind stress therefore more (less) surface roughness. Thus, higher (lower) SST will cause more (less) backscattering, the scatterometer will record higher (lower) σ_0 values and the derived wind speed will be higher (lower). Moreover, SST party adjusts the atmospheric stratification which also affects the backscattered signal. Under very stable conditions, the surface winds are decoupled from the higher layers and tend to be lower, thus the surface stress is lower and also σ_0 is lower. But the atmospheric stability also defines if there is any discrepancy between the scatterometer derived wind speed and the "surface truth" (see Section 2.1, The Equivalent Neutral Wind).

Since the scatterometer receives the backatter signal from the sea surface, the derivation of surface stress will be relative to the sea surface. Strong currents can contaminate the wind velocity measurement. Halpern (1988) measured higher (lower) stresses when the wind and current were in opposite (same) direction. Dickinson et al. (2001) used measurements from the Tropical Atmosphere Ocean (TAO) buoy array and found that NSCAT measured the stress relative to the moving ocean surface and that when the current and wind had the same (opposite) direction, the scatterometer speed was expected to be lower (higher) than in situ wind speeds.

As stated in Hoffman & Leidner (2005), light winds can pose a problem for the wind retrieval as in such cases the ocean surface is very smooth and acts more as a reflector rather than a scatterer. Very high winds can also be problematic as the buoy and modelled data used to calibrate the GMFs under-represent very high

winds.

The range of applications for scatterometer winds is wide, including storm tracking, climate studies, air-sea interactions, propagation of polluted air masses, CO_2 fluxes (Boutin et al., 2009), assimilation in Numerical Weather Prediction (NWP) models and commercial applications, like ship route monitoring and recently wind energy. An overview of the progress in scatterometry applications can be found in Liu (2002).

Missions

The first operational space-borne wind scatterometer was the Seasat Scatterometer (SASS), launched in 1978 and sponsored by the National Aeronautics and Space Administration (NASA) of the United States. It operated at the Ku-band frequency (14.6 GHz) and provided data for 105 days. More than a decade later, in 1991, the European Space Agency (ESA) launched the first European Remote Sensing (ERS)-1 satellite which failed in the year 2000. The Advanced Microwave Imager (AMI) on board ERS-1 operated at 5.3 GHz (C band), allowing for a low resolution scatterometer mode and a high resolution SAR mode.

ERS-2 was launched in 1995 and in 1996, the NASA Scatterometer (NSCAT) was launched on board the Advanced Earth Observing Satellite (ADEOS) mission of Japan. In 1999, NASA launched the SeaWinds scatterometer onboard the QuikSCAT platform while in 2002, NASA in collaboration with the National Space Development Agency of Japan (NASDA) launched another SeaWinds instrument on board the Midori-II (ADEOS-II) satellite, with which communication was lost as of October 2003.

ESA launched the Advanced Scatterometer (ASCAT), a C-band instrument onboard the MetOp platform in 2007. Most recently, the Indian Space Research Organization (ISRO) launched Oceansat-2 in the 23rd of September 2009, carrying a Ku band scatterometer with a swath of 1400 km.

Throughout the years of scatterometer space missions, the geophysical model functions have evolved as more scatterometer measurements were available and more validation studies were performed. The SASS-2 GMF was developed by Wentz et al. (1984), using the statistics from 3 months of SASS measurements and a mean global wind speed from a climatology.

When the ERS-1 was launched, due its different operating frequency compared to the SASS, a new type of GMF was required. Several campaigns collected data to

relate σ_0 from air-borne instruments with in situ observations from research ships and buoys, resulting in the pre-launch CMOD2 GMF (Offlier, 1994). The operational ERS-2 CMOD4 function was developed by Stoffelen & Anderson (1997), using satellite derived σ_0 and 10 m winds from the European Centre for Medium-Range Weather Forecasting (ECMWF) analysis.

Hersbach et al. (2007) released the CMOD5 function to correct for deficiencies in the CMOD4 version, fitting measurements of extreme backscatter and winds, obtained from aircraft and in situ data. Hersbach (2010) developed the CMOD5.N version tuned to wind at 10 m above the surface assuming neutral atmospheric stratification,

The NSCAT mission resulted in a new GMF, based on the correlation of the radar backscatter with modelled winds from ECMWF and SSM/I wind speeds, as described in Wentz & Smith (1999). The SSM/I GMF was based on a model for the brightness temperature of the ocean and the atmosphere above, which is calibrated using buoy and radiosonde data as described in Wentz (1997).

The Equivalent Neutral Wind (ENW)

The GMFs resulting from the SASS scatterometer in the Ku band of the electromagnetic spectrum, related σ_0 to the wind at 10 meters above the sea surface assuming a neutral atmospheric stratification. This is known as the ENW (Liu & Tang, 1996). To get the ENW, observations from buoys are used to estimate the friction velocity using the observed stability. The friction velocity is then used to estimate the 10 m wind assuming a neutral atmosphere. Finally, this 10 m wind is related to the observed σ_0. The GMFs of the CMOD family refered to non-neutral winds until CMOD5.N which is currently being used for the ASCAT scatterometer (Hersbach, 2010).

The stratification between the sea surface and the first 10 m is not always neutral, and depending on the conditions the ENW may be an overestimated (if unstable) or underestimated (if stable) version of the true wind. Brown et al. (2006) found that the globally averaged 10 m neutral winds from the ECMWF were 0.19 m s^{-1} stronger than the standard 10 m ECMWF winds and concluded that the marine boundary layer is overall slightly unstable.

2.2 QuikSCAT

The SeaWinds scatterometer on board NASA's QuikSCAT platform, hereafter named QuikSCAT, was the first scatterometer to operate for many consecutive years. It provided valuable, consistent and frequent observations of the global ocean both in terms of speed and direction. QuikSCAT was launched in June 1999 with a design life-time of 3 years, as a quick recovery mission to fill the gap from the loss of NSCAT. The scatterometer's antenna failed rotating on the 23rd of November 2009, far exceeding the design life-time.

At an altitude of 803 km, QuikSCAT completed each orbit in approximately 101 minutes, ascending in the morning and descending in the afternoon (see Figure 2.2 for an example). With a wide swath of 1800 km it covered 90% of the global ocean each day. The SeaWinds scatterometer, onboard QuikSCAT, was an active microwave radar operating at 13.4 GHz (Ku band), radiating microwave pulses through a 1 m diameter antenna, and measuring the power of the signal returning back to the instrument. The σ_0 "footprint" cell had dimensions of 25·37 km and the averaging area, the Wind Vector Cell was a square box of 25·25 km.

Note that, each σ_0 "footprint" cell, also called "the egg", consists of 12 slices. σ_0 is calculated for both the full "egg" and for each of the 8 inner slices. This means that SeaWinds measures σ_0 at a variety of sizes, i.e. the "footprint", the inner slices and a variety of "footprints" composed of combinations of slices. For more information, see Martin (2004). Backscattered signals were received from the sea, land and ice but the scattering processes over land and ice are different than those over open ocean. Therefore, the scattering from land and ice can contaminate the WVC and needs to be identified and removed. For this reason, a land and sea ice mask is applied and σ_0 measurements falling over this mask are not included in the WVC.

The mission was managed by the Jet Propulsion Laboratory (JPL), operational products were produced at the National Oceanic and Atmospheric Administration (NOAA) for the international meteorological community and were released Near-Real-Time (NRT), i.e. within 3 hours of the data collection. More information can be found in http://winds.jpl.nasa.gov/missions/quikscat/index.cfm. The mission requirements were i) an rms of 2 m s^{-1} for a wind speed range between 3-20 m s^{-1} and 10% within the 20-30 m s^{-1} range and ii) an rms of 20° for the direction within the wind speed range 3-30 m s^{-1}. Science products were distributed through the Physical Oceanography Distributed Active Archive (PO.DAAC). More information on the science data products can be found in JPL (2006).

Different scientific groups applied different GMFs and methodologies for the wind

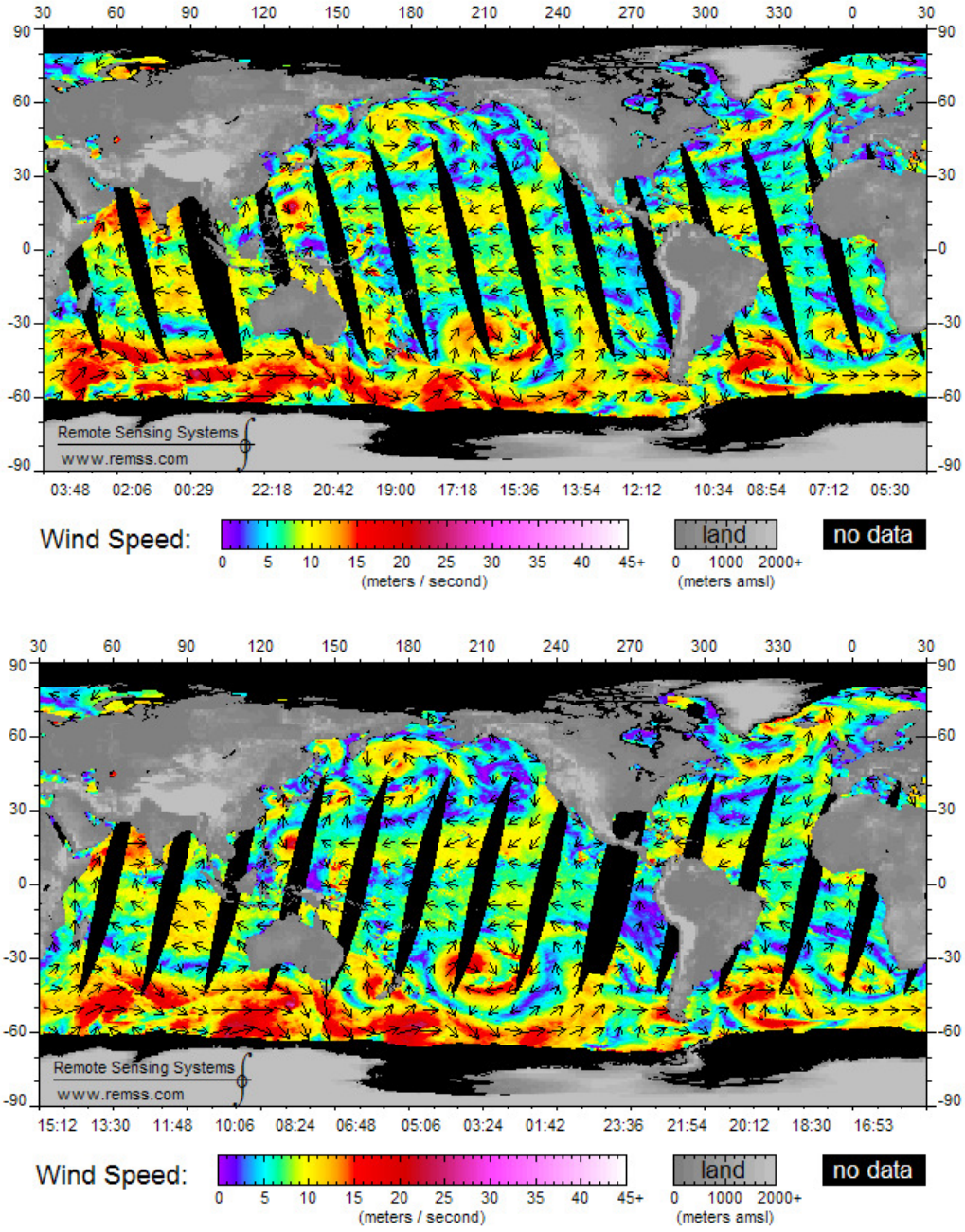

Figure 2.2: Examples of the ascending, in the morning (top) and descending, in the afternoon (bottom) swath modes of QuikSCAT. The example is from the 4th of July, 2006 like the measurements from Figure 1.1a. Note the low wind speeds in the North Sea. Images are courtesy of RSS.

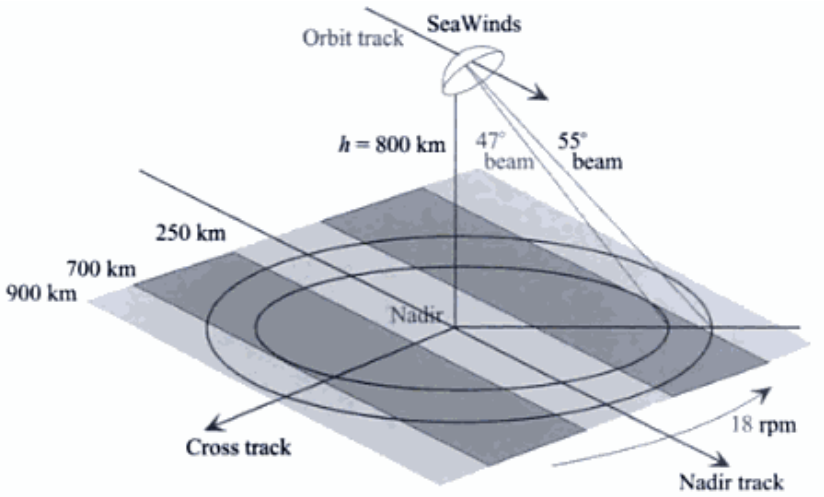

Figure 2.3: Graphical representation of the scanning geometry of the SeaWinds scatterometer on the QuikSCAT platform. The darker areas are covered by four looks of the antenna beams, while the light areas by two looks. Taken from Martin (2004).

retrieval, resulting in a variety of different products. Some of these products are being reprocessed when new, improved GMFs are released. The initial GMF was the NSCAT-2 but from 2000 to 2006 JPL derived wind velocity from QuikSCAT using the QSCAT-1 GMF (PO-DAAC, 2001), developed during the calibration/validation phase. From 06/2006 and afterwards, they used the QSCAT-1/F13, recalibrated for wind speeds above 16 m s^{-1} using speeds from SSM/I 13. The Dutch Meteorological Institute (Koninklijk Nederlands Meteorologisch Instituut (KNMI)) has processed data using the NSCAT-2 GMF for the Ocean & Sea Ice Satellite Application Facility (OSI SAF). They also applied a rather different methodology for the ambiguity removal and selection of the "best" solution for the WVC. RSS has been releasing swath and gridded QuikSCAT data using a family of descendants from the NSCAT-2 GMF, named Ku-2000, Ku-2001 and recently Ku-2011.

In addition to the different GMFs used to derive winds, various products exist ranging from the σ_0 observations time-ordered and earth-located (Level 1 (L1)), ocean wind vectors in a swath grid (Level 2B (L2B)) and gridded ocean wind vectors (Level 3 (L3)). The data set used in the present study has been processed with the Ku-2001 GMF which is a descendant of the NSCAT-2 GMF, itself being an improved version of the NSCAT-1 GMF (Wentz & Smith, 1999). For this product, σ_0 values are mapped to a 0.25° Earth grid. The data and documentation are available from RSS (see http://www.ssmi.com/qscat/qscat_browse.html).

2.3 Synthetic Aperture Radar (SAR)

Side looking SARs also transmit microwave pulses and receive the backscattered signal from a surface, similar to the scatterometer. The difference is that, using a variety of techniques, the return signal from a large area is separated in the contributing signals from many small areas. The relative changes in the backscattered signal are displayed as an image, where darker areas correspond to lower backscattered signals and brighter signals, to stronger backscatter (Martin, 2004).

The high spatial resolution of SAR is of great importance for various applications as a wide variety of surface phenomena can be displayed. Examples are ocean swell, surface slicks, internal waves and sea ice (Martin, 2004). Meteorological phenomena that can be visualized, after wind retrieval has been performed are island and mountain wakes, gap flows, synoptic fronts and lows, meso-scale lows, convection, coastal barrier jets (Beal et al., 2005) and offshore wind farm wakes (Christiansen & Hasager, 2006; Hasager et al., 2006).

Depending on the signal processing, the resolution can be very high, in the order of meters. Also, for the operating frequencies of SAR instruments, from 1 up to 9 GHz, the atmosphere is almost transparent except for heavy rain. For frequencies less than 1 GHz, radar signals are affected by absorption and reflection in the ionosphere, by terrestrial sources of radiation and by galactic radiance. At frequencies higher than 10 GHz, the signal is affected by atmospheric absorption (Martin, 2004).

SAR instruments consist of two parts; the antenna and the memory or "echo store". They depend on the spacecraft's motion to generate an image and have very large antennas; typical dimensions are 10 m in the along track and 2 m in the cross track direction. The antenna looks at the side of the spacecraft, at incidence angles ranging between 20° and 50°. It consists of many transmitter/receiver modules, distributed over the area of the antenna, in what is known as an active phased array. The cross track resolution is determined by the pulse length while the along track resolution depends on the azimuth angle (azimuthal resolution). SARs can achieve an optimum azimuthal resolution of half the antenna length.

Such resolutions are achieved due to the "echo store", that stores the amplitude and phase of each radar pulse backscattered from a small surface, forming what is known as a coherent radar. Thus every point that has been illuminated by a radar pulse, has a unique record of information stored. If the relative positions of the surface elements do not change during the illumination period, then a computationally expensive processing of the pulse sequence takes place to produce the high resolution image (Martin, 2004).

SARs operate in different modes; the Standard mode has a 100 km swath and a typical resolution of 25 m. The ScanSAR mode has a wider swath, between 350 and 500 km and a lower resolution of 75-150 m. In order to reduce random noise in the SAR imagery (speckle) and effects of long-period oceanic waves, which affect the radar incidence angle, it is necessary to average the pixels to approximately 500 m before wind retrievals are performed. Note that these resolutions are far higher than the typical 25 km scatterometer ones. Routine wind retrievals from SAR are not performed by the space agencies. The processing of radar backscatter to wind speed must be performed by the data users.

A basic difference is that SARs operate with one viewing angle therefore multiple wind speed and direction measurements correspond to one σ_0 value thus no ambiguity selection can be performed only based on the SAR data. An a priori knowledge of the wind direction is required during the wind retrieval, to derive the wind speed. This requirement introduces errors in the derived wind speed that depend on the source of the wind direction input. Such inputs can be obtained from NWP models, scatterometers, in situ measurements (improved accuracy (Christiansen et al., 2006)) or from streak features in the SAR images that are assumed to be approximately aligned to the wind direction.

Missions

Like the first operational scatterometer, the first operational SAR at 1.3 GHz, was on board NASA's SEASAT mission. In 1991, the Soviet Union launched a SAR instrument on the ALMAZ satellite, a mission that lasted 1.5 years. ERS-1 and ERS-2 had AMI, operating at 5GHz and with three modes, the SAR Image and Wave modes and the wind scatterometer mode. The Japanese Earth Remote Sensing (JERS)-1 platform carried a SAR instrument and the mission lasted for 2 years.

The Canadian RADARSAT-1 was launched in 1995, with a mission life-time of 5 years. The SAR instrument operated at 5.3 GHz and was the first operational satellite SAR with a wide swath. RADARSAT-2 was launched in 2007. ESA's ENVironmental SATtelite (ENVISAT), launched in 2002, carries the Advanced SAR (ASAR) operating at 5.6 GHz. The Phased Array L-band Synthetic Aperture Radar (PALSAR) instrument on board the Japanese Advanced Land Observing Satellite (ALOS) operates at 1.3 GHz and the mission started in 2006. TerraSAR-X is a German earth observation platform, launched in 2007, carrying an active phased array X-band SAR operating at 9.6 GHz. In 2010, a second satellite was launched, TerraSAR-X Add-oN for Digital Elevation Measurement (TanDEM-X). Future missions include ESA's Sentinel-1, scheduled for 2013, that will carry an

ASAR instrument on board.

The Johns Hopkins University Applied Physics Laboratory (JHU/APL) has developed the APL/NOAA SAR Wind Retrieval System (ANSWRS), currently used for near-real-time SAR wind retrievals in various facilities, including the DTU Wind Energy Department. ANSWRS produces high resolution SAR wind fields using wind directions from the Navy Operational Global Atmospheric Prediction System (NOGAPS) model (Christiansen et al., 2008). SAR retrieved wind maps can also be accessed from Collecte Localisation Satellites (CLS), through the SAR Ocean Products Demonstration (SOPRANO).

ENVISAT ASAR

The Advanced SAR on board the ENVISAT platform operates at the C-band frequency (5.6 GHz), looking at the right of the flight path. It has a variety of operational modes, ranging from the SAR Image and Wave modes, two types of ScanSAR modes, one with a 1 km resolution and the other with 150 m and an alternating polarization mode with a resolution ranging between 30 and 150 m and a swath between 58 and 110 km. Its antenna consists of 320 transmit/receive modules.

The data from the various operational modes can undergo several levels of processing, to provide products of different levels. Level 0, or RAW data, contain all the information required for imaging. Level 1 is the geo-coded version of the RAW data while no gridded products are provided. The gridding procedure is up to the user.

SAR for Wind Resource Assessment

SAR wind fields have been used in the past for wind resource assessment purposes. Hasager et al. (2005) used C-band SAR retrievals from the ERS-2 to evaluate the quality of the retrieved winds compared to high quality meteorological data from an offshore mast. From a series of 56 SAR images, they found that when using wind directions from an offshore met. mast to retrieve the wind speed from SAR, the bias between in situ and SAR wind speeds was 0.5 m s^{-1}, the standard error 0.9 m s^{-1} and the correlation coefficient (R2) was 0.88. They also noted a strong spatial wind speed gradient at Horns Rev, in the west coast of Denmark where an offshore wind speed of 8 m s^{-1} was reduced to 5 m s^{-1} near the coast, for a distance between offshore and coastal areas of 60 km.

Hasager et al. (2006) used 85 ERS SAR images and 4 years of QuikSCAT observations to quantify the offshore wind resources in the North Sea. They concluded that SAR images were very appropriate for local-scale studies while QuikSCAT, very useful for basin-scale studies.

Christiansen et al. (2006) used C-band SAR from ERS-2 and ASAR wind retrievals at moderate wind speeds from 2 m s^{-1} to 15 m s^{-1} to quantify the total accuracy of wind resource assessment. From a total of 91 SAR images, they found a wind speed standard deviation of 1.1 m s^{-1} against in situ wind speeds when the in situ wind directions where used to initialize the wind retrieval. They also tested different GMFs for the wind retrieval, finding an agreement to $\pm 15\%$ of the in situ measurements for all the tested methods.

Hasager et al. (2008) used SAR and QuikSCAT to evaluate their potential use for offshore wind resource mapping. They produced average wind speed maps for the Baltic Sea based on more than 100 SAR images, highlighting the variability from coastal areas to the centre of the basin. From comparisons between QuikSCAT and 1-hr averaged in situ measurements they reported a standard error of 1.3 m s^{-1} for the wind speed and $\sim 15^{\circ}$ for the wind direction.

Recently, Hasager et al. (2011) performed a study on the statistics of wind resources in the Baltic Sea, using again ASAR retrievals from ENVISAT. Wind speeds from 10 offshore meteorological stations where compared to ASAR wind speeds. For a set of 875 collocated samples, they reported a correlation (R^2) of 0.783, standard deviation of 1.88 m s^{-1} and root mean square error (RMS) of 1.17 m s^{-1}.

2.4 QuikSCAT for Wind Resource Assessment Studies

One of the scopes of this study is to examine the applicability of scatterometer winds for the purposes of wind resource assessment. The main reasons are that, in particular QuikSCAT has an extended spatial coverage and a long temporal availability. Scatterometer winds are sensitive to the presence of rain therefore rain contaminated retrievals have to be excluded. One may argue that removing rain contaminated observations, alters the 10 year-long wind "climate" that this study aims to describe. This would typically be the case in the Tropics where rain is typically associated with storms and high wind speeds.

The impact of excluding rain contaminated QuikSCAT winds on the averaged statistics is investigated by examining the bias in mean wind speed and wind

power density. Figure 2.4 shows the estimated difference in data availability when the rain-free winds are subtracted from the full record. Thus, the figure shows the spatial distribution and amount of rainy grid cells.

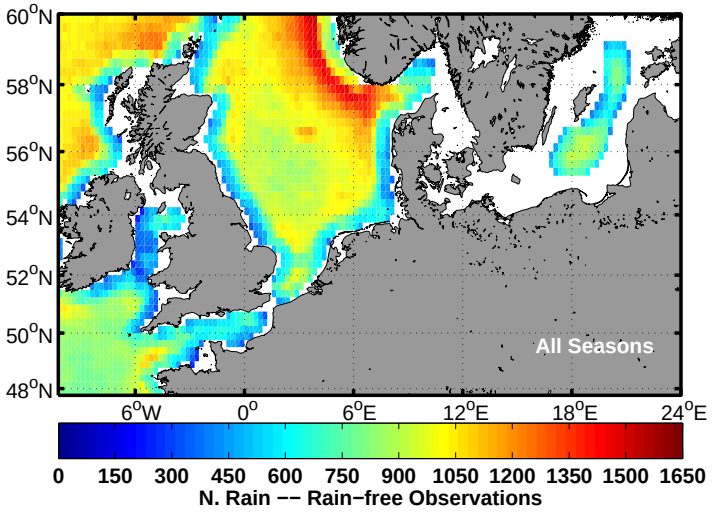

Figure 2.4: Difference in data availability between rain contaminated and rain-free QuikSCAT wind fields.

Maximum data loss reaches up to 1650 observations, while there is a maximum of 7215 rain contaminated observations and a maximum of 6913 rain free observations. In coastal areas of the North Sea differences are no more than 600 observations. The coastal areas of the Baltic Sea are excluded from the analysis due to insufficient coverage during winter and spring. The difference in mean wind speed (Figure 2.5) does not exceed 0.25 m s^{-1}. The wind power density estimates (Figure 2.6) differ by a maximum of 50 W m^{-2}. When the data availability difference is up to 600 observations, biases are very small; $\sim 0\ m\ s^{-1}$ for u and $\sim 5-10\ W\ m^{-2}$ for the wind power density.

The reduced difference in rain-contaminated versus rain-free data availability along the coasts of the British Isles and Europe is an artefact of the SSM/I rain flag. The QuikSCAT gridded product includes two different rain flags, one of which comes from SSM/I observations. Due to the proximity to the land this flag does not contain information in these coastal areas. Therefore, for these locations only one rain flag is active and less observations are classified as rain-contaminated. The remaining rain flag, is a "goodness-of-fit" flag and provides information regarding the match between the observation and the GMF. The scatterometer flag may be zero while the collocated radiometer measures rain and vice versa. In general, the scatterometer rain flag is less reliable at very high winds when it is more often zero even in the presence of rain, due to a large variability of observations within a wind cell (RSS support, personal communication).

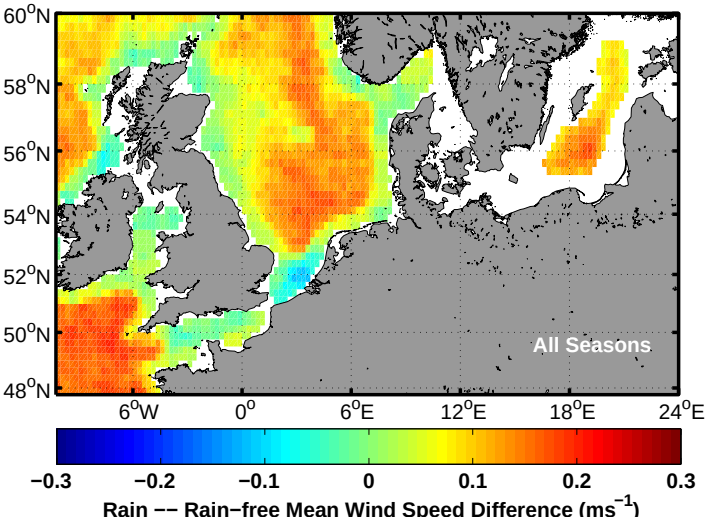

Figure 2.5: Mean wind speed difference between the rain contaminated and rain-free winds.

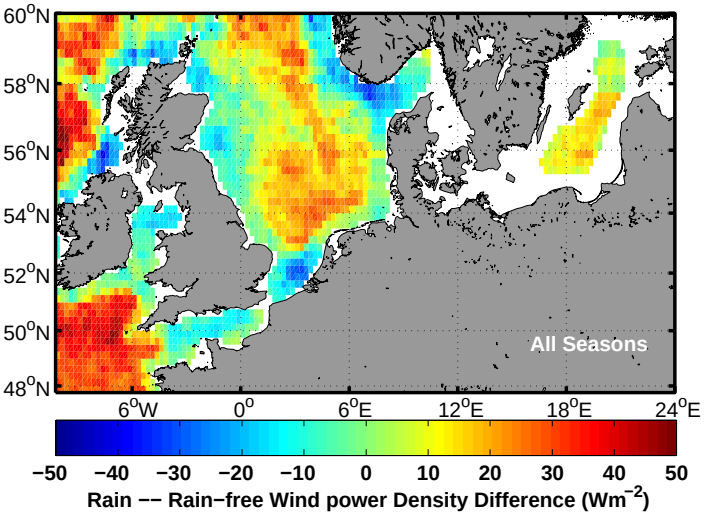

Figure 2.6: Difference in wind power density estimates from rain contaminated and rain-free winds.

One should keep in mind that these estimates refer to 10 m above the surface. The possibility of underestimating the wind at 10 m, when using only rain free wind retrievals, is thought to be a safer approach therefore more preferable. It is important to clarify that no inter-comparison of different QuikSCAT products was attempted. In Appendix B some basic sensitivity studies are presented, using the JPL L3 product. Results show that this product has many gaps and that the rain-

flagging schemes applied in the two products are different. The gaps in the JPL L3 product are interpolated in the RSS product, using a standard technique. Thus, the RSS product is thought to be more appropriate for wind resource assessment studies, as the interpolation of gaps is standardized. Further investigations were not performed as it was outside the scope of the study to compare scatterometer flagging schemes or products.

QuikSCAT and In Situ Measurements

Despite the extended validation studies existing for QuikSCAT that compare the satellite observations with in situ measurements from buoys and research ships and investigate potential biases, not many studies have used measurements from the North Sea or the Baltic Sea. Winterfeldt (2008) compared a L2B 12.5 km QuikSCAT product with in-situ observations from buoys and rigs in the Eastern North Atlantic and the North Sea for 2002. The study concluded that biases were negligible for all stations and that the mission requirements are met for these areas of the global ocean. A study for wind resource assessment from Hasager et al. (2008) compared the RSS product with in situ measurements from an offshore met. mast with standard errors $\sim$1.3 m s^{-1} for the wind speed and $\sim$15 for the direction. Moreover, there was a very small difference in their estimation of the mean wind speed and the Weibull A and k parameters from $\sim$3.200 QuikSCAT observations and $\sim$260.000 in situ measurements.

To evaluate the performance of QuikSCAT winds, observations from three offshore meteorological masts in the North Sea are used for comparisons. Since QuikSCAT represents the ENW, in situ observations must be converted to that. Measurements at available heights closest to 10 m are extrapolated using local stability information. As satellite winds represent near instantaneous spatial averages over 25 km, one would average the in situ measurements over a period of typically 1 hr. This is not performed in the present study due to the lack of good quality extrapolated in situ measurements. For more information on the locations and the data availability one is referred to Paper I.

Figure 2.7 shows the scatterplots for the wind speed and direction between collocated QuikSCAT and in situ observations. Note the lower limit 3 m s^{-1} for the wind speed as the QuikSCAT biases below that threshold are expected to be high. Moreover, the scatter in speed is rather large for speeds above 15 m s^{-1} due to the limitations of QuikSCAT and the GMFs. Nonetheless, overall biases for the wind speed are in the order of zero ($\pm$1.2 m s^{-1}) and 2.3° ($\pm$15°) for the wind direction.

To assess the impact of the relatively low temporal frequency (twice daily) of

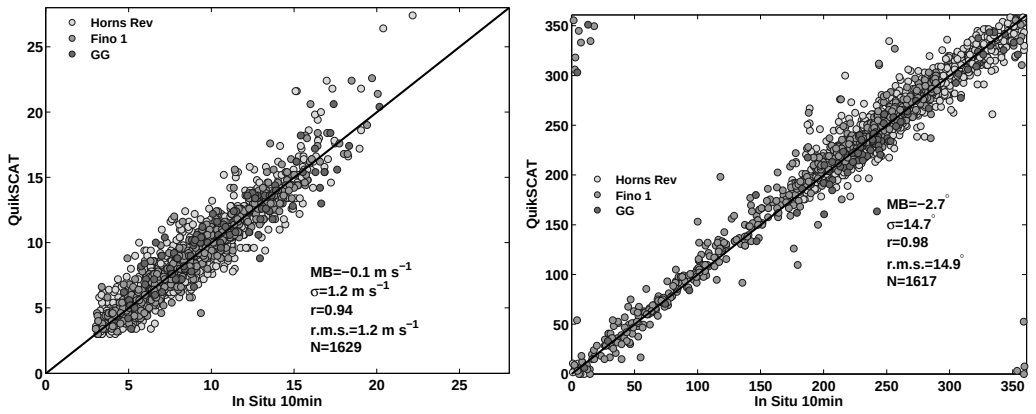

(a) (b)

Figure 2.7: Scatter plots of (a) wind speed and (b) wind direction. Only wind speeds higher than 3 m s^{-1} are considered. For one met. mast, only the open sea sectors are considered due to its proximity to land.

QuikSCAT as opposed to the high frequency 10-min in situ measurements, the mean wind speed and the wind power density are estimated. Table 2.1 shows such estimates, using the 10 m wind from QuikSCAT against the 10 m ENW and the 10 m Stability Dependent In Situ (SDIS). There is a maximum 2.7% deviation for the wind speed and 14% for the wind power density.

Another way to evaluate the impact of the low temporal frequency of QuikSCAT against the frequent 10-min measurements is to assess the monthly wind variability over a long term mean, i.e. the intra-annual index. Figure 2.8 shows this variability estimated using in situ measurements from one offshore location, QuikSCAT and the NWP model Weather Reasearch & Forecasting (WRF) (more on QuikSCAT and WRF follows in Section 2.5). All available 10-min in situ measurements are used (50426), the QuikSCAT rain-free retrievals (956) and the time coincident WRF 10 m neutral wind fields. No filtering for wind speed below 3 m s^{-1} is applied. Values of 1 indicate monthly wind speeds equal to the averaged long-term mean, while values above and below 1 indicate higher and lower mean monthly winds.

Note that QuikSCAT provides a slightly higher index from January until March and does not capture the local minimum of February. The variability during spring, summer and early autumn is properly resolved. From September until December the proper trend is reproduced but the magnitude of the variability from QuikSCAT is smaller than the in situ winds. This is highlighted by the value of the intra-annual index which for QuikSCAT is closer to 1, showing less variability around the mean value.

Table 2.1: Wind power density estimates from QuikSCAT and in situ observations for two of the three offshore locations.

	Product	Sample N.	u ($m\ s^{-1}$)	u Dev.(%)	E ($W\ m^{-2}$)	E dev. (%)
M2						
	QSCAT	1601	7.97	2.7	515	14.0
	10 m ENW	1601	7.93	2.2	479	6.0
	10 m SDIS	1601	7.88	1.5	470	4.0
	All 10 m SDIS	137717	**7.76**	–	**451**	–
Fino 1						
	QSCAT	642	8.42	0.8	593	2.6
	10 m ENW	642	8.26	−1.1	563	−2.5
	10 m SDIS	642	8.45	1.5	575	−0.5
	All 10 m SDIS	50349	**8.35**	–	**578**	–

	Product	Sample N.	U ($m\ s^{-1}$)	Weibull k	E ($W\ m^{-2}$)	Weibull A ($m\ s^{-1}$)
M2						
	QSCAT	1601	7.98	2.38	509	9.00
	10 m ENW	1601	7.94	2.55	477	8.94
	10 m SDIS	1601	7.89	2.55	467	8.89
	All 10 m SDIS	137717	**7.77**	2.54	**449**	8.76
Fino 1						
	QSCAT	642	8.43	2.45	588	9.51
	10 m ENW	642	8.23	2.34	567	9.30
	10 m SDIS	642	8.45	2.55	574	9.52
	All 10 m SDIS	50349	**8.36**	2.43	**575**	9.42

The lowest below-mean variability from in situ measurements at FINO-1 is ∼48%, observed in July. The QuikSCAT computed lowest below-mean variability is ∼45% for the same month. Highest above-mean variability is observed in January, reaching ∼10% from both in situ measurements at FINO-1 and QuikSCAT. In general, QuikSCAT can be descriptive of the synoptic conditions, properly reproducing the seasonal trends but lacks the local accuracy of the in situ wind measurements. For more details see Paper II.

Wind Characteristics from QuikSCAT

A parameter of interest in wind resource assessment studies is the mean wind speed. Figure 2.9 shows this as estimated from more than 10 years of QuikSCAT observations over a large domain; information like that can not currently be obtained from in situ measurements. Interesting local features include an area of

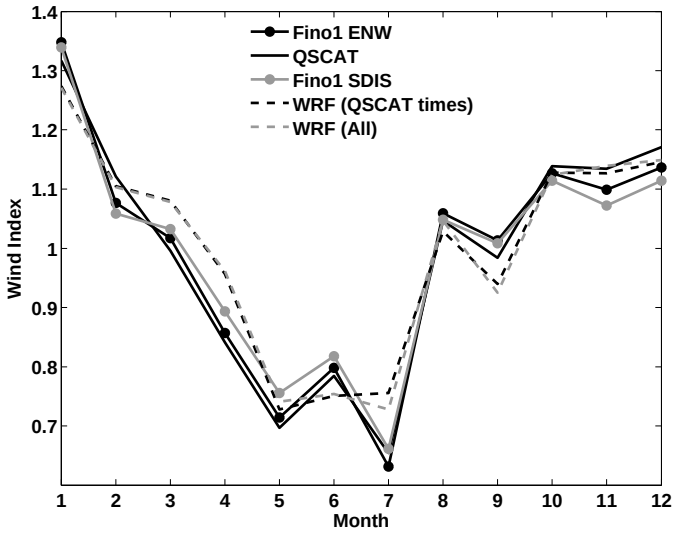

Figure 2.8: Intra annual index at FINO-1 from in situ observations, QuikSCAT and the neutral WRF model re-analysis.

significantly high wind speeds offshore from Belgium, the Netherlands and the UK, due to channelling effects from the English Channel. Strong lee effects in the western North Sea are likely due to land effects from the British Isles. In the eastern North Sea, around 55°N–8°E, an area of lower wind compared to the surroundings can be a result of lee effects when winds blow from southerly and easterly directions. Another explanation may be linked with the tidal currents existing in the area that will cause errors in the scatterometer winds. Note the higher wind speeds in the North Atlantic and the northern North Sea.

Wind rose distributions can be computed from QuikSCAT to demonstrate the wind direction frequency distribution. The extended spatial coverage of QuikSCAT allows such estimations over large domains as seen in Figure 2.10, where a variation according to topographic features can be identified. The spatial variation of the wind direction from offshore to coastal areas is well captured. A strong channelling flow is observed in the English Channel and the Baltic Sea. Also note the dominant westerlies over the British Isles. In the North Atlantic when approaching the Norwegian coast, the wind rose distributions adapt to the coastal morphology as the main wind direction aligns parallel to the coast. However, the wind roses along the Norwegian North-West coast show a strong land component most likely due to katabatic winds from the mountains that extend at least 50 km offshore. For further details see Paper II.

QuikSCAT due to the twice daily coverage in early morning and evening is not able to properly resolve the diurnal variability. Figure 2.11a shows the mean morning

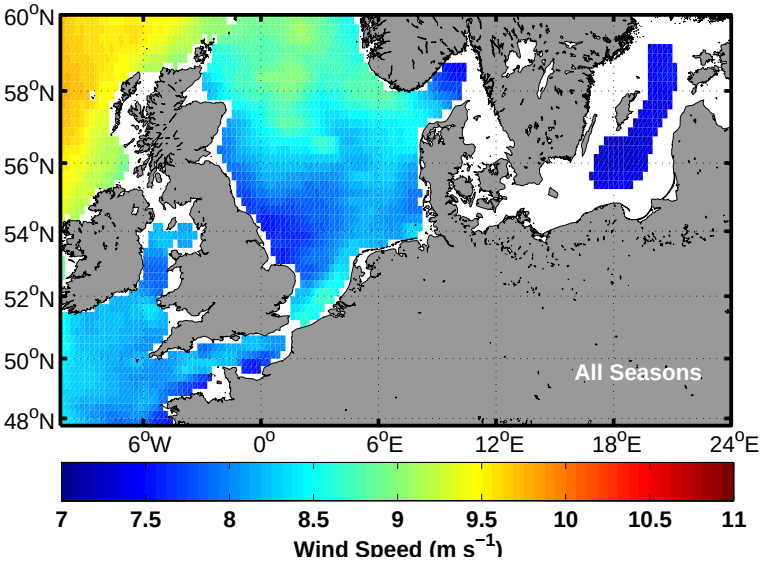

Figure 2.9: Mean wind speed from QuikSCAT, using twice daily observations from 08/99 to 10/09.

minus afternoon wind speed during summer. Warm colours indicate higher morning wind speeds, very pronounced in the east coast of the British Isles. This, in parallel with the wind roses from Figure 2.10 that show dominant westerly directions, may be an indication of land breezes, due to the faster cooling of the land during the night compared to the adjacent relatively warm sea. To the contrary, the waters between Denmark and Norway, experience higher wind speeds in the afternoon possibly due to diurnal warming of the sea surface temperature that drives unstable conditions and an increase in the near-surface wind field. In Section 3.5, Figure 3.7 shows a relatively high number of warming exceeding 2 K in this area. Figure 2.11b shows the number of observations for which the wind direction changes by 180°±45° between morning and evening. Most occurrences are found along the coastlines.

The spatial correlation between different locations is another important parameter as it can define the distances over which in situ measurements are representative. In addition, wind farms in areas with high spatial correlation are likely to have similar temporal wind power production as they will experience similar wind conditions.

Figure 2.12 shows the seasonal variability of the spatial correlation between one location with available in situ measurements (M2) and all other locations in the North Sea. The correlation is estimated using QuikSCAT observations. Values higher than 0.9 are identified for an area with seasonally stable size, approximately 160 km by 200 km around the west coast of Denmark. During winter and

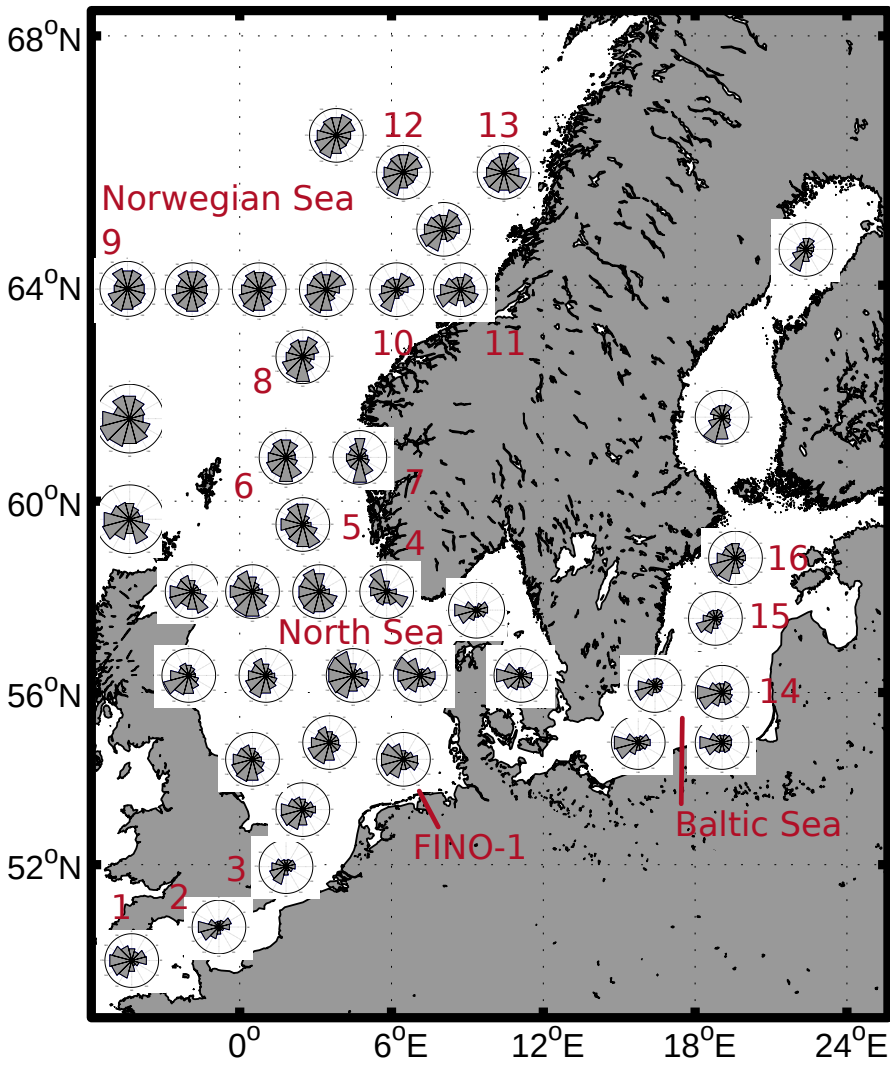

Figure 2.10: Wind roses for various locations in the domain, computed from 10 years of QuikSCAT data.

autumn correlation is higher further away from M2, due to the dominant synoptic weather patterns. This changes in spring and especially during summer, when distances between well correlated areas decrease due to the very local conditions. Nonetheless, high correlation is only limited to a fraction of the North Sea.

Typical quantities computed during a wind resource assessment study are the Weibull A and k parameters along with the wind power density. QuikSCAT observations can be used to evaluate such parameters, see for example Paper I. In order to estimate the wind power density, one can use the Weibull A and k parameters in Eq. 1.4 or directly the measured wind speed in Eq. 1.5. When QuikSCAT

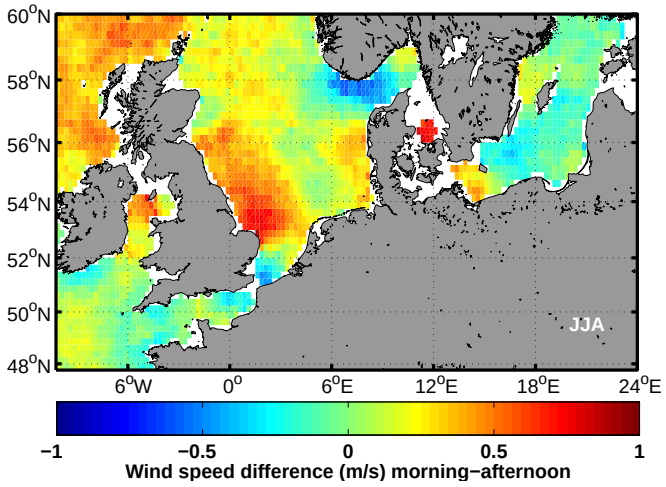

(a)

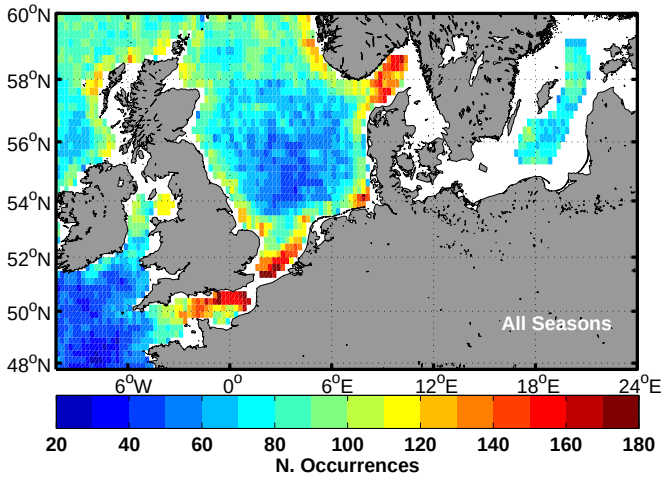

(b)

Figure 2.11: a)Mean morning minus afternoon wind speed from QuikSCAT for summer. b) Number of observed cases with a 180°±45° change in wind direction between the morning and evening pass.

winds are used, differences are observed between the two methodologies.

Figure 2.13a shows such differences; they are only around 10 W m^{-2}, in most of the domain. Both methods utilize the same number of rain free observations, shown in Figure 2.13b. Increased biases, that do not exceed 50 W m^{-2}, are identified for the North Atlantic. There the higher wind variability causes this bias, where the time-series method gives higher estimates. The Weibull fit is performed with a maximum

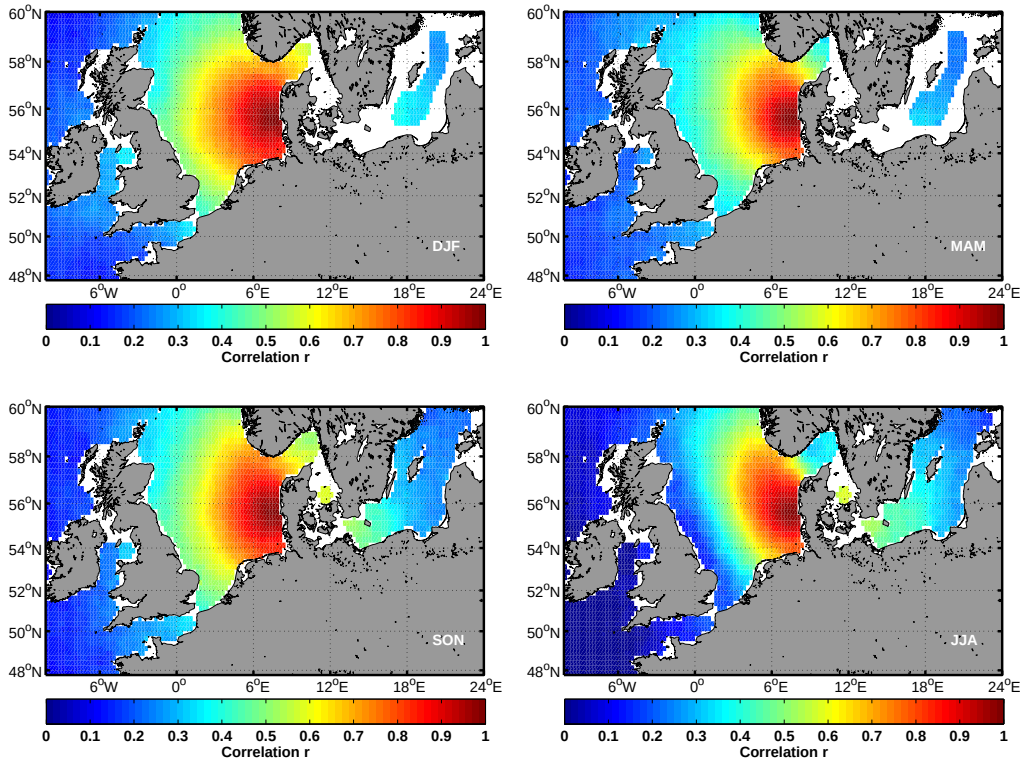

Figure 2.12: Seasonal spatial correlation of wind speed between QuikSCAT observations of the grid cell containing M2 and all other grid cells.

likelihood estimation algorithm that will maximize the fit of the distribution, thus above mean values may be under-represented.

2.5 QuikSCAT and NWP models

NWP models have been assimilating QuikSCAT until the end of the mission. Specific near-real time QuikSCAT products were developed for such purposes (Hoffman & Leidner, 2005). Within the context of wind energy, meso-scale models are used in different steps of the wind resource assessment study, e.g. as "observations" at heights or in locations where in situ measurements are not available, to evaluate the climatological means and for wind forecasting.

The advanced WRF model, developed at the National Center for Atmospheric Research (NCAR) is an atmospheric simulation and NWP system (http://www.

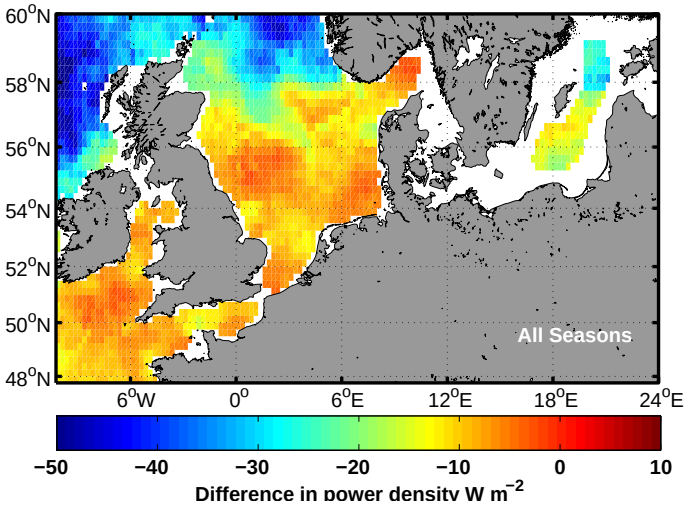

(a)

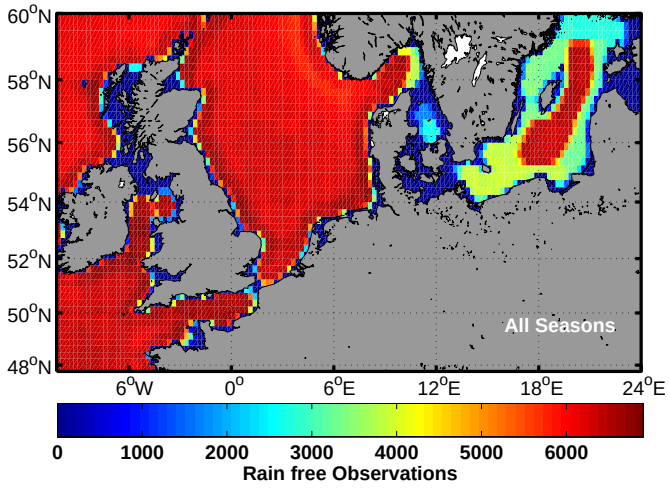

(b)

Figure 2.13: a) Difference in estimated wind power density from the Weibull fit to the QuikSCAT time-series (Eq. 1.4) and the QuikSCAT time-series (Eq. 1.5). b) Number of rain free observations used to estimate the wind power density.

mmm.ucar.edu/wrf/users/docs/user_guide/users_guide_chap1.html) that can be used for forecasting or producing re-analysis fields. A re-analysis is a climate or NWP model simulation of the past, that includes data assimilation of historical observations. Detailed information on the methodology used to produce the WRF climatography, hereafter mentioned as re-analysis, can be found in Hahmann et al. (2010).

Modelled wind fields can be compared with QuikSCAT at the 10 m level, to evaluate potential discrepancies. For example, in Paper II QuikSCAT is compared with the re-analysis dataset described in Hahmann et al. (2010). Figure 2.14a shows the computed mean bias; negative values indicate higher WRF wind speeds and positive values signify higher QSCAT wind speeds. Biases do not exceed 1 m s^{-1}, minimized in the North Atlantic. Generally, WRF wind speeds are higher for large parts of the North Sea and the central part of the Baltic Sea.

Figure 2.14b shows the standard deviation (σ) of the mean bias. Highest values are observed around Norway and the North Atlantic, in areas where the mean bias is low. There seems to be a strong north-south component for which the standard deviation is minimum in the South and increases towards the North. This signifies an area of discrepancy between the modelled and satellite fields. An explanation for this can be derived in combination with Figure 2.10, that shows the wind rose distributions in various locations. Note the constant wind direction frequency in the south-west, which indicates most frequent westerly winds. The wind roses at higher latitudes (around 60°N) along the same meridian, show much higher variability with wind directions from multiple sectors. This variability, likely not captured by the model, is depicted in the standard deviation of the mean bias.

The correlation between QSCAT and WRF is shown in Figure 2.15a, where values of R^2 higher than 0.65 are observed in most parts of the domain. Note the lower correlation in coastal areas and in the straight between Norway and Denmark, most likely due to contamination of the model winds from land winds, as discussed in Kara et al. (2009). The difference between the QSCAT and WRF estimated wind power density, shown in Figure 2.15b, ranges between 0 and 100 W m^{-2} in the largest part of the domain. An exception is the North Atlantic part, where the low mean wind speed bias found before, gives rise to differences of up to 200 W m^{-2}, where mostly QSCAT is higher. The large biases in the observed minus modelled wind power density in the North Atlantic are likely due to i) the wind variability not captured by the model and ii) the smoothing of winds from WRF.

The WRF climatography is descriptive of the long-term conditions and is not expected to be accurate when the day-to-day variability is of interest. Therefore, while the daily QSCAT-WRF biases are averaged out during the years producing a generally low mean bias not exceeding ± 0.6 m s^{-1}, the standard deviation is high, at least three times the overall mean bias and the correlation does not exceed 0.8.

The largest standard deviations and smaller correlations are observed in coastal areas of complex morphology and adjacent to land masses. There both data sources may be contaminated by errors. Due to the proximity of land masses, QSCAT may suffer from land contamination to the backscattered signal while WRF may underestimate the wind due to an uncertainty in the land mask and a lag in the

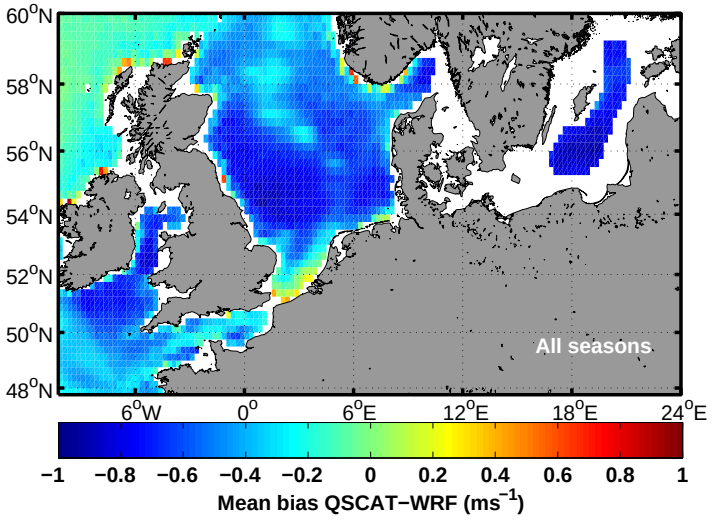

(a)

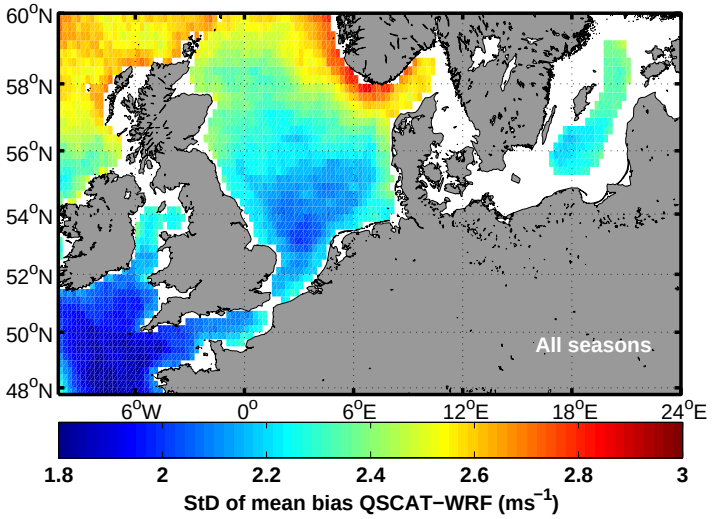

(b)

Figure 2.14: a) Mean bias and b) standard deviation of QSCAT minus WRF re-analysis.

change of the surface roughness and its value.

Other than validating re-analysis fields, QuikSCAT can be used to test the model set-up, as described in more detail in Appendix C. There, WRF is run with different set-ups for a test period of a month and the output fields are compared with QuikSCAT to evaluate which produces better agreement with the satellite

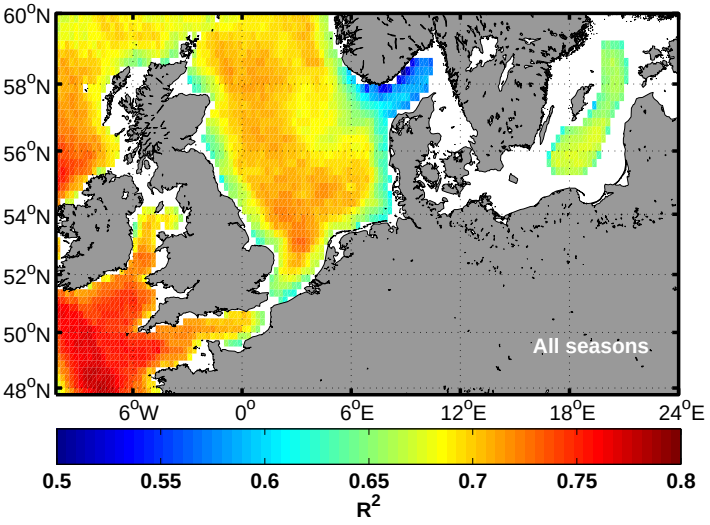

(a)

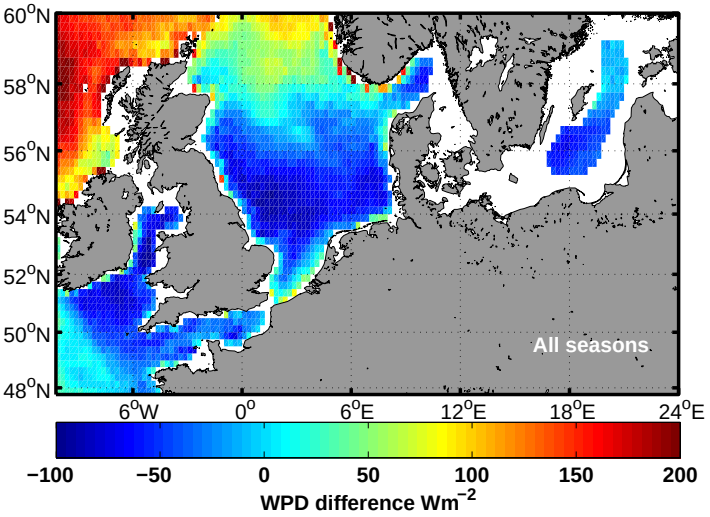

(b)

Figure 2.15: a) R^2 and b) wind power density difference of QSCAT minus WRF re-analysis.

observations. In addition, WRF can be used to test the temporal representativity of QuikSCAT, which has a maximum of two daily observations.

The mean wind speed and power density are estimated using all the available hourly WRF fields (maximum 87480) and only the ones time coincident with QSCAT (maximum 6913).The differences are shown in Figure 2.16. Data availability

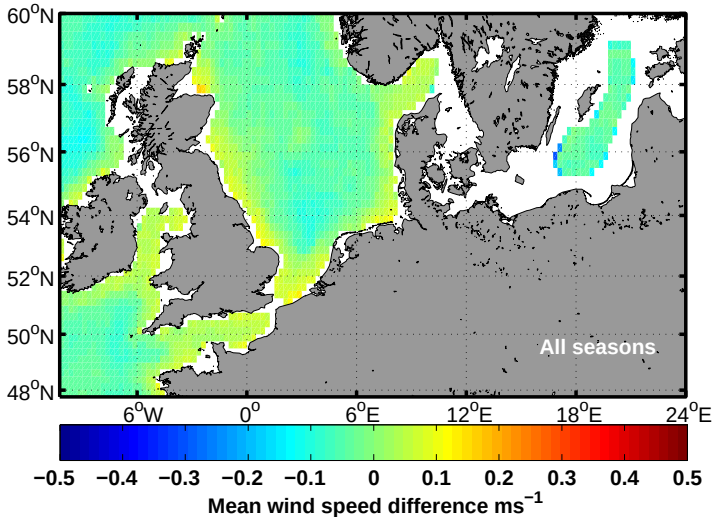

(a)

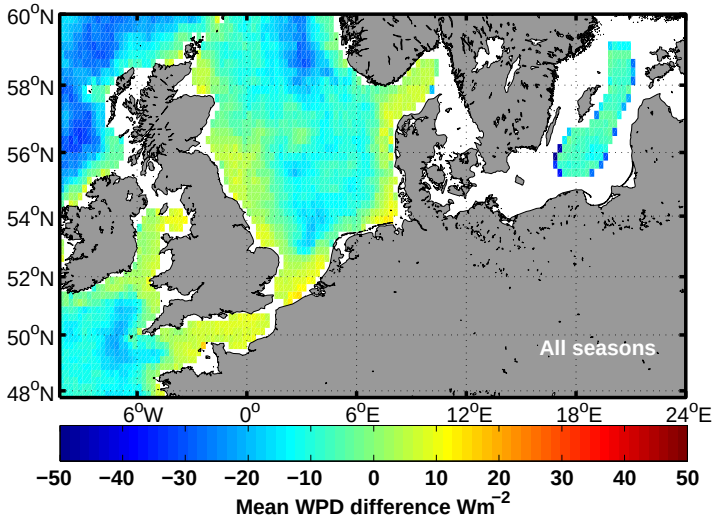

(b)

Figure 2.16: Difference between WRF on QSCAT times and all WRF fields for a) mean wind speed, b) wind power density.

differences are ∼81000 fields. Discrepancies are remarkably small; mean wind speed biases range between -0.1 and 0.15 m s^{-1} but they are around 0.5 m s^{-1} for a few grid cells in the Baltic Sea. The power density biases, see Figure 2.16b, range between -10 and 15 W m^{-2} for the largest part of the domain, while biases of 60 W m^{-2} are identified for the few grid cells mentioned above.

From this investigation it can be concluded that the temporal representativity of

QuikSCAT is high when the full dataset of 10 years is considered, as derived from a WRF re-analysis dataset. This conclusion is also supported by the very good comparison of QuikSCAt's intra-annual variability to the one derived from in situ observations, shown in Figure 2.8.

Thus, QuikSCAT other than being assimilated in NWP models, it can be useful for examining the model's performance in terms of spatial variability, which could only be achieved if a very dense network of in situ observations was available. In addition, QuikSCAT can be used to evaluate the temporal variability of re-analysis fields and help identify areas where the re-analysis datasets may not be representative.

2.6 Spatial resolution of satellite winds

As has been mentioned, multiple σ_0 values over the WVC of 25·25 km are used during the wind retrieval to finally derive one set of wind speed and direction estimates. Thus, QuikSCAT winds used in this study, represent near-instantaneous spatial averages, where small scale variability is eliminated. This is the case not only for QuikSCAT but for other types of satellite products as well, for example from SAR.

Currently, winds retrieved from space-borne SAR instruments are used in DTU Wind Energy to perform wind resource assessment studies (Christiansen et al., 2006). Therefore, it is important to examine the resolvable length scales as very often the mentioned resolution describes the field of view of the instruments (for SAR) or the wind vector cell dimensions (for QuikSCAT) rather than the minimum distance between two objects for them to be distinguishable.

SAR winds are available at much higher spatial resolutions compared to the QuikSCAT used in this study. Therefore, it is of high interest to evaluate the capabilities of the two products and examine their combined use. Due to temporal, spatial and availability mismatches it is thought that an effective way to evaluate them is the spatial spectral analysis. In this way, the spectral properties of each can be examined and more information on their spatial resolution can be obtained. While the QuikSCAT spatial spectral properties have been previously examined by other studies, only scales down to 12.5 km were investigated. This study examines the spectral slopes for scales between 2.5 and 800 km. Moreover, no available study regarding the spatial spectral properties of SAR fields so far exists.

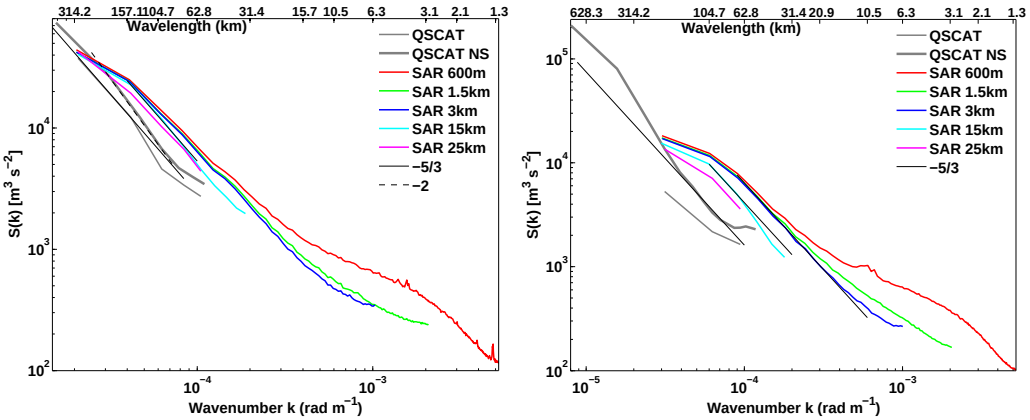

Figure 2.17: Averaged meridional (left) and zonal (right) spectra from SAR of various resolutions and QuikSCAT. Black lines show the -5/3 (solid) and -2 (dashed) slopes.

QuikSCAT fields have a resolution of 25 km. SAR wind retrievals are performed for a specific set of scenes after the image pixels have been averaged to different dimensions; i.e. 600 m, 1.5, 3, 15 and 25 km. The area of interest is a rectangle from 53°N–56°N and 6°E–8°E, selected as such due to the overlapping of 135 SAR images. This number is further reduced to 87 scenes. For more details on the data filtering, see Paper III.

Figure 2.17 shows the zonal and meridional component spectra of QuikSCAT and SAR, where the impact of resolution in the spectral power range is evident. QuikSCAT spectral tails turn and become horizontal for length scales around 60 km. This behaviour of QuikSCAT for spatial scales close to the Nyquist frequency has also been mentioned in Stoffelen et al. (2010), where it is attributed to noise. Similar findings are observed for the SAR 1.5 and 3 km products but for much smaller scales of 6 km.

For the meridional component, the 25 km SAR product shows higher spectral power content than the corresponding QuikSCAT. The length scales resolvable by the 600 m product are in the order of 2.5 km while for QuikSCAT ∼60 km. The spectral power of all SAR resolutions is higher than the QuikSCAT estimated one. This indicates the higher potential of SAR to capture small scale variability even when the resolution is coarse.

Comparisons are limited by the availability of SAR retrievals, for which frequent observations of the same area are not consistent. To the contrary, QuikSCAT offers 10 years of twice daily observations for the area of interest. To investigate how representative are the 87 available scenes, QuikSCAT spectra are also computed

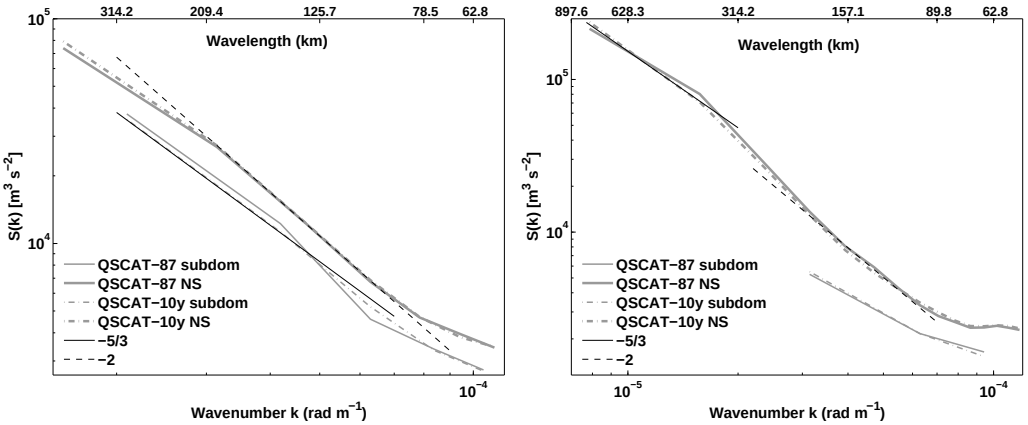

Figure 2.18: Averaged meridional (left) and zonal (right) spectra from QuikSCAT 87 scenes vs. QuikSCAT 10 years. Black lines show the -5/3 (solid) and -2 (dashed) slopes.

from the 10 years of available observations.

Figure 2.18 indicates that there is practically no difference between the 87 scenes and the 10 year-long dataset, which has a maximum of approximately 7000 scenes. When the seasonal variability is examined, the sample size ranges from 17-25 to 1200-1400 fields. In this case, there are more pronounced differences with general higher spectral power content for the larger sample sizes and all length scales, especially in winter and autumn. A detailed description of the analyses and results can be found in Paper III.

2.7 Summary

The objective of this chapter was to provide a brief introduction to radar scatterometry and demonstrate the applicability of near-surface ocean winds from scatterometers for wind resource assessment. Key concepts are summarized below:

- **Paper I** discusses the evaluation of the scatterometer wind fields when compared to in situ observations to asses the performance of the remotely sensed observations. Moreover, it examines various wind characteristics and provides wind resource estimates accounting for various different factors such as the methodology, the sample size and the sampling time.
- Comparisons of QuikSCAT with in situ measurements show in general good agreement, but the effective wind speed range limitations are obvious. Nonetheless, biases are found lower than in other studies.
- The biases of wind speed and wind power density estimates accounting for sample size, sampling time and stability related biases for two locations show a maximum 14% overestimation from QuikSCAT.
- Various parameters valuable for the wind resource assessment and the description of the synoptic conditions over large domains can be derived from the QuikSCAT observations.
- The detail of the derived results is not comparable with that of in situ observations. The extended spatial coverage of QuikSCAT provides unique information about the synoptic patterns over very large areas. Information that would require an extensive network of met. masts that is currently not available.
- Caution needs to be taken when interpreting results due to biases inherent in the scatterometer winds that arise from currents, SST variability and long-term stability trends. In certain cases, QuikSCAT winds will provide an overestimation of the true wind.
- **Paper II** examines the added value of scatterometer winds by comparisons with long-term re-analysis fields from the NWP model WRF and in situ data from an offshore location in terms of the spatial and temporal variability of the 10 m winds.
- QuikSCAT successfully reproduces the seasonal wind variability observed by in situ instruments. This is highly aided by the long time series of available QuikSCAT observations.

- QuikSCAT minus WRF biases are found low for the entire domain. Areas with high biases are related to both satellite and model inherent biases due to complex flow patterns and proximity to land.
- **Paper III** evaluates the spatial information that can be obtained from different satellite wind fields and their applicability for different parts of the wind resource assessment.
- The length scales identifiable from QuikSCAT and SAR winds are evaluated through spatial spectral analysis of the wind speed fields.
- QuikSCAT represents spatial averages over areas of 25×25 km; its resolution is a limitation for coastal areas where most of the offshore wind farms in Northern Europe currently operate.
- SAR winds have a very high spatial resolution, able to resolve small scale features on the ocean, not seen with scatterometers but until recently, their availability has been a constrain.
- Such findings highlight the importance of using SAR winds for a detailed analysis of the small scale features than cannot be resolved by the scatterometer product used in this study.

Chapter 3

Sea Surface Temperature

3.1 SST from space

Most of the incoming solar energy is absorbed by the land and the ocean and since oceans cover more that 70% of the Earth's surface, most of the incoming solar energy is absorbed there. Moreover, the greatest part of the solar energy incoming in the oceans, is absorbed within the first few meters, in the oceanic surface layer that essentially has the same heat capacity as that of the entire atmosphere. Thus, the temperature of the ocean surface is an important parameter, governing processes that occur in the upper part of the water column. Biological activity, exchange of gas, heat and momentum with the atmosphere depend on the near-surface ocean layer and its properties. Activities of scientific, commercial and political interest, such as weather forecasting, modelling of air-sea interactions, climate change studies, fisheries and coastal zone management respectively, require information about the SST in order to be more accurate and effective.

Traditionally SST has been measured with the use of thermometers. It has been one of the first oceanographic parameters to be measured, now having the longest time series of observations. Such observations were made by either submerging a thermometer in the water or in a bucket containing water retrieved from the ocean. Measurements from automatic instruments located at the engine room of ships increased the coverage of SST observations but were constrained only in the sailing routes, thus leaving a very large fraction of the ocean unobserved.

Satellites allow global and frequent observations and to determine SST from space, thermal infra-red and passive microwave radiometers are used. Radiometers measure the radiant power of electromagnetic radiation. They actually measure the emission from the Earth's surface at different wavelengths of the electromagnetic spectrum and these measurements are empirically related to the surface temperature. This principle of operation is based on the black body, i.e. a theoretical body that absorbs all incident electromagnetic radiation. Under thermal equilibrium, the black body emits radiation with a characteristic pattern that depends on its temperature. The amount of energy emitted at a particular wavelength is described by the Planck function (Eq. 3.1),

$$B_\lambda(T) = \frac{2hc^2}{\lambda^5} \frac{1}{e^{\frac{hc}{\lambda k_B T}} - 1} \tag{3.1}$$

where B is the radiance at wavelength λ, T is the absolute temperature of the black body, k_B is the Boltzmann constant, h is the Planck constant and c is the speed of light. Using the brightness temperature concept, i.e. the temperature a black body should have in order to emit an amount of radiation at a specific wavelength, the temperature of a surface is inferred from measurements of its radiance at various wavelengths.

As stated in Anding & Kauth (1970), the radiance from the water surface is attenuated by atmospheric components such as clouds and absorbing gases, which also scatter and emit energy that contributes to the total signal received by the satellite radiometer. To compensate for these effects the use of different bands of the electromagnetic spectrum is suggested, to perform simultaneous measurements of the incident radiance in two chosen bands.

This is similar to the scatterometry's requirement of multiple backscatter signal measurements from different viewing angles to determine the direction of the wind. Similar with scatterometry, SST retrievals from space are performed with the use of equations relating the temperature to brightness temperatures T_λ measured at various wavelengths λ, in the form of Equation 3.2.

$$SST = f(T_{\lambda 1}, T_{\lambda 2}, ...) \tag{3.2}$$

The coefficients for the equations can be derived either through regression analysis of measured brightness temperatures matched with in situ SSTs or, instead of measured, using modelled brightness temperatures from radiative transfer functions (Merchant, 2008). Typically, either the infra-red or microwave bands of the

electromagnetic spectrum are used, with advantages and disadvantages for both.

Infra-red radiation is emitted by the very top part of the ocean surface, the "skin" which has been found to be cooler than the water below (Saunders, 1967). Moreover, clouds absorb infra-red radiation therefore no measurement can be obtained under overcast conditions. Aerosols and water vapour scatter these bands of radiation thus atmospheric corrections are required prior to the retrieval of temperature. Advantages of infra-red sensors include the very high resolution and that signal retrieval close to land can be performed without many implications.

The emitted signal of microwave radiation is weaker, therefore the accuracy and resolution of retrieved temperatures are not as high as in the infra-red case. Despite that, microwave radiation is rather insensitive to clouds and not influenced much by atmospheric effects. It is, though, affected by the surface roughness and rain, as has already been described in Chapter 2.1.

Errors in space-borne SST retrievals are due to undetected clouds that absorb in the infra-red band, thus attenuating the signal that reaches to the radiometer. Stratospheric, from major volcanic eruptions, and tropospheric aerosols such as dust, smoke and haze scatter and attenuate radiation. Near surface stratification may cause biases between satellite SSTs and in situ measurements from buoys. Errors may also occur when specifying the retrieval coefficients. For more information see Merchant (2008) and references therein.

Applications for SST measurements from space include climate modelling, modelling and estimation of CO_2 fluxes, estimation of the Earth's heat balance, studies of the atmospheric and oceanic circulation, eddies, fronts, upwelling systems for navigation and primary productivity, fisheries and aviation.

3.2 SST Definitions

The marine surface layer is the layer below the air-sea interface, where the vertical temperature structure is variable and depends on the mixing and the exchange of heat, moisture and momentum between the atmosphere and the ocean. Radiometry introduced different types of sensors with different properties that can measure the temperature at different depths inside the water column and highlighted the requirement for an accurate definition of SST. The vertical structure of SST is depicted in Figure 3.1, described in this manner in Donlon et al. (2002) while references therein support this vertical structure with observational findings.

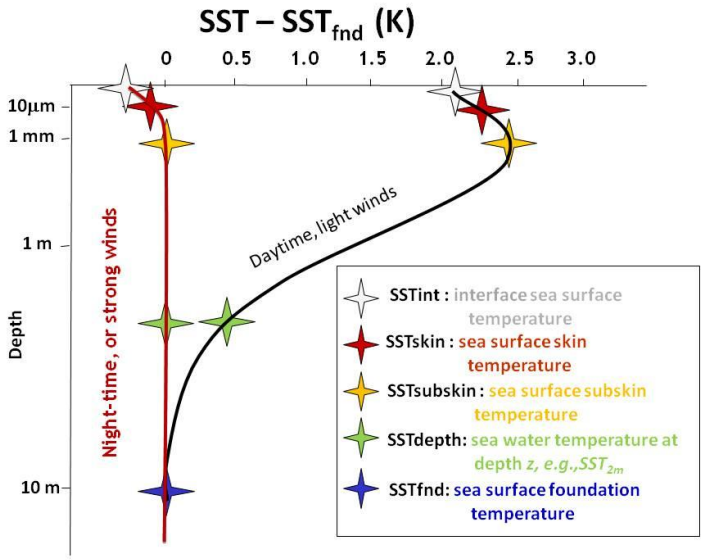

Figure 3.1: Vertical distribution of SST during night or under strong wind conditions (red line) and during the day under light winds (black line). Taken from Minnett & Kaiser-Weiss (2012), https://www.ghrsst.org/ghrsst-science/sst-definitions/.

The Group for High Resolution SST (GHRSST) Science Team has defined the "interface SST" as the temperature of the very top layer of the sea surface which is in direct contact with the atmosphere; currently there is no available technology to measure it.

The "skin SST" refers to the thin layer below the interface, between 10 and 20μm, typically measured by infra-red radiometers operating at wavelengths between 3.7μm and 12μm. The "sub-skin" layer, extending from the base of the skin layer down to approximately 1mm, has a temperature that is slightly different than the one of the skin layer, and is measured by microwave radiometers operating in the band from 6 GHz to 11 GHz.

Beneath the sub-skin layer, measurements of temperature are referred to as "depth SST" and the exact depth at which they are taken is required. The "foundation SST" refers to the temperature of the water column free of diurnal variability, thus it is the temperature upon which the diurnal heating develops. It is defined as the temperature at the first time of the day when the heat gain from the absorption of solar radiation exceeds the heat loss at the surface.

A significant percentage of the incoming solar radiation is absorbed within the

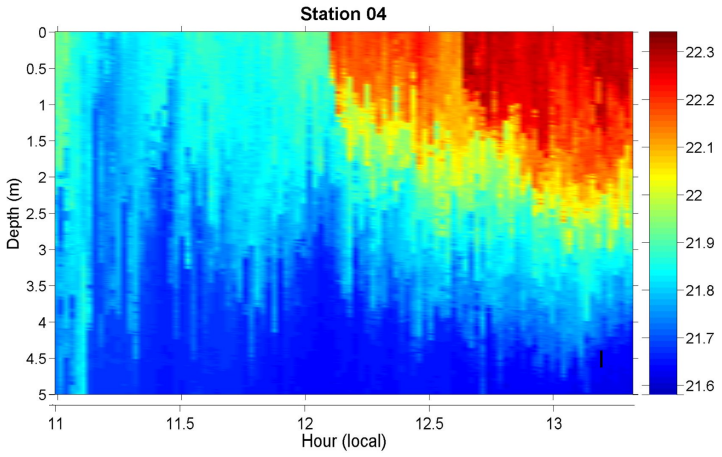

Figure 3.2: Temperature-depth measurements from the SkinDeEP profiling instrument. The temperature is in °C, the evolution from left to right is time from 11 LST to 14. Taken from Ward (2006), Figure 4a. Station 4 is located at 25°09.49N, 112°59.52W, west of the Baja peninsula, Gulf of California.

few top meters of the ocean surface, thus increasing the temperature in a manner that depends on the daily solar cycle. Lack of wind prevents mixing of the water column, thus leading to the creation of a diurnal thermal layer, the "warm layer" (Fairall et al., 1996). Diurnal differences between the temperature at the surface and at some meters deep in the water column have been observed in the past. As an example, Halpern & Reed (1976) noted an increase in the near-surface temperature up to 1.4℃ from measurements 35 km away from the coast of Western Sahara in the Atlantic Ocean.

More recently, Ward (2006) presented extended observational evidence, using vertical profiles at various stations, for the creation of the diurnal warm layer constrained in the upper few meters of the water column. See for example Figure 3.2, where a warm layer is created after 12 00 local solar time with temperature differences ∼0.6℃ between the sub-skin and the 5 m depth. This study attempted to quantify the errors in the heat flux estimates; heat flux errors associated with the warm layer were found in the range of 10 to 50 W m^{-2}.

Other than errors in surface heat flux estimates, the diurnal variation of sea surface temperature can complicate the assimilation of SST fields by ocean and atmospheric models, the derivation of atmospheric correction algorithms for satellite radiometers and merging of SST data from different sources. A review on the diurnal SST variation and its impact on the atmosphere and the ocean is available by Kawai & Wada (2007).

As noted in Donlon et al. (2009), identification of diurnal warming events across the global ocean is required in order to improve understanding of their spatial and temporal variability as well as their impact at daily, monthly, seasonal, annual and multi-annual time scales as well as in climate data records. To quantify diurnal warming, frequent observations of SST are required. Currently, hourly satellite SST retrievals from an infra-red sensor are available for the North Sea and the Baltic Sea. More information on space-borne infra-red radiometry follows in the next section.

3.3 Infra-Red Sensors

The Advanced Very High Resolution Radiometer (AVHRR) is the standard instrument onboard NOAA's Polar-orbiting Operational Environmental Satellites (POES), first launched in 1978 and continuing until present. The European Organisation for the Exploitation of Meteorological Satellites (EUMETSAT) launched an AVHRR instrument on board the first European polar-orbiting meteorological satellite MetOp-A, in 2006.

The first Along Track Scanning Radiometer (ATSR)-1 instrument was launched on board the European ERS-1 platform in 1991 followed by ATSR-2 on ERS-2 and the Advanced ATSR (AATSR) on ENVISAT. A new instrument based on the AATSR will be onboard ESA's SENTINEL-3 mission, thus continuing the monitoring of SST from space. The Moderate Resolution Imaging Spectroradiometer (MODIS) is onboard NASA's Terra, launched in 1999, and Aqua, launched in 2002, platforms.

USA's Geostationary Operational Environmental Satellite (GOES) is a series of platforms, originally launched in 1975 and continuing until today. They are equipped with a multi-channel imager, for the infra-red band and also for visible reflected solar energy. The Meteosat First Generation (MFG) platforms, initially launched in 1977 with the last in 1997, carried the Meteosat Visible and Infra-Red Imager (MVIRI) with 3 spectral bands. The Spinning Enhanced Visible Infrared Imager (SEVIRI) instrument, is on board the Meteosat Second Generation (MSG) platforms first launched in 2002.

3.4 SEVIRI

SEVIRI is the main instrument on the geostationary MSG platforms, that consists of a series of 4 platforms that will operate until 2020. Meteosat-8 was the first of

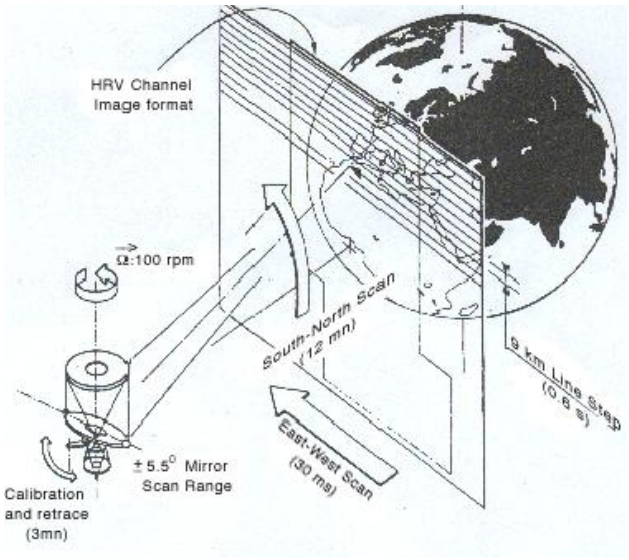

Figure 3.3: Graphical representation of SEVIRI's scanning principle. A bi-dimensional scan is achieved by the platform's spin (rapid from East to West) and the scanning mirror (slow, South-North direction). Courtesy of ESA.

the series, called MSG-1 and was launched in 2002 becoming operational in 2004. MSG-2 was launched in 2005. The mission is coordinated by EUMETSAT and ESA. Each platform is expected to remain in orbit and in an operational condition for at least seven years. The policy is to keep two operational platforms and launch the next near the time when the oldest platform is close to the end of the on-board fuel deposit. The main platform, currently MSG-2, is centred at 0° longitude and ∼0° latitude. The in-orbit spare MSG-1 is at 3.4°W and is expected to have 6 extra years of life-time, with original design life-time of 7 years.

SEVIRI at an altitude of ∼ 35800 km scans every 15 min through a 50·80 cm opening. The incoming radiation is then focused on 12 different detectors, 4 in the visible and near infra-red band (0.4-1.6 μm) and 8 in the infra-red (3.9-13.4 μm). The sampling distance is 3 km at the sub-satellite point which increases to 1 km for the high resolution visible channel. The full disc image is obtained in 12 min and 3 min are allocated for repositioning of the scanning mirror and calibration with the use of an on-board black body (Schmid, 2000). The eight channels of the thermal infra-red band allow the retrieval of cloud, land and sea temperatures. Using channels at which ozone, water vapour and CO_2 absorb the infra-red radiation MSG platforms can provide information about these atmospheric properties.

SEVIRI transmits raw data to the EUMETSAT ground control centre which are processed to geometrically and radiometrically corrected data (Level 1.5). The Satellite Application Facilities (SAF) are responsible for extracting information

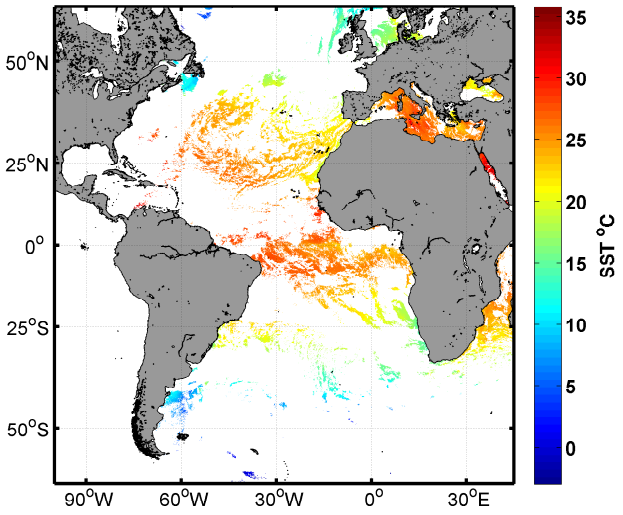

Figure 3.4: Example of the SEVIRI disc on the 04/07/2006 at 13:00 UTC. White areas signify missing data due to cloud coverage.

from the L 1.5 data and turn it to relevant products. The OSI SAF is producing SST fields, as well as products for the sea ice, the radiative fluxes and the 10 m ocean winds in an operational basis. The algorithms used for the retrieval of SST and the processing chain are explained in detail in OSI-SAF (2006). The operational algorithm used for day and night conditions for SEVIRI is described by Equation 3.3.

$$SST = (a + bS_\theta)\, T_{11} + (c + dT_{CLI} + eS_\theta)\,(T_{11} - T_{12}) + fS_\theta + g \tag{3.3}$$

T_{11} and T_{12} are the brightness temperatures at the 10.8 and 12.0 μm bands, respectively. The a, b, c, d, e, f, g coefficients are determined by simulations of brightness temperatures on a radiosonde profile database and T_{CLI} is a climatological SST value. $S_\theta = secant\,(\theta_{sat}) - 1$, where θ_{sat} is the satellite zenith angle. The radiometric noise budget for the two infra-red channels is 0.18 K (Aminou et al., 1999).

In addition, an experimental product from the Centre de Météorologie Spatiale (CMS) of Météo-France, was produced since 2004 at an hourly basis and on a regular grid from 60°N to 60°S and 100°W to 45°E with a spatial resolution of 0.05 degrees (Le Borgne et al., 2005). From 2010, this product is in pre-operational mode (LeBorgne et al., 2011). This high resolution product is used in the present study, as its high temporal availability is the most appropriate to study the diurnal cycle. As an infra-red imager, the instrument does not provide information under

overcast conditions, see for example a typical SEVIRI disc in Figure 3.4. Moreover, as infra-red instruments measure the radiation emitted from the skin layer, an adjustment to sub-skin temperatures is performed during the processing at CMS. SST retrievals are accompanied by the corresponding confidence flag, ranging from 0 (unprocessed) to 5 (excellent), signifying the quality of the retrieved glsab:SST value.

SEVIRI being in geostationary orbit, has a lower resolution in the Northern European Seas, compared to the 3 km at nadir. For the area defined between 48°S–60°N and 10°W–30°E, the resolution varies from 6 km to 8 km, depending on latitude. In addition, the infra-red radiances are sensitive to the incident angle due to different absorption along different atmospheric paths and changes in the surface emissivity. Finally, the algorithms used to derive SST are tuned to correct for water vapour, that is much higher in lower latitudes. Therefore, an overcorrection is likely for the higher latitudes. Brisson et al. (2002) reported a standard deviation of 0.5 K for SEVIRI while Marullo et al. (2010) reported annual biases between 0.4 and 0.9 K and σ of 0.4 ± 0.1 K.

3.5 Observations of diurnal warming

As recommended in Donlon et al. (2009), there is a need to "identify and catalogue diurnal SST warming events across the global ocean using satellite and in situ measurements in order to better understand the spatial and temporal variability of such events". Not accounting for the diurnal variability of SST can cause complications when validating satellite SST retrievals, when developing algorithms, when merging observations from various sensors (see for example Høyer et al. (2012)), when analysing climatic trends and when estimating the heat fluxes between the ocean and the atmosphere. It has already been demonstrated in Figures 1.2 and 1.3 that not accounting for the proper water temperature and its variability may also cause errors when extrapolating wind speed measurements to various heights, within the process of obtaining a descriptive vertical wind profile.

Diurnal warming has been extensively studied and identified in the Tropics (Clayson & Weitlich, 2007; Fairall et al., 1996), the mid-latitude region of the Western Atlantic Ocean (Cornillon et al., 1985; Price et al., 1987), in the Pacific Ocean (Flament et al., 1993; Price et al., 1986), the Mediterranean Sea (Deschamps et al., 1984; Gentemann et al., 2008), the Bay of Bengal and the Arabian Sea (Stuart-Menteth et al., 2003). Studies for the high latitudes of the North Atlantic are rather limited. Kahru et al. (1993) found that surface accumulations of cyanobacteria in the South Baltic Sea caused local increase in AVHRR SSTs of up to 1.5℃. Very

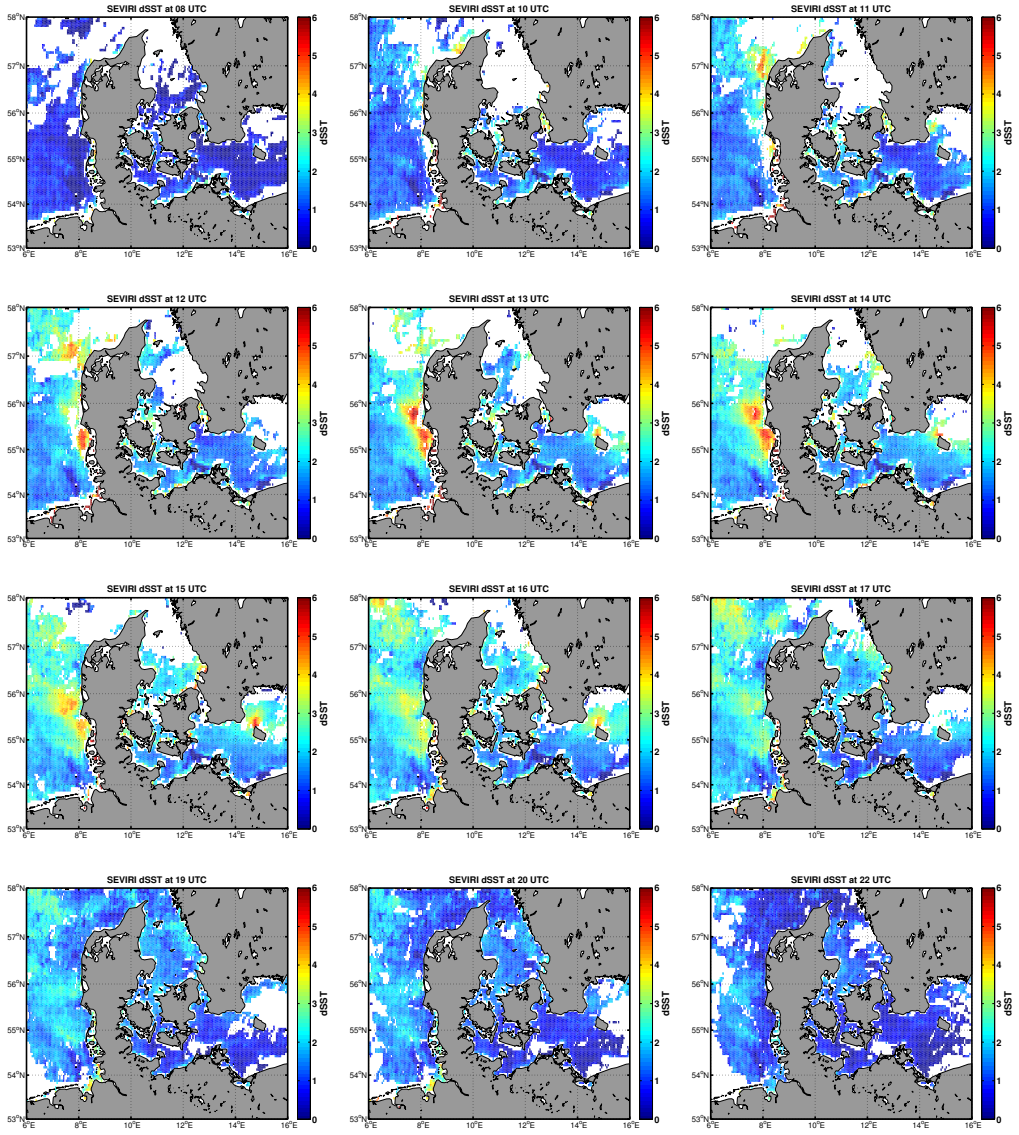

Figure 3.5: An example of hourly daytime SST anomalies (in K) from SEVIRI for the 04/07/2006.

recently, Eastwood et al. (2011) identified diurnal warming in the Arctic. Therefore, a need for a qualitative and quantitative assessment of the diurnal warming events in the North Sea and the Baltic Sea has been identified.

To achieve this, hourly observations from the SEVIRI instrument from 2004 to 2009 are used, for the area extending from 48°N to 60°N and 10°W to 30°E. Due to the latitude dependent resolution, it is very important to evaluate the quality

Table 3.1: Validation of hourly SEVIRI observations with quality≥3, against in situ observations from the shallowest sensor of every location. The mean bias is defined as satellite minus in situ. N is the number of observations.

Name	Sensor Depth	Mean bias [K]	σ [K]	R^2	RMSE [K]	N
Arkona Becken	2 m	0.2385	0.7188	0.9832	0.7573	8675
Darßer Schwelle	2 m	0.2382	0.7888	0.9778	0.8239	8008
Fehmarn Belt	1 m	0.0259	0.7055	0.9806	0.7060	6515
Kiel	0.5 m	0.0886	1.1747	0.9540	1.1779	5771
Oder Bank	3 m	-0.0041	0.5985	0.9904	0.5984	2572
Nordseeboje II	4 m	0.0387	0.5035	0.9863	0.5048	1131
Nordseeboje III	4 m	0.0690	0.6291	0.9840	0.6327	1789
Deutsche Bucht	3 m	0.0031	0.5537	0.9860	0.5536	4002
EMS	3 m	-0.0718	0.5514	0.9852	0.5560	3924
FINO-1	3 m	0.2386	0.7197	0.9798	0.7580	1353
M2	4 m	0.1744	0.5951	0.9880	0.6200	2153

of the SST observations at such latitudes. For example, Høyer et al. (2012) have demonstrated that sensor biases are latitude dependent and that they are generally lower for night-time observations compared to day-time. In situ water temperature observations from various buoys, research platforms and met. stations are used and the statistics can be found in Table 3.1. In general, biases do not exceed 0.24 K, while standard deviation σ ranges from 0.5 to 0.79 K. An exception is found for the Kiel platform, where σ is 1.17 K. Correlation is high, with minimum R^2 values of 0.954, for the Kiel platform, and maximum of 0.99. Root mean square errors (RMSE) range from 0.5 to 1.18 K. The latter is a unique case for the Kiel sensor, that despite the very shallow depth (∼0.5 m) and the low mean bias (-0.08 K), has the highest σ (1.17 K) and lowest correlation (0.95). These comparisons are very good, considering the error from comparing spatially averaged to point measurements, depth sampling errors and biases introduced by the buoy locations (shallow, coastal areas).

Diurnal warming occurs during the day time when the insolation is high and mixing in the water column is weakened by the lack of strong winds. At night the sea surface emits the heat stored during the day back to the atmosphere. The night-time sea surface temperature is considered the reference one and its difference from the daytime SST is denoted the “anomaly” (see Figure 3.5). But the exact definition of the night-time reference temperature can vary. In Section 3.2, it is mentioned that the foundation temperature is defined as the value at the first time of the day when the heat gain from the surface exceeds the heat loss. The last pre-dawn value, i.e. the value prior to local sunrise is also sometimes considered. In our case, as SEVIRI does not penetrate clouds, selecting one single value would

most likely result in reference fields with many missing values because of cloud cover.

Therefore, there is the need to define a proper night-time field which will be preferably composed by the SEVIRI SST. It is needed to establish a proper night-time period referred to as "night-time window", an averaging window of some days, referred to as "day window", in order to ensure minimum gaps due to cloud cover in the foundation temperature fields and decide on the quality of SST retrievals to be used. An important consideration regarding the "night-time window" is the variation of the "length of day" for these latitudes, especially during spring and summer, when most of the warming is expected to occur, in combination with the potential residual warming that would persist during the night. Finally, regarding the quality of SST retrievals, the amount of SST retrievals flagged as excellent (5) as opposed to other categories (3, 4) was taken into consideration.

A sensitivity analysis is performed for the test period between April and December 2006, by estimating the anomalies between a validation field, which is selected to be the last pre-dawn quality 5 SST retrieval, and some candidate night-time reference fields (see Paper IV). These are composites from the SEVIRI SSTs using different options for the "night-time window", the "day window" and the quality flags. The term pre-dawn describes the last SST retrieval before the local sunrise. From this analysis, the optimal parameters for the foundation fields are defined. Ideally, the choice of night-time SST fields should not influence the diurnal warming signals drastically. This assumption is tested with the use of another night-time reference product. The operational, blended SST product from the Danish Meteorological Institute (DMI) is used (Høyer & She, 2007) for that purpose, produced with the use of an Optimal Interpolation (OI) method. The statistics of the comparison can be found in Appendix D.

In general, it is found that the DMI-OI product is warmer than the validation field, similar to the results from the SEVIRI reference fields. For the DMI-OI product, most anomalies range between -0.4 and -0.2 K while in the SEVIRI cases this range is between -0.2 and 0 K. The standard deviation is slightly higher for the DMI-OI case, mostly ranging between 0.3 and 0.5 K (0.2-0.4 K for the SEVIRI reference fields). It should be noted here, that the DMI OI foundation fields are composed of SST observations from various sensors. From such results, it is decided to proceed using the SEVIRI reference fields because it is important to be able to use night-time reference fields from the data set, as systematic SEVIRI biases will not affect the results, and not to rely on external products that may have resolution issues and unidentified errors from the various sensors used for the blending.

To quantify diurnal warming it is required to establish a threshold above which

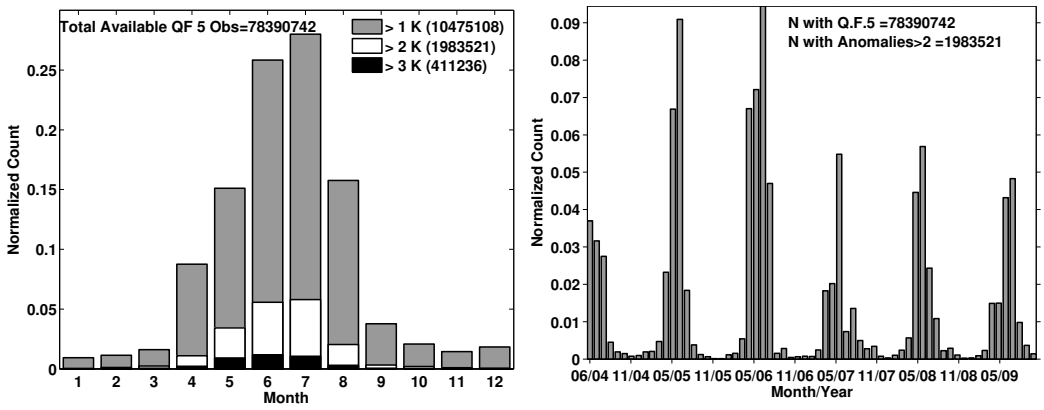

(a) (b)

Figure 3.6: a) Annual distribution of anomalies exceeding the threshold of 1, 2 and 3 K from June 2004 to October 2009 and b) temporal distribution of anomalies≥2 K.

the anomaly will be considered as warming. Figure 3.6a shows the quantified anomalies exceeding 1, 2 and 3 K. There is a dramatic difference of observed anomalies between the 1 and 2 K thresholds; anomalies exceeding 2 K consist ∼20% of the ones exceeding the 1 K threshold. Previously, errors in the order of 0.8 K between SEVIRI and in situ measurements were identified, therefore the 1 K is not considered a safe threshold for the definition of a warming case. Diurnal warming exceeding 2 K is recorded from April to August of every year (see Figure 3.6b).

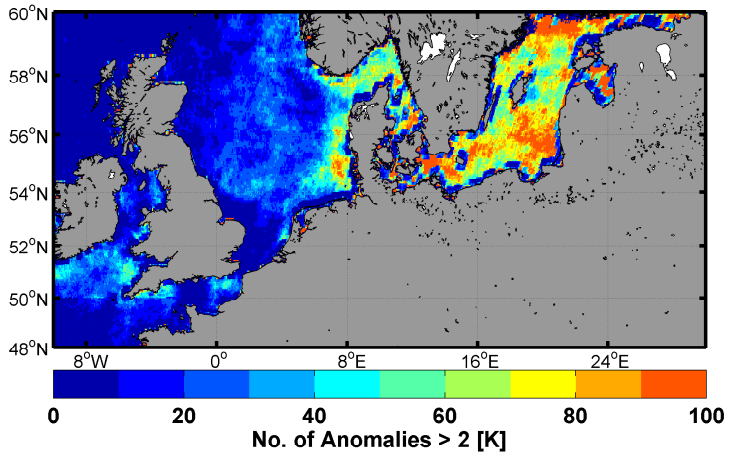

Figure 3.7: Spatial distribution of anomalies≥2 K.

In such cases, the amplitude of the diurnal cycle ranges from 0 K at night-time to

1.5 K at ∼10:00 local solar time and a maximum of ∼2.5 K around 14:00. 75% of the observed anomalies do not exceed 3 K, but cases up to 6 K are identified. Areas of frequent warming are typically coincident with areas of frequent low winds and increased water turbidity (see Paper IV). Moreover, a dependence on the bathymetry and distance to the coast is identified (see Figure 3.8). In both basins, 75% of the warming events occurred at depths up to 80-90 m with most cases occurring in depths between 20 and 40 m. Most of the warming cases are also identified within 50 km from the closest land mass. This is a very interesting finding, as these are generally the locations where most offshore wind farms are currently located and the new ones are being planned.

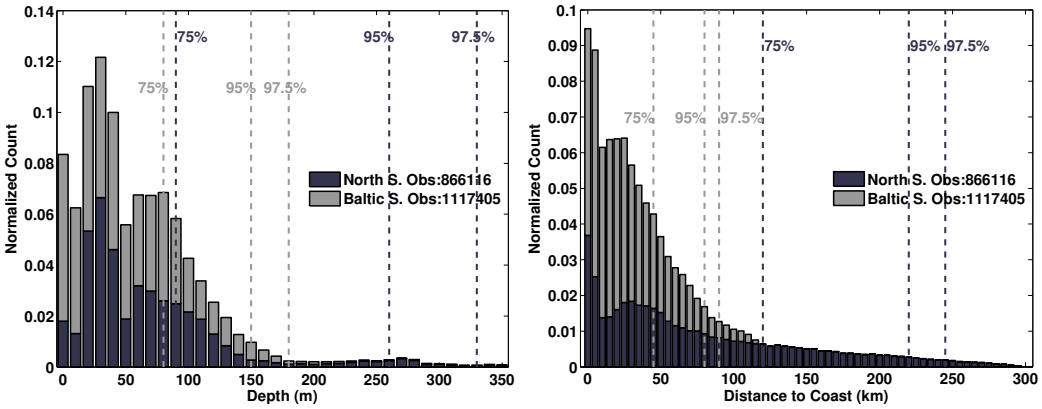

(a) (b)

Figure 3.8: Distribution of anomalies larger than 2 K according to (a) depth and (b) distance to the nearest coast, for the North Sea and the Baltic Sea.

To examine the depth of the near surface layer that experiences diurnal variability, based on the recorded anomalies, a simplified 1D model is applied. It is found that the penetration depth has a seasonal variability that resembles the one of the solar elevation angle and no depths greater than 1.8 m are identified, shown in Figure 3.9. Thus, water temperature sensors located at 3 or 4 meters below the water surface, typical for offshore meteorological masts, will most likely not record such variability. This is also a reason why the observed anomalies from SEVIRI are not compared with in situ observations as the available in situ sensors are mostly located at least 2 m below the surface. The Kiel platform has a sensor located at 0.5 m below the mean water surface but that shows large errors when compared with the available SEVIRI retrievals. For more information on the quantitative assessment on diurnal warming in the North Sea and Baltic Sea, one is referred to Paper IV.

It has been shown that it is important to use the SST instead of a bulk temperature of the water column when attempting to accurately describe the vertical wind

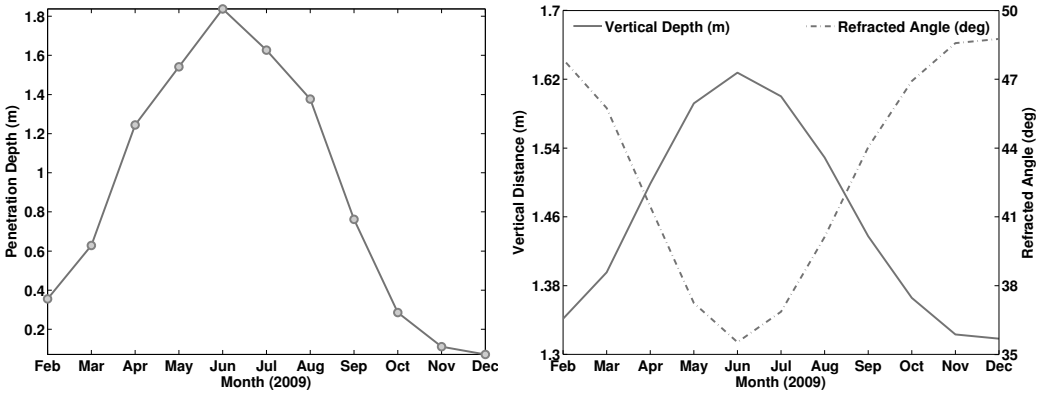

(a) (b)

Figure 3.9: a) Averaged monthly penetration depth from February to December 2009. b) Average monthly values of penetration depth of light (dashed), depending on solar elevation and accounting for defraction (dotted). Estimated for 55^oN, 4^oE assuming a constant distance of 2 m in the water column.

profile using extrapolation methods. Diurnal warming may cause sudden stability variations that for example, will not be described by a short-term wind forecasting system that does not account for the diurnal cycle. This is, currently, often the case. Therefore, the problem is twofold. It is not only enough to quantify diurnal warming, it is also important to be able to successfully predict it numerically.

3.6 Modelling the diurnal cycle

One of the big advantages of SST from space, is the global spatial coverage and the high temporal frequency as the concurrent availability of various polar orbiting platforms results in at least some SST retrievals per day. Different locations are observed during different fractions of the day, very often once during the day and once during the night. Day-time observations may be contaminated by diurnal warming, therefore there is "a desire to provide detailed error estimates with all satellite SST retrievals" (Donlon et al., 2009). Properly modelling the diurnal variability will also aid oceanic and atmospheric modelling as most often, the temperature of the upper ocean is considered uniform and stable during the course of a day, thus leading in errors when calculating the surface heat fluxes (Ward, 2006).

Within the context of the present study, it is sought to simulate the observed events

with the use of different modelling schemes. This would be of great interest as such a product could be directly incorporated in the in situ bulk temperature measurements to improve their representativity. A diurnal warming model will need to be of low computational cost and easy to implement. Such models are generally referred to as parameterization schemes; the parameter of interest, in this case the daytime anomaly $dSST$, is most often described by simple equations, based on empirical relationships derived from in situ observations. A parameterization able to reproduce the observational evidence to a satisfactory degree can also be incorporated in NWP models that are used for short term wind forecasting, in the context of offshore wind energy. The three different parameterizations applied in this study, use as inputs modelled surface net heat flux and wind fields from the NWP model High Resolution Limited Area Model (HIRLAM) citeprefHIRLAM, and are briefly described below.

Filipiak et al. (2010) Model This statistical model, here referred as FMKLB, evaluates $dSST$ from dawn to next dawn. It has been derived using 1 year of data over the Atlantic and the Mediterranean Sea from SEVIRI SST observations and operational and analysis fields from the European Centre for Medium-Range Weather Forecasts (ECMWF). Diurnal warming is described as a function of time, maximum wind speed since the net heat flux became positive and integrated net heat flux Q since the net heat flux became positive. Cooling periods are identified when the integrated net heat flux is negative. It also requires the climatological mixed layer depth, for which the entire water column depth is used in this study, as both the North Sea and the Baltic Sea are characterized by very small depths.

Zeng & Beljaars (2005) Model The prognostic scheme of Zeng & Beljaars (2005), referred as ZB, requires wind and surface fluxes, along with an a priori knowledge of foundation temperatures. In this case, the SEVIRI reference fields are used, as representative of night-time conditions. The scheme, as described in Zeng & Beljaars (2005) consists of two parts; the first predicting the skin SST and the second the sub-skin SST. It also includes a parameter than defines the depth of the diurnal-free layer d. In the present study, two different thresholds are selected, d_1=3 m and d_2=6 m. In addition, as the scheme computes both the skin and sub-skin SST, we use the sub-skin to be comparable with SEVIRI.

Clayson & Curry (1996) Model The parameterization, referred from hereafter as CC, was developed within the framework of the Tropical Ocean-Global Atmosphere – Coupled Ocean-Atmosphere Response Experiment (TOGA-COARE) project and it is described originally in Webster et al. (1996). This scheme uses a

peak solar insolation, the averaged daily wind speed and the daily average precipitation through a regression equation. The coefficients of the regression equation are derived using a Neural Network (NN) system, developed by Bogdanof & Clayson (personal communication). The CC scheme estimates the skin SST and does not resolve the full daily cycle but only produces a peak $dSST$ value. Therefore, comparison with the other predicted $dSST$s and the SEVIRI observed ones can be achieved only through the distribution of the peak $dSST$s and the mean peak $dSST$ and it will carry the "cool skin" bias.

Inter-comparisons

The distributions of peak modelled anomalies are compared with the distribution of peak anomalies observed from SEVIRI, shown in Figure 3.10. Especially the FMKLB parameterization reproduces very well the SEVIRI observed distribution. 75% of the daily maximum anomalies from SEVIRI do not exceed 0.8 K but 5% is higher than 1.6 K. Note the relatively few number of total observations, due to missing values either in the day-time SSTs or the night-time reference fields. The 99.9% of the maximum recorded anomalies does not exceed 5 K.

The distribution of peak $dSST$ from the FMKLB model indicates that the 75th percentile is lower; around 0.4 K, while the 95th percentile does not exceed 1 K. The ZB d_1 scheme has a 75th percentile at 0.5 K but the 95% and 97.5% of peak $dSST$s are higher than the observed SEVIRI ones. The d_2 version produces a distribution of peak $dSST$s with percentiles similar to SEVIRI. Finally, the CC scheme has a much narrower distribution with no $dSST$ exceeding 1.1 K and 75% not exceeding 0.3 K.

All candidate models significantly overestimate the number of warming cases. One reason for this is that NWP fields contain no gaps, thus the FMKLB model will estimate anomalies for the full domain. SEVIRI is bound by cloud cover and has missing values in both the night-time reference fields and the day-time anomaly fields while the ZB and CC use the SEVIRI night time fields as foundation temperatures. The averaged peak $dSST$s are shown in Figure 3.11. Note the different scaling for the FMKLB and CC models, so the spatial variability can be visible. Averaged peak $dSST$ from SEVIRI is between 0.3 and 0.5 K for the largest part of the study area.

Peak $dSST$s higher than 0.6 K are observed in the west coast of Denmark, the Baltic Sea, the west coast of Norway and the Irish Sea. The models capture the peak $dSST$ in some of these areas, like the west coast of Norway (58°N–60°N, ∼6°E), the Baltic Sea (54°N–60°N, ∼20°E–30°E) and the Irish Sea (52°N–54°N,

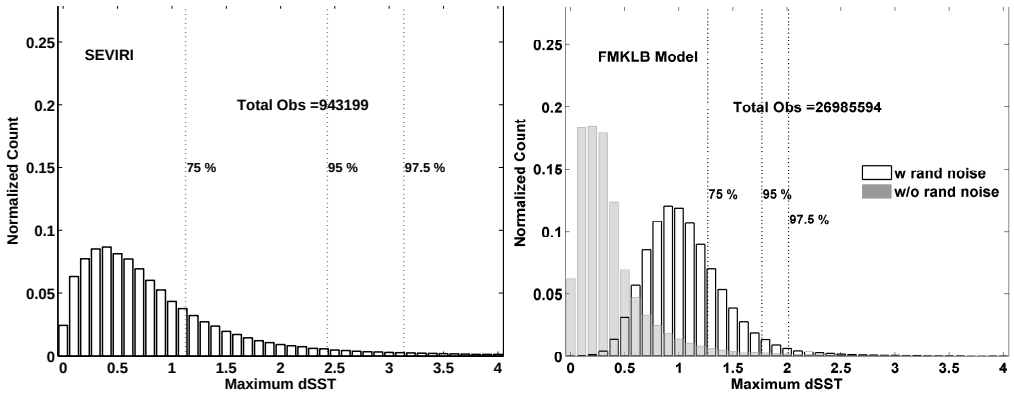

(a) SEVIRI

(b) FMKLB

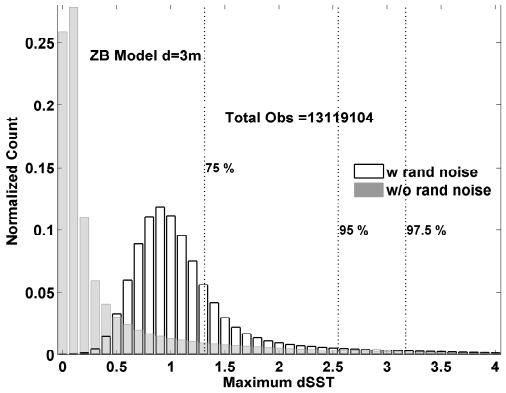

(c) ZB d_1

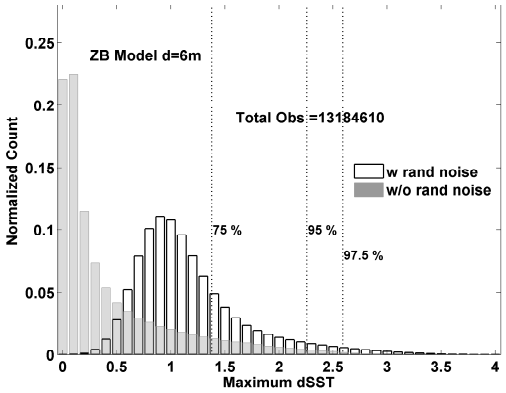

(d) ZB d_2

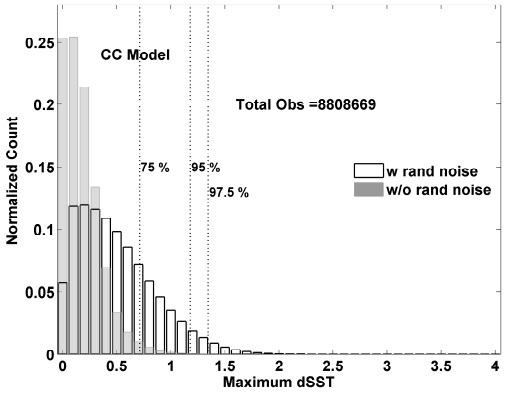

(e) CC

Figure 3.10: Distribution of maximum anomalies, counted for every grid cell, from 02/2009 to 01/2010. The distributions when random noise with a zero mean and a 0.5 K standard deviation is added to the models, are also shown.

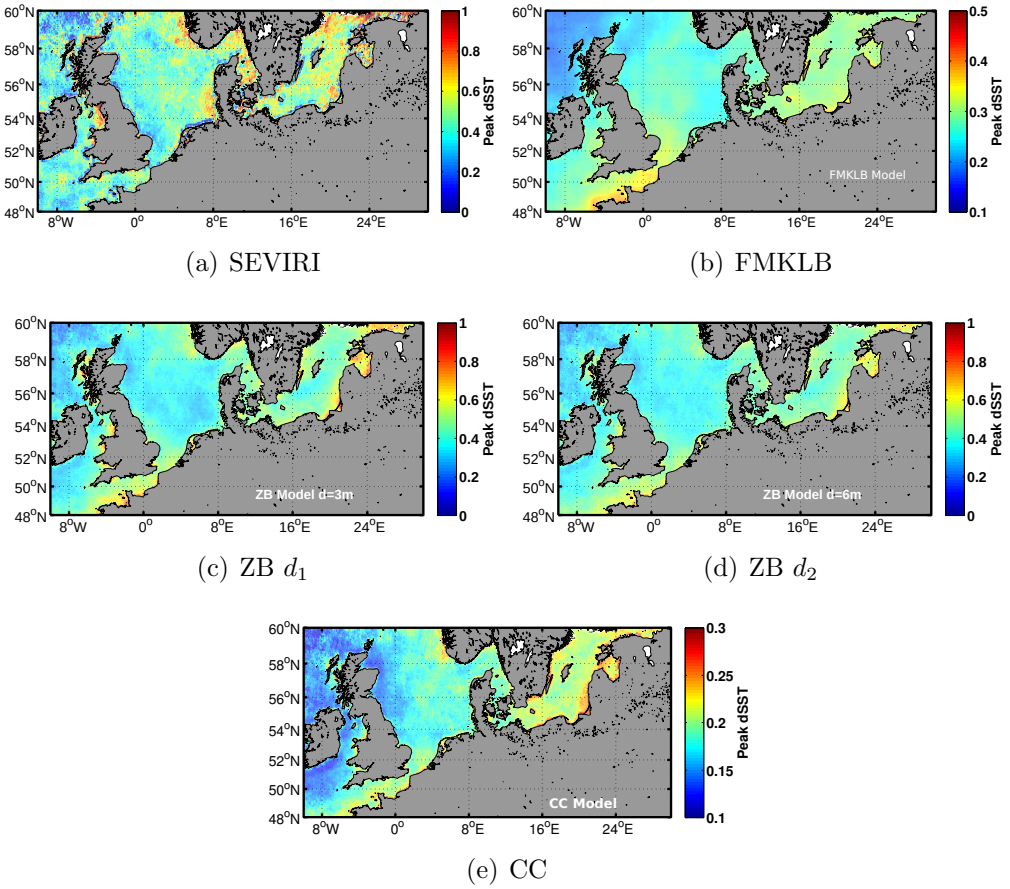

(a) SEVIRI (b) FMKLB

(c) ZB d_1 (d) ZB d_2

(e) CC

Figure 3.11: Spatial extend of averaged daily peak warming from 02/2009 to 01/2010. Note the reduced range of dSST for the FMKLB and CC schemes, to render spatial difference visible.

∼4°W). They also show a similar pattern as SEVIRI, where more warming is identified in the Baltic Sea compared to the North Sea.

An example of the maximum $dSST$ during a warming event on the 03/07/2009, as estimated from SEVIRI and modelled by the different schemes is shown in Figure 3.12. A peak $dSST$ of 5.5 K is observed from SEVIRI in an extended area of the west coast of Denmark and smaller areas where peak $dSST$ is ∼4 K are observed in the waters around the country. Another area with a peak $dSST$ of 5 K is observed in the Baltic Sea. Each model shows a rather different behaviour, with the FMKLB failing in the west coast area but capturing warming in the inland waters and in the Baltic Sea with a spatial mismatch. The ZB d_1 scheme predicts $dSST$s of the correct magnitude but with a much larger spatial extend while the d_2 version essentially reproduces the same spatial extend but with a

reduced amplitude. Finally, the CC scheme shows a much lower peak $dSST$, in the order of 2 K .

Figure 3.13 shows the SEVIRI anomalies from 14:00 to 16:00 UTC and modelled anomalies from the FMKLB and ZB d_1 and d_1 schemes, from 15:00 to 17:00 local time. The date is the same as in the example shown before. Note the warm patch on the west coast of Denmark around 55°N and 8°E with anomalies reaching up to 5.5 K, as observed from SEVIRI. Warming up to 4 K is found around 56°N, 11°E and 57°N, 8°E. Very high anomalies are also observed in the Baltic Sea around 55°N, 15°E but the cloud masking unfortunately does not allow a full coverage of the area.

Also note, the different results from the models. The FMKLB scheme (row 2), reproduces better the warming in the Baltic Sea and the Danish waters but misses warming in the west coast of Denmark. In particular the warm patch observed at 57°N–8°E does not appear or is misplaced towards the West. The ZB d_1 (row 3), highly overestimates warming but represents better the observed warm patches. Finally, the ZB d_2 version (row 4), shows a lower maximum anomaly but more or less distributed over the entire area. The spatial comparisons can show discrepancies because the modelled anomalies are driven by the input fields from HIRLAM. Any spatial disparity between HIRLAM and the real wind, will be translated in a mismatch between the observed and modelled anomalies.

When the daily cycle is averaged over a month, as shown in Figure 3.14 for July 2009, issues related to the spatial discrepancies of warming are excluded but other features are highlighted. All modelled curves show less warming during largest fractions of the day as the distributions are narrower. Moreover, both the ZB d_1 and d_2 versions show a time lag for the peak warming. They all account for a residual warm layer persisting until late in the evening but they underestimated its magnitude compared to SEVIRI.

The correlation between observed and modelled anomalies and other parameters such as the wind speed u, the integrated heat flux Q, the Surface Solar Irradiance (SSI) and the water turbidity $K_{d(490)}$ is shown in Figure 3.15a. For the $K_{d(490)}$, two different products are used, one from DMI suitable for type-II water and one from the ESA Global Colour Project (GlobCol), suitable for type-I water. To estimate the correlation between observed and modelled $dSST$ and u, Q, SSI and SSI', the number of coincident match-ups ranges from 1368344 to 1429894. For the correlation with $K_{d(490)}$ this number is decreased to 510308 match-ups for the DMI and 679884 match-ups for the GlobCol product. The models show a relatively high negative correlation with u and a positive correlation with Q, as both u and the heat flux Q are input fields. The observed $dSST$ from SEVIRI has a low correlation with both but the correct trends are captured.

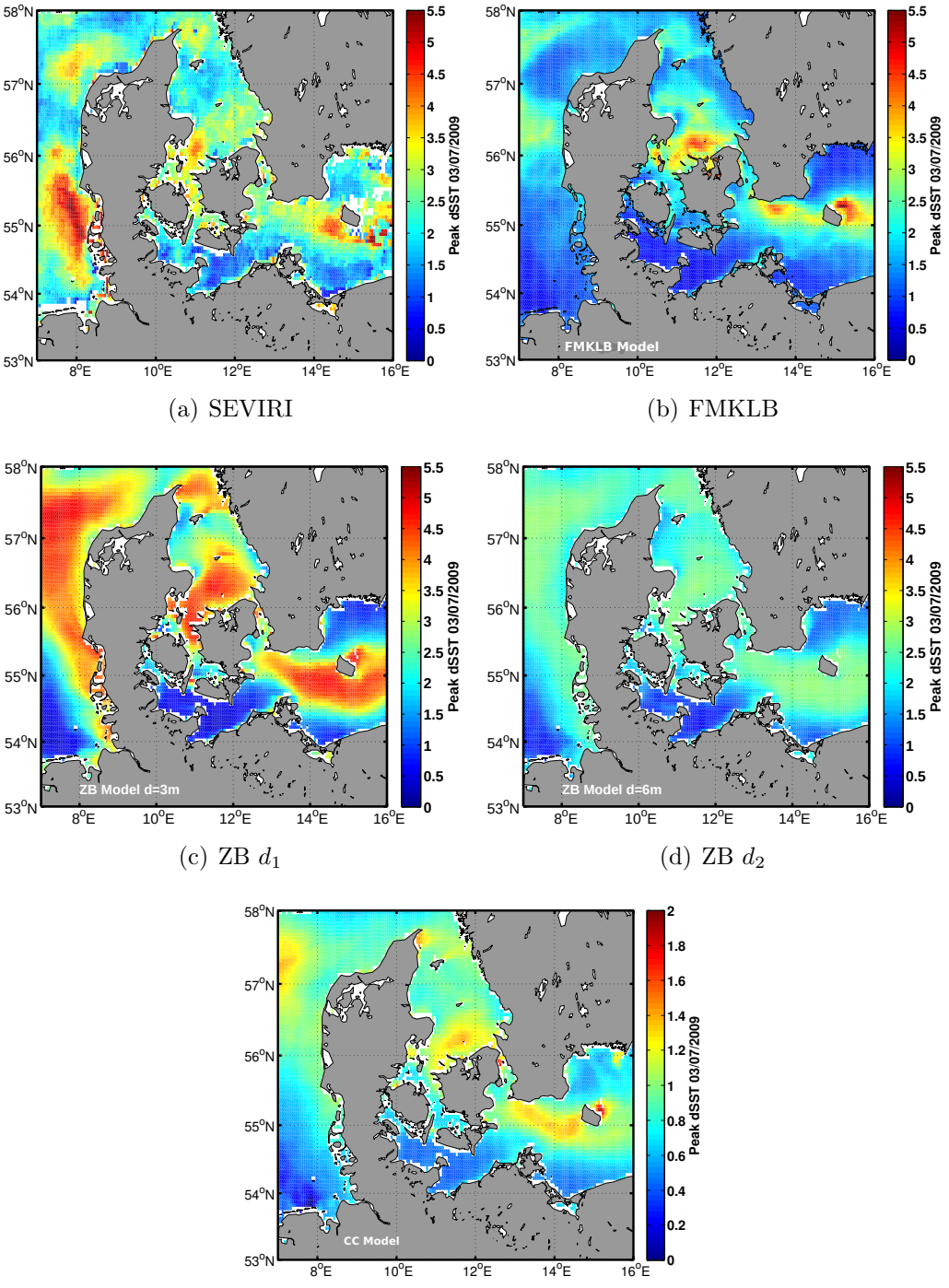

(a) SEVIRI (b) FMKLB

(c) ZB d_1 (d) ZB d_2

(e) CC

Figure 3.12: Spatial extend of peak dSST during a diurnal warming event on the 03/07/2009 as observed from SEVIRI and reproduced by the models. SEVIRI anomalies with quality $\geq$3 are used to avoid gaps in the field. Note the reduced range of the CC dSST, to make the spatial variability visible.

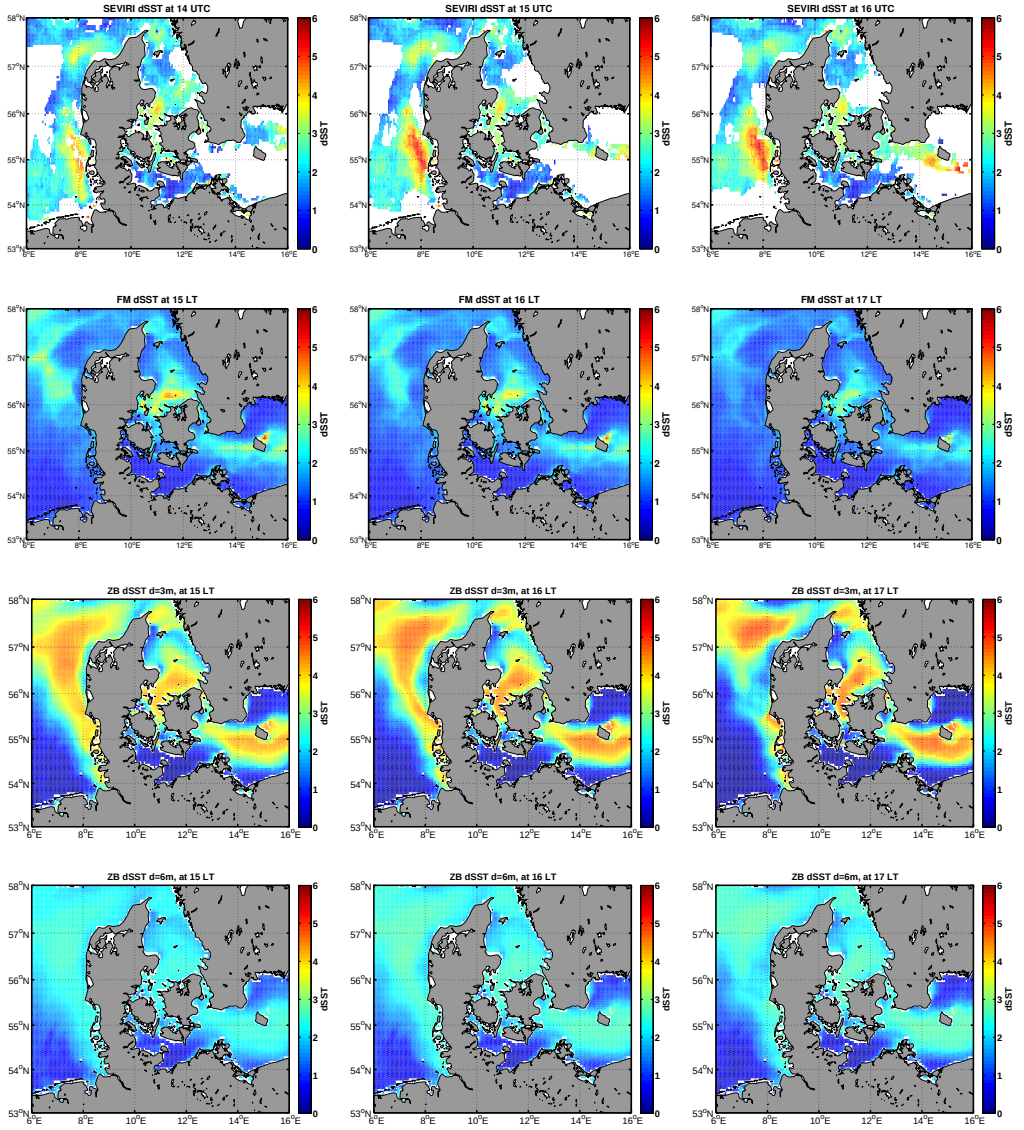

Figure 3.13: Warming from SEVIRI on the 03/07/2009 at 14:00, 15:00 and 16:00 UTC, along with the modelled fields from 3 different schemes.

There is also a positive correlation with the water turbidity, but of very low value. This can be explained by the daily nature of the $K_{d(490)}$ products used in this study; the temporal variability of $K_{d(490)}$ is not resolved therefore it can hardly be correlated with the temporal variability of SST. When the time lag dependence of the correlation is examined, shown in Figure 3.15b, a phase shift is identified. As an example SEVIRI anomalies show a higher anti-correlation with HIRLAM winds having a time lag of $\sim$ 2 hours.

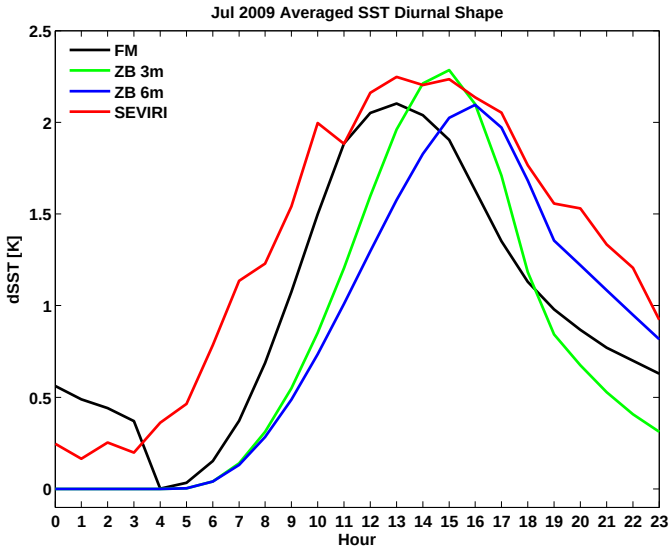

Figure 3.14: Averaged diurnal cycle based on grid cells that show anomalies exceeding 2 K at least once during the day. Observed anomalies from SEVIRI are shown in red and from the 3 models in black, green and blue.

Moreover, the dependence of the $dSST$ parameterizations on the water turbidity is examined, with the use of the diffuse attenuation coefficient at 490 nm ($K_{d(490)}$). This is a parameter that describes the depth in which the light travels in the water column. Hence, higher values are equivalent to more turbid waters. Results from the sensitivity analysis of the modelled warming dependence on $K_{d(490)}$ are shown in Appendix E. Generally, a contribution of $K_{d(490)}$ is identified, since there is a stratification of warming for low and high $K_{d(490)}$. For the ZB scheme, that includes a parameter to account for the depth of the surface layer where warming occurs, higher dependence on $K_{d(490)}$ is found.

Robust conclusions that can be drawn from the modelling attempts are that, the quality of the modelled anomalies highly depends on the input parameters. Most conveniently such parameters will be the outputs of NWP models. Therefore it is important to test the performance of such models in the area of interest. For example, if the modelled wind speeds are biased low compared to reality, the modelled anomalies will be more than in reality. In addition, it is considered important to account for a warm layer depth that will in principle constrain the heat in the upper few meters, thus leading to a more realistic representation. Finally, in such models, $dSST$ is more dependent on the wind as the correlation matrix indicated. In addition, diurnal warming does depend very much on low winds, that NWP models generally fail to capture properly. For more results and relevant discussion, see Paper V.

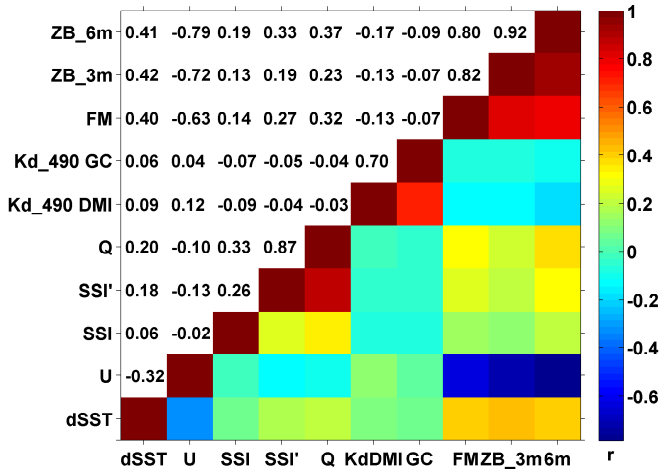

(a)

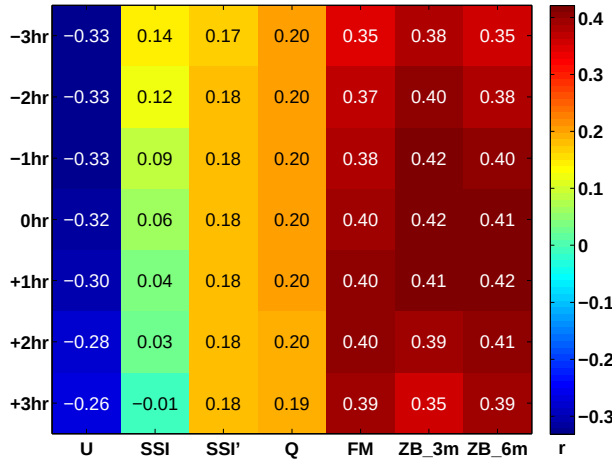

(b)

Figure 3.15: a) Correlation matrix of SEVIRI dSST, u, SSI, SSI′, Q and dSST from the FMKLB and ZB models. b) Correlation of U, SSI, SSI′, Q and dSST from the FMKLB and ZB models with SEVIRI dSST for different time lag intervals. All correlations are for SEVIRI dSST between 13:00 and 16:00 LST.

3.7 Summary

This chapter has dealt with the use of hourly satellite SST fields for the identification and quantification of diurnal signals in the sea surface temperature. Thus, by

understanding the marine environment and its variability, a better representation of the physical processes can be achieved.

- **Paper IV** assesses the use of hourly SEVIRI SST fields when compared to in situ observations and provides a thorough statistical description of the diurnal SST cycle in the North Sea and the Baltic Sea.
- SEVIRI observations have low biases compared to in situ measurements, thus the satellite SST fields are representative of real conditions.
- Diurnal warming of the upper water column has been quantified in the North Sea and the Baltic Sea. It occurs especially in areas relevant for offshore wind farms.
- Warming of the sea surface exceeding 2 K has been identified, observable in late spring and summer.
- The depth of the warm layer has been estimated to $\sim$2 m, much shallower than typically installed thermistors for in situ observations.
- As the diurnal cycle of SST is very important for various applications, **Paper V** addresses the comparisons between different models and SEVIRI observations of the diurnal cycle in the North and Baltic Sea.
- The overall biases between maximum modelled and observed warming are low and the models successfully reproduce more warming in the Baltic compared to the North Sea.
- When SEVIRI and modelled temperatures are compared to measurements from the shallowest available sensors at various locations, overall biases are $\sim$0.7 K independent of the dataset (SEVIRI or models).
- The statistical distributions are better resolved from some models but they all somewhat fail to capture the spatial extend of warming.
- The correlation between observed and modelled warming and various other parameters shows the correct trends but with low signal values.

Chapter 4

Discussion

This PhD study has been performed within the context of offshore wind energy and the community's attempt to increase our understanding of the natural processes that take place over the ocean and may affect the overlaying atmosphere, through observational evidence. Systematic observations of the marine atmospheric boundary layer and the underlying ocean are not easily available. Satellite remote sensing observations can aid to overcome this issue, due to their extended spatial coverage and temporal availability.

Since the main reason for using QuikSCAT ocean winds in this study, is for wind energy related purposes and wind resource assessment, it is thought that the use of an already gridded product, preferably with no gaps, is rather appropriate for such an application. After, hopefully, demonstrating the potential of scatterometer winds, in this case QuikSCAT, to aid the offshore wind energy sector, the author hopes that more of the community members will consider satellite scatterometry as a source of wind speed and direction measurements in future studies.

The applicability of scatterometer winds can be through assimilation in mesoscale models, use of scatterometer data for validation of model performance and calibration in specific areas and wind resource assessment, to complement other data sources. Hence, a gridded product, ready to be used as is, will likely be more applicable. In addition, it will be preferable if the product has the highest data availability possible and if that needs to be achieved through gap filling, it is probably better if it is standardized rather than leaving the option to the user.

Despite the variety of QuikSCAT products, there does not seem to be a source of information properly listing all the different scatterometer products and the GMFs they have been processed with. The author feels that while this should not be an important issue for the scatterometry experts, it will likely complicate the end user that wishes to get access to some wind data and use it. The choice of the RSS product was rather arbitrary. One may argue that many scientific investigations, mainly validation and comparison studies between the observed winds and modelled wind fields or in situ observations use typically L2B products, very often from JPL. This alone is a reason for not choosing such a product, as many studies are available and the performance of the assessed winds is already well documented.

Parameters relevant for the wind resource assessment that have been derived from QuikSCAT in this study, are the wind speed and direction in order to examine the spatial and temporal wind variability. Persistent features of large scale channelling flows and lee effects are identified through observations of the near-surface wind field. The spatial correlation amongst different locations demonstrates the spatial scale of such features. The seasonal variability highlights the existence of synoptic patterns. In addition, QuikSCAT observations have been used to evaluate the Weibull A and k parameters, the annual and monthly wind variability in comparison to the 10-year mean wind speed, to examine the spatial variability of the wind rose distributions and of the spatial correlation of wind speed, to define the frequency of the cut-in threshold and to examine the daily wind speed and direction difference in an attempt to quantify land-sea breeze systems.

Certain limitations exist concerning the applicability of scatterometer winds, that constrain the accuracy and the level of detail. Scatterometer wind biases are large below 3 m s^{-1}, which happens to be the typical lower cut-in threshold for wind turbines. The accuracy of QuikSCAT is 2 m s^{-1} within the range 3-20 m s^{-1}, properly covering the typical range of rated wind turbine speeds; the upper limit is coincident with the start of the cut-out range. For wind speeds above 15 m s^{-1}, there is a "failure" of the GMFs to retrieve the correct speed due to the lack of in situ observations to correlate with the backscattered signal. As more scatterometer observations become available, new and more accurate GMFs are being developed, improving the accuracy of the retrieved wind and extending the effective range. For example, recently RSS reprocessed the QuikSCAT σ_0 with a new function that is believed to increase accuracy for wind speeds up to 30 m s^{-1}. Nonetheless, such accuracies are nowhere close to the cup anemometer uncertainties used for in situ measurements. Such uncertainties are defined by the calibration, mounting and operation of the instrument and for wind speeds ranging from 4 to 25 m s^{-1}, they are between 0.16 and 0.25 m s^{-1}.

The limitation of satellite winds to properly identify high and low wind speeds

poses a constrain in their representativity. In this study it has been found that when applying the Weibull fit to the QuikSCAT time series in order to estimate the wind power density, lower estimates are computed as opposed to when estimating the power density directly from the QuikSCAT observations. The biases did not exceed 10 W m^{-2} in most areas, but increased up to 50 W m^{-2} in the North Atlantic. This is thought to originate from a combination of the high variability of the wind speed along with the fitting of the Weibull distribution to the QuikSCAT time-series, for which very low and very high wind speeds are under-represented. Such a limitation has to be taken into consideration when estimating long term averages.

Satellite wind fields are near instantaneous measurements over large areas, that are then averaged to provide measurements representative of spatial averages. This is a disadvantage compared to in situ measurements at a specific location. QuikSCAT winds are most commonly available at 25 km. This means that σ_0 observations are averaged over bins of 25 km·25 km, thus providing an averaged wind retrieval. This eliminates any type of local features that can be captured by in situ observations, at least in the product version used in the present study. Moreover, due to the contamination of land to the backscattered signal, retrievals were so far obtained at a distance of ∼30 km from the land. This has been a limitation, as most offshore wind farms have been traditionally constructed within this distance from the land. The solution to this issue is twofold. On the one hand, new offshore foundation techniques are driving offshore wind farms very far from the coast, where no land contamination to the backscattered signal is expected. On the other hand, scientific working groups are improving the resolution of scatterometer winds and are working towards products that are available closer to land than previously.

Considering the spatially averaged nature of satellite fields, it is very important to identify the resolvable length scales, i.e. how much small scale variability is preserved. For that, spatial spectral analysis of the coarser QuikSCAT product and the much finer SAR wind retrievals was very useful to highlight the importance of using the most relevant type of satellite winds depending on the type of investigation. SAR wind fields show higher spatial variability even when they are processed with a resolution similar to QuikSCAT. This is a very interesting finding as it creates new possibilities for combining the existing archives from QuikSCAT and SAR to increase the daily temporal availability and improve the accuracy of satellite based wind resource assessment when long-term averages are of interest.

The impact of rain on the quality of the retrieved scatterometer winds from QuikSCAT is another issue, as it forces flagging and exclusion of the rain contaminated observations. This may bias the average statistics since high winds, possibly associated with rainy conditions, have to be excluded. A sensitivity analysis performed during the present study, showed that biases were in the order of

0.2 m s^{-1} but this may be different depending on the product and has to always be taken into consideration. Note that if products from other scatterometers operating at other bands of the electromagnetic spectrum, like ASCAT, or from C-band SARs, only heavy rain may pose a significant problem.

The temporal frequency of QuikSCAT winds, i.e. two daily observations, is not useful for diurnal warming studies, as the daily cycle is not properly captured. Still certain persistent features can be identified, for example areas where typically the early morning speeds are found higher compared to the early evening even by 1 m s^{-1}. Other studies (Barthelmie et al., 2005; Motta & Barthelmie, 2004) have found that the number of unstable conditions peaked at approximately sunrise which is about the time of the QuikSCAT morning pass over the Northern European Seas.

Also, such a temporal frequency is very low compared to in situ measurements, typically acquired as 10-min averages. When long term averages are described, such a disadvantage has been shown to have a smaller impact than one would expect. More specifically, by evaluating the 10 m mean wind speed and the wind power density, at two offshore locations in the North Sea, between 1769 (643) QuikSCAT twice daily observations and 137772 (50359) 10-min in situ measurements, it is found that the mean wind deviation is 2.2% (0.9%) and the wind power deviation is 11.2% (2.2%). On the other hand, the intra-annual variability, described by the monthly wind speed over the long-term mean, is very well captured by QuikSCAT when compared to in situ observations. All the above strengthen the conclusion that for average, descriptive statistics the scatterometer winds can be very helpful. Of course, this does not signify that in situ measurements can be substituted by space-borne observations.

QuikSCAT has been found useful for the validation of re-analysis NWP fields from WRF. Through comparisons it was possible to identify areas where the model does not resolve the wind variability, as observed from QuikSCAT and from in situ observations. Both QuikSCAT and WRF have certain limitations that can inflate the estimated biases, especially in areas of complex morphology and in coastal areas where QuikSCAT may be contaminated by land backscatter and WRF may have issues with the land mask, the change of surface roughness and its value. It is important to keep such limitations in mind when drawing conclusions from the comparisons. In addition, QuikSCAT was tested against WRF outputs to evaluate the use of different planetary boundary layer schemes in WRF. Such a task is valid for winds at 10 m above the surface and cannot provide solid conclusions for the model's performance at higher levels, relevant for wind turbines.

The satellite observed winds are referenced at the height of 10 m above the surface. This is a limitation, as wind turbine relevant heights extend from 20 or 30 m

above the surface up to 180 m. Even with in situ measurements available, detailed information at high levels is rarely acquired. In such cases, vertical extrapolation of the measured quantities is performed using the diabatic wind profile formulation, that describes the evolution of the wind profile with height as a function of the atmospheric stratification, the surface roughness and the boundary layer height. When the sea surface is considered in this methodology, water temperatures are used, usually from a depth within the water column. But, large diurnal warming of the sea surface temperature occurs under clear sky, strong solar insolation and light winds.

Diurnal warming of the sea surface occurs under low winds. Thus, one may argue that it is not relevant for wind energy purposes. Surface winds below 5 or 6 m s^{-1} may not be strong enough to promote mixing of the upper water column, but they are well above the typical wind turbine cut-in thresholds. Therefore, turbines can be operating for wind speeds that allow warming. In addition, most diurnal warming cases have been found to occur in areas with water depth and at a distance from the coast typically chosen for wind turbine installations. Thus, warming events can affect the stability of the atmosphere, increasing turbulence that will drive an increase of the near surface wind speed. Under unstable conditions, the diabatic wind profile dictates that wind speeds at, for example, 100 m above the surface will be lower than under neutral or stable conditions. In addition, diurnal warming events may cause errors in the extrapolation of wind speed from measurement heights to turbine relevant heights, if a water temperature other than the SST is used. Measuring campaigns, providing information at various atmospheric levels would be very relevant for the exact description of instability caused by the sudden warming of SST and how it progresses further up in the atmosphere.

A recent study by Sathe et al. (2011) for the atmospheric stability in two offshore locations of the North Sea, used water temperatures at -3.8 m and -4 m and air temperatures at 21 m and 15 m respectively. They did not find any pronounced daily variation of stability, most likely due to the depth of the water temperature sensors. Nonetheless, they identified a "marked increase" of unstable conditions during the late summer and an overall prevalence of neutral to unstable conditions. The author can not help but wonder what would their findings be, if actual SST observations were used rather than bulk water temperatures. The increase of unstable conditions during late summer is due to the seasonal increase of the water temperature. Similar results could be expected during a day when diurnal warming occurs.

Chelton et al. (2004) used QuikSCAT swath winds to examine the curl and divergence of the surface wind stress. This study revealed small scale variability in the divergence filed over open ocean, which was attributed to the acceleration and

deceleration of the surface winds blowing across SST fronts. They stated that the resulting convergence and divergence generates vertical motions which can influence higher atmospheric levels. Such a study clearly demonstrates the coupling of the oceanic winds and the SST. Similar investigations, although very interesting, have not been performed in the present study. The author strongly believes that such features can be identified only using swath winds and that in higher level products, such information is not preserved.

Regarding the quantification of diurnal warming in the North Sea and the Baltic Sea, one may argue that the occurrence of very large warming events, above 2 K, is not frequent enough to be of importance in these latitudes. There is some doubt regarding the severity of the cloud masking and the quality flagging. SEVIRI data have been recently reprocessed with a new cloud mask control and revised algorithms (LeBorgne et al., 2011). Users are advised to use quality levels 3 and above for quantitative purposes. This new processing and in particular the cloud mask control may alter the findings of the current study, possibly towards the identification of more diurnal warming cases.

SST measurements from SEVIRI have been validated for the North Sea and Baltic Sea. They have proven valuable for the identification and quantification of diurnal warming of the sea surface temperature. As such, they could be considered in cases when in situ temperature measurements are not available and for the evaluation of potential diurnal warming in prospective sites for offshore wind turbine installations.

Observations from other sensors, on board polar orbiting platforms would solve the resolution issue, as SEVIRI resolution is much lower for the high latitudes. It would also compensate for the accuracy and land mask issues. But polar orbiters usually have a much longer re-visiting time, thus observations from various sensors on various platforms would have to be combined to resolve the daily cycle. This would increase uncertainty on the quantification of warming due to different resolutions of the sensors and sensor-dependent biases.

Modelling the diurnal cycle of SST is of high interest, in order to compensate for biases in day-time satellite SST retrievals, to improve the representativity of bulk temperature measurements and to improve the performance of NWP models that use night-time composite SST fields. The three models used in the present study are easily applicable and of low computational cost. They have been found very sensitive especially to the input wind field that typically is taken from NWP model outputs. Such model outputs perform poorly in low wind speeds, i.e. when diurnal warming occurs. This is a limitation of the $dSST$ models that could be compensated by the use of actual wind speed measurements, e.g. from satellite observations.

From the diurnal warming model inter-comparisons, the FMKLB scheme successfully reproduces the statistical distribution of warming as observed from SEVIRI. The ZB scheme performs better in modelling the spatial extend of warming, but more sensitivity tests are required to find the optimal combination of its warm layer depth parameter and the shape exponent of the warm layer parameter. This may improve the overall performance of the model. Both the FMKLB and ZB schemes perform well in reproducing the averaged daily SST cycle especially in accounting for the residual warm layer that persists at night-time. The CC scheme produces a peak warming for the skin SST and it that sense it is not as relevant if the full daily SST cycle needs to be resolved. In addition, the skin bias is expected to be larger under low wind conditions and therefore comparisons with sub-skin SST are not straightforward. Such a scheme is applicable for properly estimating the surface fluxes and improve heat budget approximations.

Other types of models for diurnal warming include diffusion and bulk models. These models include turbulence quantities, do not resolve the upper few meters of the water column discretely, and in order to do so the computational cost will be enormous. As such they are useful for coupled ocean-atmospheric models. The author feels that if the daily cycle needs to be resolved in a simple and efficient manner, for example in order to be included in daily composite SST fields from multiple sensors, such complicated and computationally heavy models will not be practical.

This study has hopefully demonstrated that in addition to the many well established scientific applications of scatterometry from space, offshore wind energy is yet another. Lifting the satellite winds from the reference height of 10 m to higher levels, relevant for wind turbines, will strengthen their applicability for offshore wind energy purposes. To successfully achieve this, accurate information about the atmospheric stability and the boundary layer height over large areas is required; such information can currently be obtained through NWP models. Studies attempting such a task are currently available, e.g. Badger et al. (2012) and their results are promising but not as accurate as expected. The information obtained from the NWP models is questionable as the lower atmospheric levels are not best resolved by such models. The typical use of bulk, multi-day averages of SST as inputs to such models surely does not aid their improved performance. Higher spatial and temporal resolution SST fields, able to capture the daily variability are thought to improve the model performance at low levels thus improving the accuracy of the output fields that will then be implemented for the lifting of the satellite winds.

The author would like to highlight a personal difficulty to sort out all the available QuikSCAT products and their specifications. The common platform for scatterometry and ocean vector winds is the International Ocean Vector Winds Science Team

(IOVWST). But, for example, the RSS QuikSCAT product is missing from their list of products. A personal opinion is that a more general scatterometry platform would be useful, especially for the dissemination of scatterometer winds. This could somewhat simplify the access to different products and gather all the information available under one common group, thus simplifying the process for the end users. Something similar exists for the space-borne SST observations. The Group for High Resolution SST has successfully created such a common platform where organizations interested in SST observations but also individuals can find complete information on the available products and the background of their development.

Chapter 5

Conclusions

The aim of the present study has been twofold. To demonstrate the applicability of satellite observations of near-surface ocean winds over large areas, for the purposes of wind resource assessment and for general implementation in the offshore wind energy sector. Moreover, to promote the understanding of factors that may influence the marine atmospheric boundary layer, through identifying and quantifying the diurnal warming of the sea surface temperature. To achieve this, hourly satellite observations have been used, over the North Sea and the Baltic Sea where most of Europe's offshore wind farms operate.

Within this context, it has been shown that space-borne scatterometer winds from QuikSCAT can be used for the initial wind resource mapping to highlight areas where more accurate measurements are required. The long-term data availability aids at capturing the average statistics but QuikSCAT observations have certain limitations in terms of accuracy; 2 m s^{-1} for speeds between 3-20 m s^{-1}. Depending on the algorithm used to relate the backscattered signal to the 10 m wind, the range of derived wind speeds can vary and there are now well documented biases above and below certain wind speed thresholds.

Comparisons of QuikSCAT with in situ observations from three offshore locations in the North Sea indicate very good agreement. The mean wind speed bias was found to be almost zero when wind speeds above 3 m s^{-1} were used, while the standard deviation was 1.2 m s^{-1}. The wind direction mean bias was $-2.3°$ with a standard deviation of 15°. Nonetheless, satellite winds are instantaneous spatial

averages and in that sense they are not comparable neither can they substitute in situ measurements that capture the temporal wind variability in a specific location.

The 10-year long QuikSCAT dataset provided multi-year statistical properties and coverage of large areas. Even though the North Sea and the Baltic Sea are dominated by strong westerly winds, it has been shown that the North Sea is particularly subjected to spatial variability of various wind related parameters. Adjacent land masses with complex terrain and the complex coastal morphology result in lee effects and strong jet and channelling flows. The spatial correlation of wind speed indicates that correlation higher than 0.9 is identified for an area with seasonally stable size, approximately 160 km by 200 km.

The temporal representativity of QuikSCAT's twice daily observations was evaluated against the frequent 10 min in situ measurements. From a total of 1769 QuikSCAT observations compared against 137772 in situ measurements, a maximum 2.2% deviation for the wind speed and 11.2% for the wind power density was found for a location ∼14 km offshore. For a location further offshore (∼35 km), such estimated deviations were 0.9% for the wind speed and 2.2% for the power density, between 643 QuikSCAT retrievals and 50359 in situ measurements.

QuikSCAT was found to reproduce the temporal wind variability as observed from in situ measurements at an offshore location. When examining the mean monthly wind speed variability over a long term mean wind speed, the lowest below-mean variability from in situ measurements was ∼48% for July while the QuikSCAT computed variability was ∼45% for the same month. Highest above the mean variability was observed in January and reached ∼10% from both in situ measurements and QuikSCAT.

The spatial representativity of satellite winds is a limitation when seeking to describe local conditions. For such a purpose, SAR wind fields are found to better capture the spatial variability of the wind field, compared to QuikSCAT and they are appropriate for a more detailed description of local scales. Even when SAR winds are re-processed to match the resolution of QuikSCAT, the spectral power of SAR is still higher for the same wave number range and the spectral slope of SAR is smoother.

It is shown that QuikSCAT spectral slopes for the mid-latitude region of interest follow the theoretical predicted value of $-5/3$. The SAR spectral slopes are lower and increase for decreasing resolution. SAR fields maintain a high energy content for length scales of 2 km. Such findings demonstrate the ability of SAR winds to resolve spatial scales and their lower degree of averaging. Thus, SAR fields can be used along coarser resolution scatterometer products to improve the spatial information available from satellite winds.

For a detailed wind resource assessment, satellite observations of winds are not sufficient and more sources of information should be combined. The extended spatial and temporal coverage of scatterometer near-surface ocean winds can provide an initial description of the conditions over large areas, serving as a "road-map" for specific site selection. It can also serve for the initial set-up of meso-scale NWP models used for wind energy purposes, be assimilated in them or for the validation of the model set-up.

The extended spatial comparisons between QuikSCAT and WRF re-analysis outputs, indicate areas where discrepancies are very small. The largest discrepancies between QuikSCAT and WRF are observed in coastal areas, of complex morphology and adjacent to land masses. There both the satellite winds and the re-analysis fields suffer from issues related to the land proximity. This kind of comparison though, may not be entirely fair as the WRF re-analysis is not formulated to capture the day-to-day wind climate but rather the long-term trends.

If the wind resource assessment studies are to be as accurate as possible, all available information for the wind over the ocean has to be integrated. Moreover, better understanding of the processes that can influence the wind conditions offshore should be achieved. As over land the surface temperature is considered important because it varies significantly within the course of a day, also above water it is the surface temperature that should be taken into consideration.

It is commonly accepted that the water temperature does not vary much during a day, but this study has demonstrated that this is not actually the case especially when the temperature within the first meter is considered. The very top of the water column is the part where most of the incoming solar radiation is absorbed and where the exchange of heat with the atmosphere takes place. Rapid increase of the SST can occur during the course of a day and it should be taken into account for the extrapolation of surface winds to wind turbine hub-heights.

Hourly satellite observations from SEVIRI have been found accurate when compared to in situ measurements and very useful to quantify the occurrence of diurnal warming in the North Sea and the Baltic Sea. Biases are generally low and correlation high, when hourly SEVIRI retrievals of quality 3-5 are compared against in situ observations from platforms and moored buoys. On average validation results of the hourly SEVIRI fields show a bias of 0.65 K when compared to in situ observations. Diurnal warming exceeding 2 K was observed from April to August, mainly occurring from 1400 to 1600 local time. The maximum amplitude reached 6 degrees in a few cases. The spatial extend of warming reaches 180 km^2 or more, and has a dependence on bathymetry and distance to coast. Estimation of the vertical extend of the warm layer, showed maximum depths of 1.8 meters in June that rapidly decrease towards autumn. Thus temperature sensors, typically

located at 3 or 4 m will most likely not capture this daily variability.

Since detailed SST observations are not always available, modelling the diurnal cycle is necessary to compensate for the loss of vertical structure information in bulk water temperature measurements. The simplified models for predicting diurnal warming used in the present study represent possible candidates due to their simple implementation and their low computational cost. Collocated maximum warming has almost zero biases for the Zeng & Beljaars (2005) scheme, ∼0.14 K for the Filipiak et al. (2010) scheme and a 0.39 bias is found for the Clayson & Curry (1996) scheme. The overall correlation of maximum warming between the models and SEVIRI does not exceed 0.5. When hourly SSTs are compared to in situ measurements from different locations, the correlation with SEVIRI, the Zeng & Beljaars (2005) and the Filipiak et al. (2010) schemes is ∼0.98-0.99, the biases are ∼0.1 K and the standard deviations range between 0.63 and 0.72 K.

The correlation between observed and modelled warming and parameters such as u and u from HIRLAM, SEVIRI SSI and $K_{d(490)}$ shows the correct trends. Negative correlation with u is found, low for SEVIRI and rather large for the models, as they are forced by the field. Positive correlation is found for Q, SSI and SSI', higher for the models (∼0.1-0.3) than for the SEVIRI warming (∼0-0.2). SEVIRI correlations with u and SSI are maximum when there is a 3-hour time-lag.

It is shown that the FMKLB model is representative of the distribution of warming cases as observed from SEVIRI. The ZB scheme is able to resolve the spatial extend of the observed warming also accounting for the depth of the warm layer. The CC scheme provides a quick estimation of the peak skin dSST which is useful for an estimation of potential warming but not representative enough, as the "cool skin" bias is expected to be rather large under very low wind conditions. All models are sensitive to the input wind fields and should be further investigated.

Hopefully, this study has successfully demonstrated the applicability of near-surface ocean wind observations from satellite sensors. QuikSCAT has proven valuable for the description of the average wind characteristics over large areas. SAR winds have been shown to contain much more spatial variability. SEVIRI, on a geostationary orbit, has been found accurate when compared with in situ measurements and appropriate for the identification of diurnal warming of the sea surface.

Diurnal warming of the upper ocean has been found to occur in latitudes up to 60°N, routinely observable during spring and summer. Sush findings highlight the importance of properly accounting for SST and its daily variability in order to better describe the processes that influence the wind field over the ocean. Simple models that can predict diurnal warming are thought to be of aid when accurate

SST measurements are not readily available but their implementation needs to be investigated further.

Chapter 6

Future Work

Despite the end of the QuikSCAT mission, other scatterometers such as the European ASCAT on Metop-A and the Indian OCEANSAT-2 are currently in orbit. This continuity of scatterometer observations is of high interest for the offshore wind resource community. Investigations on the differences between the past and existing products will result in methodologies of merging the data, thus creating long, almost continuous time-series of ocean vector winds.

Some higher resolution scatterometer products are available and KNMI has an ASCAT 12.5 km product available in operational mode and a coastal product in pre-operational mode. Such products will be useful for wind resource assessment studies as they achieve higher proximity to the coast, where most typically offshore wind farms are currently installed.

The spectral properties of the satellite wind fields can be further investigated. As the coverage of SAR observations is not fixed, it is difficult to obtain continuous datasets that frequently cover the same area. In this context, it would be interesting to examine the sensitivity of the spectral slopes as a function of the domain.

This spectral analysis study was constrained only in a small part of the North Sea, due to an overlapping of 135 SAR images. It would be interesting to examine the impact of keeping a constant domain size and applying it as a "moving window", in different areas of the North Sea depending on the availability of SAR scenes.

The time mismatch between the SAR and scatterometer fields can possibly be used to create a daily tandem product. By processing the SAR fields to a 25 km resolution, both products can be combined to ensure a maximum availability of 4 times per day.

When quantifying diurnal warming from SEVIRI observations, the night-time reference fields are composed of SST retrievals with quality 3 and above. But the anomaly fields require only quality 5 day-time retrievals. It would be of interest to examine the quantitative impact of lowering the quality flag for the anomalies as well.

Moreover, the night-time reference fields have gaps due to cloud masking that prevent day-time anomalies to be computed. A solution would be to apply some interpolation scheme to fill the gaps and re-evaluate diurnal warming. Such a study has been performed for the Tropical Atlantic with promising results, see Marullo et al. (2010).

Such an interpolation scheme can be actually applied to all the hourly SEVIRI SSTs, to achieve a better description of the anomalies. This has to be done in a proper manner, to ensure that the interpolated fields are realistic and representative of the physical conditions. Moreover, the hourly interpolated SSTs can be used in an NWP model, such as WRF in order to evaluate the impact of properly resolving the diurnal SST cycle on the modelled wind fields. Regarding the modelling of the diurnal cycle, other parameterizations can be tested and other model inputs can be used. Especially for some parameterizations tested already, derivation of new coefficients may be required.

To examine the exact impact of diurnal warming on the vertical wind profile, in situ observations at multiple heights will certainly aid to shed light on the exact processes that take place during diurnal warming events. With such information at hand, it can be possible to evaluate the response of the air temperature and wind speed at various heights to the sudden increase of SST.

Bibliography

Aminou DMA, Ottenbacher A, Jacquet B, & Kassighian A, 1999. Meteosat second generation: on-ground calibration, characterisation and sensitivity analysis of SEVIRI imaging radiometer. *Proc. Earth Observing Systems Conf. SPIE, 3750*, 419-430

Anding D, & Kauth R, 1970. Estimation of sea surface temperature from space. *Rem. Sens. Env., 1*, 217–220

Archer CL & Jacobson MZ, 2005. Evaluation of global wind power. *J. Geophys. Res., 110*, D12110, doi: 10.1029/2004JD005462.

Badger, M., Peña, A., Bredesen, R.E., Berge, E., Hahmann, A., Badger, J., Karagali, I., Hasager, C.B., Mikkelsen, T., 2012. Bringing satellite winds to hub-height. *Proceedings EWEA - The European Wind Energy Association*, 2012.

Barthelmie R, Hansen OF, Enevoldsen K, Højstrup J, Frandsen S, Pryor SC, Larsen S, Motta M, & Sanderhoff P, 2005. Ten years of meteorological measurements for offshore wind farms. *J. So. En. Eng., 127*, 2, 170-176.

Beal RC, Young GS, Monaldo FM, Thompson DR, Winstead NS, & Scott CA, 2005. High resolution wind monitoring with Wide Swath SAR: A user's guide. *U.S. Department of Commerce, National Oceanic and Atmospheric Administration*, Washington DC, June 2005.

Boutin J, Quilfen Y, Merlivat L, & Piolle JF, 2009. Global average of air-sea CO2 transfer velocity from QuikSCAT scatterometer wind speeds. *J. Geophys. Res., 114*, C04007.

Brisson A, Le Borgne P, & Marsouin A, 2002. Results of One Year of Preoperational Production of Sea Surface Temperatures from GOES-8. *J. Atm. Ocean. Technol, 19*, 1638–1652.

Brown AR, Beljaars ACM, & Hersbach H, 2006. Errors in parametrizations of convective boundary-layer turbulent momentum mixing. *Q. J. R. Meteorol. Soc., 132*, 1859–1876.

Capps SB, & Zender CS, 2010. Estimated global ocean wind power potential from QuikSCAT observations, accounting for turbine characteristics and siting. *J. Geophys. Res. 115*, D09101, doi:10.1029/2009JD012679.

Charnock H, 1955. Wind stress on a water surface. *Quart. J. Roy. Meteor. Soc. 81*, 639-640, doi: 10.1002/ qj.49708135027.

Chelton D, Esbensen SK, Schlax MG, Thum N, Freilich MH, Wentz FJ, Gentemann C, McPhaden MJ, & Schopf PS, 2001. Observations of coupling between surface wind stress and sea surface temperature in the Eastern Tropical Pacific. *J. Clim, 14*, 1479–1498

Chelton D, Schlax MG, Freilich MH & Milliff RF, 2004. Satellite measurements reveal persistent small-scale features in ocean winds. *Science, 303*, 978–983.

Christiansen M, Koch W, Horstmann J, Hasager C, & Nielsen M, 2006. Wind resource assessment from C-band SAR. *Rem. Sens. Env., 105*, 68–81.

Christiansen M, & Hasager C, 2006. Using airborne and satellite SAR for wake mapping offshore. *Wind Energy, 9*, 437–456.

Christiansen M, Hasager C, Thompson D, & Monaldo F, 2008. Ocean winds from Synthetic Aperture Radar. *Oc. Rem. Sens.: Recent Techniques and Applications*, 31–54, Research Signpost.

Clayson CA, & Curry JA, 1996. Determination of surface turbulent fluxes for the Tropical Ocean-Global Atmosphere Coupled Ocean-Atmosphere Response Experiment: Comparison of satellite retrievals and in situ measurements. *J. Geophys. Res., 101*, C12, 28515–28528.

Clayson CA, & Weitlich D, 2007. Variability of tropical diurnal sea surface temperature. *J. Climate, 20*, 334–352.

Cornillon P, & Stramma L, 1985. The distribution of diurnal sea surface temperature events in the western Sargasso sea. *J. Geophysical Research, 90*, C6, 11811–11815

Davies AM, & Furnes GK, 1980. Observed and Computed M2 Tidal Currents in the North Sea. *J. Phys. Oceanogr., 10*, 237–257, doi: 10.1175/1520-0485(1980)010.

Deschamps PY, & Frouin R, 1984. Large Diurnal Heating of the Sea Surface Observed by the HCMR Experiment. *J. Phys. Oceanogr., 14*, 177–184

Dickinson S, Kelly KA, Caruso MJ, & McPhaden MJ, 2001. Comparisons between the TAO buoy and NASA scatterometer wind vectors. *J. Atmos. Oceanic Technol., 18*, 799–806.

Donlon C, Minnett PJ, Gentemann C, Nightingale TJ, Barton IJ, Ward B, & Murray MJ, 2002. Toward improved validation of satellite sea surface skin measurements for climate research, *J. Clim., 15*, 353–369.

Donlon C, Robinson I, Casey KS, Vazquez-Cuervo J, Armstrong E, Arino O, & co-authors, 2007. The Global Ocean Data Assimilation Experiment High-resolution Sea Surface Temperature Pilot Project. *Bull. Am. Met. Soc., 88(8)*, pp. 1197–1213.

Donlon C, Casey KS, Gentemann C, Le Borgne P, Robinson IS, & co-authors, 2009. Successes and challenges for the modern Sea Surface Temperature observing system: the Group for High Resolution Sea Surface Temperature (GHRSST) Development and Implementation Plan (GDIP), *OceanObs09*, community white paper.

Eastwood S, Le Borgne P, Préré S, & Poulter D, 2011. Diurnal variability in sea surface in the Arctic. *Rem. Sens. Env., 115*, 2594–2602

Fairall CW, Bradley EF, Godfrey JS, Wick GA, Edson JB, & Young GS, 1996. Cool-skin and warm-layer effects on sea surface temperature, *J. Geophys. Res., 101*, 1295–1308, doi:10.1029/95JC03190

Filipiak MJ, Merchant CJ, Kettle H, & Le Borgne P, 2010. A statistical model for sea surface diurnal warming driven by numerical weather prediction fluxes and winds. *Ocean Sci. Discuss., 7*, 1497–1532.

Flament P, Firing J, Sawyer M, & Trefois C, 1993. Amplitude and horizontal structure of a large diurnal sea surface warming event during the Coastal Ocean Dynamics Experiment. *J. Phys. Oceanogr., 24*, 24–139, 199 (SOEST contr. 3275)

Gentemann CL, Minnett PJ, Le Borgne P, & Merchant C, 2008. Multi-satellite measurements of large diurnal warming events. *Geophys. Res. Let., 35*, L22602.

Global Wind Energy Council, 2010. Global Wind Report: Annual market update 2010. Brussels, Belgium.

Hahmann AN, Rostkier-Edelstein D, Warner TT, Vandenberghe F, Liu Y, Babarsky R, & Swerdlin SP, 2010. A reanalysis system for the generation of mesoscale climatographies. *J. Appl. Meteor. Climatol., 49*, 954–972.

Halpern D, & Reed RK, 1976. Heat budget of the upper ocean under light winds. *J. Phys. Oceanogr. 6*, 972–975.

Halpern D, 1988. Moored surface wind observations at four sites along the Pacific Equator between 140° and 95°W. *J. Clim., 1*, 1251–1260.

Hasager CB, Nielsen M, Astrup P, Barthelmie RJ, Dellwik E, Jensen NO, Jørgensen BH, Pryor SC, & Rathmann O, 2005. Offshore wind resource estimation from satellite SAR wind field maps. *Wind Energy 8*, 403–419

Hasager CB, Barthelmie RJ, Christiansen MB, Nielsen M, & Pryor SC, 2006. Quantifying offshore wind resources from satellite wind maps: study area the North Sea. *Wind Energy 9*, 63-74, doi:10.1002/we.190

Hasager CB, Peña A, Christiansen MB, Astrup P, Nielsen M, Monaldo F, Thompson D, & Nielsen P, 2008. Remote sensing observation used in offshore wind energy. *IEEE J. Sel. Top. Appl. Earth Obs. Rem. Sens.1(1)*, 67–79, doi:10.1109/JSTARS.2008.2002218.

Hasager CB, Badger M, Peña A, Larsen XG, & Bingöl F, 2011. SAR-based wind resource statistics in the Baltic Sea. *Remote Sensing 3(1)*, 117–144, doi:10.3390/rs3010117.

Hersbach H, Stoffelen A, & de Haan S, 2007. An improved C-band scatterometer ocean geophysical model function:CMOD5. *J. Geophys. Res., 112*, C03006, 476–493.

Hersbach H, 2010. Comparison of C-band Scatterometer CMOD5.N equivalent neutral winds with ECMWF. *J. Atmos. Ocean. Techn., 27*, 721–736.

Hilburn KA, Wentz FJ, Smith DK, & Ashcroft PD, 2006. Correcting active scatterometer data for the effects of rain using passive radiometer data. *J. App. Meteor. Clim. 45*, 382–398.

Høyer J, & She J, 2007. Optimal Interpolation of sea surface temperature for the North Sea and Baltic Sea. *J. Mar. Sys., 65*, 176–189.

Høeyer J, Karagali I., Dybkjær, & Tonboe R, 2012. Multi sensor validation and error characteristics of Arctic satellite sea surface temperature observations.*Rem. Sens. Env.*, in press.

Hoffman RN, & Leidner SM, 2005. An introduction to the near-real-time QuikSCAT data. *Wea. Forec., 20*, 476–493.

Jet Propulsion Laboratory, 2006. NASA Quikck Scatterometer - QuikSCAT science data product user's manual: overview and geophysical data products. Version 3.0, D-18053-RevA, California Institute of Technology.

Jury MR, 1993. A thermal front within the marine atmospheric boundary layer over the Agulhas Current south of Africa: composite aircraft observations. *J. Geophys. Res., 99*, 3297–3304

Kahru M, Leppänen J-M, & Rud O, 1993. Cyanobacterial blooms cause heating of the sea surface, *Mar. Ecol. Prog. Ser., 101*, 1–7.

Kara AB, Wallcraft AJ, & Bourassa MA, 2008. Air-sea stability effects on the 10-m winds over the global ocean: Evaluation of air-sea flux algorithms. *J. Geophys. Res. 113*, C04009, doi:10.1029/2007JC004324.

Kara AB, Wallcraft AJ, Martin PJ, & Pauley RL, 2009. Optimizing surface winds using QuikSCAT measurements in the Mediterranean Sea during 2000-2006. *J. Mar. Sys. 78*, 119–131, doi:10.1016/j.jmarsys.2009.01.020.

Kawai Y, & Wada A, 2007. Diurnal sea surface temperature variation and its impact on the atmosphere and ocean: A review. *J. Oceanogr., 63*, 721–744.

Kolstad EW, 2008. A QuikSCAT climatology of ocean surface winds in the Nordic seas: Identification of features and comparison with the NCEP/NCAR reanalysis. *J. Geophys. Res. 113*, D11106, doi:10.1029/2007JD008918.

Météo France (2005). Surface Solar Irradiance Product Manual, Ocean & Sea Ice SAF, Version 1.5, SAF/OSI/M-F/TEC/MA/123, November 2005.

LeBorgne P, Legendre G, & Marsouin A, 2005. Ocean and Sea Ice SAF hourly products of Sea Surface Temperature and Radiative fluxes. *Météo France/DP/CMS, 2005*, Decemper 2005.

LeBorgne P, Legendre G, Marsouin A, Roquet H, & Merchant C, 2006. OSI-SAF SEVIRI SST new processing chain: method, operational & experimental products. *Proc. EUMETSAT Conf. 2010*, Cordoba, Spain. EUMETSAT P.57, http://www.eumetsat.int/Home/Main/AboutEUMETSAT/Publications/ConferenceandWorkshopProceedings/2010/SP_2010129112551446?l=en

Liu WT, Tang W, 1996. Equivalent neutral wind. *National Aeronautics and Space Administration, Jet Propulsion Laboratory, California Institute of Technology, National Technical Information Service, distributor.*

Liu WT, 2002. Progress in Scatterometer Application. *J. Oceanogr., 58*, pp. 121–136.

Liu WT, Tang W, & Xie X, 2008. Wind power distribution over the ocean. *Geophys. Res. Let. 35*, L13808, doi:10.1029/2008GL034172.

Martin S, 2004. An introduction to ocean remote sensing. *Cambridge Un. Press*, ISBN 0521 802806.

Marullo R, Santoleri V, Banzon R, Evans H, & Guarracino M, 2010. A diurnal-cycle resolving sea surface temperature product for the tropical Atlantic. *J. Geophys. Res., 115*, C05011, doi:10.1029/2009JC005466.

Mahura A, Sattler K, Petersen C, Amstrup B, & Baklanov A, 2005. DMI-HIRLAM Modelling with High Resolution Setup and Simulations for Areas of Denmark. *DMI Technical Report 05-12*, 44.

Merchant CJ, Le Borgne P, Marsouin A, & Roquet H, 2008. Optimal estimation of sea surface temperatures from split-window observations. *Rem. Sens. Env., 112*, 2469–2484.

Minnett P, 2003. Radiometric measurements of the sea-surface skin temperature: the competing roles of the diurnal thermocline and the cool skin. *Int. J. Rem. Sens., 24(24)*, 5033–5047.

Minnett, P, & Kaiser-Weiss A, 2012. Discussion document: Near-surface oceanic temperature gradients. *GHRSST*, Version 12.

Mostovoy GV, Fitzpartick PJ, & Li Y, 2005. Regional accuracy of QuikSCAT gridded winds. *Int. J. Rem. Sens., 26(18)*, 4117–4136, doi:10.1080/01431160500165864.

Motta M, & Barthelmie RJ, 2004. The influence of non-logarithmic wind speed profiles on potential power output at Danish offshore sites. *Wind Energy, 8*, 219–236, doi:10.1002/we.146.

Naderi FM, Freilich MH, & Long DG, 2002. Spaceboren radar measurement of wind velocity over the ocean - an overview of the NSCAT scatterometer system. *Proc. IEEE, 79(6)*, 850–866.

Offiler D, 1994. The Calibration of ERS-1 Satellite Scatterometer Winds. *J. Atmos. Oceanic Technol., 11*, 1002–1017.

O'Neill LW, Chelton DB & Esbensen SK, 2010. The effects of SST-induced surface wind speed and direction gradients on midlatitude surface vorticity and divergence. *J. Clim., 2010*, 255–281.

Météo-France 2006. Atlantic Sea Surface Temperature Product Manual. *EUMETSAT Ocean and Sea Ice Satellite Application Facility*, http://www.osi-saf.org/biblio/voir_info.php?did=27&safosi_session_id=55678bd92ab85ef3fdc32a1dbf91d851.

Physical Oceanography DAAC, 2001. SeaWinds on QuikSCAT Level 3 Daily, Gridded Ocean Wind Vectors (JPL SeaWinds Project) Guide Document. *PODAAC, JPL*, **Version 1.1**, October 2001, D-20335.

Price J, Weller R, & Pinkel R, 1986. Diurnal Cycling: Observations and Models of the Upper Ocean Response to Diurnal Heating, Cooling and Wind Mixing. *J. Geophys. Res., 91(C7)*, 8411–8427.

Price J, Weller R, Bowers C, & Briscoe M, 1987. Diurnal Response of Sea Surface Temperature Observed at the LongTerm Upper Ocean Study (34° N, 70° W) in the Sargasso Sea. *J. Geophys. Res., 92(C13)*, 14480–14490.

Risien CM, & Chelton DB, 2006. A satellite-derived climatology of global ocean winds. *Rem. Sens. Env. 105(3)*, 221–236, doi: 10.1016/j.rse.2006.06.017.

Sathe A, Gryning SE & Peña A, 2011. Comparison of the atmospheric stability and wind profile climatology at two wind farm sites over a long marine fetch in the North Sea. *Wind Energy*, DOI:10.1002/we.456

Satheesan K, Sarkar A, Parekh A, Ramesh Kumar MR, & Kuroda Y, 2007. Comparison of wind data from QuikSCAT and buoys in the Indian Ocean. *Int. J. Rem. Sens., 28(10)*, 2375–2382.

Saunders PM, 1967. The temperature at the ocean-air interface. *J. Atm. Sci., 24*, 269–273.

Schmid J, 2000. The SEVIRI Instrument. *Proc. EUMETSAT Conf.*, Bologna, Italy, 29 May-2 June, 13–32, Darmstadt, Germany: EUMETSAT ed.

Soloviev A, & Lukas R, 2006. The near-surface layer of the ocean: structure, dynamics and applications. *Atm. Ocean. Sci. Lib., 31*, 1–31

Stoffelen A, & Anderson D, 1997. Scatterometer data interpretation: estimation and validation of the transfer function CMOD4. *J. Geophys. Res., 102*, C3, 5767–5780.

Stoffelen A, Vogelzang J, & Verhoef A, 2010. Verification of scatterometer winds, *10th International Winds Workshop*, Tokyo, Japan, 20-26 February 2010, EUMETSAT P.56. Available from http://www.eumetsat.int/Home/Main/AboutEUMETSAT/Publications/ConferenceandWorkshopProceedings/2010/SP_20101122112352839.

Stuart-Menteth AC, Robinson IS, & Challenor PG, 2003. A global study of diurnal warming using satellite-derived sea surface temperature. *J. Geophy. Res., 108*, C5, 3155.

Stull RB, 1988, An Introduction to Boundary Layer Meteorology. *Atm. Ocean. Sci. Lib., 13*, 383–386.

Sweet WR, Fett R, Kerling J, & LaViolette P, 1981. Air-sea interaction effects in the lower troposphere across the north wall of the Gulf Stream. *Mon. Wea. Rev., 109*, 1042–1052.

Troen I, & Petersen EL, 1989. European Wind Atlas. ISBN 87-550-1482-8. Risøoe National Laboratory, Roskilde.

Ward B, 2006. Near-surface ocean temperature. *J. Geophys. Res., 111*, C02004.

Webster PJ, Clayson CA, & Curry JA, 1996. Clouds, radiation, and the diurnal cycle of sea surface temperature in the Tropical Western Pacific. *J. Climate, 9*, 1712–1730.

Wentz FJ, Peteherych S, & Thomas LA, 1984. A model function for ocean radar cross sections at 14.6 GHz. *J. Geophys. Res., 89*, C3, 3689–3704.

Wentz FJ, 1997. A well-calibrated ocean algorithm for special sensor microwave/imager. *J. Geophys. Res., 102*, C4 8703–8718.

Wentz FJ, & Smith DK, 1999. A model function for the ocean-normalized radar cross section at 14GHz derived from NSCAT observations. *J. Geophys. Res., 104*, 11499–11514.

Winterfeldt J, 2008. Comparison of measured and simulated wind speed data in the North Atlantic. *PhD Thesis, GKSS 2008/2*, ISSN 0344-9629, 3689–3704.

Xie SP, 2004, Satellite observations of cool ocean-atmosphere interaction. *Bull. Amer. Meteor. Soc., 85*, 195–208.

Zeng X, & Beljaars A, 2005. A prognostic scheme of sea surface skin temperature for modelling and data assimilation. *Geoph. Res. Let., 32*, L14605.

Appendix A

Offshore wind farms in Northern Europe

Table A.1: List of the Northern European offshore wind farms in the planning stage (U.P.) and under construction (U.C.) shown in Figure 1.1.

Name	Stage	Latitude	Longitude
Dogger Bank	U.P.	54° 43' 28" N	02° 46' 06" E
Irish Sea	U.P.	55° 45' 43" N	01° 23' 41" W
Hornsea	U.P.	53° 57' 54" N	01° 28' 47" E
Firth of Forth I	U.P.	56° 35' 41" N	01° 49' 12" W
Firth of Forth II	U.P.	56° 21' 57" N	01° 36' 28" W
Blekinge Offshore	U.P.	55° 56' 15" N	14° 59' 37" E
Atlantic Array	U.P.	51° 21' 00" N	04° 30' 39" W
Moray Firth	U.P.	56° 08' 38" N	02° 48' 03" W
Triton Knoll	U.P.	53° 28' 44" N	00° 50' 13" E
London Array	U.C.	51° 38' 38" N	01° 33' 13" E
Greater Gabbard	U.C.	51° 52' 48" N	01° 56' 24" E
Borkum West II	U.C.	53° 57' 25" N	06° 29' 38" E
BARD Offshore 1	U.C.	54° 22' 00" N	05° 59' 00" E
Anholt	U.C.	56° 36' 10" N	11° 12' 32" E
Sheringham Shoal	U.C.	53° 07' 00" N	01° 08' 00" E
Lincs	U.C.	53° 11' 00" N	00° 29' 00" E
Walney Phase 2	U.C.	54° 05' 02" N	03° 36' 46" W
Ormonde	U.C.	54° 06' 00" N	03° 24' 00" W
Thorntonbank Phase II	U.C.	51° 33' 46" N	02° 59' 05" E
Thorntonbank Phase III	U.C.	51° 32' 16" N	02° 55' 15" E

Table A.2: List of the operating Northern European offshore wind farms shown in Figure 1.1.

Name	Latitude	Longitude
Thanet	51° 26' 00" N	01° 38' 00" E
Horns Rev II	55° 36' 00" N	07° 35' 24" E
Rodsand II	54° 33' 00" N	11° 42' 00" E
Lynn & Inner Dowsing	53° 07' 39" N	00° 26' 10" E
Walney 1	54° 02' 38" N	03° 31' 19" W
Robin Rigg	54° 45' 00" N	03° 43' 00" W
Gunfleet Sands	51° 43' 16" N	01° 17' 31" E
Nysted	54° 32' 00" N	11° 43' 00" E
Bligh Bank	51° 39' 36" N	02° 48' 00" E
Horns Rev I	55° 31' 47" N	07° 54' 22" E
Princess Amalia	52° 35' 24" N	04° 13' 12" E
Lillgrund	55° 31' 00" N	12° 47' 00" E
Egmond aan Zee	52° 36' 21" N	04° 25' 08" E
Kentish Flats	51° 27' 36" N	01° 05' 24" E
Barrow	53° 59' 00" N	03° 17' 00" W
Burbo Bank	53° 29' 00" N	03° 10' 00" W
Rhyl Flats	53° 22' 00" N	03° 39' 00" W
North Hoyle	53° 26' 00" N	03° 24' 00" W
Scroby Sands	52° 38' 56" N	01° 47' 25" E
Alpha Ventus	54° 01' 00" N	06° 36' 00" E
Baltic 1	54° 36' 36" N	12° 39' 00" E
Middelgrunden	55° 41' 27" N	12° 40' 13" E
Vindeby	54° 58' 08" N	11° 07' 44" E
Beatrice Demo	58° 05' 52" N	03° 04' 40" W
Hywind	59° 08' 24" N	05° 01' 55" E

Appendix B

RSS and JPL L3 QuikSCAT Gridded Products

After an initial analysis of the RSS QuikSCAT product the use of the JPL L3 product was also considered. There seems to be a fundamental difference between the two products as the JPL L3 has systematic gaps, related to the retrieval of the wind vector cells and remapping. An example of a typical ascending pass for both products is shown in Figure B.1. From a visual inspection, the effective range of wind speeds is the same, the spatial patterns are the same and the only difference is the appearance of gaps in Figure B.1a. Figure B.2 shows the spatial distribution of the valid wind vector cells for the JPL L3 product, where 0 signifies no retrieval and 1, a valid WVC count. The RSS product has no such quality flag. As stated in the user's manual for the JPL L3 product (PO-DAAC, 2001),

> The L3 data are given on a global grid of 1440 pixels in longitude by 720 pixels in latitude (0.25° grid). This is nearly the same sampling resolution as the Level 2B. Therefore, users wishing to use their own interpolation schema to fill data gaps can do so easily...A list of alternate QuikSCAT Level 3 products created by members of the QuikSCAT Science Working Team is available on the PO.DAAC QuikSCAT Links Page for those users who require lower resolution or gap-filled QuikSCAT data but do not wish to perform their own averaging or interpolation.

This is already a good reason not to proceed with the JPL L3 product as it contains gaps, that need to be interpolated. This interpolation will be based on the user,

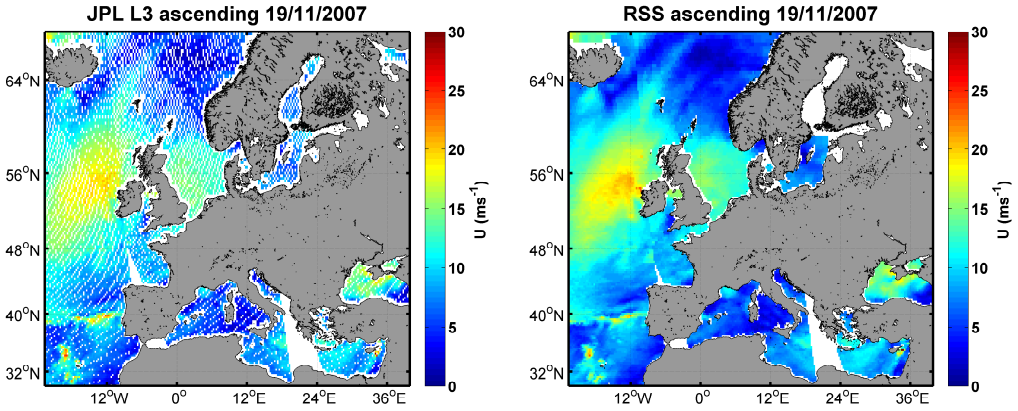

(a) (b)

Figure B.1: a) QuikSCAT JPL L3 ascending (morning) pass on the 19/11/2007 with no flagging applied. b) QuikSCAT RSS ascending (morning) pass on the 19/11/2007 with no flagging applied.

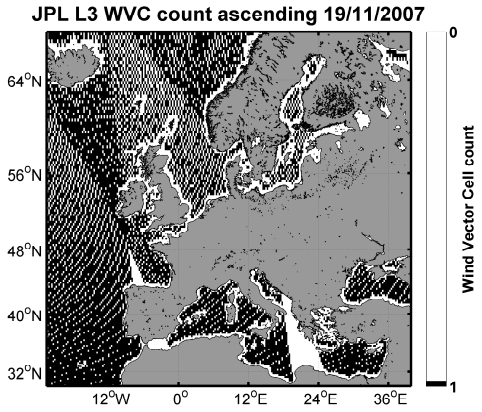

Figure B.2: Wind Vector Cell count for the JPL L3 pass shown in Figure B.1a. The white areas are grid cells with no wind information.

thus allowing different handling of the data. For wind resource assessment, it is useful to have a standard product that will not give different results depending on who uses the data. Therefore, the RSS product, already interpolated to fill gaps seems more appropriate for a standard use.

Nonetheless, a sensitivity analysis is performed to quantify any potential differences between the two products. No rain contaminated retrievals are allowed, so

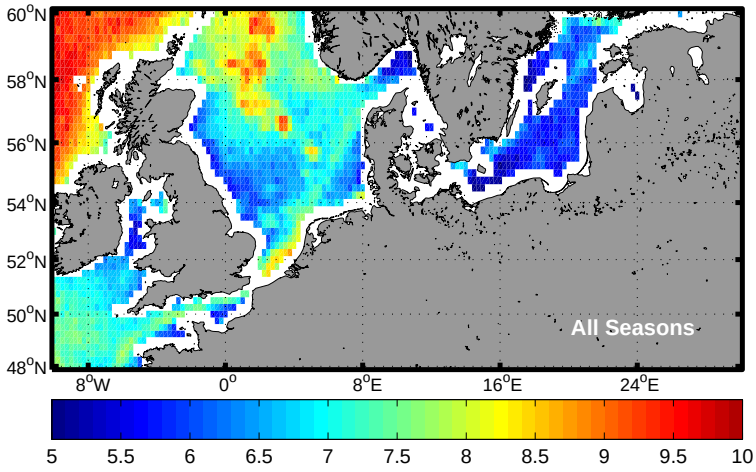

(a) JPL mean u (rain-free)

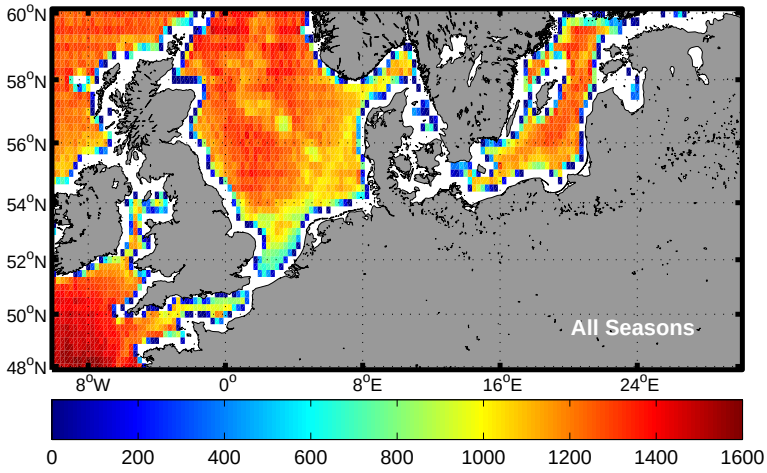

(b) JPL rain free observations

Figure B.3: Mean u and number of rain free retrievals from the JPL L3 gridded product.

both the RSS and JPL products are flagged for rain. More specifically, the JPL flagging scheme and the selected values were "rain_flag" 0 or 4, "rain_prob" 0 and "wvc_count" 1. The RSS flagging scheme and the selected values were "scatflag" 0 and "radrain" 0 or -999. For the entire 10-year long available data sets the mean wind speed u and the number of rain free retrievals are estimated, shown in Figure B.3 for the JPL L3 product and in Figure B.4 for the RSS gridded product.

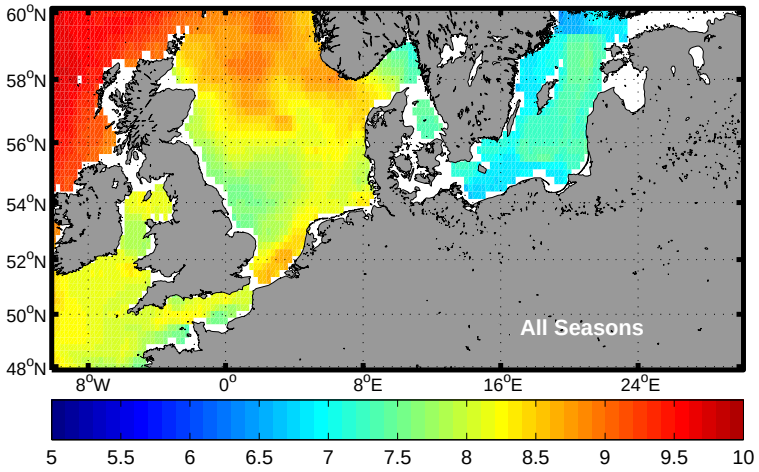

(a) RSS mean u (rain-free)

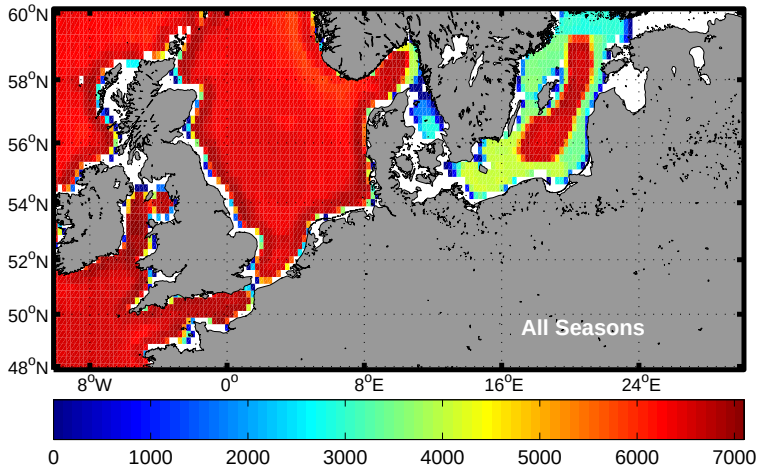

(b) RSS rain free observations

Figure B.4: Mean u and number of rain free retrievals from the RSS gridded product.

When the independent rain flags are applied in each product data availability is significantly different and wind speed biases may reach up to 2.5 m s^{-1}. The difference in data availability and mean u is shown in Figure B.5. The difference in mean wind speed is thought to arise from the difference in data availability, which can be attributed to i) the original gaps in the JPL L3 product and ii) the different rain and sea-ice flagging schemes applied. The RSS products uses data from SSM/I for the rain and ice mask while JPL uses an ice mask generated from weekly National Ice Center ice edge data. The rain flag of JPL is the Multidimensional

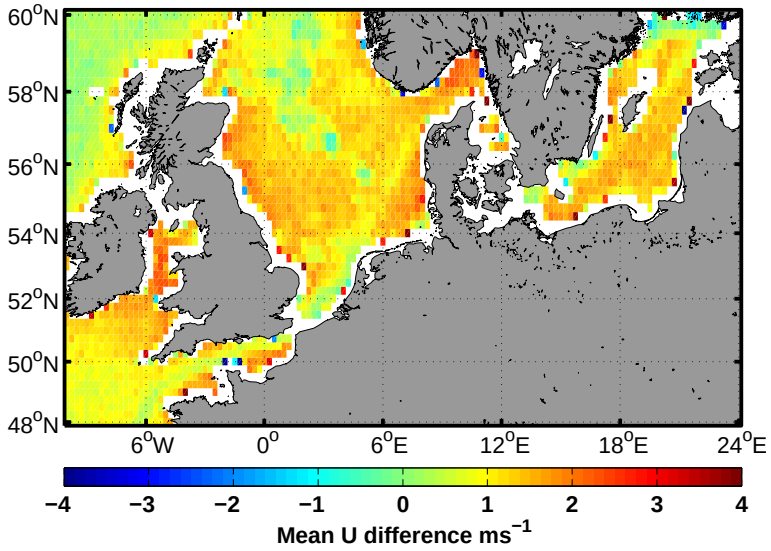

(a) RSS-JPL mean u (rain-free)

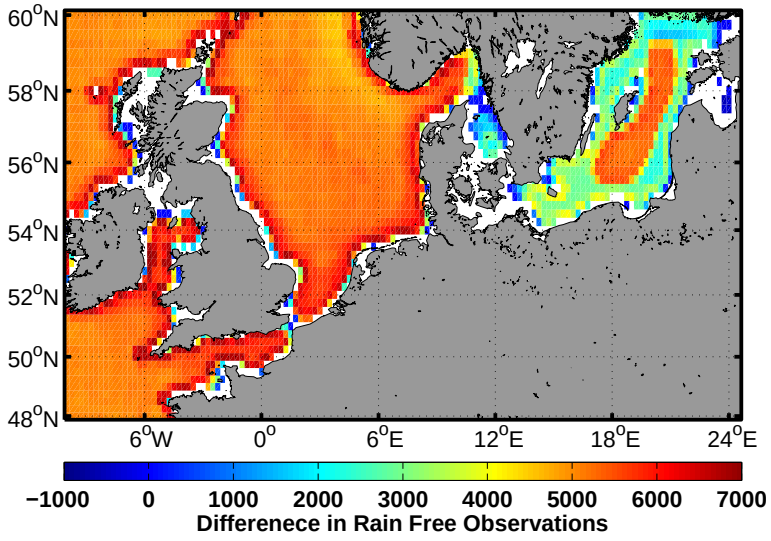

(b) RSS-JPL rain free observations

Figure B.5: Difference in the mean u and the number of rain free retrievals between the RSS gridded and JPL L3 products.

Histogram Rain Flagging (MUDH) technique (JPL, 2006) that relies solemnly on QuikSCAT data.

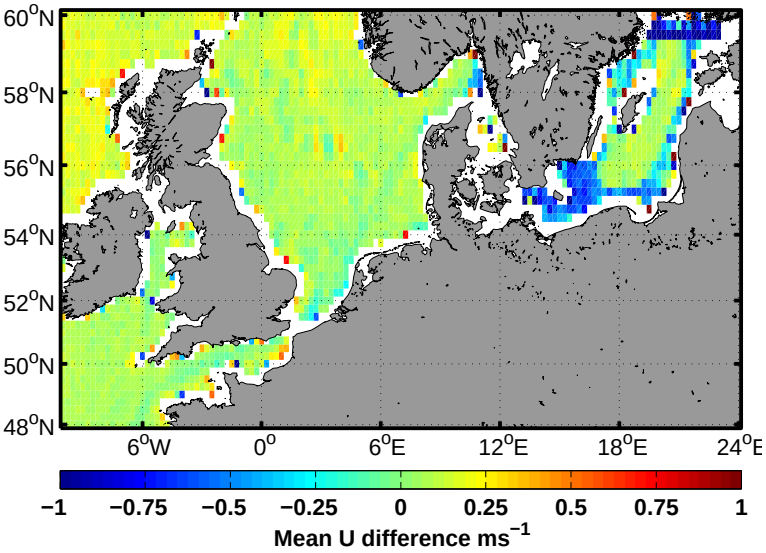

Figure B.6: Difference in the mean u between the RSS gridded and JPL L3 products when the JPL rain-flagging scheme is applied to both products. Areas with zero data difference between the two products are shown as white areas.

When the JPL rain flags are applied to the RSS product, the number of available data is almost the same for both products. By almost it is meant that, there are differences in the areas where RSS undercovers, such as the Gulf of Riga and Finland and the South Baltic. The wind speed biases are mostly within the 0.1 $m\ s^{-1}$ range, shown in Figure B.6. This indicates that the actual differences between the two products are, in this case, very small.

One may argue that the rain flag of the JPL product is not properly applied. That was not investigated further as the purpose of this sensitivity test was not to compare different QuikSCAT products but to identify if the choice of one product rather than another, would significantly change the results of the analysis. The author has concluded that qualitatively the two products do not seem to have significant differences. Given the original gaps in the JPL product, that can be interpolated but that is a choice of the user, it is thought more reasonable to avoid using such a product for wind resource assessment studies. Especially when the purpose is to disseminate the applicability of scatterometer observations to the offshore wind energy community, it is most probably better to use a standard product that does not provide much room for subjective data handling.

Appendix C

Using QuikSCAT to test WRF set-ups

In this part of the study, the applicability of QuikSCAT for testing and validation of the WRF set-up is demonstrated. During a particular study for the South Baltic, we were called to decide which is the optimal Planetary Boundary Layer (PBL) scheme for the particular characteristics of the domain of interest. Six PBL parameterizations are used in WRF. The experiments consist of month-long simulations for the period 1–30 October 2009, using the 6 different PBL and their respective surface layer schemes listed in Table C.1.

Table C.1: Summary of PBL schemes used the model sensitivity study.

Scheme	Closure type	Surface scheme
YSU	1st order	M-O scheme
MYJ	TKE 1.5 order	M-O scheme
QNSE	TKE 1.5 order	QNSE
MYNN2	TKE 1.5 order	MYNN
MYNN3	TKE 2.5 order	MYNN
BouLac	TKE 1.5 order	M-O scheme

The WRF 10 m wind speeds are derived from extrapolating the wind speed values from the first 3 WRF levels. WRF values are interpolated to the QuikSCAT grid and only times available in both datasets are used, thus early morning (05:00-06:00) and evening conditions (18:00-19:00) are captured. A comparison of the mean biases, standard deviations, correlation r and root mean square error (RMSE)

of the 10-m wind speeds in the various WRF simulations as compared to the QuikSCAT data is shown Figures C.1, C.2, C.3 and C.4 respectively.

In general, the mean biases are very similar among the simulations. Over the North Sea and most of the Baltic Sea 10 m wind speeds simulated by WRF are within ± 1 m s^{-1} of those observed. Over the eastern coast of Poland, Russia and Lithuania biases are slightly larger (1–2 m s^{-1}) in all simulations. Small areas with negative biases (i.e. WRF wind speeds larger than observed) occur in the MYNN2 and MYNN3 simulations over the western Baltic Sea.

The RMSE errors between WRF simulations and QuikSCAT observations are also quite similar among the various schemes. Most areas show RMSE$<$2.5 m s^{-1}. As seen in the biases, the RMSE are slightly larger along the southeastern Baltic coast (2.5-3.5 m s^{-1}) and the western Danish coast.

Since QuikSCAT represents "neutral" winds some of these errors are a consequence of differences in stability between the model simulations and the observations. Much larger errors are seen in the north-west corner of the domain. This feature is also observed in the comparisons between QuikSCAT and the WRF derived climatography (see Paper II) and they may be attributed to the observed wind variability from QuikSCAT that may not be captured by the model.

Based on these results it is not at all clear which PBL outperforms the others. Good performance at 10 m, does not guarantee good agreement further up in the boundary layer. Nonetheless, it is helpfull to identify any systematic features common for the different PBL schemes and areas where observations and modelled fields are systematically different.

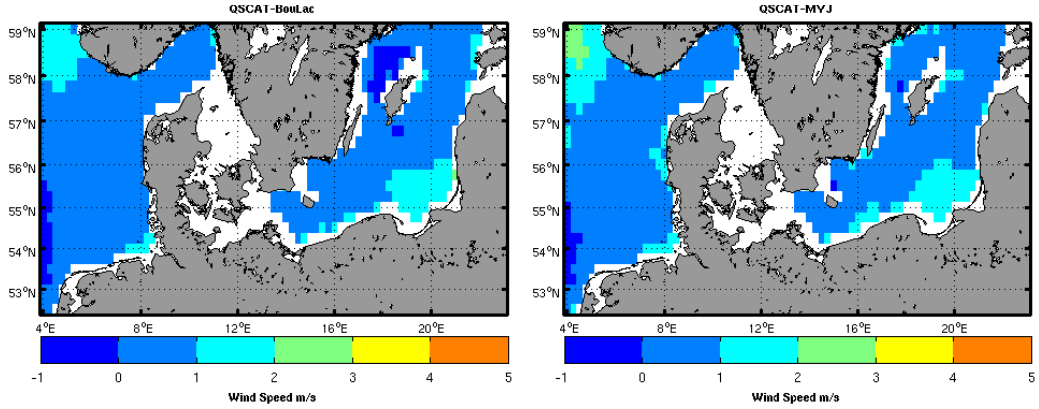

(a) BouLac

(b) MYJ

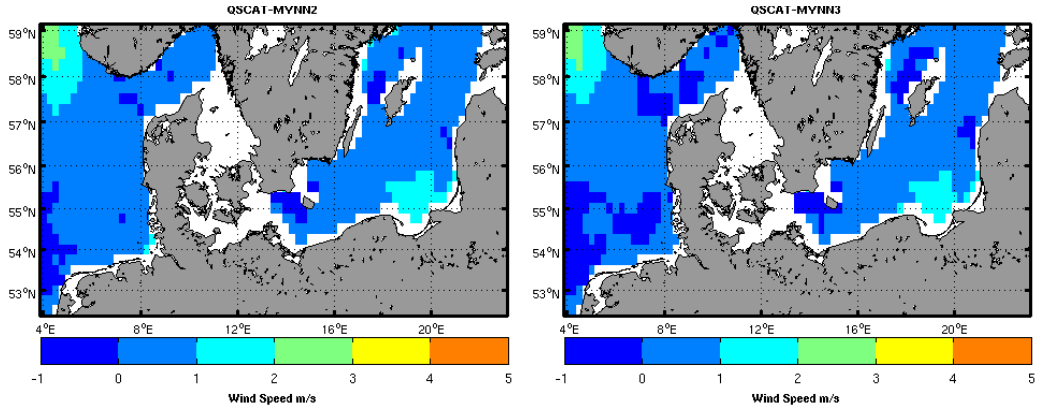

(c) MYNN2

(d) MYNN3

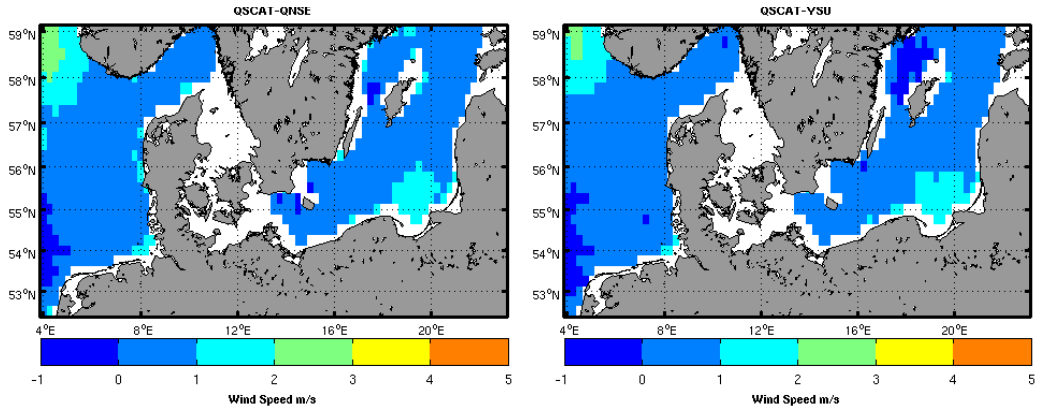

(e) QNSE

(f) YSU

Figure C.1: Mean bias for QuikSCAT minus WRF with different PBL schemes for October 2009.

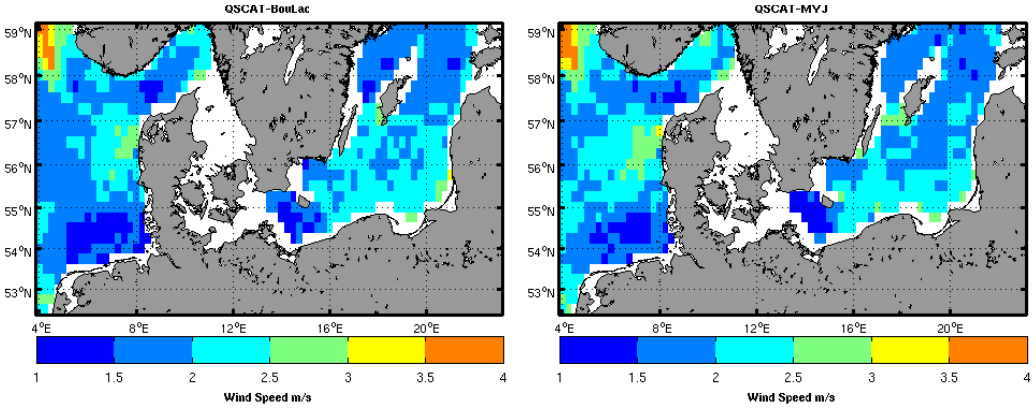

(a) BouLac

(b) MYJ

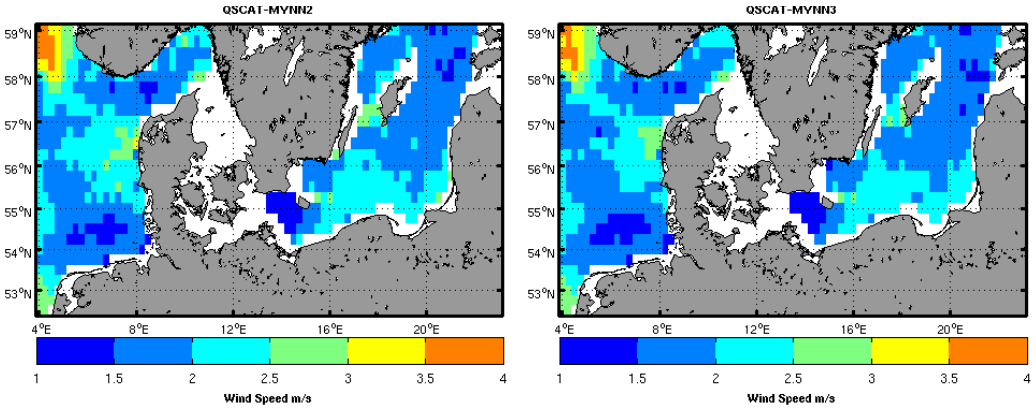

(c) MYNN2

(d) MYNN3

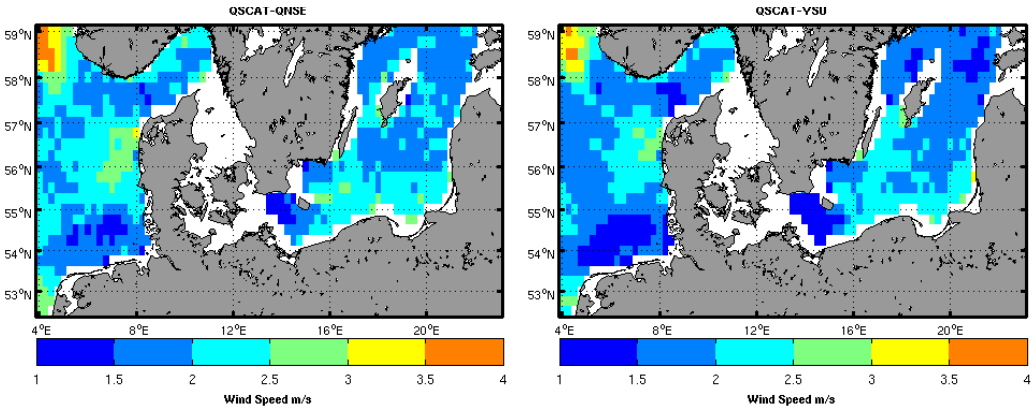

(e) QNSE

(f) YSU

Figure C.2: Standard deviation for QuikSCAT minus WRF with different PBL schemes for October 2009.

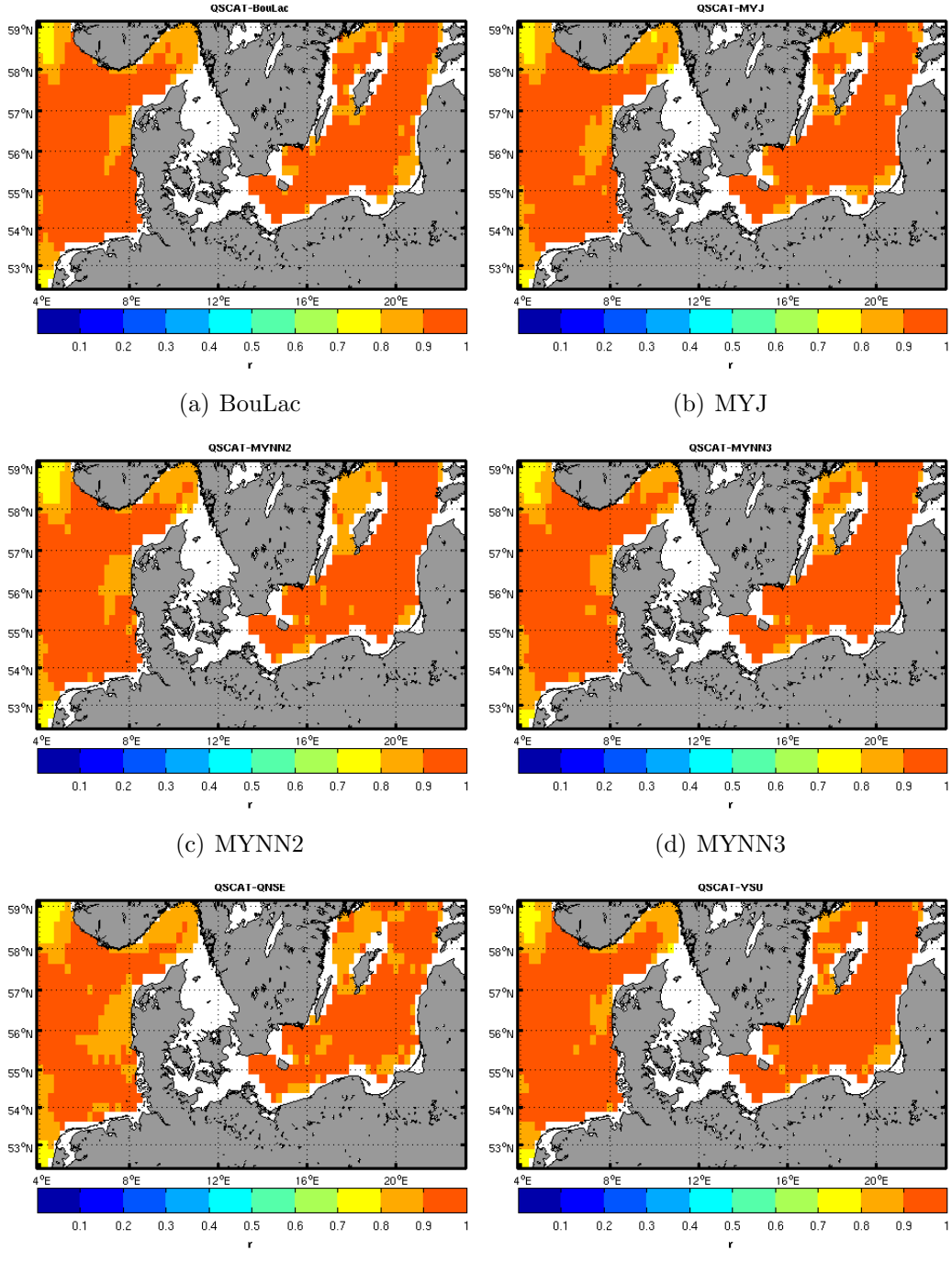

(a) BouLac (b) MYJ

(c) MYNN2 (d) MYNN3

(e) QNSE (f) YSU

Figure C.3: Correlation coefficient r for QuikSCAT minus WRF with different PBL schemes for October 2009.

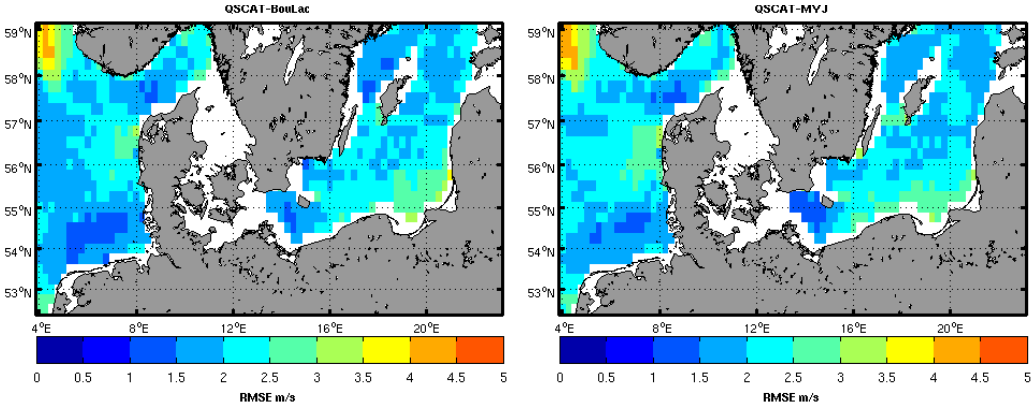

(a) BouLac

(b) MYJ

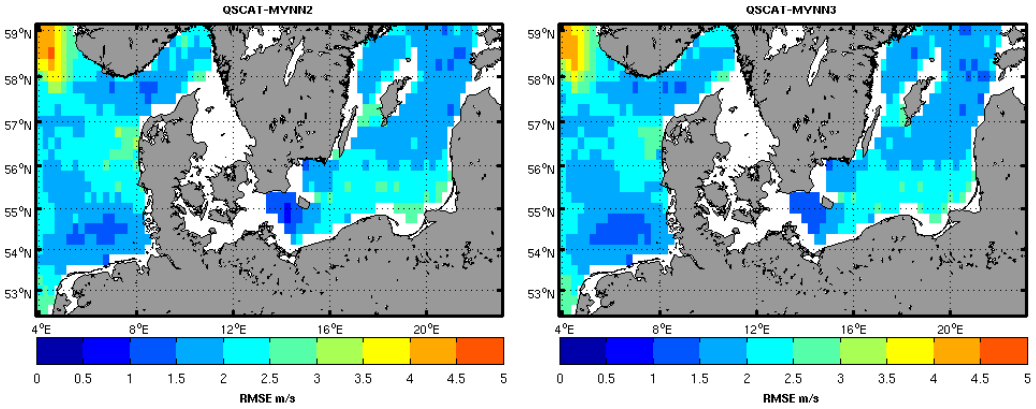

(c) MYNN2

(d) MYNN3

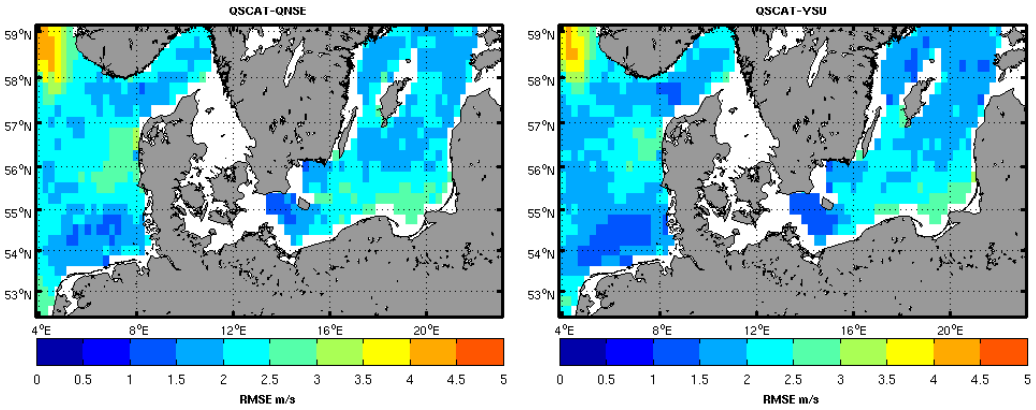

(e) QNSE

(f) YSU

Figure C.4: RMSE for QuikSCAT minus WRF with different PBL schemes for October 2009.

Appendix D

Deriving a proper foundation temperature

In order to define the day-time anomalies in the SST fields, a foundation temperature is required. This represents the temperature of the upper water column under well mixed conditions, free of diurnal warming. In the beginning of Section 3.5, some sensitivity analyses are described, performed in order to conclude on the composition of night-time reference fields from SEVIRI. These candidate composites were inter-compared with the use of "validation" fields, serving as the day-time warming fields. The "validation fields" were composed from the last pre-dawn SST retrieval of the day. Thus, anomalies were defined as validation minus candidate nigh-time reference field and the statistics of this analysis are shown in Paper IV, Figure 2(a,c,d).

To examine the sensitivity of the statistics to the candidate reference fields, an independent foundation temperature field is used in this analysis. The operational, blended SST product from the DMI is produced with the use of an OI method and is described in detail in (Høyer & She, 2007). The methodology followed here is the same as described above, i.e. the DMI-OI product is subtracted from the SEVIRI "validation fields" and the statistics of the anomalies are estimated, similar to Figure 2(a,c,d) in Paper IV.

The distribution of the mean bias, i.e. the anomaly between the SEVIRI validation field (generated daily from the last pre-dawn, quality 5 SST retrieval) and the DMI-OI product, is shown in Figure D.1. The number of cases in each bin of

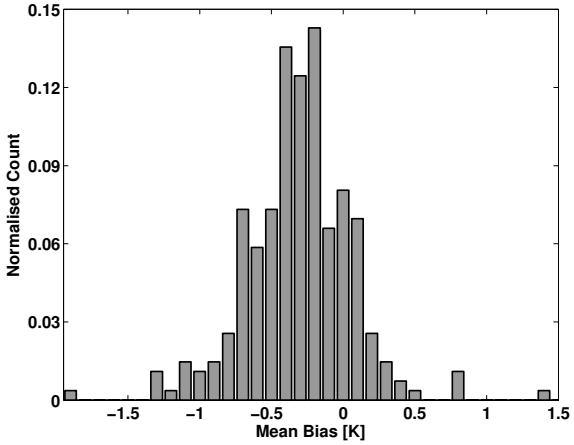

Figure D.1: Mean bias of the last SEVIRI pre-dawn SST field minus the DMI-OI field.

the distribution has been divided with the total number of days included in the test period and for which data are available (273), thus estimating the normalised count, shown in the ordinate.

In most cases the DMI-OI fields are found somewhere between 0.2 and 0.4 K warmer than the validation fields. The standard deviation ranges mostly between 0.3 and 0.5 K. This blended product uses night-time retrievals from approximately 10 sensors, including polar orbiting infra-red and microwave sensors and geostationary sensors.

The main purpose of this analysis is to evaluate if the DMI-OI blended fields behave very different when compared to the SEVIRI reference fields, against the same validation fields. The differences found are rather small, especially if one considers that the blended product uses observations from 10 different sensors while the SEVIRI fields are the products of aggregated night time SST fields from a single sensor.

Figure D.3 shows the distribution of valid pixels used to estimate the mean bias and the standard deviation shown in the previous figures. Since the DMI-OI fields are interpolated, they have no gaps. Therefore all water pixels, 74645 in total, have an SST value. This figure shows the number of available pixels in the validation fields which are composed from the last pre-dawn, quality 5 SST retrieval. If the last pre-dawn value has a lower confidence level, then no value is considered and no anomaly is estimated for that grid cell.

What can generally be seen is that the validation fields have rather poor coverage

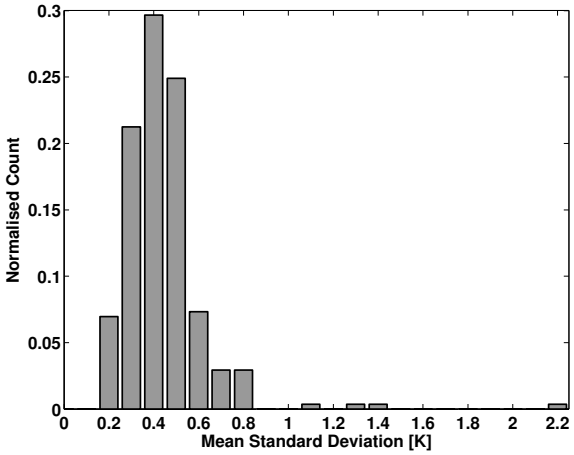

Figure D.2: Standard deviation of the last SEVIRI pre-dawn SST field minus the DMI-OI field.

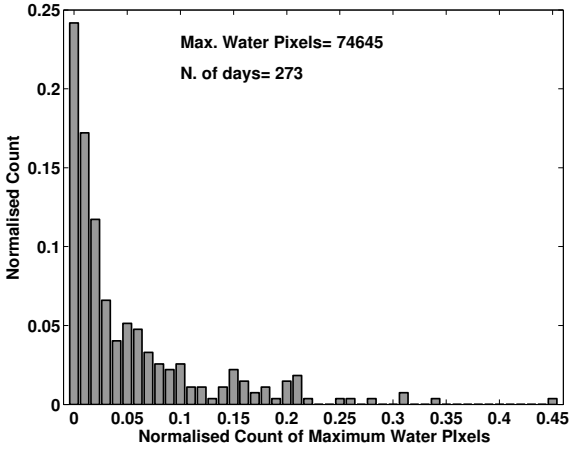

Figure D.3: Pixels with anomalies from the last SEVIRI pre-dawn SST field minus the DMI-OI field, as a normalised count of the total available water pixels in the domain.

and this provides some confidence on the choice to compose the night-time reference fields not from a single hour and day but by aggregating observations over a night-time window and a day window, to ensure as few gaps as possible.

In summary, the distribution of the mean bias and standard deviation of the "validation" minus the DMI-OI field is not radically different than the corresponding distributions estimated from the "validation" minus candidate night-time reference fields from SEVIRI. For the DMI-OI product, most anomalies range between -0.4 and -0.2 K while in the SEVIRI cases this range is between -0.2 and 0 K. The

standard deviation is slightly higher for the DMI-OI case, mostly ranging between 0.3 and 0.5 K while it is between 0.2 and 0.4 K for the SEVIRI reference fields. The number of valid grid cells radically changes, as the DMI-OI product has no gaps while all candidate composites from SEVIRI suffer from missing values. Considering all the above and that the DMI-OI product is blended using observations from multiple sensors that have different error characteristics in the area of interest, it is decided to proceed to the quantification of diurnal warming using a SEVIRI composite night-time reference field.

Appendix E

Sensitivity tests on the FMKLB and ZB models

The purpose of this analysis is to examine the dependence of modelled anomalies $dSST$ from two different simple parameterization schemes on the different physical parameters.

Some of the parameters considered are the input fields for the parameterizations, i.e. wind speed u and the integrated heat flux Q. Others such as the surface solar irradiance SSI and the mean attenuation coefficient at 490 μm $K_{d(490)}$ are not included in the models.

For $K_{d(490)}$ the DMI product is used, which is specifically developed for case-II waters that generally characterise the Baltic Sea and the North Sea. The surface solar irradiance SSI is another product from the SEVIRI observations, described in Paper V.

This analysis is performed by creating match up datasets of time coincident and space collocated $dSST$, u, integrated Q from 08:00 until the time of $dSST$, one daily $K_{d(490)}$ value and the SSI value from the time of $dSST$. Then, according to the type of dependence under examination, $dSST$ is categorize according to u, Q and SSI values.

Ideally, one would expect that $dSST$ increases for increasing Q and SSI and decreasing u. Once the relationship between the different parameters is established,

the impact of $K_{d(490)}$ is examined. This is done by identifying a threshold to classify $K_{d(490)}$ values as low or high; this is set to the 75th percentile of the entire $K_{d(490)}$ range.

All the other parameters, i.e. $dSST$, u, Q and SSI are separated in two groups based on the coincident value of $K_{d(490)}$. For each of the two sub-groups, the same analysis as described previously is performed. Ideally, one would expect that at least for the high $K_{d(490)}$ sub-group, stratification will be very clear.

The results are presented first for the $dSST$ from the Filipiak et al. parameterization, referred to as FMLKB scheme and then for the Zeng-Beljaars parameterization, referred to as ZB scheme.

Filipiak et al. parameterization Initially, the dependence of the modelled $dSST$ on the input wind fields u and integrated net heat flux Q is examined. Figures E.1a and E.2a, highlight this dependence. Ideally, one would expect that for increasing u, $dSST$ will decrease which is generally the case.

Moreover, for a certain u, dSST should be higher for higher Q or SSI values. This is, also, generally the case but the signal is not very clear for the medium range of values of SSI or Q. Figures E.1b and E.2b show the dependence of dSST on Q and SSI for different u ranges, where u increases from top to bottom. The top curve in these figures corresponds to winds of 1 ms^{-1} and the bottom one, to 9 ms^{-1}.

For the lower wind speeds, the increase of dSST with increasing Q or SSI is not very clear. For Q up to 3000 W hr m^{-2} there is an increase, but at that threshold there is a kink especially for low u. Similar for SSI, for low u, dSST varies for increasing SSI values and not always increasing.

Daily $K_{d(490)}$ values have been collocated with $dSST$, u and Q. Note that due to the daily nature of the $K_{d(490)}$ product, only one value is available for every grid cell therefore the temporal variability of $dSST$ can not be correlated with $K_{d(490)}$. Based on the 75th percentile value of 0.37 m^{-1}, $K_{d(490)}$ has been classified as low ($\leq$0.37) or high ($>$), and the associated $dSST$, u and Q values have been split in two groups.

Figure E.3 shows the dependence of $dSST$ on u and Q for the different $K_{d(490)}$ levels along with the corresponding numbers of observations in each subgroup. In general, the correct trends are there but especially for the high $K_{d(490)}$ level, one would wish the stratification for increasing Q to be more prominent.

Figure E.4 shows a similar analysis but for SSI instead of Q.

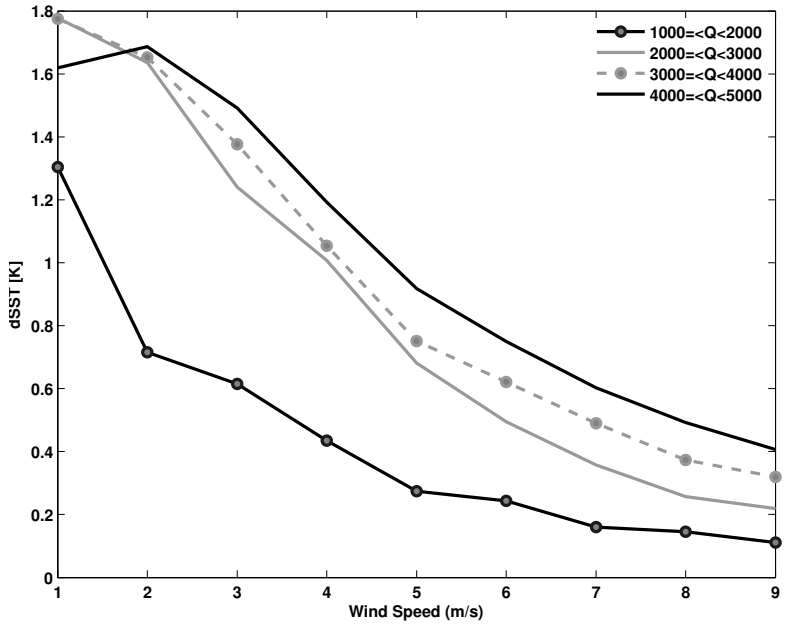

(a) dSST dependence on u for different Q ranges

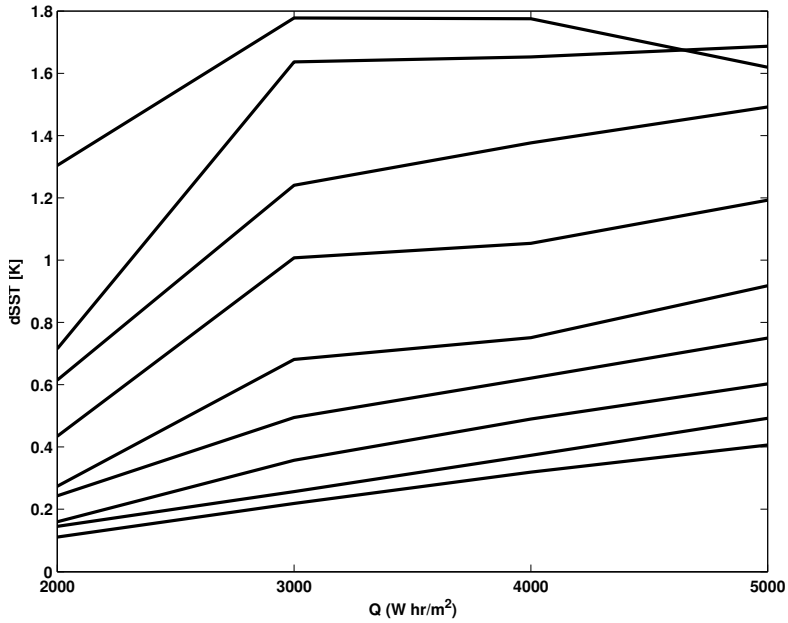

(b) dSST dependence on Q for different u ranges

Figure E.1: a) Dependence of the FMKLB $dSST$ on u for different Q ranges. b) Dependence of dSST on Q for different u ranges, with increasing u from the top curve (1 ms^{-1}) to bottom (9 ms^{-1}).

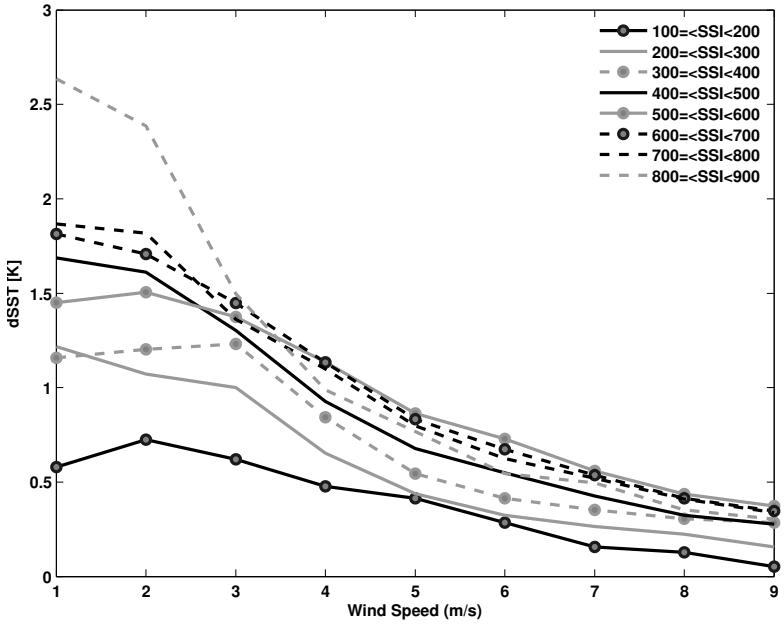

(a) $dSST$ dependence on u for different SSI ranges

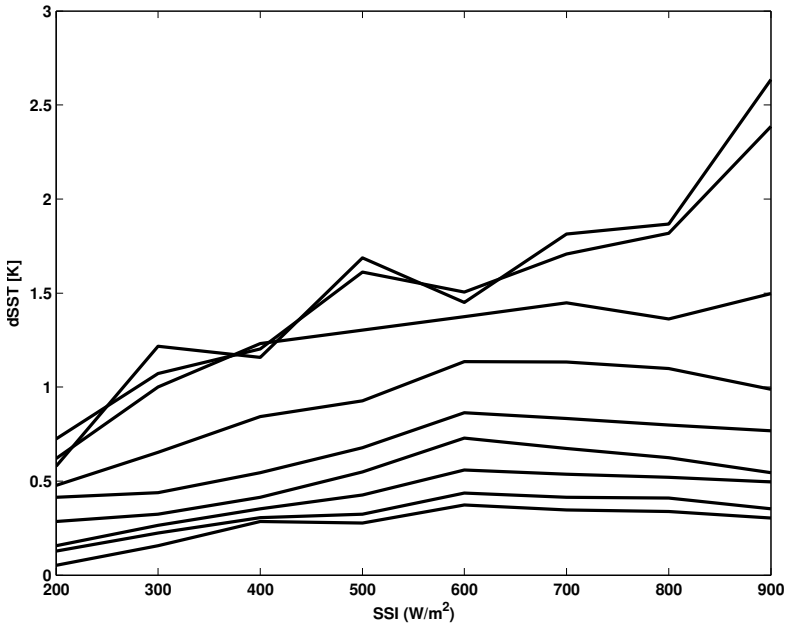

(b) $dSST$ dependence on SSI for different u ranges

Figure E.2: a) Dependence of $dSST$ on u for different SSI ranges. b) Dependence of dSST on SSI for different u ranges, with increasing u from the top curve (1 ms^{-1}) to bottom (9 ms^{-1})

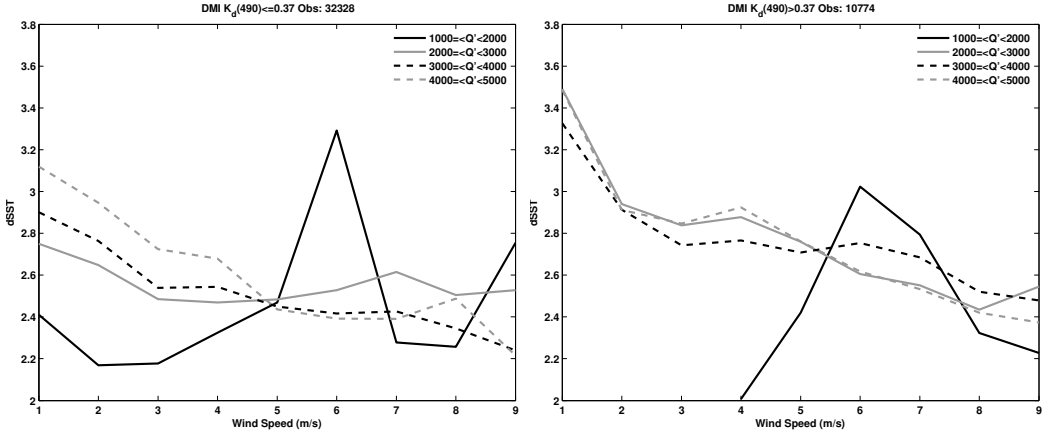

(a) dSST dependence on u and Q for low $K_{d(490)}$

(b) dSST dependence on u and Q for high $K_{d(490)}$

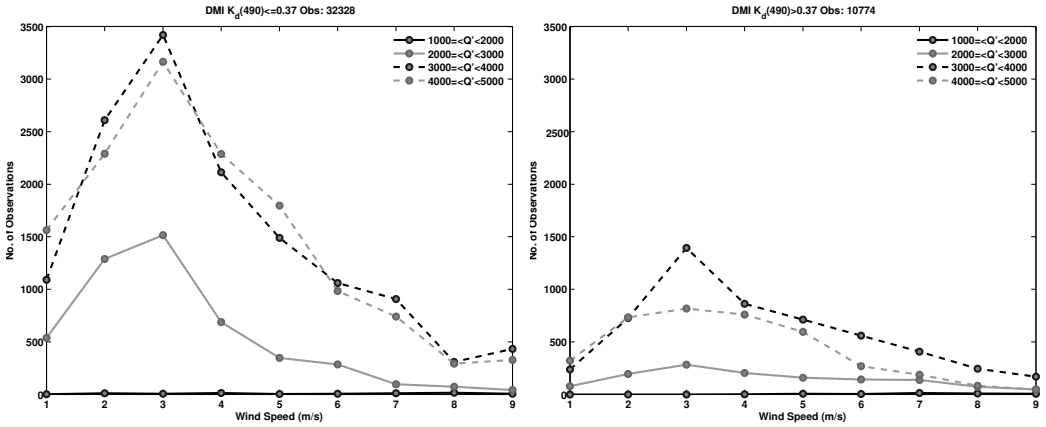

(c) Number of observations

(d) Number of observations

Figure E.3: Stratification curves as in Figure E.1a but separated in low and high $K_{d(490)}$ values.

Zeng & Beljaars scheme Similar as before, the sensitivity analysis of $dSST$ on u, Q and SSI for different $K_{d(490)}$ levels has been performed for the modelled anomalies from the Zeng-Beljaars scheme. Initially, the dependence of dSST using the d =3 m value on u, Q and SSI independent of the $K_{d(490)}$ values is examined (Figures E.5a and E.5b).

The Zeng-Beljaars scheme shows more clear trends on the dependence of $dSST$ on u and Q as the curves are more clearly apart, i.e. the stratification is more apparent when compared to the Filipiak et al. scheme. The kink for Q =3000 W hr m^{-2} is still there for low u thresholds but much less prominent than in Figure E.1b.

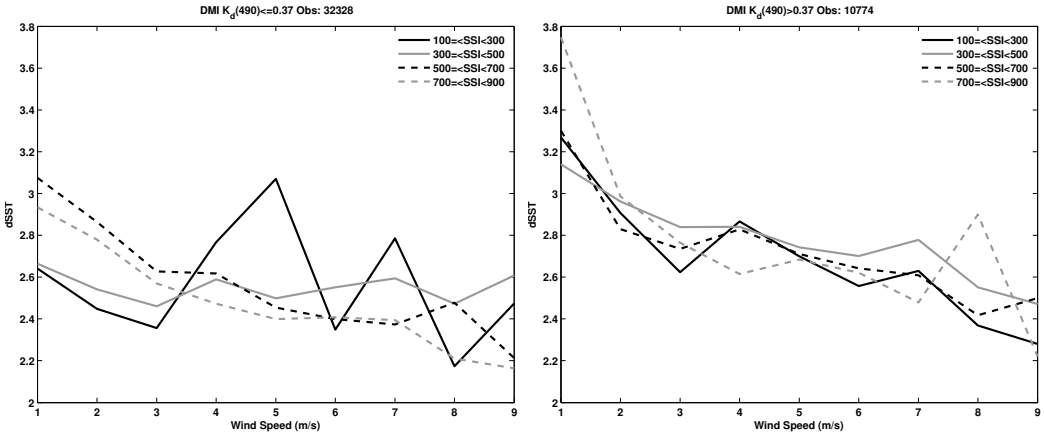

(a) $dSST$ dependence on u and SSI for low $K_{d(490)}$

(b) $dSST$ dependence on u and Q for high $K_{d(490)}$

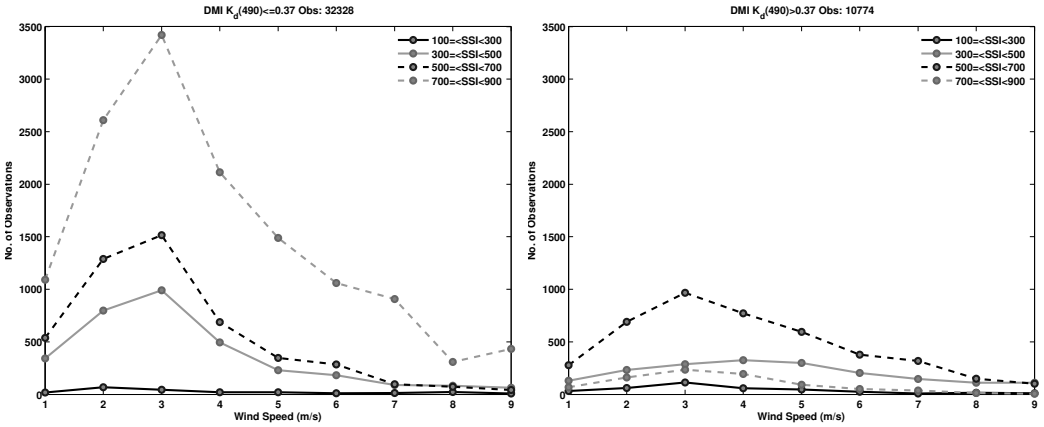

(c) Number of matchups

(d) Number of matchups

Figure E.4: Stratification curves as in Figure E.2a but separated in low and high $K_{d(490)}$ values.

Similar for Q, the stratification of $dSST$ for different SSI ranges is clear between the very high and very low values, but for high SSI thresholds above 500 W m^{-2} the curves almost collapse. Note how the curves collapse also for u higher than 5 m s^{-1}, indicating practically no warming independent of the SSI value.

Now, using as a threshold the 75th percentile of $K_{d(490)}$ (0.37 m^{-1}), the $dSST$ dependence on u and Q has been examined for the low ($\leq$0.37 m^{-1}), in Figure E.7a, and high (>0.37), in Figure E.7b, $K_{d(490)}$ values.

The Zeng-Beljaars scheme has also been evaluated for a value of the near surface

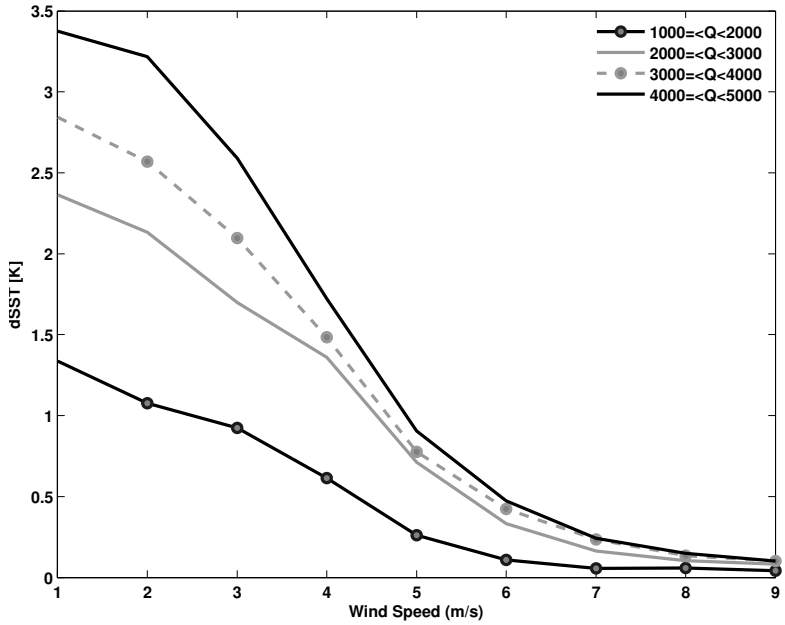

(a) $dSST$ dependence on u for various Q ranges

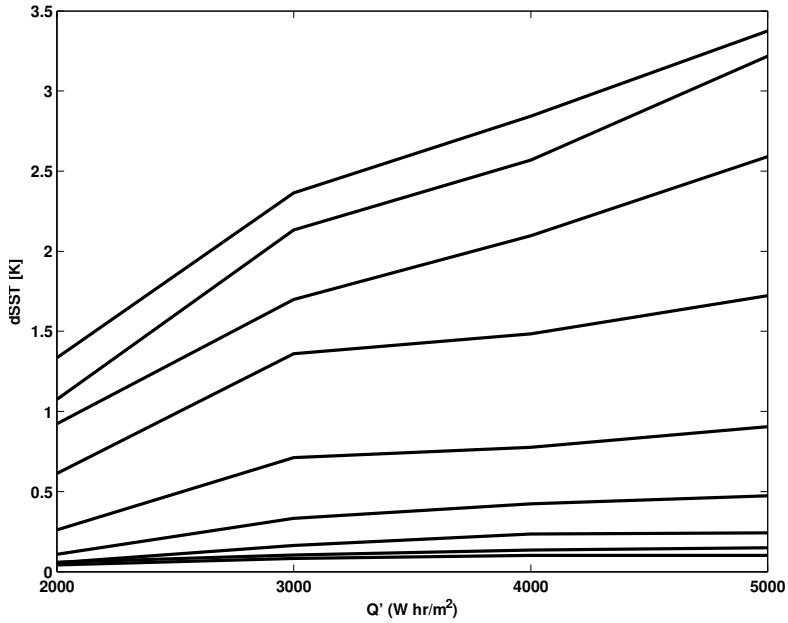

(b) $dSST$ dependence on Q for various u ranges

Figure E.5: a) Dependence of the ZB $dSST$ on u for varying Q levels, b) dependence on $dSST$ on Q for different u thresholds, with increasing values from top to bottom. All for the Zeng Beljaars $dSST$ for d=3 m.

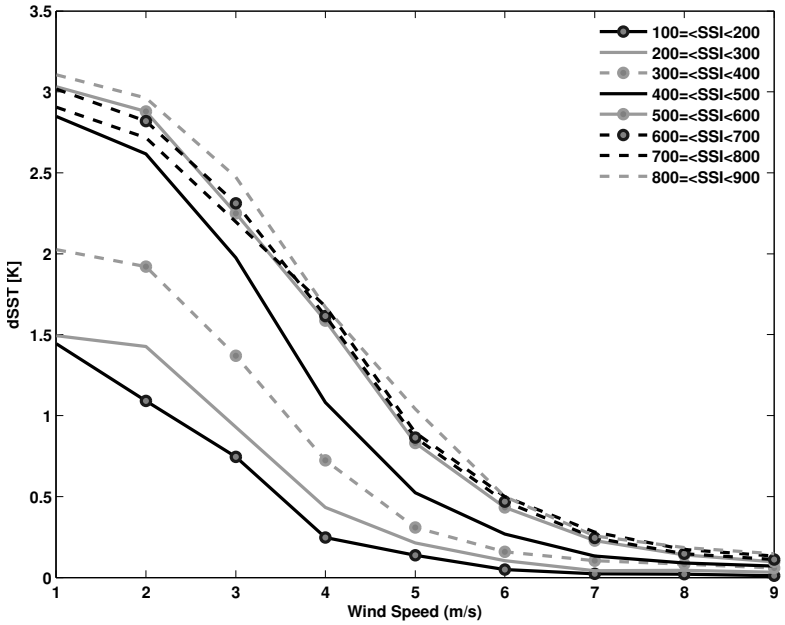

(a) $dSST$ dependence on u for various SSI ranges

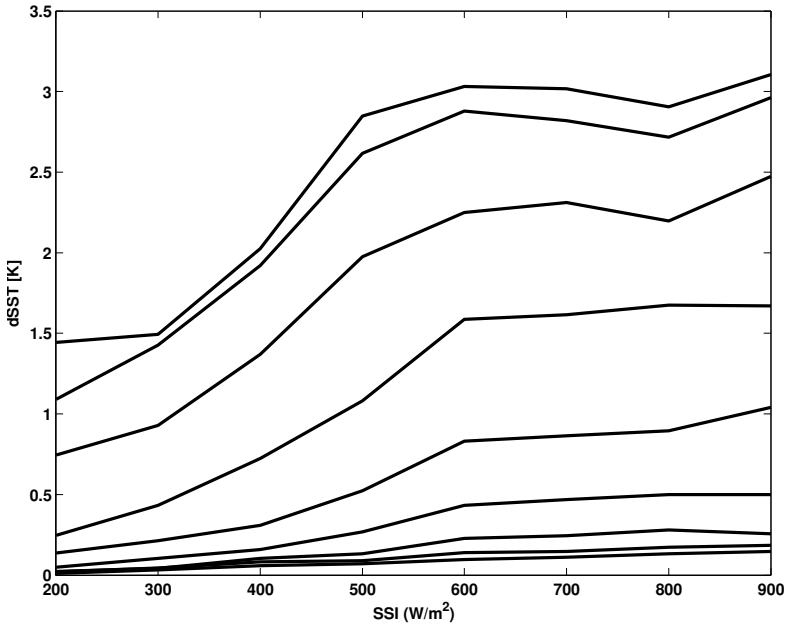

(b) $dSST$ dependence on SSI for various u ranges

Figure E.6: a) Dependence of the ZB (d=3 m) $dSST$ on SSI for varying Q levels, b) dependence on $dSST$ on SSI for different u thresholds, with increasing values from top to bottom.

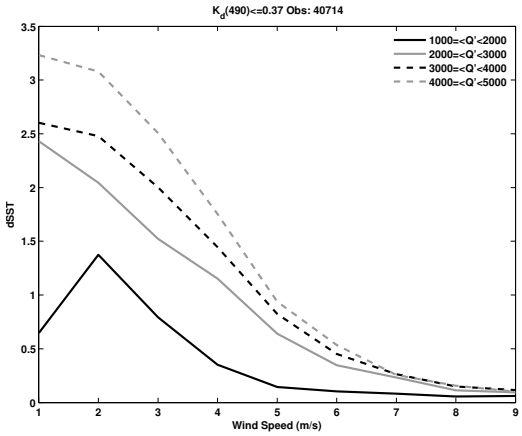

(a) ZB $dSST$ dependence on u and Q for low $K_{d(490)}$

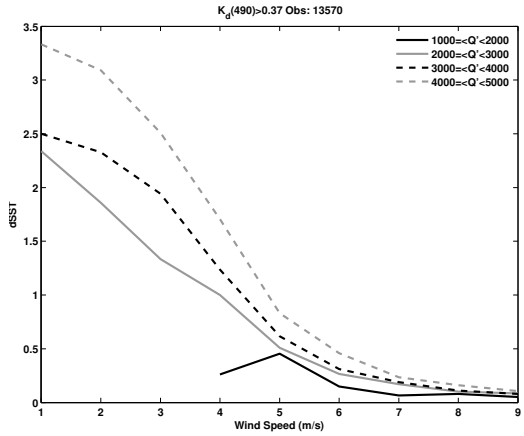

(b) ZB $dSST$ dependence on u and Q for high $K_{d(490)}$

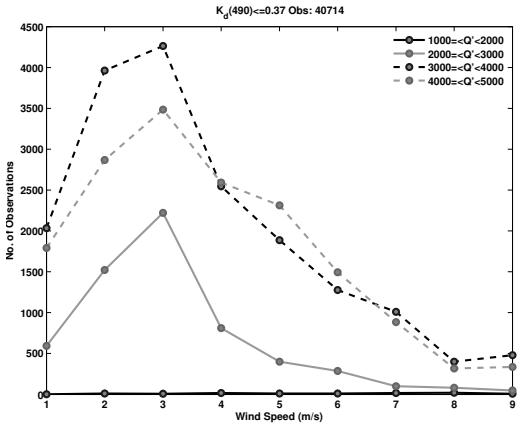

(c) Number of observations

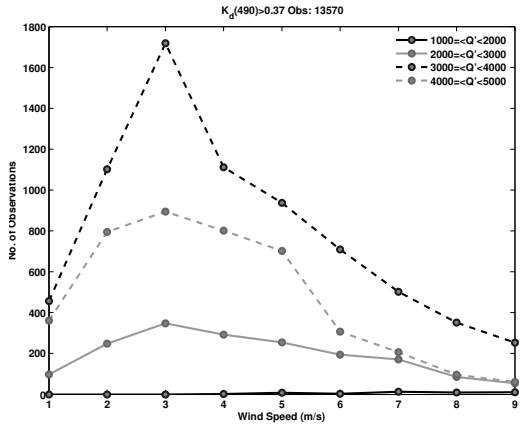

(d) Number of observations

Figure E.7: Stratification curves as in Figure E.5a but separated in low and high $K_{d(490)}$ values.

layer of d =6 m. The $dSST$ produced by this set-up, is also examined in terms of its stratification depending on Q, u and $K_{d(490)}$. For high $K_{d(490)}$ values, the stratification is very clear as generally has been observed for the Zeng-Beljaars scheme when compared to the Filipiak et al. one.

The main reason for this different behaviour of the schemes to the possibility of including the $K_{d(490)}$, is that the Zeng-Beljaars parameterization already includes the d parameter, to control the depth of the near surface layer where warming occurs. This acts somehow as the $K_{d(490)}$ parameter would, by limiting the penetration depth of the incoming radiation to shallow layer, thus advancing diurnal

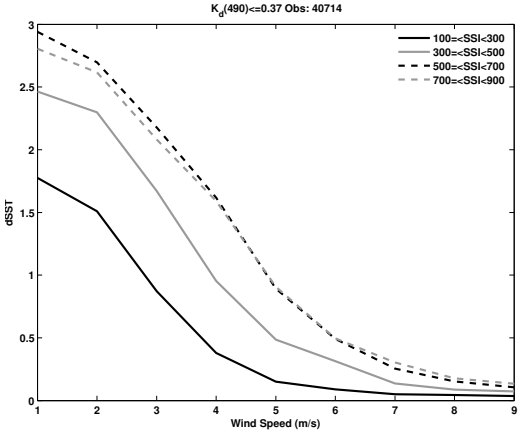

(a) ZB $dSST$ dependence on u and SSI for low $K_{d(490)}$

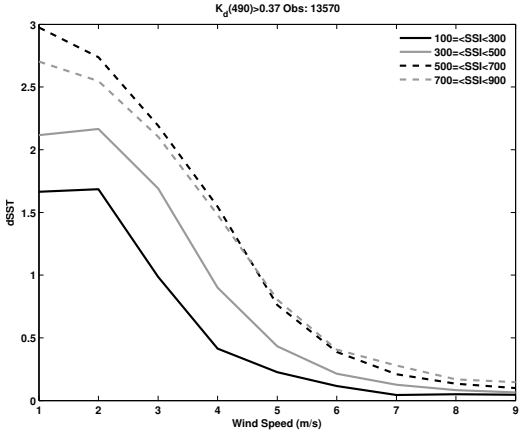

(b) ZB $dSST$ dependence on u and SSI high low $K_{d(490)}$

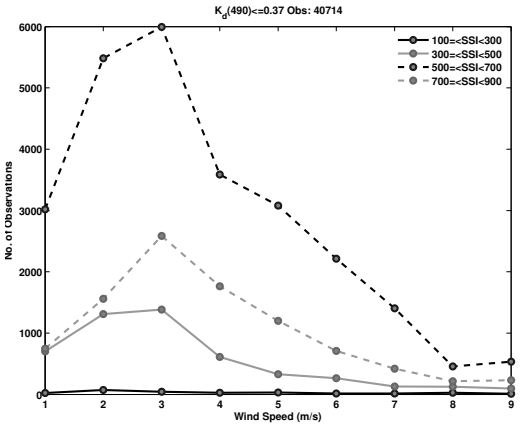

(c) Number of observations

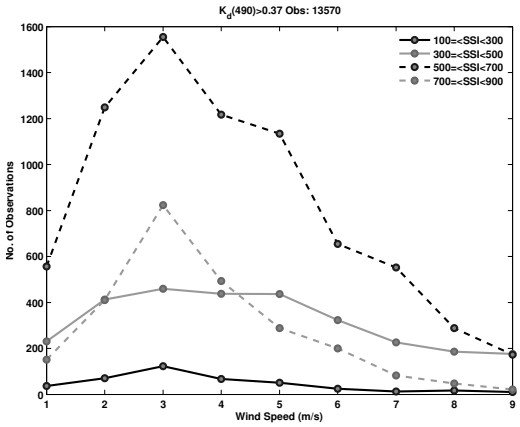

(d) Number of observations

Figure E.8: Stratification curves as in Figure E.6a but separated in low and high $K_{d(490)}$ values.

warming.

In summary, it has been shown that $K_{d(490)}$ does have an impact on the diurnal warming predicted by the two schemes and therefore it is a relevant parameter to consider. The ZB scheme already includes a parameter that behaves in a similar manner as the $K_{d(490)}$ would. The FMKLB scheme does not and the author believes that at least for the Northern European Seas, the model would benefit by including $K_{d(490)}$ as an extra parameter to adjust the climatological mixed layer depth d that is already in the model. In addition the model coefficients could be derived again accounting for $K_{d(490)}$. The latter is a rather complicated task that

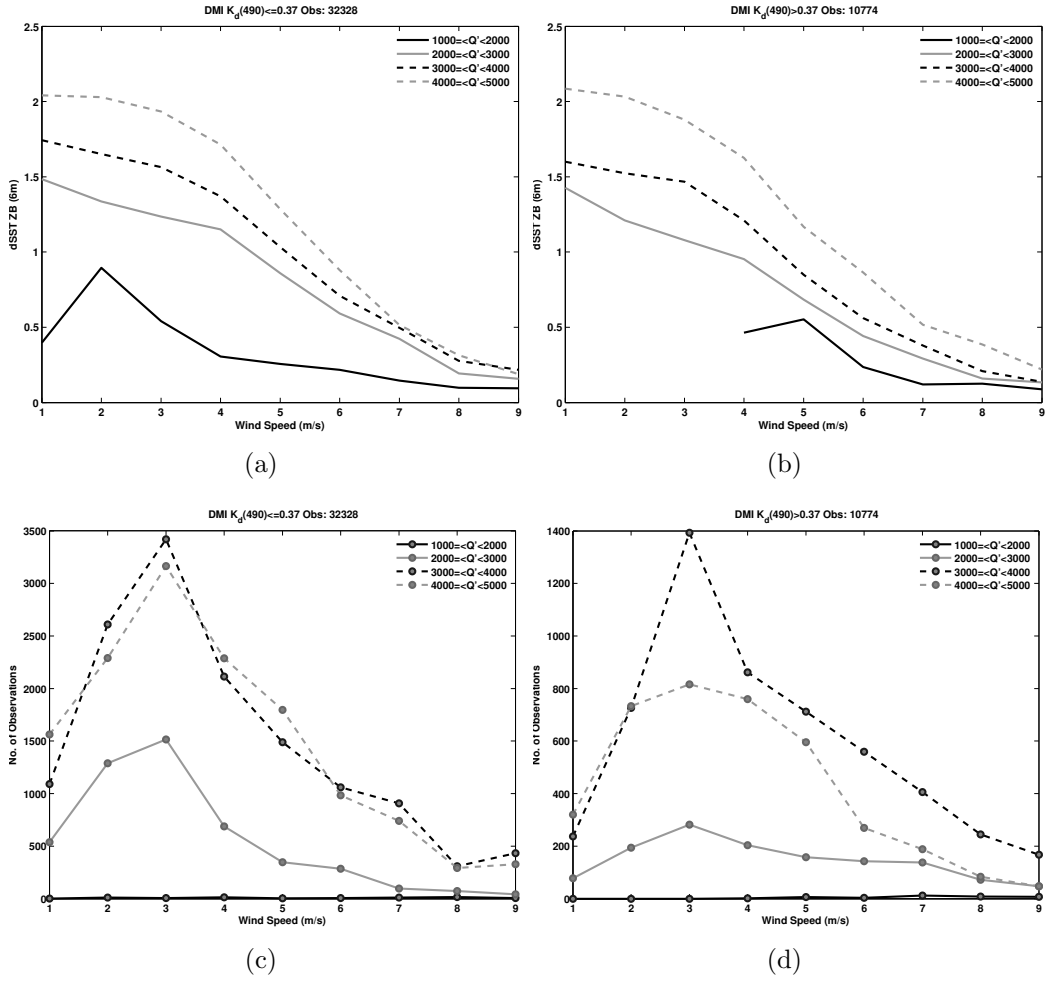

Figure E.9: Stratification curves as in Figure E.7 but separated in low and high $K_{d(490)}$ values

requires a longer time period of investigation than the one year of modelled results. During the PhD study, there was no time to investigate further this topic but it is considered as a task to be undertaken in the feature.

Paper I

Wind characteristics in the North and Baltic Seas

WIND ENERGY
Wind Energ. 0000; **00**:1–23
DOI: 10.1002/we

Research Article

Wind characteristics in the North and Baltic Seas from the QuikSCAT satellite

Ioanna Karagali[1], Alfredo Peña[1], Merete Badger[1], and Charlotte Bay Hasager[1]

[1]DTU Wind Energy, Risø Campus, Technical University of Denmark, Frederiksborgvej 399, Building 125, DK-4000, Roskilde, Denmark.

ABSTRACT

The QuikSCAT mission provided valuable daily information on global ocean wind speed and direction from July 1999 until November 2009 for various applications including numerical weather prediction, ocean and atmospheric modelling. One new and important application for wind vector satellite data is offshore wind energy, where accurate and frequent measurements are required for siting and operating modern wind farms. The greatest advantage of satellite observations rests in their extended spatial coverage. This paper presents analyses of the 10-year dataset from QuikSCAT, for the overview of the wind characteristics observed in the North and Baltic Seas, where most of Europe's offshore wind farms operate and more will be constructed. Significant issues in data availability are identified, directly related to the flagging schemes. In situ observations from three locations in the North Sea are used for comparisons. Mean biases (in situ minus satellite) are close to zero for wind speed and $-2.7°$ for wind direction with a standard deviation of 1.2 m s^{-1} and 15°, respectively. The impact of using QuikSCAT and in situ measurements extrapolated to 10 m for wind power density estimations is assessed, accounting for possible influences of rain contaminated retrievals, the sample size, the atmospheric stability effects and either fitting the Weibull distribution or obtaining the estimates from the time-series of wind speed observations. Copyright © 0000 John Wiley & Sons, Ltd.

KEYWORDS

QuikSCAT; offshore wind energy; in situ; North Sea; Baltic Sea

Correspondence

DTU Wind Energy, Risø Campus, Technical University of Denmark, Frederiksborgvej 399, Building 125, DK-4000, Roskilde, Denmark.
E-mail: ioka@dtu.dk

Received . . .

1. INTRODUCTION

Space-borne scatterometer observations of the ocean surface have been traditionally used in data assimilation for weather prediction, storm tracking and ocean and atmospheric modelling. Scatterometers have provided long records of wind speed and direction observations from space. NASA's QuikSCAT mission was launched in July 1999 and kept functioning until November 2009, far exceeding the mission's original design life-time. At a height of approximately 800 km, completing each orbit in 100 minutes and observing a wide swath of

1800 km, it provided daily near-global coverage of the ocean's surface. The final product is the Equivalent Neutral Wind (ENW, [28]), i.e. the wind at 10 m assuming neutral atmospheric stratification. The mission characteristics for wind speed are in the range of 3 to 20 m s^{-1}, with an accuracy of 2 m s^{-1} while for direction the accuracy is 20° (`http://winds.jpl.nasa.gov/missions/quikscat/index.cfm`).

The purpose of the present study is to demonstrate the applicability of scatterometer observations for wind resource mapping in the North and Baltic Seas. The mean wind speed, the spatial correlation of mean wind speed, the Weibull A and k parameters and the power density are mapped using 10 years of twice daily QuikSCAT observations. Assessment of the uncertainty associated with each step in the calculation of wind resources is just as important as the final resource estimates. Other studies, e.g. [5, 39], have attempted to characterize such uncertainties, introduced by different averaging periods, the satellite sampling, and the truncation of time series to certain wind speed ranges, amongst others. For the purposes of the present study, we evaluate QuikSCAT winds with in situ observations from three offshore meteorological masts, installed for wind farm siting studies. In addition, we provide estimates of the mean wind and wind power density for different sample sizes in order to account for the biases introduced by the different size of available in situ and remotely sensed data, any possible diurnal bias inherent in the satellite observations and stability related biases.

The North Sea has an area of approximately 750000 km^2 and an average depth of 90 m. The Baltic Sea covers an area of approximately 337000 km^2 and, on average, is 55 m deep. Both basins are located within the North Hemisphere storm track, thus strong prevailing westerly winds are frequent. Due to their shallow depth and exposure to strong winds, the North and Baltic Seas have been in the centre of offshore wind energy activities for more than 10 years; most of the planned offshore wind farms are being installed there (`http://www.4coffshore.com/offshorewind/`). Thus, it is of high interest to expand the sources of observations in order to achieve a better representation of the physical conditions. Demonstrating that satellite observations can be successfully implemented for such purposes will strengthen their applicability in the field of wind energy, thus providing one more reason for future missions. Studies of remote sensing for offshore wind energy in the Northern European seas, such as [17, 18], used a fraction of the available QuikSCAT dataset and were limited in comparisons with in situ locations. In addition, studies on offshore wind energy have revealed some long-term features, regarding mean wind statistics and atmospheric stability but they were restricted to areas of reduced size, where in situ observations were available [35].

QuikSCAT data are available from different processing and distribution centres. Various products have been released by members of the SeaWinds on QuikSCAT Science Working Team. An extensive list of distributors can be found in the Physical Oceanography Distributed Active Archive Center (PO.DAAC, [38]). Different processing levels result in various products available to the users. Level 0 (L0) products refer to raw instrument data at original resolution. L1A data are reconstructed but unprocessed instrument data at full resolution with ancillary information. L1B data are radiometrically corrected and geolocated L1A data. L2 data include the derived geophysical parameters at the same resolution and locations as L1 data. L3 data are L2 data that have been spatially and/or temporally re-sampled.

Numerous studies deal with inter-comparisons between different QuikSCAT products from different algorithms and various levels and their validation using in situ observations. [36] compared QuikSCAT swath and gridded winds with nearshore and offshore buoy data and found a maximum wind speed bias of 0.5 m s^{-1} with a root mean square (r.m.s.) error of 1.6 m s^{-1}. The maximum mean bias, for the direction, was 11° with 26° r.m.s. error, while r.m.s. errors up to 38° were also found. The quality of QuikSCAT retrievals using different algorithms (JPL L2B, DIRTH, RSS v2) has been discussed in [12]. They used offshore buoy data and found wind speed r.m.s. differences of 1 m s^{-1} and ∼20° for the direction, when wind speeds higher than 3 m s^{-1} were used. [6] evaluated the Ku-2000 QuikSCAT from RSS against winds from research vessels and found a maximum wind speed bias of 0.7 m s^{-1} and 10° for direction.

DOI: 10.1002/we
Prepared using weauth.cls

Especially for gridded (L3) products like the ones used in this study, [41] compared the gridded QuikSCAT product from RSS with buoy data from the Indian Ocean; they reported a wind speed bias of 0.37 m s^{-1} and r.m.s. error of 1.57 m s^{-1} when all wind speeds were used. For the wind direction, the bias was 5.81° and the r.m.s. error was 44.1°. [32] evaluated QuikSCAT L3 from JPL against buoy data in the Lingurian Sea, reporting maximum mean bias of 1.09 m s^{-1} and r.m.s. error of 1.97 m s^{-1} for wind speed and bias of −8.7° and r.m.s. error of 79.5° in direction. [30] stated that the smoothing effect caused by the interpolation schemes used to produce the gridded data (L3), reduced the original variance of swath data. In particular for the Northern European Seas, [44] compared QuikSCAT L2B products with buoy wind speeds in the eastern North Atlantic Ocean and the North Sea, addressing the sensitivity of biases to collocation criteria and algorithms for converting in situ measurements to ENW. Average wind speed biases ranged from 0.18 to 0.30 m s^{-1} depending on collocation criteria and from 0.1 to 1.6 m s^{-1} depending on the conversion algorithm.

Different QuikSCAT products have been used for the description of mean spatial wind characteristics and the climatology of the Mediterranean Sea [45], the Nordic Seas [26] and the global ocean [40]. Within the context of offshore wind energy, [29] estimated the wind power distribution over the ocean from eight years of QuikSCAT measurements. [8] estimated the global ocean wind power potential from QuikSCAT and lifted the satellite winds from 10 m to 100 m, relevant for wind turbine hub heights. [14] used eight years of QuikSCAT for wind resource mapping in the Mediterranean Sea, concluding that the satellite observations are valuable for the first phase of wind farm planning, e.g. during the identification of promising sites. While many of the studies listed above used lower level QuikSCAT products, L3 data are thought appropriate for wind resource mapping purposes as the data handling and filtering required by the end user are minimised. Although not bankable, satellite observations can be extremely valuable to assess the wind regime and various wind energy related quantities with extended spatial coverage. They can help for an initial evaluation of high interest areas, to highlight attractive locations where in situ instruments may later be installed.

A description of the data and the methodologies applied in this study is presented in section 2. Results from comparisons of satellite and in situ observations, and an overview of the various wind energy related parameters are presented in section 3. Discussion concerning the results and conclusions can be found in sections 4 and 5, respectively.

2. DATA AND METHODS

2.1. In situ Measurements

In situ observations are obtained from three different locations in the North Sea (Figure 1a). More information regarding the exact locations and measurement heights can be found in Table I. The meteorological mast M2 was operated by DONG Energy, located north-west of the Horns Rev (HR) offshore wind farm (Figure 1b). Due to the mast's position relative to the wind farm and its proximity to the land, only QuikSCAT and in situ winds from the south to the north sectors will be considered for comparison ($174° < \theta_{M2} < 13°$, where θ_{M2} is the in situ wind direction). Meteorological observations were collected at 2 Hz and stored as 10 minute averages.

Due to the nature of the satellite (instantaneous spatial) and the in situ (point temporal) averages, it is common to aggregate in situ observations, normally on a 10-min basis, to hourly values. In the present study this is not performed due to the frequent lack of six consecutive 10-min high quality in situ measurements. From a sensitivity analysis it was found that the statistics between satellite and 1-hr in situ averages are similar to the ones between satellite and 10-min averages. In the former combination the number of coincident match-ups decreased and therefore, the latter combination was preferred. The QuikSCAT grid cell that contains the in situ location is selected for spatial collocation, while the 10-min in situ observation closest to the QuikSCAT

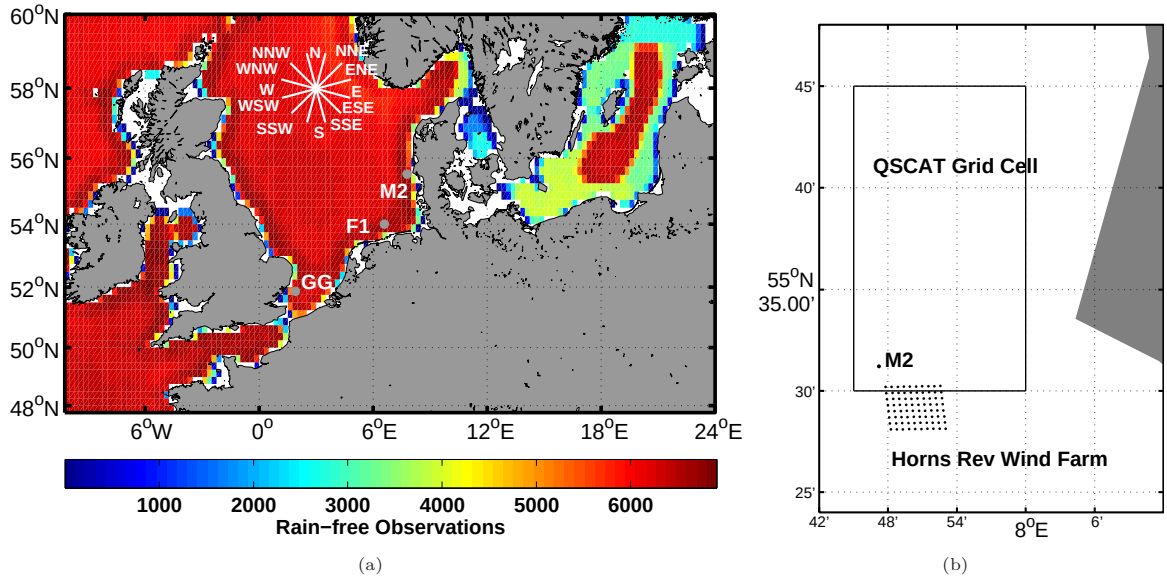

Figure 1. a) Location of the three platforms (GG:Greater Gabbard, F1:Fino-1 and M2:Horns Rev 1) in the North Sea (grey dots) and the number of available QuikSCAT rain-free observations. b) The meteorological mast M2 (grey dot) relative to land, the Horns Rev offshore wind farm (black dots) and the surrounding QuikSCAT grid cell.

overpass time is selected for temporal collocation. Both satellite and in situ observations are required to be higher than 3 m s^{-1} for the estimation of the biases and mean wind speed and direction residuals.

When estimating the wind direction statistics, to avoid discrepancies occurring from the discontinuity at 0/360°, the QuikSCAT wind direction is corrected based on the difference ($\Delta\theta$) between satellite (θ_{QSCAT}) and in situ (θ_{insitu}) direction, following the approach in [6, 32]. Thus, if $\Delta\theta > 180^0$, then $\theta_{QSCAT} = \theta_{QSCAT} - 360^0$, while if $\Delta\theta < -180^0$, then $\theta_{QSCAT} = \theta_{QSCAT} + 360^0$.

2.2. QuikSCAT Gridded Data

The SeaWinds instrument on board the QuikSCAT platform was an active radar operating at 13.4 GHz. Radar pulses transmitted from the instrument are backscattered from the sea surface, due to small scale waves assumed to be in equilibrium with the surface stress. Multiple backscattered signals, σ_0, are measured within the instrument's footprint. Empirical algorithms, known as Geophysical Model Functions (GMFs) are applied to σ_0 in order to obtain wind speed and direction information.

Daily gridded data from RSS are processed with the v3 Ku2001 GMF (`http://www.remss.com/qscat/qscat_description.html`). Grid resolution is 0.25°, thus the grid cell size is 16.83 km × 27.82 km in the area of interest. Overpass time is approximately at 06:00 and 18:00 UTC, capturing early morning and early evening conditions.

Due to the scatterometer's principle of function no wind information can be obtained over sea ice. In addition, QuikSCAT is sensitive to rain because it changes the ocean surface and attenuates and scatters the radar energy at 13.4 GHz [37, 22]. Thus, RSS uses contemporaneous satellite microwave radiometer measurements for sea ice and rain detection from SSM/I (Special Sensor Microwave/Imager).

To guarantee rain free observations, only data with $scatflag = 0$ indicating no rain, $radrain = 0$ (no rain from collocated radiometer) or $radrain = -999$ (no collocation available) are used. Data between 01/08/1999 and 31/10/2009 are considered, accounting for 3745 days. If for all days both passes were available, there would be 7490 wind retrievals. The total number of available passes is 7417; i.e. 99% of the time. The maximum

DOI: 10.1002/we
Prepared using weauth.cls

number of obtained rain-free retrievals for a given grid cell is 7085, corresponding to a maximum of 95.5% data availability.

One may argue that the wind turbines located within the QuikSCAT grid cell used for comparisons with M2 can have an impact on the backscattered signal. In such a case, the wind field observed from QuikSCAT will be biased towards higher speeds. After tests using two other grid cells, one north and one south of the cell shown in Figure 1b, no such evidence was found.

Table I. Characteristics of in situ and satellite measurements.

	QuikSCAT	Horns Rev M2	Fino 1	Greater Gabbard
Max. Available Obs.	7085	153041	50426	4234
Days	3542	1594	1071	1627
Period	08/99-10/09	01/03-05/07	02/04-01/07	01/06-07/10
Measurement Height [m]				
Wind speed	10	15	33	42.5,52.5,72.5,82.5
Wind direction	10	28	33	62.5
Temperature	–	13, −4	30, −3	83
Latitude	–	55°31'N	54°00'N	51°52'N
Longitude	–	07°47'E	06°35'E	01°54'E
Minimum distance from land	–	20 km	40 km	36 km

2.3. Methods

2.3.1. Atmospheric Stability Corrections

Since scatterometers provide ENWs at 10 m above the sea surface, in situ measurements need to be corrected according to the stability conditions. According to the definition of ENW by [28], the wind speed is calculated by using stress and roughness length consistent with the observed atmospheric stratification but the stability term of the modified logarithmic wind profile is set to zero. Several correction algorithms exist to estimate the ENW. Differences between them, as discussed in [44], are in the order of 0.01 m s^{-1}, at various locations in the North Sea. In the present paper, to parameterize the sea surface roughness we use Charnock's roughness length model [9]

$$z_0 = \alpha_c \frac{{u_*}^2}{g}, \tag{1}$$

where z_0 is the sea roughness length, u_* is the friction velocity, α_c is the Charnock parameter and g is the gravitational acceleration. Here, we use a value of 0.0144 for α_c, in agreement with [42]. To extrapolate winds within the surface layer the modified logarithmic wind profile is used,

$$u = \frac{u_*}{\kappa}\left[\ln\left(\frac{z}{z_0}\right) - \Psi_M\right], \tag{2}$$

where u is the wind speed at height z, κ is the von Kármán constant (0.4) and Ψ_M the stability correction. When air and sea temperature measurements are available, in situ wind speed observations from the available height (15 m for M2 and 33 m for Fino-1) are used to compute the 10 m ENW. This is done by first estimating Ψ_M, which is stability and height dependent, using the bulk Richardson number derived from the sea-air temperature difference and the wind speed as in [33, 35]. Then, u_* is estimated from Eq. 2 using the wind speed at the available height, z_0 from Charnock's model (Eq. 1) and the Ψ_M value previously estimated. Finally, the ENW is computed at 10 m using u_* from the previous step, Charnock's model for z_0 and assuming $\Psi_M = 0$.

At Greater Gabbard there is only one temperature measurement, so atmospheric stability cannot be estimated. We therefore only compare winds under neutral conditions by estimating z_0 using the wind speed at

two different heights and assuming $\Psi_M = 0$. For each 10-min wind profile, 3 different z_0 values are estimated using the 42.5 m and 52.5 m, the 42.5 m and 72.5 m, and the 42.5 m and 82.5 m levels. When the conditions are near-neutral, the logarithmic wind profile (i.e. Eq. 2 with $\Psi_M = 0$) gives similar values for the three different estimates of z_0; values are allowed to be between 1.5×10^{-5} and 3.0×10^{-3} m. When this is the case, the 10 m wind speed is derived using Eq. 2 with the z_0 obtained from the 42.5 m and 52.5 m calculation.

2.3.2. Wind Speed Distributions

The seasonal wind characteristics are calculated from 11/1999 to 10/2009. Only grid cells with at least 730 rain-free retrievals are considered, to avoid spurious grid cells from being included in the processing. The seasonal distribution follows the conventional separation, i.e. September-October-November (S-O-N) as autumn, December-January-February (D-J-F) as winter, March-April-May (M-A-M) as spring and June-July-August (J-J-A) as summer. Thus, each season has an average of 182 passes. Wind direction information is separated in 12 sectors of 30°, with North between 345° and 15°. The frequency distribution of wind speed, $f(u)$, can be represented by the Weibull distribution [43] expressed as

$$f(u) = \frac{k}{A}\left(\frac{u}{A}\right)^{k-1} \exp\left[-\left(\frac{u}{A}\right)^{k}\right], \tag{3}$$

where the scale parameter A is associated with the mean wind speed and the shape parameter k indicates the spread (width) of the distribution. The mean wind speed U estimated from the Weibull distribution is

$$U = A\Gamma\left(1+\frac{1}{k}\right). \tag{4}$$

For wind resource assessment, the wind power density (E) can be estimated in different ways but two approaches are common. One can derive the A and k parameters of the Weibull distribution using, for example, the maximum likelihood estimation (mle) method. Then E is estimated as

$$E = \frac{1}{2}\rho A^3\Gamma\left(1+\frac{3}{k}\right), \tag{5}$$

where ρ is the air density (assumed to be constant and $\sim$1.225 kg m^{-3} at 10 °C). Alternatively, the wind speed time-series can be directly used to get the best power density estimate from

$$E = \frac{1}{2}\overline{\rho u^3}, \tag{6}$$

where ρ is normally taken as constant thus moved out of the overbar which denotes the ensemble mean. In the present study, both methods are applied to evaluate potential differences.

3. RESULTS

3.1. RSS Gridded Data vs. In Situ Measurements

The statistics of the comparisons between QuikSCAT and in situ observations are presented in Table II. Two approaches have been implemented; all collocated observations are considered, regardless of wind speed thresholds or wind direction sectors. In addition, a threshold for wind speeds lower than 3 m s^{-1} and a direction threshold for M2, to avoid wind farm and land affected sectors is applied. Wind direction estimates for which the direction bias exceeds 90° are excluded, hence the different amount of match-ups for the speed

DOI: 10.1002/we
Prepared using weauth.cls

and direction. In total, the number of discarded match-ups is 59 for all match-ups and 11 when applying the $u > 3$ m s^{-1} threshold correspondingly.

The mean bias, defined as in situ minus satellite, does not exceed 0.23 m s^{-1} and is always negative for the wind speed. For the wind direction the mean bias is negative for M2 and Fino-1 and does not exceed 5.1° but it is positive for Greater Gabbard, reaching up to 8°. The correlation is high for both wind speed ($r \geq 0.92$) and wind direction ($r \geq 0.96$). Mission requirements are met both for the wind speed and the wind direction, independent of filtering. When the wind direction is separated in the U and V components for $u > 3$ m s^{-1} and $174° < \theta_{M2} < 13°$, the mean bias for the U component is -0.02 m s^{-1}, the standard deviation (σ) and RMSE are 1.9 m s^{-1} and $r = 0.95$ for a total number of 1617 match-ups. The V component has a mean bias of -0.39 m s^{-1}, the σ is 1.76 m s^{-1} while the RMSE is 1.80 m s^{-1} and $r = 0.96$.

Table II. Statistics of the comparison between QuikSCAT and in situ measurements using all observations (first column) and filtered for speed and/or direction (second column). Mean bias (MB), standard deviation σ and root mean square error (RMSE) are in m s^{-1} for wind speed and degrees for direction. The correlation coefficient r is also given. N indicates the number of collocated pairs.

		Horns Rev M2		Fino 1		Greater Gabbard		All	
		All Obs	$u > 3$ m s^{-1} $174° < \theta_{M2} < 13°$	All Obs	$u > 3$ m s^{-1}	All Obs	$u > 3$ m s^{-1}	All Obs	$u > 3$ m s^{-1} $174° < \theta_{M2} < 13°$
Mean Bias	Spd	−0.04	−0.09	−0.16	−0.07	−0.23	−0.19	−0.08	−0.09
	Dir	−1.2	−2.1	−4.8	−5.1	7.6	8.0	−1.9	−2.7
σ	Spd	1.36	1.32	1.04	0.96	1.43	1.43	1.28	1.21
	Dir	17.4	14.4	16.1	14.3	18.4	15.3	17.3	14.7
r	Spd	0.92	0.93	0.96	0.96	0.93	0.92	0.94	0.94
	Dir	0.98	0.96	0.98	0.99	0.97	0.98	0.98	0.98
RMSE	Spd	1.36	1.33	1.02	0.97	1.43	1.43	1.28	1.21
	Dir	17.5	14.5	16.8	15.2	19.8	17.2	17.4	14.9
N	Spd	1601	951	642	594	88	84	2331	1629
	Dir	1562	946	629	587	88	84	2279	1617

Figure 2 shows the residuals of wind speed and direction, defined as in situ minus satellite observations for all three locations. When binned according to the in situ wind direction, observed differences in wind speed (a) are very small, with the highest median reaching approximately 0.3 m s^{-1} for the North-NorthEast (NNE) sector. The standard deviation is relatively constant with respect to direction, highest for the North-NorthWest (NNW) and North sectors.

The median of direction residuals (c) does not exceed ∼8°, observed for the South-East and South sectors. The standard deviation is highest, ∼20°, for the South sector, but generally does not exceed 15°. For two of the three locations, westerly and south-westerly sectors correspond to large fetch. In these cases, westerly winds may cause large swell that may introduce a bias in the retrieved direction [11] explaining the larger scatter seen for these sectors. The distribution of observations (e) binned according to the in situ wind direction indicates that winds are most frequently from the South to North sectors.

When residuals are binned according to the mean wind speed, the median of speed biases (b) does not exceed 0.4 m s^{-1}. Values of σ are increasing for increasing wind speeds and are rather constant (around 1.2 m s^{-1}) within the range 5–13 m s^{-1}. Biases and σ increase above 16 m s^{-1}, where observations are sparse. This is related to the overestimation of wind speed from QuikSCAT, arising from the GMF due to the lack of high wind speed observations for the calibration of the algorithm.

Direction residuals (d) have an almost constant median of ∼3° for speeds up to 16 m s^{-1}. The standard deviation, for the direction, increases with decreasing wind speed. This finding has been well documented in previous studies [13, 11] and is related to the weak nature of the radar backscatter for very low winds and the problematic ambiguity removal during the wind retrieval process. When observations are binned according to the mean wind speed (f) it is evident that most observations are within the 4–13 m s^{-1} wind speed range.

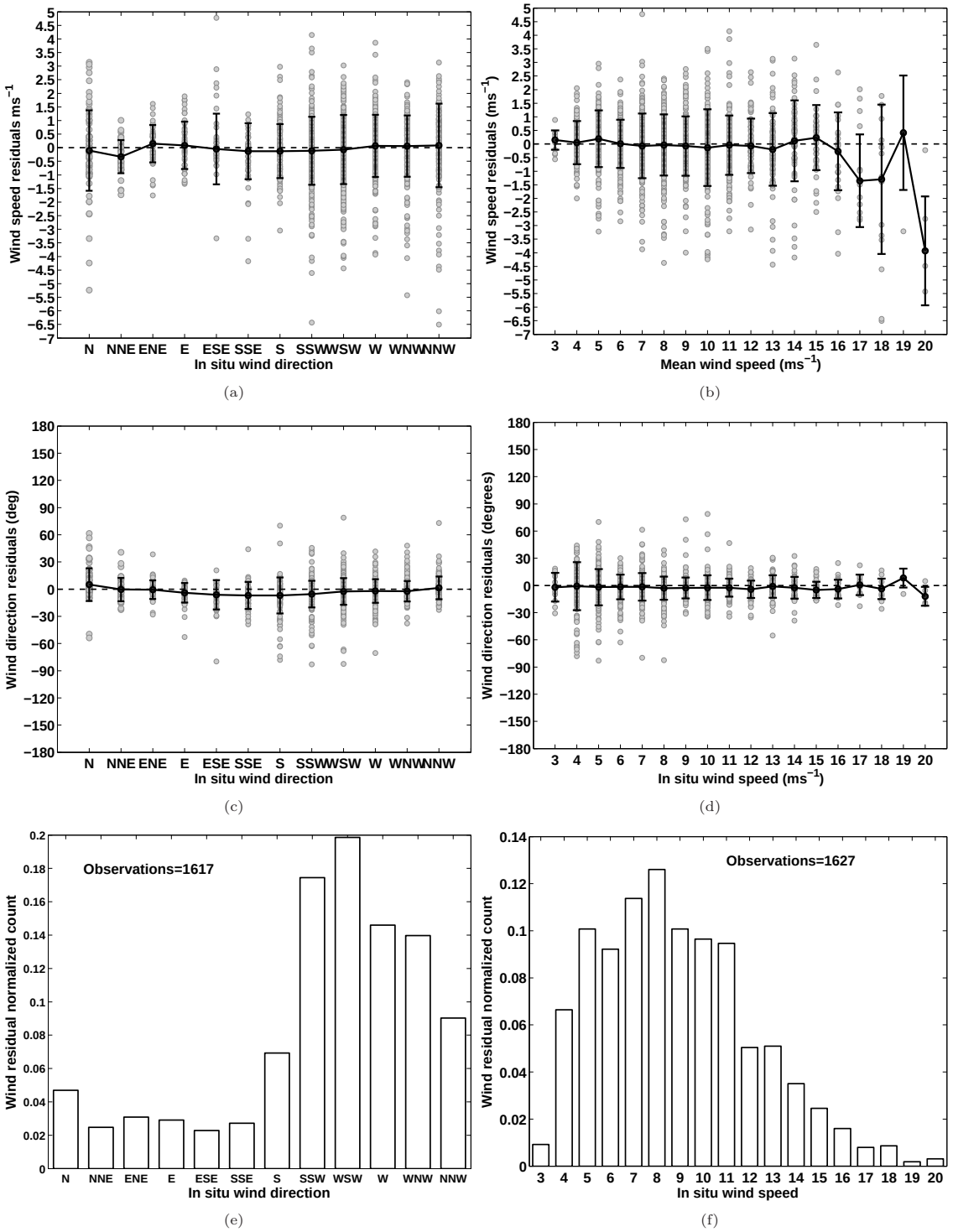

Figure 2. a) Wind speed residuals and c) wind direction residuals binned according to the mean wind direction. e) Histogram of number of collocated pairs as normalised counts. Figures b, d, f are as a, c, f but binned according to the mean wind speed. Grey circles are the residuals, black circles the median values and the bars correspond to $\pm 1\sigma$.

In the comparisons above, collocated observations from all locations are included. For M2 and Fino-1 western winds are ideal for comparisons as they correspond to unperturbed offshore directions. For Greater

DOI: 10.1002/we
Prepared using weauth.cls

Gabbard, the land mass located 40 km west of the mast may increase discrepancies between the in situ and satellite observed winds. As seen from Table II, most collocated observations are from M2, thus the general statistics will be strongly influenced by the local statistics at M2.

Figure 3a shows the monthly variation of in situ (all stations) and QuikSCAT wind speeds and of the mean wind speed residuals (all stations). Minimum wind speeds are observed in July and maximum in December and January. QuikSCAT winds are lower from April to July, when compared to in situ observations, but are higher from October to March. Mean wind speed residuals peak in May and during October-December; however they do not exceed 0.5 m s^{-1}.

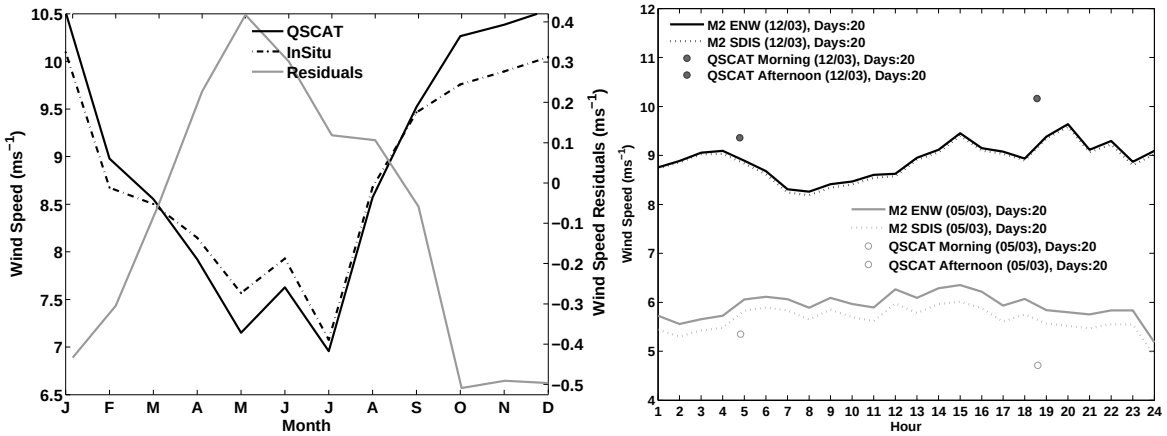

Figure 3. a) Monthly variation of mean wind speed from QuikSCAT (black line), in situ observations from all stations (dashed line) and wind speed residuals (grey line). b) Averaged diurnal cycle of 10 m ENW from M2 for December (black) and May (grey) 2003 (20 days). QuikSCAT mean morning and afternoon wind speeds are shown as circles. The dashed lines correspond to the stability dependent in situ (SDIS) wind speed at 10 m.

Figure 3b shows the monthly averaged diurnal wind speed cycle for May and December at M2, because these months exhibit the highest wind speed residuals. The year 2003 is the one with most days (20) when coincident M2 and QuikSCAT observations exist, thus the derived mean diurnal cycles are based only on these occurrences. The 10-min observations for every hour are averaged during 20 days of December and May (2003) to produce the mean diurnal cycle. Both the 10 m ENW and the stability dependent in situ wind at 10 m (SDIS) are shown. The latter one is estimated using almost the same procedure as the ENW, with the difference that Ψ_M is not assumed to be zero at 10 m, but the actual value estimated from the bulk Richardson methodology, is used. In December, QuikSCAT is found higher both for morning and afternoon passes, while in May the opposite occurs.

[27] and [42] showed that for the Danish and Dutch parts of the North Sea, conditions were most often neutral or unstable. In addition, [42] showed that for the offshore sectors at M2, stable conditions were most often observed in December and a mix of neutral and unstable conditions in May. They used 7 years of in situ observations exceeding 4 m s^{-1}, from specific sectors. If the conditions in December and May are indeed as stated in [42], QuikSCAT will underestimate the wind in winter and overestimate it in spring compared to in situ winds. The results in this study show the opposite, but they are only based on one specific year (2003) and only 20 days in each month are considered; this can explain the difference from the long-term trends presented in [42].

In December, in situ winds decrease, by ∼0.5 m s^{-1}, from a local maximum around 03:00 to a morning minimum at 07:00. QuikSCAT winds are found lower for the morning compared to the afternoon pass. In May, in situ winds are lower in the early morning and late evening while they become slightly higher during

daytime (06:00-18:00). QuikSCAT morning winds are higher than the afternoon ones, during May at M2. For both months, QuikSCAT afternoon winds differ more from the in situ winds when compared to the morning case. For the Danish straits, [31] and [4] found an overall prevalence of near-neutral and slightly unstable conditions. Moreover, they found that the number of very stable conditions peaked in the early afternoon while unstable conditions were mostly observed around sunrise. This can explain the diurnal signal seen from QuikSCAT in May but there is no pronounced diurnal signal seen from the in situ data.

3.2. General Climatological Features

The advantage of satellite observations is the instantaneous coverage of extended areas, and in the particular case of QuikSCAT, this is complemented by a valuably long temporal coverage. Figure 4 shows the seasonal availability of rain free observations. A maximum of 1820 passes is expected for the 10 years of available observations but neither all passes are available nor rain-free conditions are always satisfied. A maximum of 1757 rain-free observations is recorded in autumn.

One may argue that removing rain contaminated QuikSCAT wind retrievals may bias the derived results due to the exclusion of, typically, higher winds speeds associated with rainy conditions. It is found that by excluding rain-contaminated retrievals, data availability is reduced by a maximum of 1600 observations offshore from Norway. In all coastal areas this difference is about 600 observations. In the North Sea and North Atlantic it is around 1000, while in the Baltic Sea differences range from zero in coastal areas to 900 in the centre of the basin. Nonetheless, mean wind speed differences between rain-contaminated and rain-free observations do not exceed 0.2 m s^{-1}. The reduced difference of data availability between rain-contaminated and rain-free retrievals on coastal areas when compared to offshore locations is associated with one of the rain flags which is derived from collocated SSM/I observations. Due to the nature of the microwave signal, no information close to land is obtained, thus this rain flag is not active.

At the three sites used for the in situ comparisons, the seasonal variability of data availability is very small; the maximum number of observations is 1702, recorded at Fino 1 during winter. The minimum is 1467, recorded at M2 during autumn. Data availability at the coastal areas of the Baltic Sea is severely reduced during winter and a part of spring, due to the sea ice mask applied. This is obtained from SSM/I which has an extended land mask, thus all coastal areas of the Baltic Sea are masked out during the months that the ice flag is active. Therefore, QuikSCAT captures the yearly variation of wind speed only in the central part of the basin where the amount of data is comparable to that in the North Sea. At the coastal areas of the Baltic Sea, results will be biased towards the summer and autumn wind regimes.

The seasonal mean wind speed over the 10 years is shown in Figure 5. Arrows indicate the most frequently observed wind direction. This is estimated from the wind direction distribution for each grid cell as the sector from which most occurrences are observed. Spatial variability is lowest in the Baltic Sea compared to the North Sea, independent of season for both wind speed and direction. Local features include an area of significantly high wind speeds offshore from Belgium, the Netherlands and the UK, due to speed-up effects along the English Channel. Especially offshore from the harbour of Rotterdam (52°N, 3°E), higher winds are partially associated with the increased backscatter from ships anchored in the area (Ad Stoffelen, personal communication). Strong lee effects in the western North Sea are due to land effects from the British Isles. Another explanation may be related to the nature of the ENW and long-term stable conditions in this area [35]. In the eastern North Sea, around 55°N-8°E, an area of lower wind compared to the surroundings is observed in the winter and autumn. It can be a result of lee effects when winds blow from southerly and easterly directions.

Within the context of wind energy, when in situ observations are limited, it is of interest to relate the available information at one location to adjacent areas and to investigate the spatial extend for which information can be used. Figure 6 shows the spatial correlation estimated using two different locations,

Wind Energ. 0000; **00**:1–23 © 0000 John Wiley & Sons, Ltd.
DOI: 10.1002/we
Prepared using weauth.cls

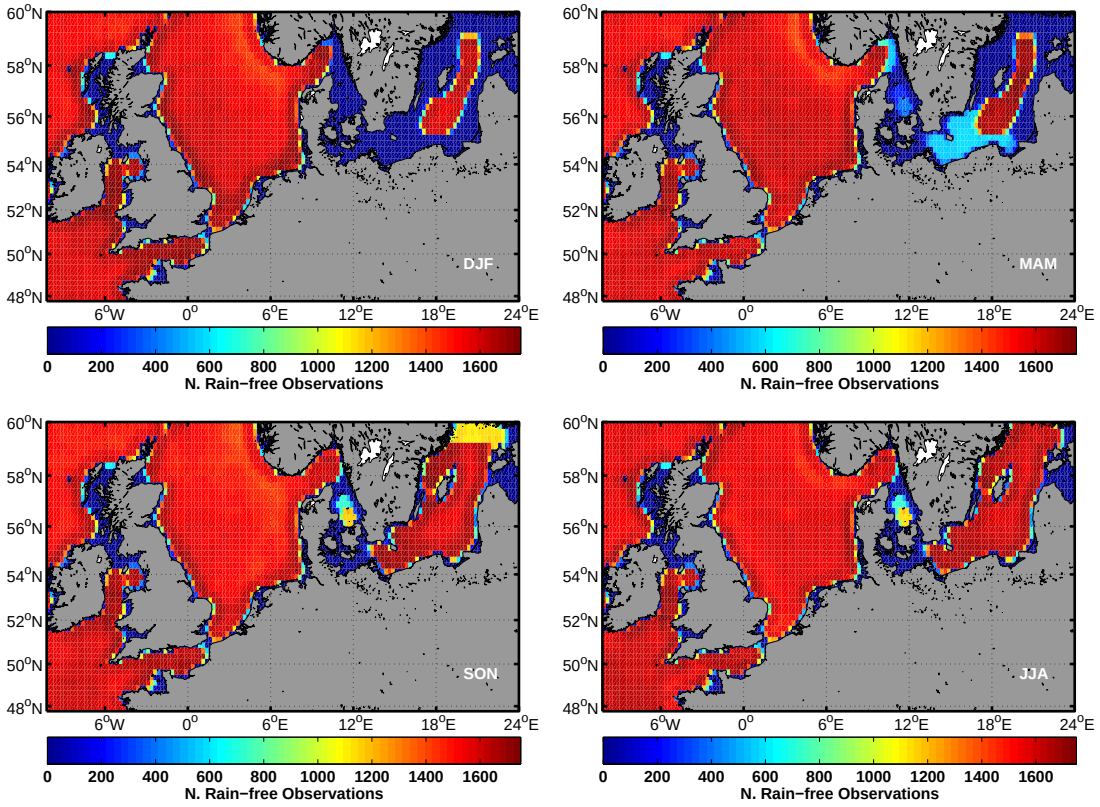

Figure 4. Seasonal availability of QuikSCAT rain free observations.

shown as grey circles. For the grid cell containing M2, correlation is higher than 0.9 for 68 adjacent grid cells, thus covering an area of $\sim 32 \times 10^3$ km^2 which is about 4% of the North Sea. This pattern is independent of seasonal variability. During winter and autumn correlation is higher further away from M2, due to the dominant synoptic weather patterns. Correlation higher than 0.9 is found for 94 grid cells adjacent to the location of Figure 6b, i.e. $\sim 44 \times 10^3$ km^2.

The diurnal variability of wind speed is of importance due to its impact on the planned power production. The seasonal mean differences of daily morning and afternoon wind speeds are shown in Figure 7. Maximum differences do not exceed 0.6 m^{-1} while higher spatial variability is observed during spring and summer; local effects are pronounced due to the lack of synoptic weather patterns. In the North Sea, differences are close to zero for a large part of the basin in autumn and winter while higher morning winds are observed during spring and summer. In the Baltic Sea winds are higher in the afternoon for the largest part of the basin during all seasons but very close to zero. The signal is stronger in autumn and this can be explained by the complex morphology of the basin, which is surrounded by land masses. Advection of cold air from the land when the sea is still warm may create unstable conditions thus giving rise to higher afternoon winds.

The spatial variation of the standard deviation (not shown) has a strong South-North component, where lower wind variability is observed in the South compared to the North, with a boundary at 56°N. Especially around western Norway and in the North Atlantic the wind variability is highest. The Baltic Sea has the lowest variability and is spatially uniform. The variability of the wind speed decreases from winter towards summer but the North-South component is present for all seasons. Visually inspecting the seasonal patterns of the wind variability did not provide any conclusive results regarding its correlation with the mean morning minus afternoon wind speed differences. As an example, during summer, in the area east of the British Isles

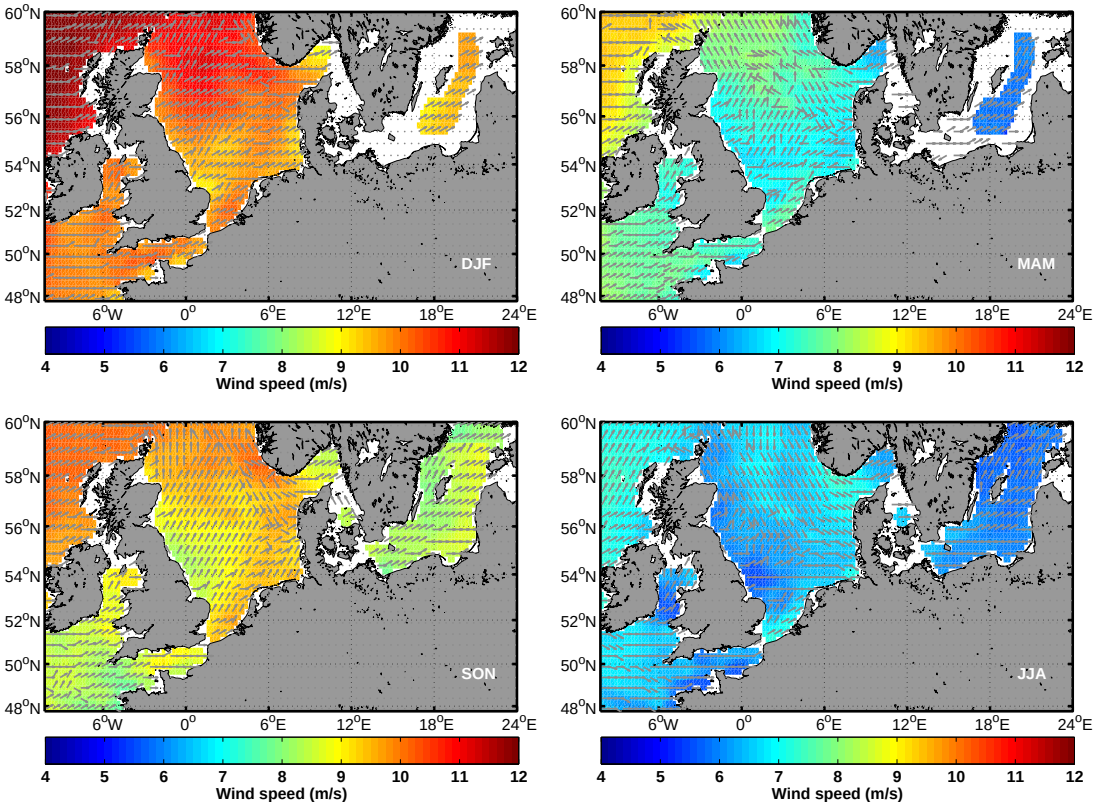

Figure 5. Seasonal mean wind speed with most frequently observed direction.

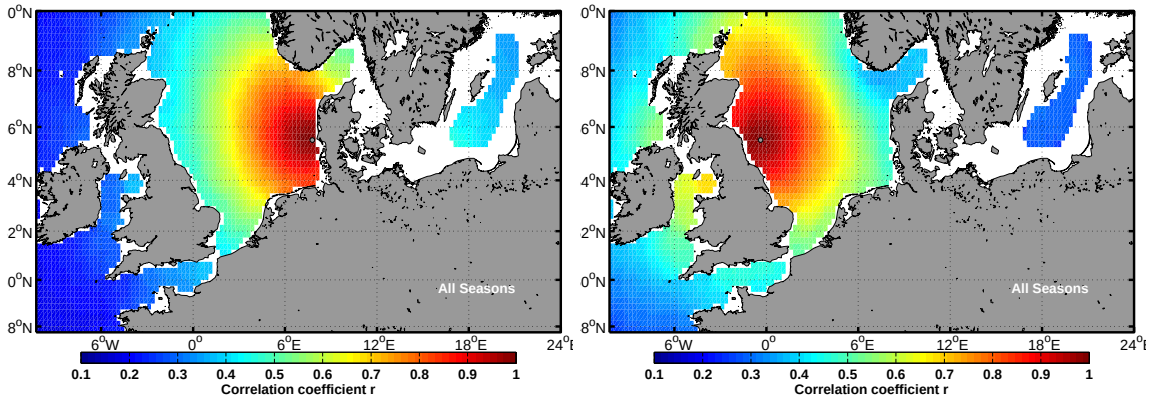

Figure 6. Spatial correlation of wind speed from QuikSCAT observations of the grid cell a) containing M2 and b) across M2 in the North Sea. The locations are shown as grey circles.

where morning wind speeds are found higher, the standard deviation of the wind speed had some of the lowest observed values. To the contrary, for Skagerrak, where the winds are found higher in the afternoon during summer, the standard deviation was highest compared to other areas. In particular for the North Atlantic and the northern North Sea, higher standard deviation was found for the seasons and areas that have morning minus afternoon differences exceeding 0.2 m s^{-1}.

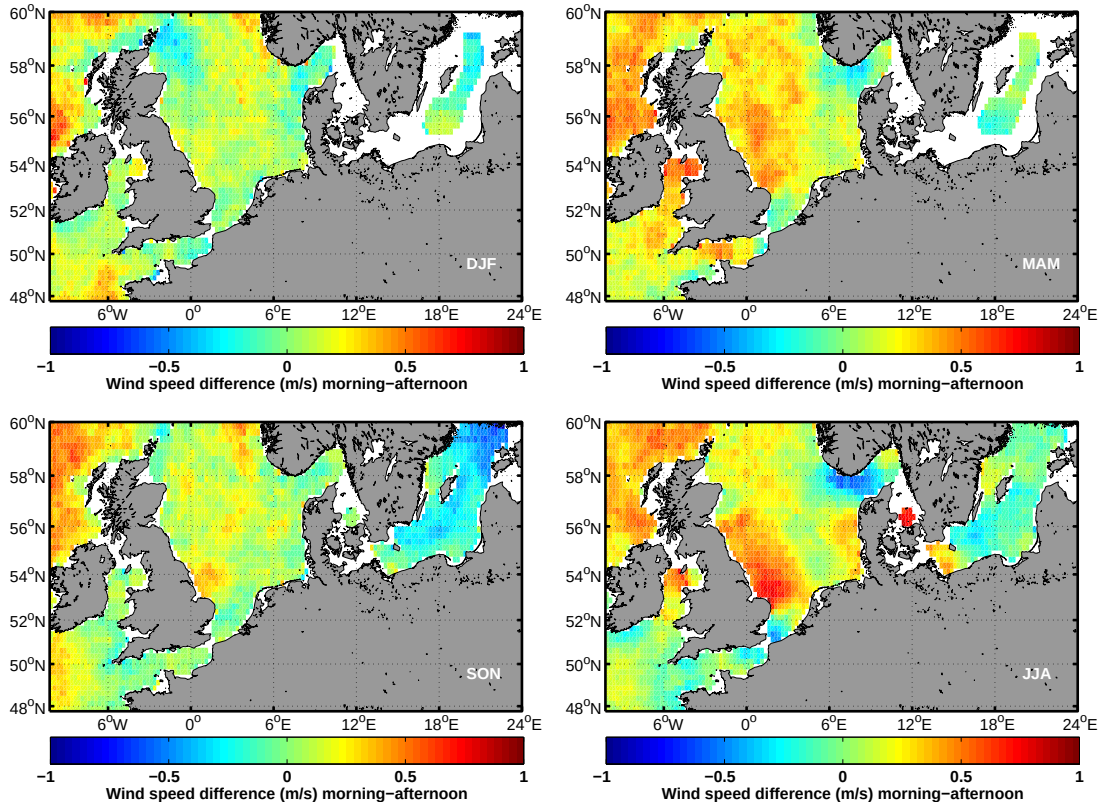

Figure 7. Seasonal mean wind speed difference defined as morning minus afternoon passes.

For the identification of sea-land breeze systems the difference in direction between morning and afternoon passes should be approximately 180°. During early morning hours when the land is colder than the sea, the land breeze flows towards the ocean while the opposite occurs during afternoon. The occurrences of wind direction differences in the range of 180±45° are shown in Figure 8. Only wind directions associated with wind speeds higher than 3 m s^{-1} are used due to the ambiguity in the wind retrieval for low winds. To estimate such differences, it is required that both the morning and afternoon retrievals are rain-free. Results are shown for the grid cells with at least 2000 rain-free occurrences, to eliminate the bias possibly introduced by the seasonal variability of the data availability in the coastal areas of the Baltic Sea.

Most observations within this range are recorded in the Skagerrak strait, between Denmark and Norway and the southern part of the English Channel. In most coastal areas of the North Sea there is an indication of such diurnal direction differences, with higher number of observations in sheltered areas. In the central part of the North and Celtic Seas, away from land, occurrences are very rare. The western Norwegian coast exhibits a relatively high number of such occurrences. In the central Baltic Sea, the number of observed cases is relatively low.

The seasonal variability of such occurrences (not shown), indicates that ∼27% of the events occur in the winter months, ∼22% in spring, ∼27% in summer and ∼25% in autumn, when grid cells with less than 400 rain-free observations are excluded. In general, during winter, diurnal direction differences are mostly found in Skagerrak, Western Norway, the Atlantic and around the coasts of the North Sea. In spring, most occurrences are found in the English Channel, Skagerrak and the Wadden Sea; a situation that persists over summer. Visual inspection of the wind direction distributions showed that land components exist especially in the east coast of the British Isles, the Wadden Sea, the Baltic Sea, the English Channel and the Outer

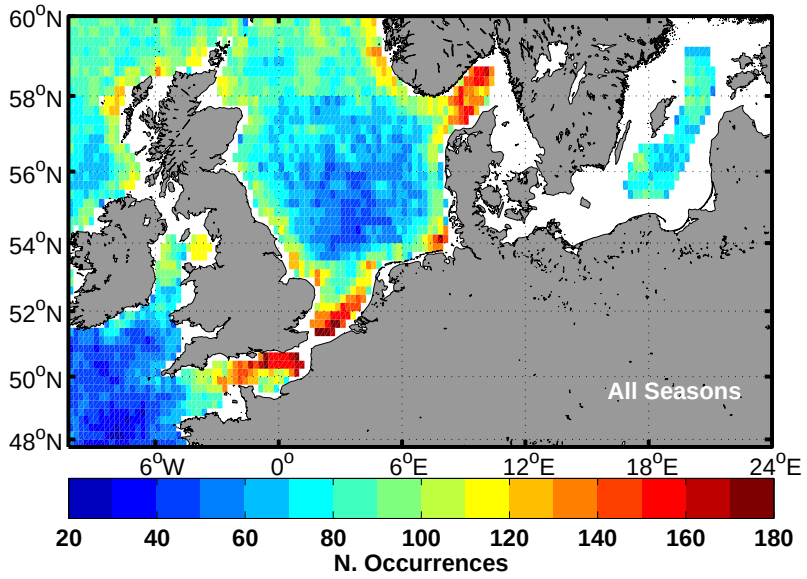

Figure 8. Number of occurrences where the morning minus afternoon wind direction is 180±45°.

Hebrides. Such components strengthen the theory of sea-land breezes. For the Western Norwegian coast and Skagerrak, visual inspection of the wind direction distributions showed no such land components but rather flows parallel to the land, supporting the steering effect explanation. Sea-land breezes have been previously reported in particular around the southern coast of Norway [16], mainly during the spring and summer. In the present study, it is not possible to verify similar findings from QuikSCAT, likely due to the fact that such systems are of scales that may be eliminated during the wind retrieval process and may occur close to the coast where the retrieval of the backscattered signal is contaminated from the land.

The estimation of wind power density is of extremely high interest within the context of wind resource assessment and for offshore wind energy. In order to apply the Weibull fit for each grid cell, the all sectors wind time series is retrieved and the Weibull parameters are estimated from the timeseries. Figure 9a shows the spatial distribution of the scale parameter A. Highest values are observed in the eastern North Atlantic and the northern North Sea while lowest values are observed in the Baltic Sea in agreement with the mean wind speed shown in Figure 9c. The spatial variability of A is generally low.

For the shape parameter k (Figure 9b), higher values are associated with narrower wind speed distributions with a clearly defined, dominant peak. Maximum values are observed in the English Channel. Lower k values are expected close to land because of the increased turbulence, caused by the change in surface roughness and the varying stability conditions. This is indeed the case for some areas but no clear trend of increasing k with the distance from land can be identified other than the corridor of higher k in the centre of the North Sea with a South-East to North-West direction. High values are found in the Wadden Sea and the area between Belgium, the Neatherlands and England.

Wind power density using the estimated Weibull A and k parameters is illustrated in Figure 9d. Only grid cells with at least 730 rain free observations are included. Higher values are found in the North Atlantic and northern North Sea, where also the mean wind speed is higher. When estimating the difference in mean wind speeds derived from the Weibull fit (Eq. 4) to the QuikSCAT observations and by simply averaging the QuikSCAT observations, differences are in the range of 0.02 m s^{-1} to -0.06 m s^{-1} (not shown). Therefore, differences are expected between the power density from time series (Eq. 6) and that from the Weibull parameters (Eq. 5).

Wind Energ. 0000; **00**:1–23 © 0000 John Wiley & Sons, Ltd.
DOI: 10.1002/we
Prepared using weauth.cls

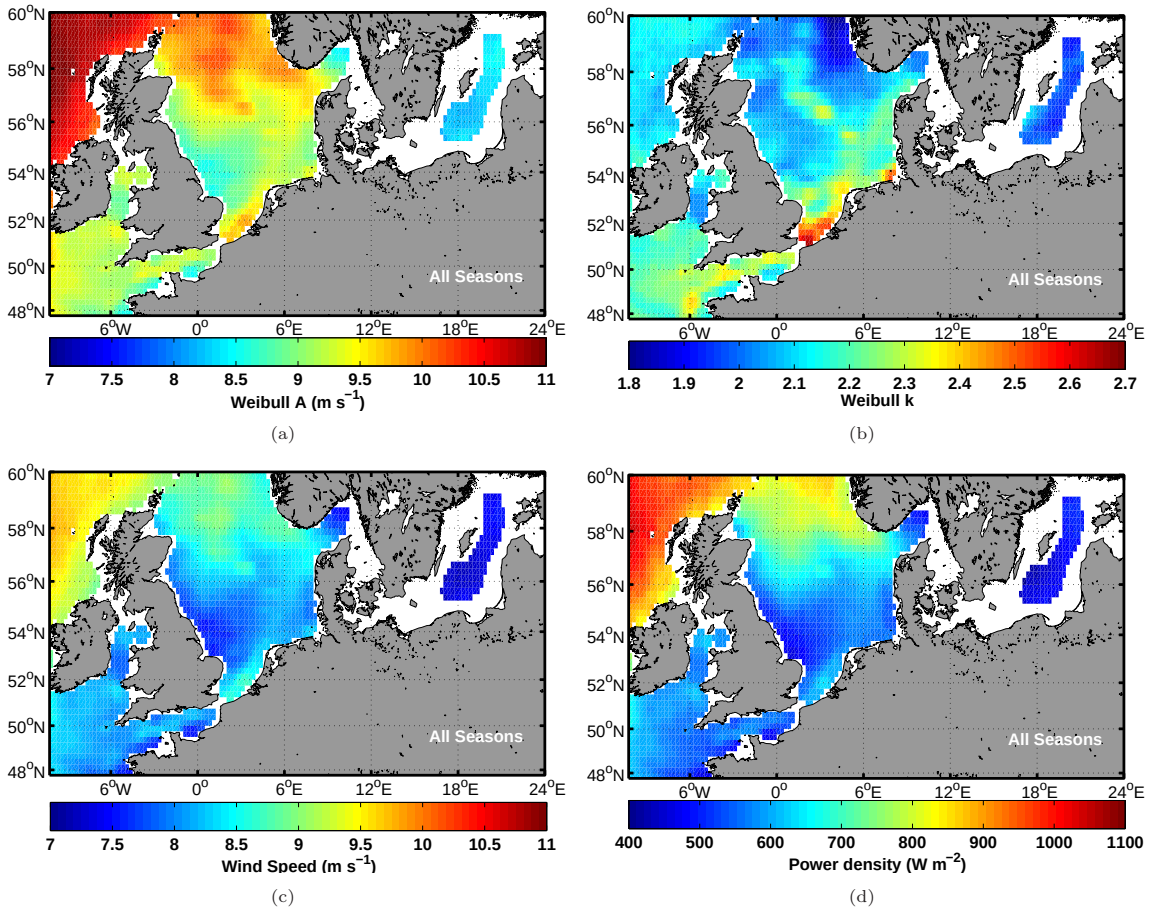

Figure 9. a) Weibull A and b) k parameters. c) Mean wind speed. d) Mean wind power density estimated from Eq. 5.

Such differences are shown in Figure 10. They are around 10 W m^{-2}, in most of the domain. Both methods utilize the same number of rain free observations, shown in Figure 1a. Increased biases, not exceeding 50 W m^{-2}, are identified for the North Atlantic. There the higher wind variability causes this bias, where the time series method gives higher estimates. The Weibull fit is performed with an mle algorithm that maximizes the probability of the observed data. By visual inspection of the Weibull fit versus the wind speed histogram from a grid cell in the North Atlantic area (not shown), an underestimation from the Weibull methodology of the probability for wind speeds in the range 8-10 m s^{-1} is identified and a very good fit for the observed QuikSCAT winds exceeding 30 m s^{-1} is found.

Regarding the rain-contaminated versus rain-free retrievals, the difference in the estimated wind power density does not exceed 40 W m^{-2} in any location of the domain, when using Eq. 6. Rain-contaminated retrievals yield higher estimates due to the higher wind speeds retrieved by scatterometers under rainy conditions. Biases are minimised along the coasts where the more accurate SSM/I flag, which filters most of the rain associated winds, is inactive. When applying the Weibull fit, power density differences are similar to the ones mentioned above. In general the difference between methodologies when evaluating the biases between rain-contaminated and rain-free retrievals does not exceed 10 W m^{-2}.

To evaluate the difference of estimated wind power density between QuikSCAT and in situ observations accounting for sample size, sampling time and stability related biases, the locations of M2 and Fino 1 are selected. Greater Gabbard is excluded due to the very low availability of collocated pairs (approximately

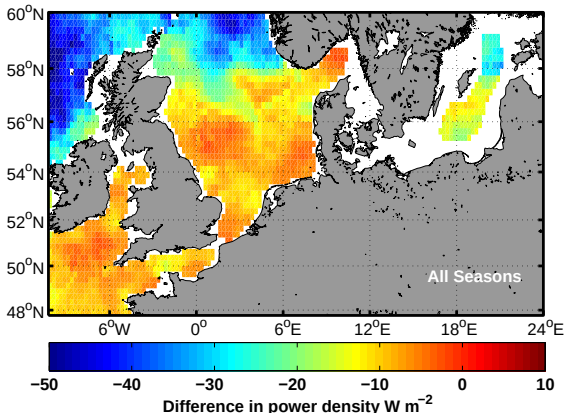

Figure 10. Difference in estimated wind power density from the Weibull fit (Eq. 5) and the time-series (Eq. 6) for grid cells with at least 4500 rain-free observations (see Figure 1a).

90). Table III shows the results for the mean wind speed, the wind power density (Eq. 6) and the Weibull estimates from QuikSCAT, the in situ derived ENW and the SDIS wind at 10 m. Only times of available rain-free QuikSCAT observations are used. For completeness we also compute the wind power density from all the available SDIS wind speeds at 10 m.

Table III. Wind power density estimates from QuikSCAT and in situ observations for M2 and Fino 1.

	Product	Sample N.	u ($m\ s^{-1}$)	u Dev.(%)	E ($W\ m^{-2}$)	E dev. (%)	Weibull A ($m\ s^{-1}$)	k	E ($W\ m^{-2}$)	U ($m\ s^{-1}$)
M2										
	QSCAT	1601	7.97	2.7	515	14.0	9.00	2.38	509	7.98
	10 m ENW	1601	7.93	2.2	479	6.0	8.94	2.55	477	7.94
	10 m SDIS	1601	7.88	1.5	470	4.0	8.89	2.55	467	7.89
	All 10 m SDIS	137717	**7.76**	–	**451**	–	8.76	2.54	**449**	**7.77**
Fino 1										
	QSCAT	642	8.42	0.8	593	2.6	9.51	2.45	588	8.43
	10 m ENW	642	8.26	−1.1	563	−2.5	9.30	2.34	567	8.23
	10 m SDIS	642	8.45	1.5	575	−0.5	9.52	2.55	574	8.45
	All 10 m SDIS	50349	**8.35**	–	**578**	–	9.42	2.43	**575**	**8.36**

Table III highlights how relatively small differences in measured wind speed can cause significant differences in the estimated wind power density. Differences between satellite and in situ observations are more pronounced at M2, possibly due to its proximity to land and the possible contamination of the backscattered signal. The deviation of the E estimate from QuikSCAT, compared to the in situ SDIS, at M2 is higher than at Fino-1. Nonetheless, the QuikSCAT E estimate at M2 is in good agreement with results from [1], who found E to be around 500 W m^{-2} from Synthetic Aperture Radar (SAR) retrievals and in situ data for 2005–08. When the Weibull fit is applied to the time series of wind speeds, estimates of mean wind speed and power density are almost the same regardless of the dataset; thus no significant difference in the estimates arises from the different methodologies. In general QuikSCAT over-predicts the wind power density in both sites, independent of the methodology (Weibull fit or time series). The deviation arising from the sample size, evaluated using the SDIS winds of different sizes, is in the order of 1% for the speed and 3% for the wind power density, when the time series of wind speed measurements are used.

Regarding the estimation of the A and k parameters, [5] stated that the bias introduced due to the truncated wind speeds from satellite sensors, especially by excluding very low wind speeds, is typically seen as an increase in the mean of the wind speed distribution. In addition, the Weibull scale parameter A increases and the shape parameter k decreases. For the estimates shown in Table III, wind speeds below 3 $m\ s^{-1}$ have

DOI: 10.1002/we
Prepared using weauth.cls

not been explicitly excluded. Despite that, the results agree with the findings from [5], where higher A and lower k estimates are provided by QuikSCAT compared to in situ measurements from M2. For Fino-1 both A and k QuikSCAT estimates are higher. When wind speeds below 3 m s^{-1} are excluded (independently for each dataset), the corresponding wind power density estimates increase independent of the dataset or the methodology. When using the time series of wind speed measurements, E estimates at M2 are 545.5 W m^{-2} from QuikSCAT, 502.1 W m^{-2} from the 10 m ENW, 491.5 W m^{-2} from the 10 m SDIS and 471 W m^{-2} from the large dataset of the 10 m SDIS. Thus, the deviation in the estimates from the time series increases to 15.8% for QuikSCAT, 6.7% for the 10 m ENW and 4.4% for the 10 m SDIS. When the Weibull fit is applied to the truncated time series, E estimates at M2 are 540 W m^{-2} from QuikSCAT, 500 W m^{-2} from the 10 m ENW, 489.7 W m^{-2} from the 10 m SDIS and 468 W m^{-2} from the large dataset of the 10 m SDIS.

4. DISCUSSION

The aim of the present study is to obtain an overview of the wind regime over large domains through an evaluation of a QuikSCAT gridded product for wind resource assessment and an examination of the seasonal variability of various wind characteristics as captured by the 10-year long dataset. In situ observations from three masts in the North Sea are used for comparison with QuikSCAT, where the satellite winds are found to meet the mission requirements. In addition, a close examination of the previously reported error estimates from the available literature shows that the bias estimates in this study are lower than in other studies.

Despite the good comparison between QuikSCAT and in situ observations, a number of factors introduce uncertainties in the satellite winds. The presence of rain, the varying sea surface temperature (SST), atmospheric stability trends, the proximity to land and oceanic surface currents can complicate the retrieval and accuracy of scatterometers. The spatial series of QuikSCAT cannot substitute the high frequency time series of in situ observations but it can serve as a road map for the description of averages and their spatial variation. Such information would otherwise only be provided by models. Care has to be taken especially in areas with particular conditions such as strong currents, SST fronts and atmospheric stability trends; there QuikSCAT will provide an over/underestimation of the true wind.

Regarding the stability and SST influence, for example, the North Atlantic part of the domain is a challenging area, as the warm North Atlantic surface current continues the Gulf Stream towards northeast. Over this area of warm water, scatterometer wind retrievals are challenging due to the impact of SST on both the surface winds and the backscatter signal. Surface winds will increase over the the warm water [10], while higher SST will cause a decrease in the water viscosity thus more backscatter for a given wind speed. The current's direction will also introduce a bias [11]. [25] have shown that QuikSCAT wind directions in this area are very often following the general flow of the current, in which case the backscatter signal will be lower for a given wind speed. The interaction of these phenomena certainly renders the accurate retrieval of winds problematic over this area.

Discrepancies between QuikSCAT and the in situ observations converted to ENW also arise by the accuracy of the in situ measurements and in particular the temperature measurements used for the vertical extrapolation. In the area of M2 frequent diurnal warming of the SST has been recently reported [24]. This can increase the wind at 10 m due to unstable conditions but it will also introduce a bias in the scatterometer's algorithm, thus QuikSCAT may provide an overestimate of the true wind. Also, at M2 the water temperature sensor is located at a depth of 4 m, where the daily variability of SST will most likely not be captured. Thus, errors in the stability information obtained by the in situ measurements will also cause biases between QuikSCAT and the in situ winds.

As an example, the peak satellite−in situ wind speed residuals found in December and May are rather difficult to connect with the long-term stability trends described in [42]. They used 7 years of in situ observations from only some specific sectors for specific locations in the North Sea, including M2. In the present study much less observations are used and more wind direction sectors are included. In addition, the results shown in Figure 3b are for one year and only 20 days in each month. Moreover, we would expect more unstable conditions in December when the sea is still warm but the atmosphere is cooling while the opposite is expected in May. In such cases, indeed the trends we have identified in Figure 3b would be justified due to the nature of the ENW compared to the stability dependent winds.

[23] found that on average the ENWs are 0.2 m s^{-1} higher than stability dependent winds from 208 buoys; in some locations this difference reached to 0.5 m s^{-1}. We have identified similar trends for M2 and Fino-1, where the 10 m stability dependent winds have been computed (Table III); biases did not exceed 0.2 m s^{-1}. For wind energy purposes, atmospheric stability is very important as modern offshore wind turbines operate at approximately 80 to 100 m above sea surface. Extrapolation of satellite observations to these levels is of high interest, although it is not the scope of the present study. Such a task requires accurate information of the atmospheric stability conditions and other related parameters such as the boundary-layer height [33, 34].

[35] estimated a long term stability correction for the long-term wind profile at the North Sea area, which may be used for extrapolation of the long term satellite observations to offshore wind turbine heights. They found that a long term correction for stable conditions should be applied for an area that matches the area of lower mean winds on the east of the British Isles (Figure 9c). If stable conditions are often present in this area, the ENW provided by QuikSCAT is an underestimation of the true wind speed and the feature of lower mean winds speed may not be entirely related to lee effects.

The observed higher winter and autumn wind speeds are the result of the increased storm activity as low pressure systems cross especially the North Sea and the eastern North Atlantic. In addition, during these months the atmosphere is colder than the ocean surface, leading to prevailing unstable conditions, which drive momentum transfer from higher atmospheric layers and result in increased wind speeds. Unstable conditions have been reported in these areas [44]; in this case the QuikSCAT ENWs provide an overestimation of the true wind. Thus, the high wind speeds observed in winter and autumn may not completely correspond to real conditions but be overestimated.

Rain is known to affect the backscattered signal and the overall effect is to increase the retrieved wind speed [21]. The QuikSCAT gridded product includes two different rain flags, one of which comes from SSM/I observations. Due to the proximity to land this flag does not contain information for coastal areas. For the coastal waters of the British Isles and Europe, where the data availability is higher than offshore, only one rain flag is active and less observations are classified as rain-contaminated. The remaining rain flag, is a "goodness-of-fit" flag and provides information regarding the match between the observation and the GMF. The scatterometer flag may be zero while the collocated radiometer measures rain and vice versa. In general, the scatterometer rain flag is less reliable at very high winds when it is more often zero even in the presence of rain, due to a large variability of observations within a wind cell (RSS support, personal communication).

Diurnal variations of the wind speed are of interest in wind energy applications due to their impact in the planned power production. QuikSCAT, because of the overpass time, covers the area of interest twice per day during early morning and late afternoon. This is not sufficient to capture diurnal variability, forced by the variability of other physical parameters such as the land and the SST. [15] quantified the sea breeze over the world ocean using QuikSCAT swath winds and found a very weak signal for the North Sea. In this study, a diurnal difference between morning and afternoon wind speeds has also been identified mostly during spring and summer. Recently, [24] reported diurnal warming of the SST observed from a geostationary sensor, occurring in spring and summer. The spatial extend of warming (see their Figure 6b) especially in the Baltic Sea and the Skagerrak Strait coincides with higher afternoon winds from QuikSCAT.

DOI: 10.1002/we
Prepared using weauth.cls

The higher occurrences of morning minus afternoon directional differences in the order of 180±45°, found in the Skagerrak Strait and the English Channel, can be partially attributed to steering that forces the wind direction to often be from two opposite sides. This is also verified by wind roses estimated from the QuikSCAT retrievals [25]. [7] discussed the mechanisms behind the strong speed-up effects for the Dover Straits in the English Channel, mentioning the sharp orographic and roughness changes that characterise the area. Especially for the Skagerrak Strait, dominant south-westerly flows are described in [3]. Along the western Norwegian coast, wind roses from QuikSCAT showed wind directions aligning parallel to the coast and having mainly north-west or south-east directions [25].

Weibull A and k parameters estimated from QuikSCAT at M2 are in good agreement with results obtained from SAR images in [1]. In the south Baltic Sea, QuikSCAT estimated A and k parameters are also similar to the findings from [19], using 1000 SAR images. Values of the k parameter range between 1.8 and 2.3 for most of the areas in the North and Baltic Seas in good agreement with the findings from meteorological stations in [43]. E estimates for M2 are consistent with the ones estimated from SAR winds and in situ observations for 2005–08 [1]. Wind speed biases between the in situ observations and QuikSCAT will be propagated to the wind power density estimates as this is dependent on the cube of the wind speed. In the present study, the Weibull methodology does not yield very different results from the time series estimation for neither the in situ data nor QuikSCAT.

The QuikSCAT dataset includes wind speed values below 3 m s^{-1} and despite the lower accuracy of the wind retrieval for low wind speeds, we have not truncated the QuikSCAT dataset. When excluding wind speeds below 3 m s^{-1}, the wind resource estimates were found higher independent of the methodology and the dataset (QuikSCAT or in situ data). In addition, the deviation from the long SDIS dataset increased. By including speeds below 3 m s^{-1}, the Weibull A and k estimated from the 10 m SDIS are closer to the ones reported in [1] at both locations (M2 and F1). This occurs for the E estimate at F1, but for M2 it is the truncated time series that gives an estimate closer to the one reported in [1]. These results are valid for two locations where the comparison between QuikSCAT and the in situ data is generally good (see Table II) but are not conclusive regarding whether or not one should explicitly exclude low satellite wind speeds.

RSS QuikSCAT data have been recently reprocessed with the new GMF Ku-2011 (`http://www.remss.com/qscat/qscat_description.html`), which is believed to improve the performance of the new data set. Unfortunately, no validation study or technical report exists so far. It is of high interest to use the new dataset for comparisons with the same stations in the North Sea and to evaluate potential differences in the derived wind resource parameters. In addition, other scatterometers such as ASCAT and OCEANSAT are currently in orbit and continue the long-term data record of QuikSCAT. Specifically for ASCAT a 12.5 km and a coastal product are available from the Dutch Meteorological Institute (KNMI); these can be very appropriate for wind resource estimates close to the coasts, where many offshore wind farms are sited and more are planned. An overview of existing and future missions and their applicability for wind resource assessment can be found in [20]. As satellite winds refer to 10 m above the sea surface, their use for wind resource estimation will be magnified if estimates at heights relevant for offshore wind turbines can be produced. This is a task that requires information over large areas that can be obtained through NWP models and is currently of high interest [2].

5. CONCLUSION

In this study satellite observations are used to describe the wind regime of the North and Baltic Seas in terms of wind energy statistics. For this purpose, QuikSCAT with high a spatial coverage and extended period of operation provides valuable observations over these areas, where in situ measurements are sparse, rare and

expensive. Comparison of scatterometer winds with in situ observations from three offshore locations in the North Sea, resulted in lower biases than previously estimated. The mean wind speed bias is -0.09 m s^{-1} when wind speeds above 3 m s^{-1} are used and the standard deviation is 1.2 m s^{-1}. The wind direction mean bias is $-2.7°$ with a standard deviation of 15°. Thus, the QuikSCAT mission requirements are satisfied in these offshore sites. The wind resource has been estimated for two offshore locations from in situ measurements and QuikSCAT. Deviations in the mean wind speed ranged from 0.8–2.7% compared to the available 10-min in situ winds at 10 m. The deviations in the wind power density ranged from 2.6–14%, highlighting the propagation of the bias due to the cubed relation between the wind speed and the wind power density.

Rain-contaminated QuikSCAT winds are biased towards higher winds and have been excluded from this study. In areas where only one of the two rain flags is available, i.e. in coastal areas relatively close to land, an increase in the number of available rain-free observations is found. The inclusion of rain-contaminated retrievals in these areas is a cause for the higher estimates from QuikSCAT compared to in situ observations. In addition, due to the nature of the signal backscattered from ice and the lack of wind retrievals over ice covered parts of the Baltic Sea, QuikSCAT is only representative in the central part of the basin. Coastal areas are properly covered only a fraction of the year, thus results there will carry seasonal biases.

The 10-year long dataset used in this study provides multi-year statistical properties and coverage of large areas. Even though the two basins are dominated by strong westerly winds, it has been shown that the North Sea is particularly subjected to spatial variability of various wind related parameters. Adjacent land masses with complex terrain and the complex coastal morphology result in lee effects and strong jet and channelling flows. The results of this study highlight the importance of satellite observations, when observations over large areas and with a long temporal availability are required. Scatterometer winds provide the averaged wind characteristics over the North and Baltic Seas and can be used as a roadmap for the initial understanding of the seasonal and spatial variability. For more detailed analyses, in situ measurements or satellite observations able to reveal small scale variability, like the SAR imagery, are required.

6. ACKNOWLEDGEMENTS

This study has been partially funded by the EU NORSEWInD project (TREN-FP7EN-219048) and the EU-South Baltic OFF.E.R. (EU European development Fund and the South Baltic Program). QuikSCAT data were obtained from Remote Sensing Systems (RSS). Data from Horns Rev (M2) are provided by Vattenfall and DONG Energy. Fino-1 meteorological data are obtained from DEWI (Deutsches Windenergie Institut, German Wind Energy Institute), oceanographic data from BSH, all through the NORSEWInD project. Greater Gabbard data are provided by SSE Renewables. The authors would like to thank the support team at RSS for their helpful communication and the three reviewers for their valuable comments.

REFERENCES

1. Badger M, Badger J, Nielsen M, Hasager CB, Peña A. Wind class sampling of satellite SAR imagery for offshore wind resource mapping. *Journal of Applied Meteorology and Climatology* 2010; **49**: 2474–2491.
2. Badger M, Peña A, Bredesen RE, Berge E, Hahmann A, Badger J, Karagali I, Hasager CB, Mikkelsen T. Bringing satellite winds to hub-height. *Proceedings EWEA - The European Wind Energy Association*, 2012.
3. Barstad I, Grønås S. Southwesterly flows over southern Norway–mesoscale sensitivity to large-scale wind direction and speed. *Tellus A* 2005; **57(2)**: 136–152.

4. Barthelmie R, Hansen OF, Enevoldsen K, Højstrup J, Frandsen S, Pryor SC, Larsen S, Motta M, Sanderhoff P. Ten years of meteorological measurements for offshore wind farms. *Journal Solar Energy Engineering* 2005; **124(2)**: 170–176.
5. Batrhelmie R, Pryor S. Can satellite sampling of offshore wind speeds realistically represent wind speed distributions? *Journal Applied Meteorology* 2003; (42): 83–94.
6. Bourassa MA, Legler DM, O'Brien JJ, Smith SR. SeaWinds validation with research vessels. *Journal of Geophysical Research* 2003; **108(C2)**: 3019.
7. Capon RA. Wind speed–up in the Dover Straits with the Met Office new dynamics model. *Meteorological Applications* 2003; **10**: 229–237.
8. Capps SB, Zender CS. Estimated global ocean wind power potential from QuikSCAT observations, accounting for turbine characteristics and siting. *Journal of Geophysical Research* 2010; **115**: D09101.
9. Charnock H. Wind stress on a water surface *Quarterly Journal Royal Meteorological Society* 1955; **81**: 639–640.
10. Chelton D, Schlax MG, Freilich MH, Milliff RF. Satellite measurements reveal persistent small-scale features in ocean winds. *Science* 2004; **19**: 978–983.
11. Dickinson S, Kelly KA, Caruso MJ, McPhaden MJ. Comparisons between the TAO buoy and NASA scatterometer wind vectors. *Journal of Atmospheric and Oceanic Technology* 2001; **18**: 799–806.
12. Ebuch, N, Graber HC, Caruso MJ. Evaluation of wind vectors observed by QuikSCAT/SeaWinds using ocean buoy data. *Journal of Atmospheric and Oceanic Technology* 2002; **19**: 2049–2062.
13. Freilich MH, Dunbar SR. The accuracy of the NSCAT 1 vector winds: comparisons with National Data Buoy Center buoys. *Journal Geophysical Research* 1999; **104(C5)**: 11231–11246.
14. Furevik BR, Sempreviva AM, Cavaleri L, Lefèvre JM, Transerici C. Eight years of wind measurements from scatterometer for wind resource mapping in the Mediterranean Sea, *Wind Energy* 2011; **14(3)**: 355–372.
15. Gille ST, Llewellyn Smith SG, Statom NM. Global observations of the land breeze. *Geophysical Research Letters* 2005; **32**: 1–4.
16. Grønås S, Sandvik AD. Numerical simulations of sea and land breezes at high latitudes. *Tellus* 1998; **50(A)**: 468–489.
17. Hasager CB, Barthelmie RJ, Christiansen MB, Nielsen M, Pryor SC. Quantifying offshore wind resources from satellite wind maps: study area the North Sea. *Wind Energy* 2006; **9**: 63–74.
18. Hasager CB, Peña A, Christiansen MB, Astrup P, Nielsen M, Monaldo F, Thompson D, Nielsen P. Remote sensing observation used in offshore wind energy. *IEEE Journal Selected Topics in Applied Earth Observations and Remote Sensing* 2008; **1(1)**: 67–79.
19. Hasager CB, Badger M, Peña A, Larsen XG, Bingöl F. SAR-based wind resource statistics in the Baltic Sea. *Remote Sensing* 2011; **3(1)**: 117–144.
20. Hasager CB, Badger M, Astrup P, Karagali I. Satellite remote sensing in offshore wind energy. *Hanbook Wind Power Systems* 2012; Springer, book chapter, in press.
21. Hilburn KA, Wentz FJ, Smith DK, Ashcroft PD. Correcting active scatterometer data for the effects of rain using passive radiometer data. *Journal of Applied Meteorology and Climatology* 2006; **45**: 382–398.
22. Hoffman RN, Leidner SM. An introduction to the near-real-time QuikSCAT data. *Weather Forecasting* 2005; **20**: 476–493.
23. Kara AB, Wallcraft AJ, Bourassa MA. Air-sea stability effects on the 10-m winds over the global ocean: Evaluation of air-sea flux algorithms. *Journal of Geophysical Research* 2008; **113**: C04009.
24. Karagali I, Høyer J, Hasager CB. SST diurnal variability in the North Sea and the Baltic Sea. *Remote Sensing of Environment* 2012; **121**: 159-170.

25. Karagali I, Badger M, Peña A, Hahmann A, Hasager CB, Sempreviva AM. Spatial and temporal variability of winds in the Northern European Seas. *Renewable Energy, accepted with reviews* 2012.
26. Kolstad EW. A QuikSCAT climatology of ocean surface winds in the Nordic seas: Identification of features and comparison with the NCEP/NCAR reanalysis. *Journal of Geophysical Research* 2008; **113**: D11106.
27. Larsén XG, Larsen S, Badger M. A case-study of mesoscale spectra of wind and temperature, observed and simulated. *Quarterly Journal Royal Meteorology Society* 2010; **137**: 000-000.
28. Liu WT, Tang W. Equivalent neutral wind. *National Aeronautics and Space Administration, Jet Propulsion Laboratory, California Institute of Technology, National Technical Information Service, distributor* 1996.
29. Liu WT, Tang W, Xie X. Wind power distribution over the ocean. *Geophysical Research Letters* 2008; **35**: L13808.
30. Mostovoy GV, Fitzpartick PJ, Li Y. Regional accuracy of QuikSCAT gridded winds. *International Journal of Remote Sensing* 2005; **26(18)**: 4117-4136.
31. Motta M, Barthelmie RJ. The influence of non-logarithmic wind speed profiles on potential power output at Danish offshore sites. *Wind Energy* 2004; **8**: 219–236.
32. Pensieri S, Bozzano R, Schiano ME. Comparison between QuikSCAT and buoy wind data in the Ligurian Sea. *Journal of Marine Systems* 2010; **81**: 286–296.
33. Peña A, Hasager CB, Gryning SE, Courtney M, Antoniou I, Mikkelsen T. Offshore wind profiling using light detection and ranging measurements. *Wind Energy* 2009; **12(2)**: 105–124.
34. Peña A, Gryning SE, Hasager CB. Comparing mixing-length models of the diabatic wind profile over homogeneous terrain. *Theoretical and Applied Climatology* 2010; **100(3-4)**: 325–335.
35. Peña A, Hahmann AN. Atmospheric stability and turbulence fluxes at Horns Rev–an intercomparison of sonic, bulk and WRF model data. *Wind Energy* 2012; **15(5)**: 717–731.
36. Pickett MH, Tang W, Rosenfeld LK, Wash CH. QuikSCAT satellite comparisons with nearshore buoy wind data off the U.S. West Coast. *Journal of Atmospheric and Oceanic Technology* 2003; **20**: 1869–1879.
37. Portabella M, Stoffelen A. Rain detection and quality control of SeaWinds. *Journal of Atmospheric and Oceanic Technology* 2001; **18**: 1171–1183.
38. PO-DAAC, 2001. SeaWinds on QuikSCAT Level 3 Daily, Gridded Ocean Wind Vectors (JPL SeaWinds Project) Guide Document. *PODAAC, JPL, Version 1.1*, October 2001, D-20335.
39. Pryor SC, Nielsen M, Barthelmie RJ, Mann J. Can satellite sampling of offshore wind speeds realistically represent wind speed distributions? Part II: Quantifying uncertainties associated with distribution fitting methods. *Journal Applied Meteorology* 2004; **43**: 739–750.
40. Risien CM, Chelton DB. A satellite-derived climatology of global ocean winds. *Remote Sensing of Environment* 2006; **105(3)**: 221–236.
41. Satheesan K, Sarkar A, Parekh A, Ramesh Kumar MR, Kuroda Y. Comparison of wind data from QuikSCAT and buoys in the Indian Ocean. *International Journal of Remote Sensing* 2007; **28(10)**: 2375–2382.
42. Sathe A, Gryning SE, Peña A. Comparison of the atmospheric stability and wind profile climatology at two wind farm sites over a long marine fetch in the North Sea. *Wind Energy* 2010; **14(6)**: 767–780.
43. Troen I, Petersen EL. European Wind Atlas. ISBN 87-550-1482-8. Risø National Laboratory, 1989, Roskilde.
44. Winterfeldt J, Andersson A, Klepp C, Bakan S, Weisse R. Comparison of HOAPS, QuikSCAT and buoy wind speed in the Eastern North Atlantic and the North Sea. *IEEE Transactions in Geosciences and Remote Sensing* 2010; **48(1)**: 338–347.
45. Zecchetto S, De Biasio F. Sea surface winds over the Mediterranean basin from satellite data (2000-04): meso- and local-scale features on annual and seasonal time scales. *Journal of Applied Meteorology and*

DOI: 10.1002/we
Prepared using weauth.cls

650 *Climatology* 2007; **10**: 814–827.

Paper II

Spatial and temporal variability of winds in the Northern European Seas

Spatial and temporal variability of winds in the Northern European Seas

Ioanna Karagali[a,*], Merete Badger[a], Andrea N. Hahmann[a], Alfredo Peña[a], Charlotte B. Hasager[a], Anna Maria Sempreviva[a,b]

[a] *DTU Wind Energy, Risø Campus, Technical University of Denmark, Frederiksborgvej 399, Building 125, DK-4000, Roskilde, Denmark*

[b] *National Council of Research of Italy, Institute of Atmospheric Sciences and Climate, ISAC-CNR, Area Industriale Lamezia Terme Comp. 15, Lamezia Terme, Italy*

Abstract

Satellite data are used to characterise the near-surface winds over the Northern European Shelf Seas. We compare mean winds from QuikSCAT with reanalysis fields from the Weather Research and Forecasting (WRF) model and in situ data from the FINO-1 offshore research mast. The aim is to evaluate the spatial and temporal variability of the near-surface wind field, including the inter- and intra- annual variability for resource assessment purposes. This study demonstrates the applicability of satellite observations as the means to provide information useful for selecting areas to perform higher resolution model runs or for mast installations. Comparisons between QuikSCAT and WRF reanalyses show biases ranging mostly between 0.6 and -0.6 m s^{-1} with a standard deviation of 1.8–2.8 m s^{-1}. The combined analyses of inter- and intra-annual indices and the wind speed and direction distributions allows the identification of 3 sub-domains with similar intra-annual variability. Local characteristics observed from the long-term QuikSCAT wind rose distributions are depicted in high resolution satellite Synthetic Aperture Radar (SAR) wind fields. The winds derived from the WRF reanalysis dataset slightly do not resolve all the seasonal features observed by QuikSCAT and at FINO-1.

Keywords: Offshore wind energy, satellite remote sensing, QuikSCAT, WRF, SAR, in situ measurements

1. Introduction

Current offshore wind turbine prototypes are suitable for depths up to 200 m. Future plans for wind farms extend at greater depths far offshore where installations and cabling are expensive. Thus, there is a need to identify locations that offer a compromise between potential production and costs. To identify offshore areas suitable for wind farms, observations of the wind over the ocean are required. Such observations are traditionally acquired from masts equipped with meteorological instruments. But this practise is expensive and limited to shallow depths and point locations. Hence, funding of such installations is difficult, especially for site identification studies [35].

For offshore wind resource assessment studies, where water depths exceed 200 m, classical in situ observations are not available. Remote sensing techniques from space-borne platforms provide global wind vector information over the ocean. Scatterometers and Synthetic Aperture Radars (SAR) are the most common instruments used for such purposes. Previous studies have investigated the applicability of space-borne sensors for wind resource assessment and compared the satellite observations with in situ winds.

[7] estimated the global ocean wind power potential from QuikSCAT, concluding that the 2000–2006 mean wind power increased by 69% between 10 and 100 m within the Northern Hemisphere extratropics. [12] used eight years of QuikSCAT for wind resource mapping in the Mediterranean Sea, concluding that the

*Corresponding author

Email addresses: ioka@dtu.dk (Ioanna Karagali), mebc@dtu.dk (Merete Badger), ahah@dtu.dk (Andrea N. Hahmann), aldi@dtu.dk (Alfredo Peña), cbha@dtu.dk (Charlotte B. Hasager), anse@dtu.dk (Anna Maria Sempreviva)

satellite observations are valuable for the first phase of wind farm planning, e.g. for site identification. [16] used 85 ERS SAR images and 4 years of QuikSCAT scatterometer observations to quantify the offshore wind resources in the North Sea. They concluded that SAR images were appropriate for local-scale studies and QuikSCAT useful for basin-scale studies. [9] used a total of 91 SAR scenes for wind retrievals at moderate wind speeds (2–15 m s^{-1}) to quantify the total accuracy of wind resource assessment. They found very good agreement in the wind statistics between SAR and in situ measurements (see Table 1 in their paper). [17] used SAR and QuikSCAT to evaluate their potential use for offshore wind resource mapping. Average wind speed maps for the Baltic Sea, from more than 100 SAR images, highlighted the variability between coastal and offshore areas. Yearly averaged ocean winds from the space-borne Special Sensor Microwave/Imager (SSM/I) were found in phase with the yearly averaged produced wind energy in Denmark during 20 years.

Outputs from Numerical Weather Prediction (NWP) models are used as alternatives when in situ measurements are not available, for short term forecasting of the wind and for deriving the wind climatology over extended domains. They can be of extreme value for wind resource assessment and during the wind farm's operation. [15] described a reanalysis system and tested its ability to define unassimilated near-surface winds over the eastern Mediterranean and Black Sea, reporting underestimation of wind speeds in the range of 1–2 m s^{-1} for January 2000–2007 when compared to QuikSCAT. Mean absolute differences were mostly below 1 m s^{-1} for July 2000–2007.

[25] concluded that the regional climate model REMO is well suited for wind resource assessment applications in Northern Europe as various REMO wind parameters were in agreement with in situ observations. The North American Regional Reanalysis was used in [27], to examine the climate variability of the wind power resources in the Great Lakes region. A wind atlas for the South Baltic [32] was based on the Weather Research and Forecasting model (WRF), developed at the National Center for Atmospheric Research (NCAR) but also includes analysis based on QuikSCAT and ENVISAT ASAR. Onshore wind atlases using mesoscale models include the Finnish Wind Atlas [37] the South Arfica one [14].

Comparisons between QuikSCAT and NWP model reanalysis fields from NCEP/NCAR were performed by [21], reporting a correlation between QuikSCAT and reanalysis daily and monthly mean wind speeds of 0.9. rms differences were 1.1–1.81 m s^{-1} for the daily and 0.75–1.00 m s^{-1} for the monthly means. [34] used ECMWF analysis and reanalysis fields, NCEP reanalysis and blended fields for comparisons with QuikSCAT in the Mediterranean Sea. The accuracy of the modelled fields compared to buoy data was lower than that of QuikSCAT.

While the studies above have used either remotely sensed or modelled wind fields, no available study known to the authors combines the different sources of information for offshore wind resource assessment. The aim of the present study is to examine the spatial and temporal variability of the near-surface wind field for large areas using satellite observations, model reanalysis outputs and in situ measurements when available. The spatial variability of wind is important for large-scale wind farm planning regarding the expected timing of energy production. It is relevant to quantify both the spatial and temporal variability in ocean winds, as the expected offshore energy yield is a function of location and time. This study also aims at demonstrating the use of satellite winds as the means to provide information useful for selecting areas where to perform high resolution model runs or to install meteorological masts. Such an approach will be useful for overcoming the lack of in situ measurements for the initial part of planning future offshore wind farms.

The data used and the methodologies applied are presented in Section 2. Section 3 includes results regarding the spatial wind variability. The temporal analysis is performed comparing QuikSCAT, the advanced WRF model and in situ observations when possible and results are presented in Section 4. Section 5 contains discussions and the conclusions are presented in Section 6.

2. Data

2.1. Satellite observations

Satellite-based wind observations from scatterometers or SARs have the advantage of combining large spatial coverage and long temporal availability. Scatterometers typically cover an area once or twice per day.

SAR winds have been so far available at non frequent intervals. There is a trade off between the spatial coverage and resolution.

2.1.1. QuikSCAT

The polar orbiting, sun-synchronous QuikSCAT platform, with a wide swath of 1800 km, provided daily near global coverage of the oceans from June 1999 to November 2009. The SeaWinds scatterometer, on board QuikSCAT, was an active microwave radar transmitting signals towards the Earth's surface and measuring the radiation backscattered from the sea surface. Multiple measurements of the normalized radar cross section σ_0, from different viewing angles, were used to determine the wind speed and direction, through empirical algorithms known as Geophysical Model Functions (GMFs). The final product is the equivalent neutral wind (ENW), i.e. the wind speed at 10 m above the sea surface assuming neutral atmospheric stratification [26]. Scatterometer wind retrievals are sensitive to rain as it changes the ocean surface and, attenuates and scatters the radar energy at the operating frequency.

[6] validated QuikSCAT against winds from research vessels and reported a maximum bias of 0.7 m s^{-1} for the speed and 10° for the direction. [11] reported RMS differences of 1 m s^{-1} for the speed and 20° for the direction. Comparisons with buoy data in [33] indicated larger speed and direction differences at nearshore locations when compared to offshore ones. In the studies where reported biases between QuikSCAT and in situ observations were lower than the mission requirements [6, 11, 33, 24], in situ data were converted to 10 m ENW to match QuikSCAT. Hence we also adopt this method in our study.

This study uses already retrieved winds from a gridded daily product obtained from Remote Sensing Systems (RSS). The scatterometer orbital data are mapped to a 0.25°×0.25° Earth grid. Contemporaneous microwave radiometer measurements are used for sea ice and rain detection. For the domain of interest (Figure 1a), the grid cell size is approximately 16.83 km×27.82 km and the overpass time is around 06:00 and 18:00 UTC. Only rain-free QuikSCAT observations are included in the analysis. To exclude rain contaminated retrievals, the relevant flags available from RSS are set as $scatflag = 0$ indicating no rain, $radrain = 0$ (no rain from collocated radiometer) or $radrain = -999$ (no collocation available).

2.1.2. SAR

Wind fields can be retrieved from SAR backscatter observations at a resolution up to ∼500 m, which also facilitates coverage of coastal seas. The SAR operating principle is similar to the scatterometer's, except that a SAR operates with a single viewing angle. Thus, a given backscatter coefficient can be related to multiple wind speed and direction pairs. Consequently, the wind direction must be obtained from other sources in order to retrieve the wind speed at 10 m.

Systematic comparisons with mast observations in the Baltic Sea have shown that the RMS error of 10 m wind speeds from SAR is 1.17 m s^{-1} with a negative bias of -0.25 m s^{-1} when the wind speed retrieval is initiated with model wind directions [18]. Similar analyses in the North Sea have given larger RMS errors (1.76–2.33 m s^{-1}) without any bias [2]. The accuracy of SAR wind retrievals at specific points can be improved if mast observations of the wind direction are used as input [9]. [18] performed a study comparing wind speeds from 10 offshore meteorological stations in the Baltic Sea with ASAR wind speeds. For 875 collocated samples, they reported R^2 of 0.783, standard deviation of 1.88 m s^{-1} and root mean square (rms) error of 1.17 m s^{-1}. However, the random noise found in all SAR imagery sets a limitation to the achieved wind speed accuracy [18].

DTU Wind Energy holds a large SAR imagery archive from the European Space Agency (ESA) ENVISAT satellite. Wind fields are routinely retrieved from the SAR imagery using the APL/NOAA SAR Wind Retrieval System (ANSWRS) by Johns Hopkins University, Applied Physics Laboratory, USA. Wind directions are obtained from the Navy Operational Global Atmospheric Prediction System (NOGAPS) at a 1° spatial and a 6-hourly temporal resolution. These wind directions are interpolated in space and time to match the satellite SAR acquisitions. The interpolation introduces some uncertainty on the wind speed retrieval, especially for very sudden changes of the wind directions. A benefit of using a global model is that the data availability is secure such that wind retrievals can be performed operationally. Previous comparisons between the NOGAPS model and in situ measurements from meteorological masts in the South Baltic Sea

showed an overall mean bias of 7.75°, an rms error of 6.26° and R^2 of 0.950 from a total of 927 match-ups [18].

2.2. In situ measurements

Measurements from offshore masts are the most descriptive of the conditions at the specific location for wind energy purposes but many assumptions are made to extrapolate these measurements to nearby sites. Offshore masts may reach 100 m or more, equipped with instruments to measure wind speed and direction, sea and air temperature at various heights. In situ instruments require proper calibration and maintenance, which renders this type of measurements very expensive especially under the harsh ocean conditions.

FINO-1. The German Marine Environmental Monitoring Network (MARNET) is a grid of buoys and platforms at various locations in the North and Baltic Seas. FINO-1 is a research platform, located at 54°01′N, 06°35′E. Data are collected at various heights and stored as 10 minute averages. The period of available observations is 16/02/2004–21/01/2007 but measurements exist only for 478 days.

For this study, wind speed measurements from the 33 m level at FINO-1 are extrapolated to 10 m. The extrapolation is based on the atmospheric stratification between the 33 m height and the sea surface, as described in [24, 23]. Three different data sets are created; the in situ 10 m ENW, the in situ 10 m Log and the 10 m Stability Dependent In Situ (10 m SDIS) winds.

The diabatic wind profile is described as

$$u = \frac{u_*}{\kappa}\left[\ln\left(\frac{z}{z_0}\right) - \Psi_M\right], \tag{1}$$

where z_0 is the sea roughness length (using Charnock's roughness length model [8]), u is the wind speed at height z, u_* is the friction velocity, κ is the von Kármán constant (0.4) and Ψ_M the stability correction. The logarithmic wind profile is only different in that Ψ_M is zero. From Equation 1, u_* is computed using u at 33 m and the Ψ_M expression from [13] with the values suggested in [29] for the corresponding constants. The 10 m ENW is computed using u_* and the logarithmic wind profile. The 10 m SDIS is computed using u_* and the diabatic wind profile. Finally, the 10 m Log is computed from the 33 m wind speed applying the logarithmic wind profile to estimate both u_* and to extrapolate to 10 m.

2.3. Simulated winds

WRF is an atmospheric simulation and NWP system [36]. The WRF model simulation, hereafter mentioned as "reanalysis", was originally made to generate wind time series for electric grid transmission modelling, but has also been validated for wind energy applications in [32, 30, 31]. The dynamical downscaling carried out with the WRF model V3.1 uses the technique developed by [15] but with Newtonian relaxation terms toward the large-scale analysis (also known as grid or analysis nudging). This technique has successfully been used in other wind atlas studies [32].

The model domain configuration is shown in Figure 1b. It has 41 vertical levels with the model top at 50 hPa. The lowest four vertical levels are located at approximately 21, 74, 123 and 163 m AMSL. The outer domain has a horizontal grid spacing of 45 km, and the nested inner domain 15 km. The model set-up uses the Yonsei University PBL scheme [20]. Other details of the model set-up are described in [30]. The inner domain nest is used in this study, available for section of the original domain (48°–60°N, 10°W–24°E) as it is computationally expensive to perform such long runs at higher resolution. The fields are re-sampled to match the QuikSCAT grid, using the nearest neighbour interpolation method and are corrected to compute the modelled ENW by using the stability dependent u_* provided by the model. The wind at 10 m is estimated from u_* using the Log wind profile [23].

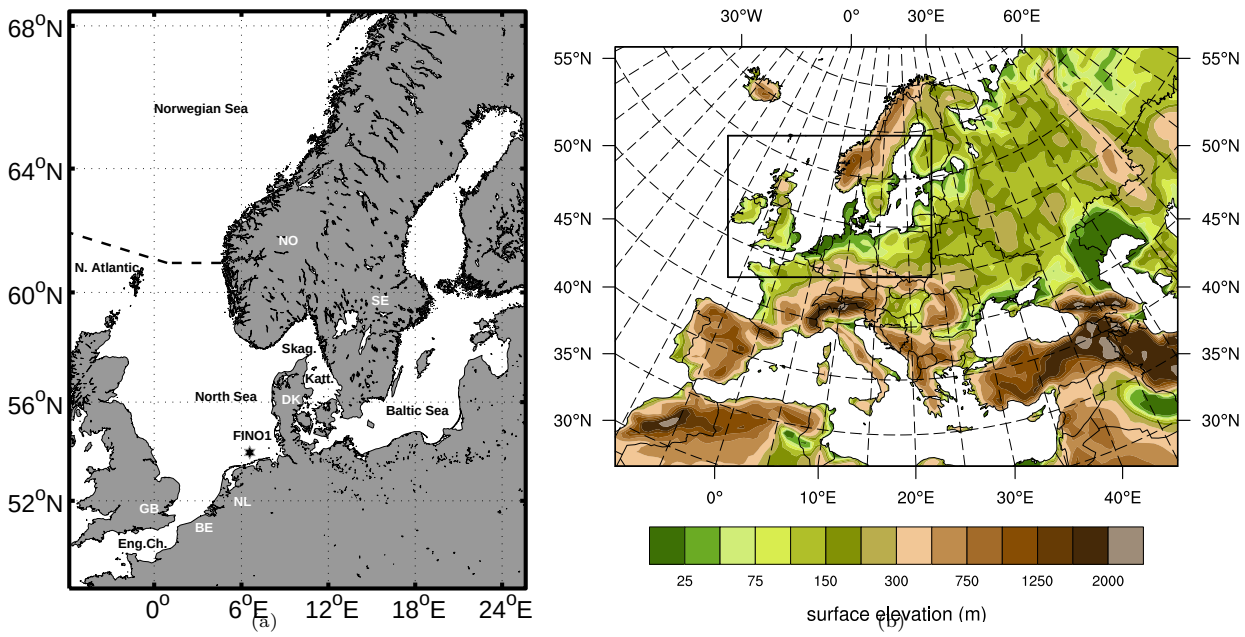

Figure 1: a) Map of the Northern European Seas, including the location of the FINO-1 platform. The dashed line represents the separation line for the Norwegian Sea. b) The WRF domains: outer box Δx=45 km, inner box Δx=15 km.

3. Spatial Wind Variability

3.1. The mean wind speed

The rain-free data availability of QuikSCAT, from 08/1999 to 10/2009 is shown in Figure 2a. From the 3745 calendar days, data are available for 3733 days. If all available retrievals were rain-free, a maximum of 7466 observations could be obtained for any given grid cell. The maximum recorded rain-free observations are 7083, i.e. 94.9% of data availability. No information is available for coastal areas due to the land contamination of the backscattered signal.

The North Sea and eastern North Atlantic are very well observed, with the exception of coastal areas extending approximately 50 km offshore. The reduced data availability in the Northern Baltic and the coastal areas of the basin, is due to the ice mask applied from November/December until April/May in some areas. Only in the central part of the Baltic Sea is the data availability similar to the one found in the North Sea/North Atlantic domain. The mean wind speed is estimated from 11/1999 to 10/2009, i.e. using exactly 10 years of observations where all months are represented equally.

Figure 2b shows the mean wind speed for the grid cells with at least 4500 rain-free observations. This threshold is applied to exclude areas in the Baltic with reduced data availability, which can bias the results towards summer and autumn. Speeds range from a minimum of 7 m s^{-1}, observed in the Baltic Sea, to a maximum of $\sim$10 m s^{-1}, for the eastern North Atlantic. A strong lee effect is observed in the western North Sea, caused by the British Isles. Note the higher speeds offshore from the Netherlands. A gradual reduction of wind speed is noted when approaching the eastern part of the Norwegian Sea, north of 62°N and east of 6°E.

3.2. QuikSCAT vs WRF reanalysis winds

To evaluate the differences in the long-term and spatial wind variability, we estimate the mean bias (QuikSCAT minus WRF) by aggregating all daily differences, for all satellite passes. The closest hourly

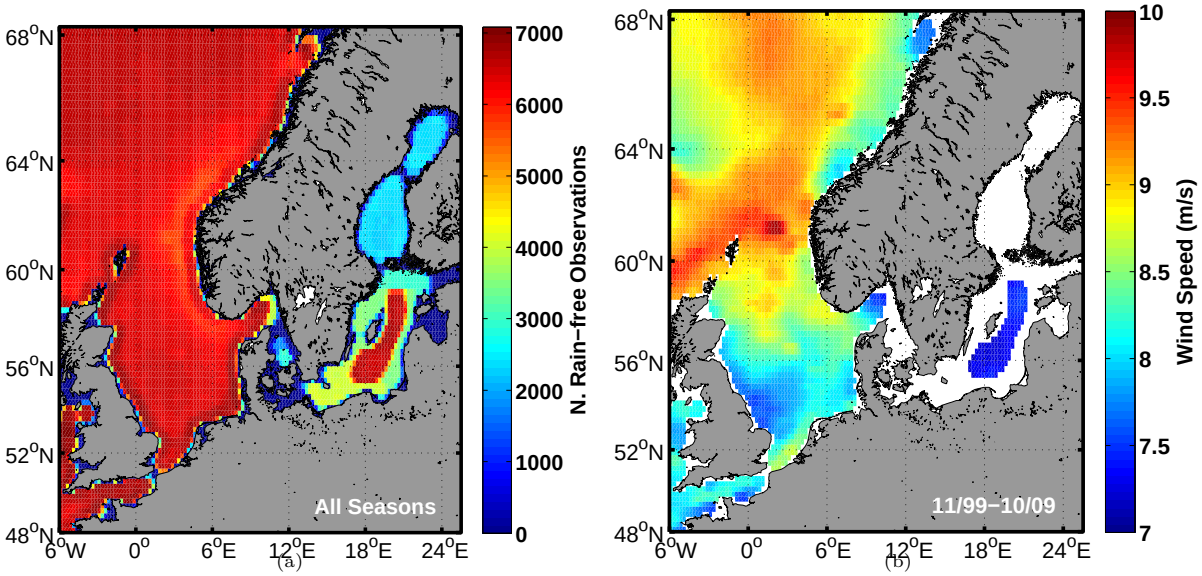

Figure 2: a) Number of rain-free observations from August 1999 to October 2009 and b) mean wind speed from QuikSCAT, for the period November 1999 to October 2009. Note that areas with less than 4500 rain-free observations are excluded from the mean wind speed estimation.

WRF output to the QuikSCAT overpass time is selected. Wind speed time-series, from QuikSCAT and the 10 m WRF ENW, can be directly used to get the best power density estimate as,

$$E = \frac{1}{2}\overline{\rho u^3}, \tag{2}$$

where u is the wind speed and ρ the air density. Here we use a constant value of 1.225 kg m^{-3} to be consistent amongst the different data types and evaluate the impact on the power estimates associated only with the wind speed time-series. The overbar denotes an ensemble mean. The power density is a measure of the effective power of the wind at the location from where the wind speed measurements are taken, therefore is height-dependent. The power extracted from a wind turbine is related to the power density and depends on the turbine characteristics.

Figure 3a shows the mean bias (QuikSCAT−WRF) computed at each grid cell, for the entire period of available rain-free QuikSCAT retrievals. Biases do not exceed 0.8 m s^{-1} and are minimized in the North Atlantic. They are on average negative for large parts of the North Sea and the central part of the Baltic. Offshore from Belgium and the Netherlands, biases are positive indicating higher QuikSCAT winds compared to WRF. An overall averaging of higher negative and positive biases is found for the low QuikSCAT−WRF bias in the North Atlantic.

Figure 3b shows the standard deviation (σ) of the mean bias, computed from the entire time series of biases at each grid cell. Highest values are observed in the North Atlantic, where the mean bias is low. There is a north-south component for which the standard deviation is minimum in the South and increases towards the North. This can be explained by the higher wind variability around 60°N, verified from the wind direction distributions shown in Figure 4. The wind roses in the south-western corner show constant winds from the western sectors; the ones around 60°N–5°W show wind directions from almost all sectors. The corresponding wind roses from WRF (not shown) are similar with QuikSCAT for the south-west. For the area around 60°N–5°W, WRF has less variable wind directions, which contributes to the high standard deviation seen in Figure 3b around that area.

The standard deviation is also high along the coast of Norway where orographic effects not properly resolved in the model may introduce biases. A strong surface current exists in the area, flowing out of the

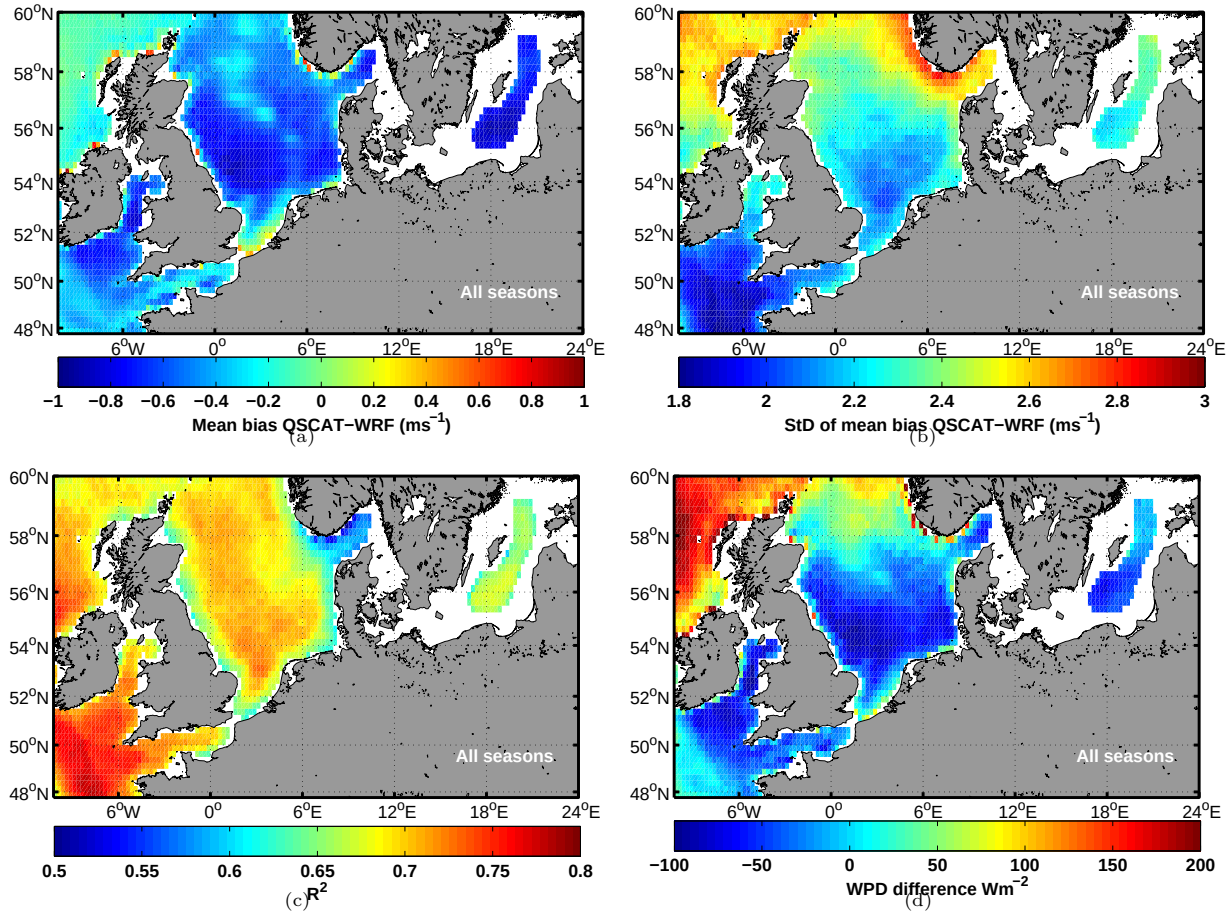

Figure 3: a) Mean bias, b) standard deviation, c) R^2 and d) wind power density difference of winds from QuikSCAT minus WRF reanalyses.

Baltic Sea and along the Norwegian coast [19]. The wind direction at location 4 (Figure 4) is dominantly either following or opposing this current. Currents aligned with the wind direction are a known source of bias for the scatterometer derived wind speeds. When the current opposes the wind direction, the backscatter received from the scatterometer is higher due to the rougher ocean surface. The QuikSCAT derived wind speed will thus, be higher that an in situ measured one [10].

Figure 3c, shows the estimation of R^2 between QuikSCAT and WRF. Values higher than 0.65 are observed in most parts of the domain. The correlation is lower in coastal areas, especially in the straight between Norway and Denmark, possibly due to higher errors in both the model and satellite winds.

The wind power density is estimated from QuikSCAT and WRF using Equation 2. The difference in estimates (QuikSCAT−WRF), shown in Figure 3d, ranges between 0 and 100 W m^{-2} in the largest part of the domain. An exception is the North Atlantic, with differences of up to 200 W m^{-2}. The wind speed distributions at a location in this area, showed that 0.34% of the QuiSCAT wind speeds were 30 m s^{-1} or above, while WRF had no wind speeds higher than 27 m s^{-1}. These very high wind speeds from QuikSCAT caused the large discrepancies in the estimated power density. The QuikSCAT mean wind speed (Figure 2b) is highest at this part of the domain. Errors in QuikSCAT retrieved winds increase for very high winds due to the calibration of the GMFs and typically result in overestimation of the high wind speeds [11, 23]. This may explain to some degree the discrepancies between QuikSCAT and WRF in this area. The standard deviation (Figure 3b) is also found highest in this area, signifying the differences in capturing the wind variability

between QuikSCAT and the WRF reanalysis. The latter is descriptive of the long-term conditions and is not expected to be accurate when the day-to-day variability is of interest. The daily QuikSCAT−WRF biases are averaged out during the years producing a generally low mean bias not exceeding ± 0.6 m s^{-1}, but the standard deviation is high, at least three times the overall mean bias and the correlation does not exceed 0.8.

3.3. Wind directions

QuikSCAT retrievals from 8/1999 to 10/2009 are used to estimate the wind rose distributions. Directions are separated in 12 sectors of 30° each, where North is centred at 0°. Figure 4 shows the wind roses for various locations. The numbers denote those locations where intra- and inter-annual indices are estimated.

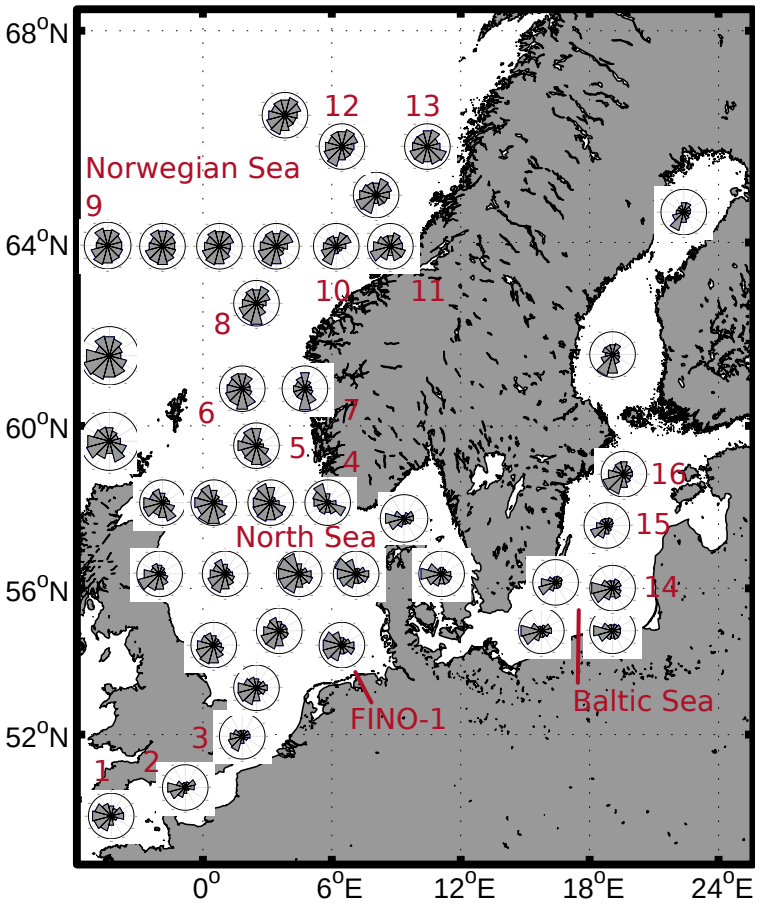

Figure 4: Wind roses for various locations in the domain from QuikSCAT wind fields for the period August 1999 to November 2009.

The spatial variation of the wind direction from offshore to coastal areas is well captured. Wind rose distributions vary according to topographic features when approaching the coast. A strong channelled flow is observed in the English Channel and the central Baltic Sea as the dominant directions in the wind roses are south-westerly. Note the dominant westerlies at the southwestern part of the domain, south of the British Isles. A larger range of wind directions is observed in the north part, around 60°N–5°W, where wind directions mainly vary between westerly and southeasterly. Around the south Norwegian coast, the wind rose distributions adapt to the coastal morphology as the main wind direction aligns parallel to the coast, in particular around Location 4. However, the wind roses 11 and 13 show a strong land component that does not appear in other locations and will be discussed in detail shortly.

Based on the spatial variation of the mean wind speed and direction, 3 sub-regions are identified. The Baltic Sea, with the western border at 9°E, is characterized by the lower mean wind speeds of 6–7 m s^{-1} and dominant south-western winds. The North Sea (49°N–61°N, 5°W–9°E) is characterized by mean wind speeds between 7.5 and 9.5 m s^{-1} and dominant westerlies. The North Atlantic and the Norwegian Sea (61°N–68°N) show the highest mean wind speeds (8–10 m s^{-1}) and all sector wind directions. The wind roses in the Norwegian Sea vary depending on the location. Offshore sites exhibit winds from almost all directions while in some coastal locations there is a strong land component.

3.4. Coastal winds near Norway

In order to resolve the wind patterns near the Norwegian coast in more detail and explain the different wind roses described previously, around 1500 high-resolution satellite SAR scenes covering locations 10–13 (Figure 4) are extracted from the archive at DTU Wind Energy. They are distributed into 12 directional sectors according to the wind direction from NOGAPS at location 11 and browsed in a sector-wise manner.

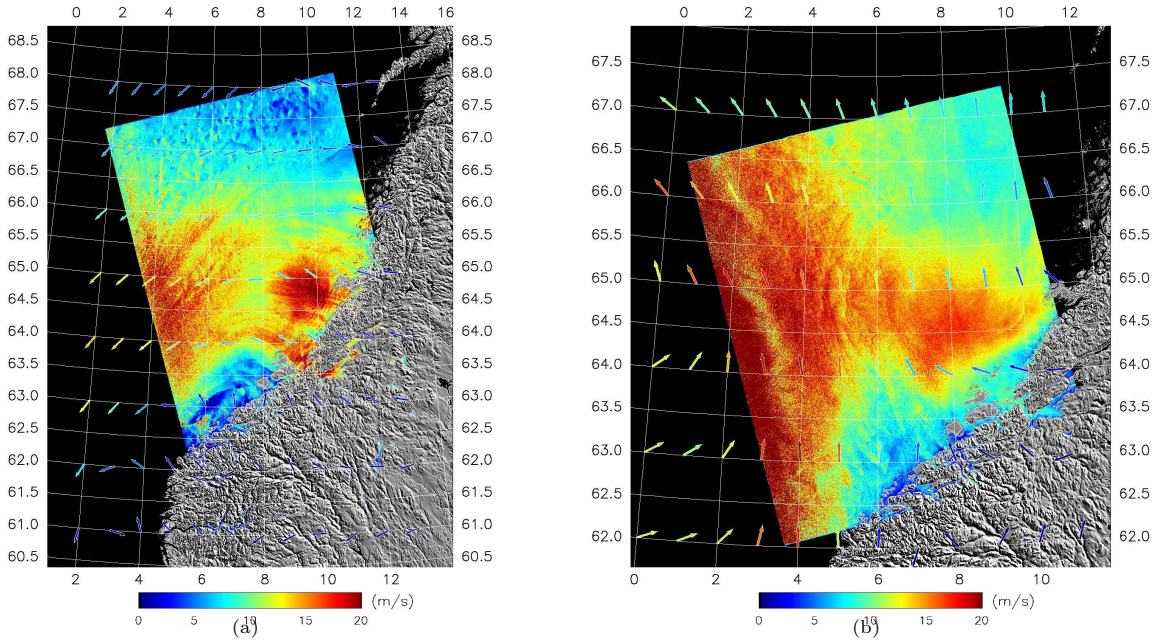

Figure 5: Wind field retrieved from ENVISAT ASAR on a) November 12, 2010 at 20:48 UTC and b) May 4, 2009 at 20:56 UTC. Arrows show model wind speed and directions from NOGAPS using the same color scale as the background image for wind speed.

Wind fields from southeasterly directions (105°–165°) represent situations where winds blow from land to sea. SAR wind fields categorized in these sectors show a strong channelling of winds through the Norwegian fjords, which leads to an increase of the wind speed. A turning of the wind is often seen both from the model wind vectors and from signatures in the SAR wind fields. The southeasterly wind flow from the land becomes more easterly, or even northeasterly, over the sea.

Figure 5a shows a wind field from SAR where such turning of the wind occurs. It may be a result of synoptic lows, which generate an anti-clockwise circulation pattern. This can explain the higher frequency of northeasterly winds at the offshore locations (10, 12) with respect to the coastal locations (11, 13). Other SAR wind fields show a synoptic situation where the wind blows from easterly directions at high latitudes and from westerly directions at lower latitudes (Figure 5b). This flow pattern is typical for the polar front around 60°N.

According to the SAR wind fields, the front is sometimes located near the area under investigation at 64–66°N and sometimes it is positioned further south. The westerly winds observed at lower latitudes are

typically deflected towards the north when they approach the coast of Norway. This may be the reason for the strong contribution from sector 8 (195–225°) at the offshore locations. At the coastal locations, the wind climate seems to be governed to a large degree by the polar easterlies. In the case of the SAR scene shown in Figure 5b, the wind direction at the time of the SAR acquisition is south–southeasterly at the offshore and coastal locations.

4. Temporal Wind Variability

Variations of the mean wind speed on inter- and intra-annual time scales can be estimated using their corresponding indices. Such indices are estimated from the annual means, normalized by long-term averages thus minimising the influence of wind speed biases [12]. In the present study, they are estimated for the period 11/1999–10/2009. The intra-annual index is defined as the fraction of monthly mean values over the decennial mean wind speed,

$$W.I._{intra} = \bar{U}_{month}/\bar{U}_{10yrs} \tag{3}$$

The inter-annual index is estimated as the fraction of annual mean wind over the decennial mean wind [35].

$$W.I._{inter} = \bar{U}_{year}/\bar{U}_{10yrs} \tag{4}$$

4.1. Intra- and Inter- Annual Indices

The intra-annual indices from in situ and satellite observations and the simulated fields at the FINO-1 location, are shown in Figure 6. The definition of indices is adjusted to the data availability at FINO-1, i.e. the denominator in Equation 3 is the annual mean wind speed, not the decennial. All available in situ measurements are used to estimate the intra-annual index. Space collocation is based on the grid cell containing the co-ordinates of the FINO-1 platform.

The similarities between in situ indices and QuikSCAT are remarkable both in variability and amplitude. Minor discrepancies in the amplitude are identified for February and between October and December. These differences reach to 10% of the variability. WRF reanalysis winds (dashed lines) capture the overall seasonal trends. They overestimate the variability between February and May by a maximum of 13%. WRF winds seem to fail in resolving the variability as observed in FINO-1 and from QuikSCAT between June and July.

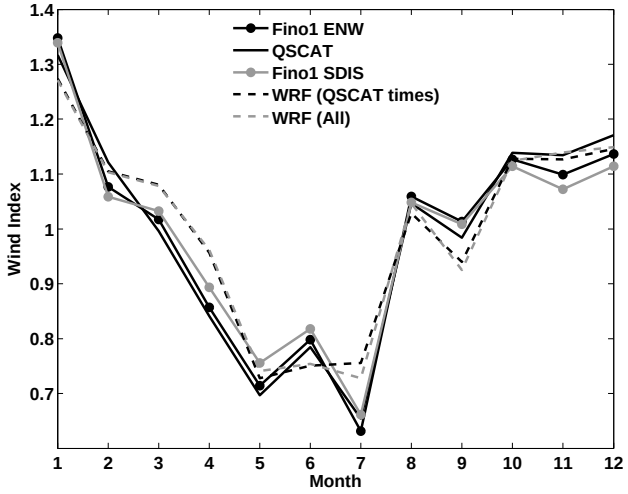

Figure 6: $W.I._{intra}$ at FINO-1 from in situ observations, QuikSCAT and the WRF model reanalysis (dashed lines). Years represented are from 2004 to 2007 but only 478 days of observations are available.

The long-term intra- and inter-annual indices defined in Equations 3 and 4, are estimated from QuikSCAT and WRF, when available (Figure 7). The ability of WRF and QuikSCAT to capture the inter-annual

variability in a similar way, is very much dependent on the location. In the North Sea (Figure 7a), largest discrepancies between the QuikSCAT and WRF derived intra-annual indices are observed for Loc4. There the mean bias between QuikSCAT and WRF is also high and R^2 is low (Figure 3). In general there is a good agreement between the model-based and the satellite derived indices; WRF derived winds capture the variability observed by QuikSCAT.

In the Norwegian Sea, where only QuikSCAT observations are available (Figure 7c), there is a significant year to year variability with below average speeds in 2002 and above average in 2007. Such year to year variability is also observed in the North Sea with below average speeds in 2001 and 2003 and above average speeds in 2002, 2005 and 2007–2008. In the Baltic Sea, the years 2002 and 2007–2008 show higher winds compared to the decennial mean while 2003 and 2006 are years with the lowest winds.

The intra-annual indices (Figures 7b, d, f) show that high above mean values occur in the winter for all sub-domains. Differences between QuikSCAT and WRF are evident in the Baltic Sea and North Sea between April–July and September–December. Minima and maxima occur at different months, depending on the sub-domain. Most locations in the North Sea (Baltic) have minima in June (May) followed by a local increase in July (June). In all locations of the Norwegian Sea, the intra-annual variability is very similar, with minima observed in July.

The lowest-below-mean intra-annual variability is ∼34% of the decennial mean wind speed, observed in the Baltic Sea, while the highest-above-mean is ∼40%, observed in the Norwegian Sea for Location 7. The lowest-below-mean and highest-above-mean inter-annual variability is ∼10% for location 10 in the Norwegian Sea.

Similar findings as for the intra-annual variability are reported by [12], especially for the Northwest Mediterranean with a shift of one month towards the summer. There, the intra-annual index is minimum in June and exhibits an increase during July and August, like for the North Sea. The range of values is also found similar between [12] and this study, varying between 0.65 and 1.3 in most cases.

4.2. Temporal Representativity

One may argue that the low temporal frequency of QuikSCAT (maximum 2 passes every day) may compromise the representativity of satellite observations when 10-year long averages are estimated. First we estimate the mean wind speed and the wind power density from all available in situ measurements, QuikSCAT and the WRF reanalysis fields for the location of FINO-1. The statistics are presented in Table 1. WRF wind speeds time coincident with QuikSCAT (WRF_{QSCAT}) and also from all WRF fields (WRF_{all}) are used. A 1.7% deviation in the mean wind speed and ∼5% in the wind power density are estimated between 883 QuikSCAT and 50426 stability dependent in situ (SDIS) wind speeds. WRF derived winds show deviations that are significantly higher, with 8% for speed and 14.7% for the power density.

Table 1: Statistics of mean wind speed and wind power density at FINO-1 from in situ data, QuikSCAT and WRF. N denotes the number of observations. The period is from 16/02/2004 until 21/01/2007, but only 478 available days. SDIS is the 10 m stability dependent in situ wind speed, ENW is the 10 m Equivalent Neutral Wind and Log is the 10 m wind estimated from the wind speed at 33 m.

	In Situ ENW	In situ Log	SDIS	QuikSCAT	WRF_{QSCAT}	WRF_{all}
$\overline{u}$ (m s^{-1})	8.14	8.35	8.18	8.32	8.83	8.80
$\overline{u}$ Dev. %	-0.5	2.1	–	1.7	8.0	7.5
WPD (W m^{-2})	565.0	577.6	564.0	591.7	646.6	640.0
WPD Dev. %	0.2	2.5	–	4.9	14.7	13.5
N	50426	50426	50426	883	883	11472

The mean wind speed and power density using all the available hourly WRF fields (maximum 87480) and only the ones time coincident with QuikSCAT (maximum 6913), are estimated for the whole domain. The differences are shown in Figure 8. Data availability differences are in the order ∼81000 fields. Discrepancies are small; mean wind speed biases range between −0.1 and 0.15 m s^{-1} but they are around 0.5 m s^{-1} for a few grid cells in the Baltic Sea. The power density biases (Figure 8b) range between −25 and 20 W m^{-2} for the largest part of the domain, while biases of −60 W m^{-2} are identified for the few grid cells mentioned above.

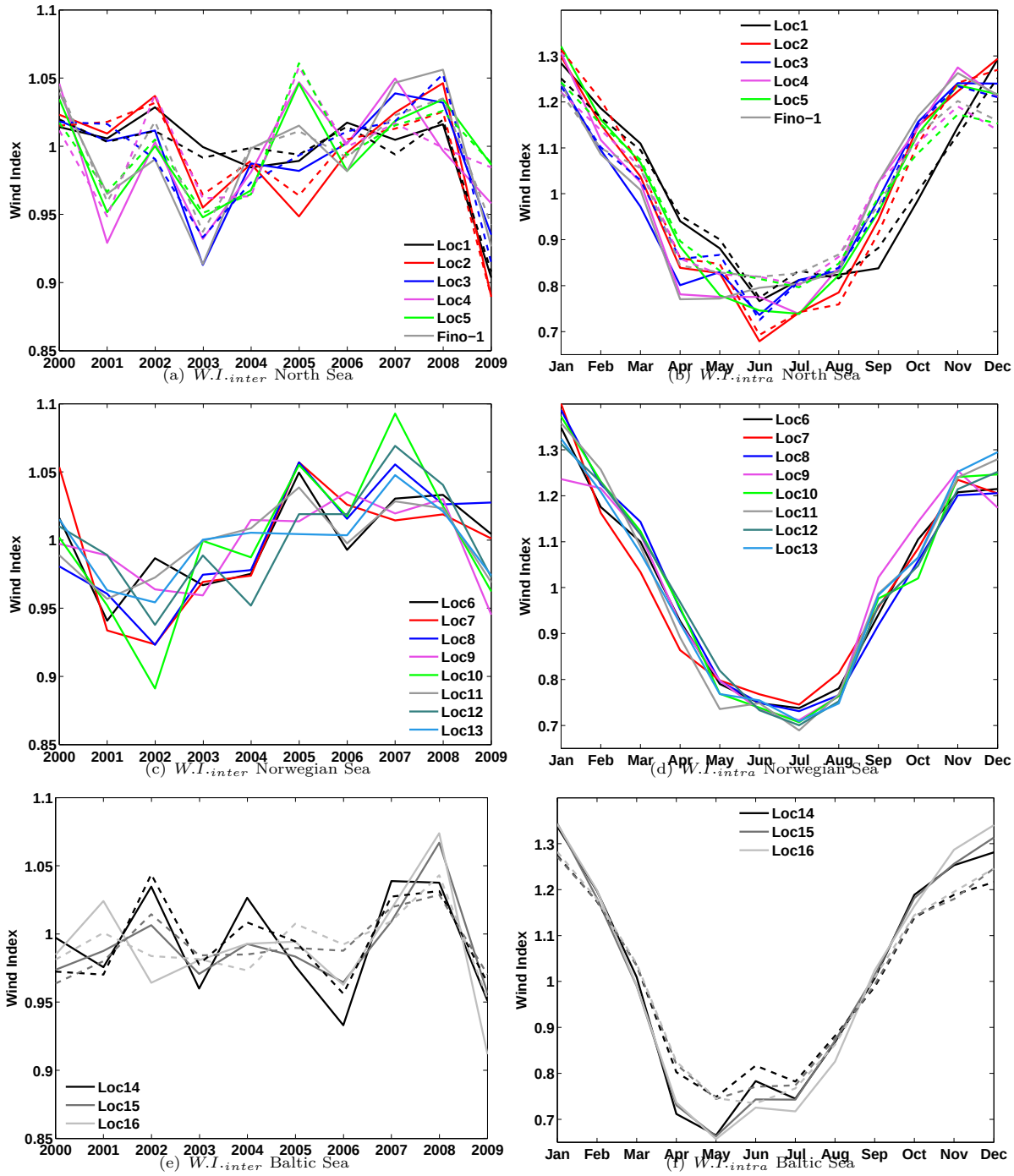

(a) $W.I._{inter}$ North Sea (b) $W.I._{intra}$ North Sea

(c) $W.I._{inter}$ Norwegian Sea (d) $W.I._{intra}$ Norwegian Sea

(e) $W.I._{inter}$ Baltic Sea (f) $W.I._{intra}$ Baltic Sea

Figure 7: $W.I._{inter}$ (left) and $W.I._{intra}$ (right) annual indices from QuikSCAT and WRF in (a,b) the North Sea, (c,d) the Norwegian Sea and (e,f) the Baltic Sea, from November 1999 to October 2009. Solid lines represent QuikSCAT-derived indices and dashed lines WRF-derived indices.

Such results indicate that there is a small impact in the average statistics when 2 daily values are used, instead of 24 hourly values. Some of the discrepancies along the coast can be explained by the QuikSCAT data availability. The findings above, are encouraging but also possibly biased by the properties of the reanalysis

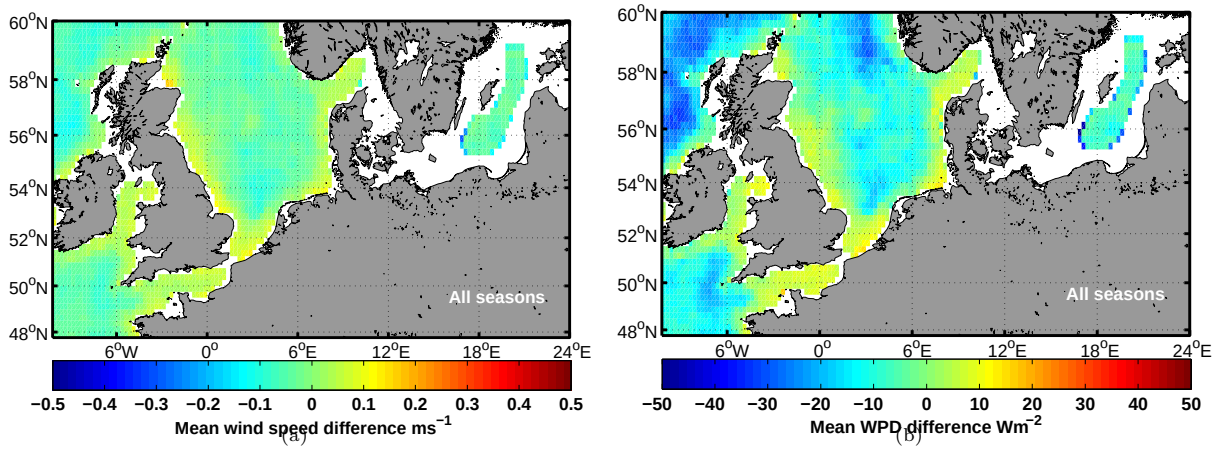

Figure 8: Difference between WRF on QuikSCAT times ($\mathrm{WRF}_{QuikSCAT}$) and all WRF fields (WRF_{all}) for a) mean wind speed, b) wind power density.

fields which are made to capture the long-term characteristics rather than the day to day variability. Given a significant number of available fields (∼7000), the overall statistics are rather well captured.

5. Discussion

The need for readily available information of the wind conditions over the ocean is increasing as more prospective wind farms are sited offshore. In this study, QuikSCAT observations have been used for the northern European seas. The Baltic Sea is poorly covered, as the sea ice mask applied to QuikSCAT backscatter measurements is acquired from SSM/I; a passive microwave instrument on board a series of platforms. This has a low resolution and there is lack of observations close to land. Therefore, QuikSCAT can only be used for the central part of the Baltic Sea basin where the data availability allows the resolution of seasonal trends.

Regarding the exclusion of rain contaminated QuikSCAT winds, [24, 23] studied the seasonal variation in the data availability. Most significant seasonal variations were attributed to the sea ice mask rather than the rain. Overall, independent of season, differences between rain-contaminated and rain-free retrievals were maximum offshore from southern Norway (1600 observations). They reported mean wind speed differences between rain-contaminated and rain-free retrievals that did not exceed 0.2 m s^{-1}.

The main focus of this study is to demonstrate the complementary use of remotely sensed, in situ and simulated winds for the evaluation of the long term spatio-temporal wind characteristics. Such a need arises as there is not a single source of information that can combine the advantages of all. In situ observations are of high frequency but are limited to specific locations and heights. QuikSCAT offers information over large domains at a much lower temporal frequency while simulated winds are available hourly over large domains but are sensitive to the model set-up and can be computationally expensive. The two daily observations are not adequate to properly resolve diurnal cycle. The extended QuikSCAT dataset offers a description of the long-term wind characteristics and has been used in other studies for similar purposes [12, 21].

[5] discussed if the SAR sampling of offshore winds can represent wind speed distributions described by the Weibull distribution, assuming an uncertainty of ±10% at a confidence level of 90%. They concluded that approximately a sample size of 60–70 observations are required to characterize the mean wind speed, about 150 for a variance estimate and nearly 2000 for a wind power density estimate. In the present study, far more QuikSCAT "scenes" were used to estimate the mean wind speed and the direction distributions. While seasonal trends should be captured, the issue of fixed overpass time for QuikSCAT still remains, which likely biases results towards early morning and evening conditions.

Satellite winds refer only to one atmospheric level, thus no information for the vertical wind profile can be obtained. QuikSCAT winds at 10 m above the surface are not very relevant for offshore wind turbine hub heights, that are typically around 90 m. Lifting the satellite winds is an ongoing aim within the wind resource assessment community and a recent study, [3], attempted to do so using NWP outputs for the estimation of the stability correction. Reported biases between lifted satellite winds and hub-height measurements were higher than those between simulated winds and hub-height measurements. Such results highlight the lack of accurate stability information to use for the stability correction of ENW and strengthen the current approach not to lift the satellite winds or transform them to account for stability.

While various QuikSCAT products are available from different processing centres, this study uses an already gridded product. Different QuikSCAT products are compared with in situ observations from buoys and research vessels. [33] compared swath and gridded QuikSCAT data with offshore and nearshore buoys concluding that swath data provided the best agreement with nearshore buoys. For the gridded data, they highlighted the trade-off between point accuracy and capturing the large-scale wind patterns. From comparisons of QuikSCAT winds derived with different GMFs against ocean buoy data, [11] reported biases within the mission requirements. In addition, they reported no significant differences between the GMFs.

The extended spatial comparisons between QuikSCAT and WRF outputs, indicate large areas where discrepancies are very small. The largest differences are observed in coastal areas, of complex morphology and adjacent to land masses. There both data sources may be contaminated by errors. Due to the proximity of land masses, QuikSCAT may suffer from the contamination of land to the backscattered signal while WRF may underestimate the wind due to disagreements between the land mask and the real topography. This introduces an error in the change of the surface roughness and its value. [22] noted differences of up to 2 m s^{-1} between QuikSCAT and NOGAPS analysis fields near land-surface boundaries. They also noted an improvement in the NOGAPS model performance near land-sea boundaries when QuikSCAT was assimilated.

The high standard deviation between QuikSCAT and WRF winds found around 60°N–5°W is due to the local variability seen from the QuikSCAT wind roses. This higher variability in the wind from QuikSCAT is represented in the standard deviation between QuikSCAT and WRF while the biases are small likely due to averaging. The high standard deviation found along the Norwegian coast may likely have its source in discrepancies arising from the model fields and current related biases in the scatterometer winds. In addition, this is an area with a strong coastal jet flow [4] that may not be captured by the reanalysis fields. This WRF reanalysis is available at DTU Wind Energy but it has not been produced specifically for this study. The WRF simulation was run in long nudged steps instead of the more common day-to-day model configuration, where the model is restarted daily. The latter method may result in the model never fully spinning up its internal regional climate [38].

The land component appearing in the wind roses of the north-west Norwegian coast (11 and 13), was further investigated with the use of two SAR wind fields. SAR wind fields have a much higher resolution compared to QuikSCAT, they are able to resolve much finer spatial scales. Such land components are due to katabatic winds from the Norwegian mountains. [1] performed similar investigations using SAR in the Adriatic and Black Sea identifying Bora winds; a type of katabatic wind. In both cases the high-resolution SAR images provided valuable insight in the precise location and magnitude of specific wind phenomena.

Inter- and intra-annual indices are typically used in wind resource assessment studies, for the initial evaluation of the long-term wind variability and the assessment of prospective areas. The inter-annual index provides information for the mean wind speed of a year compared to a long-term mean while the intra-annual index is used to evaluate the monthly wind variability compared to the long-term mean. Comparing the wind indices between various locations on a large domain provides information regarding the spatio-temporal variability of the wind field. For the purposes of the present study, QuikSCAT estimated wind indices for a large domain offer information regarding the spatial consistency of the dataset within a given geographical area, which potentially leads to identification of areas with similar wind features. The ability of QuikSCAT to reproduce the long-term temporal variability of the local wind is remarkable, despite its low temporal frequency when compared to the 10 minute in situ measurements. This is highlighted by the good comparison of the intra- annual variability from QuikSCAT and in situ observations at FINO-1.

The 10 year climatology used in the present study is found less able to resolve this intra-annual variability, nonetheless accurate for describing the seasonal trends. In [12], high above-average mean winds were observed in 2003 in the Mediterranean Sea. An anti-correlation between the Northern European Seas and the Mediterranean is thus noticed, as below-average mean winds are observed in the Northern European Seas for 2003. When estimating the mean wind speed and wind power density using the WRF reanalysis dataset of different sample size, i.e. a sub-sample that corresponds to the QuikSCAT dataset and a dataset that utilizes the full WRF reanalysis archive, biases are found to be around 0.15 m s^{-1} for the wind speed and 10 W m^{-2} for the wind power density. These biases are slightly underestimated because of the smaller variability found in the WRF reanalysis fields.

6. Conclusions

Wind information over the ocean is essential as the suitable sites for wind farm installation expand offshore. The spatial and temporal wind characteristics in the Northern European Seas, where most of Europe's offshore wind parks are located, were investigated with the combined use of satellite and in situ observations along with model reanalysis fields.

QuikSCAT, with an extended spatio-temporal coverage, was proven valuable for the description of the spatial and temporal wind variability over large areas, where in situ observations are sparse. Three sub-domains with similar average wind speed and direction distributions were identified. There higher resolution model runs can be performed and meteorological masts can be installed.

Features identified from the QuikSCAT mean winds included channelled flows, lee effects and local winds. A specific area in Norway was further investigated with the use of high resolution SAR wind fields. They showed patterns of wind turning due to local orographic features.

Comparisons between QuikSCAT and WRF reanalyses showed biases ranging mostly between 0.6 and -0.6 m s^{-1} with standard deviation of 1.8–2.8 m s^{-1}. The intra-annual wind variability ranged from a above-mean-maximum $\sim$40% in the Norwegian Sea to a below-mean-minimum $\sim$34% in the Baltic. The inter-annual variability was smaller, $\sim$10% of the decennial mean.

A $\sim$1.7% deviation in the mean wind speed and $\sim$5% in the power density between $\sim$51000 10-min measurements and $\sim$900 QuikSCAT retrievals was found. Biases of $\sim$0.2 m s^{-1} for the mean wind speed and $\sim$15 W m^{-2} for the power density were found between $\sim$7000 and $\sim$85000 reanalysis fields from WRF.

Our results demonstrate the combined use of in situ, remote sensing and simulated information for wind resource assessment applications and highlight limitations or discrepancies between the different data types. Especially for large areas the only alternative would be a dense network of in situ instrumentation which is currently not available.

7. Acknowledgements

This study has been funded by the FP7 EU ORECCA and the FP7 NORSEWiND (TREN-FP7EN-219048) projects. QuikSCAT data are courtesy of Remote Sensing Systems (http://www.remss.com). ENVISAT ASAR data are obtained from ESA. FINO-1 data from DEWI (Deutsches Windenergie Institut, German Wind Energy Institute), oceanographic data from BSH (www.bsh.de), all obtained through the NORSEWInD project. The authors would like to thank two anonymous reviewers for their valuable comments.

8. References

[1] Alpers W, Ivanov A, Horstmann J. Observations of Bora events over the Adriatic Sea and Black Sea by spaceborne Synthetic Aperture Radar. Monthly Weather Review 2009;137:1150–1161.

[2] Badger M, Badger J, Nielsen M, Hasager CB, Peña A. A hybrid method for offshore wind resource assessment, Proc. ESA Living Planet Symposium 2010, Bergen, Norway.

[3] Badger M, Peña A, Bredesen RE, Berge E, Hahmann A, Badger J, Karagali I, Hasager CB, Mikkelsen T. Bringing satellite winds to hub-height. Proceedings EWEA - The European Wind Energy Association 2012.

[4] Barstad I, Grønås S. Southwesterly flows over southern Norway–mesoscale sensitivity to large-scale wind direction and speed. Tellus A 2005;57(2):136–152.

[5] Barthelmie RJ, Pryor S. Can satellite sampling of offshore wind speeds realistically represent wind speed distributions?. Journal of Applied Meteorology 2003;42(1):83–94.

[6] Bourassa MA, Legler DM, O'Brien JJ, Smith SR. SeaWinds validation with research vessels. Journal of Geophysical Research 2003;108(C2).

[7] Capps SB, Zender CS. Estimated global ocean wind power potential from QuikSCAT observations, accounting for turbine characteristics and siting. Journal of Geophysical Research 2010;115(D09101).

[8] Charnock H. Wind stress on a water surface. *Quarterly Journal Royal Meteorological Society* 1955; 81:639–640.

[9] Christiansen M, Koch W, Horstmann J, Hasager CB, Nielsen M. Wind resource assessment from C-band SAR, Remote Sensing of Environment 2006;105:68–81.

[10] Dickinson S, Kelly KA, Caruso MJ, McPhaden MJ. Comparisons between the TAO buoy and NASA scatterometer wind vectors. Journal of Atmospheric and Oceanic Technology 2001;18:799–806.

[11] Ebuchi N, Graber HC, Caruso MJ. Evaluation of wind vectors observed by QuikSCAT\SeaWinds using ocean buoy data. Journal of Atmospheric and Oceanic Technology 2002;19:2049–2062.

[12] Furevik BR, Sempreviva AM, Cavaleri L, Lefèvre J-M, Transerici C. Eight years of wind measurements from scatterometer for wind resource mapping in the Mediterranean Sea. Wind Energy 2010;14(3):355–372.

[13] Gryning S–E, Batchvarova E, Brümmer B, Jørgensen H, Larsen S. On the extension of the wind profile over homogeneous terrain beyond the surface layer. Boundary Layer Meteorology 2007;124:251–268.

[14] Hagemann K. Mesoscale Wind Atlas of South Africa. PhD Thesis, University of Cape Town 2008.

[15] Hahmann AN, Rostkier-Edelstein D, Warner TT, Vandenberghe F, Liu Y, Babarsky R, Swerdlin SP. A reanalysis system for the generation of mesoscale climatographies. Journal of Applied Meteorology and Climatology 2010;49:954–972.

[16] Hasager CB, Barthelmie RJ, Christiansen MB, Nielsen M, Pryor SC. Quantifying offshore wind resources from satellite wind maps: study area the North Sea. Wind Energy 2006;9(1-2):63–74.

[17] Hasager CB, Peña A, Christiansen MB, Astrup P, Nielsen M, Monaldo F, Thompson D, Nielsen P. Remote sensing observation used in offshore wind energy, IEEE Journal of Selected Topics in Applied Earth Observation and Remote Sensing 2008;1(1):67–79.

[18] Hasager CB, Badger M, Peña A, Larsen XG, Bingöl F. SAR-based wind resource statistics in the Baltic Sea. Remote Sensing 2011;3(1):117–144.

[19] Haugan PM, Evensen G, Johannessen JA, Johannessen OM, Pettersson LH. Modeled and observed mesoscale circulation and wave-current refraction during the 1988 Norwegian continental shelf experiment. Journal of Geophysical Research 1991;96(C6):10487–10506.

[20] Hong S–Y, Noh Y, Dudhia J. A new vertical diffusion package with an explicit treatment of entrainment processes. Monthly Weather Review 2006;134:2318–2341.

[21] Kolstad EW. A QuikSCAT climatology of ocean surface winds in the Nordic seas: Identification of features and comparison with the NCEP/NCAR reanalysis. Journal of Geophysical Research 2008;113(D11106).

[22] Kara AB, Wallcraft AJ, Martin PJ, Pauley RL. Optimizing surface winds using QuikSCAT measurements in the Mediterranean Sea during 2000-2006. Journal of Marine Systems 2009;78:119–131.

[23] Karagali I, Peña A, Badger M, Hasager CB. Wind characteristics in the North and Baltic Seas from the QuikSCAT satellite. Wind Energy 2012, accepted, in production.

[24] Karagali I. Offshore Wind Energy: Wind and Sea Surface Temperature from Satellite Observations. Ph.D. thesis, DTU Wind Energy 2012, in press.

[25] Larsén GX, Mann J, Berg J, Götel H, Jacob D. Wind climate from the regional climate model REMO. Wind Energy 2010;13(4):279–296.

[26] Liu TW, Tang W. Equivalent neutral wind. National Aeronautics and Space Administration, Jet Propulsion Laboratory, California Institute of Technology, National Technical Information Service, 1996.

[27] Li X, Zhong S, Bian X, Heilman WE. Climate and climate variability of the wind power resources in the Great Lakes Region of the United States. Journal of Geophysical Research 2010;115(D18107).

[28] Peña A, Hasager CB, Gryning S–E, Courtney M, Antoniou I, Mikkelsen T. Offshore wind profiling using light detection and ranging measurements. Wind Energy 2009;12(2):105–124.

[29] Peña A, Gryning S–E, Hasager CB. Comparing mixing-length models of the diabatic wind profile over homogeneous terrain. Theoretical and Applied Climatology. 2010;100:325–335

[30] Peña A, Hahmann AN. Atmospheric stability and turbulence fluxes at Horns Rev–an intercomparison of sonic, bulk and WRF model data. Wind Energy 2012;15(5):717–731.

[31] Peña A, Gryning S–E, Hahmann AN. Observations of the coastal atmospheric boundary-layer height in Western Denmark. Journal of Geophysical Research 2012; in review.

[32] Peña A, Hahmann AN, Hasager CB, Bingöl F, Karagali I, Badger J, Badger M, Clausen N-E. South Baltic Wind Atlas. South Baltic Offshore Wind Energy Regions Project. Risø-R-1775(EN).

[33] Pickett MH, Tang W, Rosenfeld LK, Wash CH. QuikSCAT satellite comparisons with nearshore buoy wind data off the U.S. West Coast. Journal of Atmospheric and Oceanic Technology 2003;20:1869–1879.

[34] Ruti PM, Marullo S, D'Ortenzio F, Tremant M. Comparison of analyzed and measured wind speeds in the perspective of oceanic simulations over the Mediterranean basin: Analyses, QuikSCAT and buoy data. Journal of Marine Systems 2008;70(1-2):33–48.

[35] Sempreviva AM, Barthelmie RJ, Pryor SC. Review of methodologies for offshore wind resource assessment in European Seas. Surveys in Geophysics 2008;29:471–497.

[36] Skamarock WC, Klemp JB, Dudhia J, Gill DO, Barker DM, Duda MG, Huang X-Y, Wang W, Powers JG. A Description of the Advanced Research WRF Version 3 2008; NCAR/TN–475.

[37] Tammelin B, Vihma T, Atlaskin E, Badger J, Fortelius C, Gregow H, Horttanainen M, et al. Production of the Finnish Wind Atlas. Wind Energy 2011.

[38] Warner TT. Numerical Weather and Climate Prediction. Cambridge 2011;p.446.

Paper III

Spectral properties of QuikSCAT and ENVISAT ASAR wind fields in the North Sea

Spectral Analysis of QuikSCAT and ENVISAT ASAR surface wind fields in the North Sea

I. Karagali[1], X. Guo Larsén[1], A. Peña[1], M. Badger[1], and C. B. Hasager[1]

Scatterometer wind fields from QuikSCAT are advantageous due to their global spatial and long temporal coverage and have a spatial resolution of 25 km. Synthetic Aperture Radar (SAR) wind retrievals, have a much higher spatial resolution of 600 m, but suffer from inconsistent time and space coverage. The present study aims at investigating the spectral properties of QuikSCAT 25 km and ENVISAT ASAR products of various resolutions. Due to the inconsistent SAR coverage, a sub-domain of the North Sea is selected, where there is an overlap of 87 SAR scenes. It is shown that the QuikSCAT spectral dependency on wave number follows the theoretical $k^{-5/3}$ law, while for the SAR products slopes become smoother as the resolution increases. SAR wind fields contain significantly more small scale variability, show higher spectral power as the resolution increases and maintain a high energy content for length scales of 2 km. No significant impact of the number of scenes on the spectral slope is identified, for as many as 87 samples. A seasonal dependence of the power is identified as well as a characteristic difference between the meridional and zonal spectral components. When examining the seasonal spectra, the available sample size decreases to 25 scenes and an impact on the spectral slope is found.

1. Introduction

Observations of the oceanic surface wind field from satellites, typically from scatterometers or radars, are very useful for wind resource assessment offshore, where in situ measurements are difficult to obtain. QuikSCAT scatterometer products combine daily coverage of approximately 90% of the global ocean with a resolution of 25 km and long temporal availability. Synthetic Aperture Radar (SAR) ocean wind retrievals have a much higher resolution, up to 600 m, but so far suffer from systematic spatial and temporal coverage.

Both QuikSCAT and SAR products are currently used for offshore wind resource assessment. *Karagali et al.* [2012a, b] used a gridded QuikSCAT product from Remote Sensing Systems (RSS) to evaluate wind characteristics in the North Sea. SAR wind fields are routinely produced at Risø Campus, DTU and used for wind resource assessment [*Hasager et al.*, 2008; *Badger et al.*, 2010]. Comparisons between QuikSCAT and ENVISAT ASAR wind fields are limited by differences in the resolution, spatial and temporal coverage and the approximately 5-hour time lag between overpass times. Spectral slopes and power are robust properties that highlight potential differences and the advantages and disadvantages of using the two different types of space-borne wind observations. Moreover, *Vincent et al.* [2010] discussed the importance of studying the spectral properties in the mesoscale range as a measure of accuracy for short-term forecasting and for estimating extreme winds [*Larsén et al.*, 2012].

Vogelzang et al. [2011] used QSCAT and ASCAT data along with ECMWF model forecasts and buoy measurements to evaluate the quality of the scatterometer winds, concluding that the ASCAT-25 km product contains more intermediate scale information than the QuikSCAT-KNMI product. *Freilich and Chelton* [1986] identified a dependency on k^{-2} for the midlatitude mesoscale range using scatterometer winds from the SEASAT satellite.

Patoux and Brown [2001] performed a spectral analysis of QuikSCAT winds in the Pacific Ocean with wave numbers ranging from 50 to 1700 km. They noted that for the meso-scale range the energy fell off with a slope ranging from -2.2 to -2.4 depending on the product. *Zecchetto and De Biasio* [2003] used a 25 km QuikSCAT product to evaluate the wavenumber spectra of the Mediterranean Sea reporting spectral slopes of -5/3 for the range between 900 and 1300 km and a -3 slope for the range between 600 and 900 km. *Halpern et al.* [1999] evaluated scatterometer winds from the ERS-1 platform for the range between 50 and 1800 km, reporting slopes of -2.6 and -2.4 for the zonal and meridional wind components, respectively. *Winkle et al.* [1999] used scatterometer winds from ERS-1, re-analysis wind fields from NCEP and high resolution aircraft observations, for a wavenumber range extending from 1 to 1000 km. They reported a best fit slope very near the -5/3 law.

Studies exist that show kinetic energy deficiencies of modelled wind fields compared to ship measurements [*Bumke*, 1995], ERS [*Chin et al.*, 1998; *Halpern et al.*, 1999] and QuikSCAT [*Zecchetto and De Biasio*, 2003; *Stoffelen et al.*, 2010]. To the authors' knowledge, the spectral properties of the SAR retrieved winds have never been evaluated. As such the aim is to investigate the spectral properties of SAR wind fields retrieved with different resolution and evaluate them against QuikSCAT derived spectra which are known to be superior to modelled winds. In addition, e evaluate the resolvable length scales in the spatially averaged satellite wind fields and and investigate their power law behaviour. In the present study, the impact of ocean waves on the spectral properties of the retrieved winds is neglected due to a resolution reduction to at least 600 m prior to the wind inversion.

This is important if one needs to understand the nature of spatially coherent surface winds and very relevant for wind energy related purposes where temporal in situ observations are often compared to spatially averaged observations of wind from satellites products. We note that investigations using high resolution wind fields are currently not available in the literature. In addition, the impact of varying resolution amongst satellite winds is still under investigation. *Vogelzang et al.* [2011] performed a similar study but only using scatterometer winds with resolutions of 12.5 and 25 km.

2. Near-Surface Ocean Wind Fields

2.1. Satellite Winds

QuikSCAT data are obtained from Remote Sensing Systems (RSS), as daily files mapped on a 0.25×0.25 Earth

[1]DTU Wind Energy, Risø Campus, Roskilde, 4000, DK.

0094-8276/12/$5.00

grid. Each file includes two wind fields, corresponding to the morning (ascending) and afternoon (descending) satellite passes.

SAR wind retrievals are performed in DTU Wind Energy using the APL/NOAA (Applied Physics Laboratory/National Oceanic Atmospheric Administration) SAR Wind Retrieval System (ANSWRS) developed at the Johns Hopkins University. This system allows the selection of preferred resolution of the final wind field. This can be achieved by reducing the original 150 m resolution (the pixel dimensions are 75·75 m) to any value through averaging, prior to the wind inversion. For this study, we produce wind fields with resolutions of 0.6, 1.5, 3, 15 and 25 km.

3. Methods

The domain of interest extends from 53.875°N to 53.875°N and 5.875°E to 7.75°E, see Figure 1. For this area there is an overlap of 135 SAR wind retrievals. Due to the lag in the overpass time between QuikSCAT and the ENVISAT ASAR, time-collocation is performed by selecting the same date and fraction of day, i.e. if the SAR overpass time is at 10:00 UTC we select the QuikSCAT morning pass. Due to rain contamination, QuikSCAT data are flagged for rain. There is a maximum data loss of 20% allowed for each QuikSCAT pass. If this threshold is exceeded, the QuikSCAT pass and the corresponding SAR field are discarded.

Finally, a total of 87 sets of surface wind fields are used. The statistics of average satellite pass and date are shown in Table 1. The spatial wind speed series are extracted, for both the west-east (zonal) and north-south (meridional) directions. Each spatial series is linearly de-trended and Fourier transformed and finally all spectra are time averaged.

The domain size is not sufficient for spectral analysis, especially for the low resolution products. In particular for QuikSCAT, the meridional component has 12 points and the zonal, has 8. Therefore, we also compute the QuikSCAT spectra for a squared box that includes most of the North Sea, extending from 54° to 58°N and 0° to 8°E.

4. Results

Three topics are investigated. Initially we examine the spectral behaviour of the QuikSCAT winds and SAR winds processed with different resolutions. We discuss the computed spectra and the spectral slopes and investigate the behaviour of QuikSCAT in a larger domain. Then, we examine the seasonal variability of the computed spectra from QuikSCAT and SAR. Finally the impact of sampling is examined regarding whether the 87 available scenes are representative.

4.1. Averaged Spectra

Figure 2 shows the zonal and meridional component spectra of QuikSCAT and SAR, where the impact of resolution in the spectral power range is evident. QuikSCAT spectral tails turn and become horizontal for length scales around 60 km, especially apparent for the zonal component. This behaviour of QuikSCAT for spatial scales close to the Nyquist frequency has also been mentioned in *Stoffelen et al.* [2010], where it is attributed to noise. Similar findings are observed for the SAR 1.5 and 3 km products but for scales of 6 km. For the meridional component, the 25 km SAR product shows higher spectral power content than the corresponding QuikSCAT. Note that the difference in spectral power between QuikSCAT and SAR is higher for the zonal component.

The full North Sea domain has very similar spectral slopes with the sub-domain for the meridional component, but shows higher spectral power. A more prominent difference is identified for the meridional component, mainly because the resolvable length scales extend towards the lower wavenumber range.

The spectral slopes computed from the QuikSCAT and SAR products are shown in Table 2. Slopes range from ∼-1 to -1.8, with QuikSCAT having slopes for the meridional component closest to $-5/3$ (-1.66). SAR slopes are smoother for the very high resolutions and become steeper as the resolution decreases. Note that the SAR slopes for the 25 km product are smoother than QuikSCAT for the meridional component and steeper for the zonal component. Smoother slopes indicate a higher energy content and smaller deficit as the wave number increases, which indicates higher spatial resolution for the SAR fields.

4.2. Seasonal Variability

Seasonal spectra are computed based on a seasonally varying number of satellite wind fields (Table 1) and are presented in Figure 4. For the meridional component there is no apparent seasonal variation of the spectral power. There is an indication for a seasonal variation for the zonal component; a slight decrease in the spectral power is observed in summer. This may be an artefact of sampling, as summer is the season with the less available scenes (17).

Note the persistent feature, where for the zonal component the difference between the QuikSCAT and SAR spectral powers is larger than for the meridional component. This may be an artefact of the small domain size, as there is a low number of available grid cells for the QuikSCAT product that may introduce errors in the computed spectra.

For all seasons and both zonal and meridional components, the QuikSCAT spectral power is lower than the one of all the SAR products. This difference is almost eliminated for the spring and summer meridional components and for length scales between 314 and ∼157 km, but the deficit of QuikSCAT quickly becomes apparent for length scales smaller than 157 km.

4.3. Sampling

Comparisons are limited by the availability of SAR retrievals, for which frequent observations of the same area are not consistent. To the contrary, QuikSCAT offers 10 years of twice daily observations for the area of interest. To investigate how representative are the 87 scenes, QuikSCAT spectra are computed from the 10 years of available observations. Figure 3 indicates that the QuikSCAT winds show practically no difference between the 87 scenes and the 10 year-long dataset, which has a maximum of approximately 7000 scenes.

For the mid-latitude regions of the Pacific Ocean, *Freilich and Chelton* [1986] found a k^{-2} dependence of all zonal, meridional and kinetic energy spectra computed from scatterometer winds. The spectral slopes computed from the sub-set and full data set of QuikSCAT (87 scenes versus ∼7000 scenes) for the sub-domain and the North Sea domain, are shown in Table 2. Slopes for the meridional component range from -1.66 to -1.7 and for the zonal component, from -1.1 to -1.8. The differences in slope for the 87 QuikSCAT scenes and the full dataset are ranging between 0.02 and 0.09, highlighting the very small impact of sampling.

One may argue that the seasonal spectra may not be representative, as the maximum number of scenes used is 25, for autumn, which may not be sufficient. The seasonal spectra from QuikSCAT using 87 scenes and the 10 year-long dataset, shown in Figure 5, indicate that there are differences in the spectral power range, with the 10 year-long data set showing higher spectral power for all seasons except summer.

5. Discussion

In SAR the high energy content is maintained for lenght scales of 2 km whereas in mesoscale model results with grid resolution around 2 km the energy content is only maintained at length scalesan order of magnitude lower, around 20 km.

The range of resolvable wavenumbers varies depending on the sensor, the resolution of the product and the size of the domain. In general, spatial scales ranging between 800 and 2.5 km are discussed. *Xu et al.* [2011] state that QuikSCAT spectral slopes below 300 km can be affected by noise in the satellite wind direction. This should be taken into consideration when examining the spectral behaviour of the QuikSCAT product for scales smaller than this threshold.

The limited availability of SAR wind fields over the same area is an issue when performing wind resource assessment [*Badger et al.*, 2010]. In terms of spectral properties, though, there is no impact of the reduced temporal coverage when a sufficient number of scenes is available.

Xu et al. [2011] found a slope difference generally smaller than 0.06, between using 2 years and 10 years of QuikSCAT data while the seasonal slope difference was smaller than 0.1. This is generally in agreement with findings from the current study, where slope differences range from 0.02 and 0.09 between 87 QuikSCAT scenes and 10 years of available QuikSCAT data.

The difference in number of wind fields between the QuikSCAT wind fields time-collocated with the SAR scenes and the full 10 years of available twice daily QuikSCAT observations, is in the order of 6900. The difference of QuikSCAT spectral slopes is smaller than 0.1 for both the meridional and zonal spectral components, independent of the domain size. Therefore, the 87 scenes are proven sufficient to describe the spectral properties. When the seasonal patterns are of interest, the maximum of 25 scenes available in the present study is not found sufficient.

As has been mentioned in *Patoux and Brown* [2001], for surface winds the smaller scales are expected to have more energy and the spectrum to be shallower. This may explain why the SAR slopes are smoother than QuikSCAT, since the smaller scales are resolved in SAR.

The SAR wind retrieval processing scheme used in this study produces wind fields of varying grid cell dimensions, even for the same resolution, depending on the dimensions of the original SAR scene from ENVISAT. Some scenes are larger than others and the software handles them in such a way that they are finally gridded with the same dimensions. Depending on the size of the original SAR scene, there is a certain number of grid cells that have no values and this varies even within the same resolution set. Investigations regarding the potential impact of such a methodology to the derived results are to be performed in the future but they are currently out of scope.

A two dimensional FFT analysis is not performed due to the unequal dimensions of the domain. The possibility of reducing the dimensions to match a square domain is excluded due to its already small size.

6. Conclusion

The resolution of the different satellite wind products varies from 600 m for SAR to 25 km for QuikSCAT wind fields. The range of wave numbers corresponds to spatial scales ranging from 2.5 to 800 km. The spectral power of the SAR products is generally higher than QuikSCAT, even when the two products have the same resolution of 25 km. Thus SAR is able to resolve much smaller spatial scales than QuikSCAT.

It is shown that QuikSCAT spectral slopes for the mid-latitude region of interest follow the theoretical predicted value of $-5/3$ (-1.6). The SAR spectral slopes are smoother than -1.6 and become steeper for decreasing resolution. SAR fields maintain a high energy content for length scales of 2 km. The spectral power deficiency increases with decreasing spatial resolution.

While QuikSCAT wind products offer long temporal and spatial coverage, SAR products offer high spatial resolution but are not consistent in spatial coverage. This study has revealed the possibility of processing SAR fields with a resolution similar to QuikSCAT, thus rendering the merging of satellite observations possible in order to increase their temporal coverage.

Acknowledgments. This study has been partially funded by the EU NORSEWInD project (TREN-FP7EN-219048). QuikSCAT data were obtained from Remote Sensing Systems (RSS). ENVISAT ASAR winds are courtesy of the European Space Agency (ESA).

References

Badger, M., J. Badger, M. Nielsen, C.B. Hasager, C.B., and A. Peña (2010), Wind class sampling of satellite SAR imagery for offshore wind resource mapping, *J. Appl. Meteor. Climatol. 49*, 2474–2491.

Bumke, K. (1995), Spatial scales of surface wind observations and analysed wind fields over the North Atlantic Ocean, *J. Mar. Syst.*, *6*, 67–75.

Chelton, D. B., M. H. Freilich, J. M. Sienkiewicz, and J. M. Von Ahn (2006), On the use of QuikSCAT scatterometer measurements of surface winds for marine weather prediction, *Mon. Wea. Rev.*, *134*, 2055–2071.

Chin, T. M., R. F. Milliff, and W. G. Large (1998), Basin-scale, high-wavenumber sea surface wind fields from a multiresolution analysis of scatterometer data, *J. Atmos. Ocean. Technol.*, *15*, 741–763.

Freilich, M. H. and D. B. Chelton (1986), Wavenumber spectra of Pacific winds measured by the Seasat scatterometer, *J. Phys. Oceanogr.*, *16*, 741–757.

Gage, K. S., and G. D. Nastrom (1986), Theoretical interpretation of atmospheric wavenumber spectra of wind and temperature observed by commercial aircraft during GASP, *J. Atmospheric Sciences*, *43(7)*,729–740.

Halpern, D., M.H. Freilich, and R.A. Weller (1999), ECMWF and ERS-1 surface winds over the Arabian Sea during July 1995, *J. Phys. Oceanogr.*, *29*, 1619–1623.

Hasager, C.B., A. Peña, M.B. Christiansen, P. Astrup, M. Nielsen, F. Monaldo, D. Thompson, P. Nielsen, Remote sensing observation used in offshore wind energy, *IEEE J. Appl. Ear. Obs. Rem. Sens.*, *1(1)*, 67–79.

Karagali, I., A. Peña, M. Badger, and C. B. Hasager (2012), Wind characteristics in the North and Baltic Seas from the QuikSCAT satellite, *Wind Energy*, accepted.

Karagali, I., M. Badger, A. Hahmann, A. Peña, C. B. Hasager, and A. M. Sempreviva (2012), Spatial and temporal variability of winds in the Northern European Seas, *Renewable Energy*, accepted with revisions.

Larsén, X.G., S. Ott, J. Badger, A. Hahmann, and J. Mann (2012), Recipes for correcting the effect of mesoscale resolution on the estimation of extreme winds, *J. Appl. Meteorol. Climatol.*, *51*, 521–553.

Larsén, X.G., Vincent, C., and S. Larsen (2010), Spectral structure of mesoscale wind over the water, *Q. J. R. Meteorol. Soc.*.

Patoux, J., and R. A. Brown (2001), Spectral analysis of QuikSCAT surface winds and two-dimensional turbulence, *J. Geophys. Res.*, *106*, (D20), 23995–24005.

Skamarock, W.C. (2004), Evaluating mesoscale NWP models using kinetic energy spectra, *Month. Weath. Rev.*, *132*, 3019–3032.

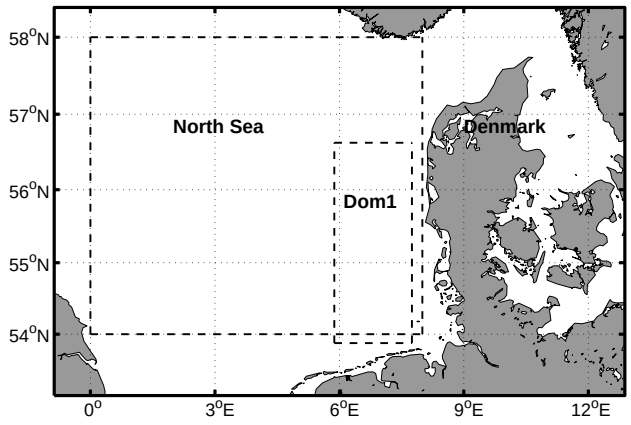

Figure 1. Graphical representation of the sub-domain Dom1 and the full North Sea domain as boxes defined by dashed lines.

Table 1. Description of wind fields used for the spectral analysis

N (total)	87
N (daily)	48: Morning 39: Evening
Overpass	04:54, 18:45 (QuikSCAT)
time	09:51, 21:07 (SAR)
Season	DJF:23, MAM:22, JJA:17, SON:25
Year	2009: 28, 2008: 26, 2007: 30, 2006: 03

Table 2. Spectral slopes for the different types of satellite products.

	Meridional	Zonal	Var. from -5/3 (%)	
			Meridional	Zonal
QSCAT sub. (10 yrs)	-1.65	-1.19	1.1	-29.0
QSCAT NS (10 yrs)	-1.69	-1.78	1.4	6.7
QSCAT sub. (87 scenes)	-1.70	-1.10	1.8	-34.7
QSCAT NS (87 scenes)	-1.65	-1.80	0.8	7.8
SAR 600 m	-0.99	-0.99	-41.0	-40.5
SAR 1.5 km	-1.10	-1.15	-34.0	-31.0
SAR 3 km	-1.32	-1.35	-21.0	-19.0
SAR 15 km	-1.48	-1.47	-11.0	-12.0
SAR 25 km	-1.40	-1.18	-16.0	-29.0

Stoffelen, A., J. Vogelzang, and A. Verhoef (2010), Verification of scatterometer winds, *10th International Winds Workshop*, Tokyo, Japan, 20-26 February 2010, EUMETSAT P.56. Available from `http://www.eumetsat.int/Home/Main/AboutEUMETSAT/Publications/ConferenceandWorkshopProceedings/2010/SP_20101122112352839`.

Vincent, C. L., P. Pinson, and G. Giebel (2010), Wind fluctuations over the North Sea, *Int. J. Climatol.*, , XXX–XXX.

Vogelzang, J., A. Stoffelen, A. Verhoef, and J. Figa-Saldaña (2011), On the quality of high-resolution scatterometer winds *J. Geophys. Res.*, *116*, C10033, doi:10.1029/2010JC006640.

Winkle, C.K., R.E. Milliff, and W.G. Large (1999), Surface wind variability on spatial scales from 1 to 1000 km observed during TOGA COARE, *J. Atm. Sc.*, *56*, 2222–2231

Xu, Y., L-L. Fu, and R. Tulloch (2011), The global characteristics of the wavenumber spectrum of ocean surface wind, *J. Phys. Oceanogr.*, *41*, 1576–1582, doi:10.1175/JPO-D-11-059.1

Zecchetto, S., and F. De Biasio (2003), Wavenumber spectra of the Mediterranean sea winds derived from the NASA QuikSCAT data, *Geoscience and Remote Sensing Symposium, 2003. IGARSS '03. Proceedings. 2003 IEEE International*, 1907–1909, doi:10.1109/IGARSS.2003.1294289.

I. Karagali, DTU Wind Energy, Technical University of Denmark, Risø Campus, Building 125, Roskilde, 4000, DK. (ioka@dtu.dk)

X. Guo Larsén, DTU Wind Energy, Technical University of Denmark, Risø Campus, Building 125, Roskilde, 4000, DK. (mebc@dtu.dk)

M. Badger, DTU Wind Energy, Technical University of Denmark, Risø Campus, Building 125, Roskilde, 4000, DK. (mebc@dtu.dk)

A. Peña, DTU Wind Energy, , Technical University of Denmark, Risø Campus, Building 125, Roskilde, 4000, DK. (aldi@risoe.dtu.dk)

C. B. Hasager, DTU Wind Energy, Technical University of Denmark, Risø Campus, Building 125, Roskilde, 4000, DK. (cbha@dtu.dk)

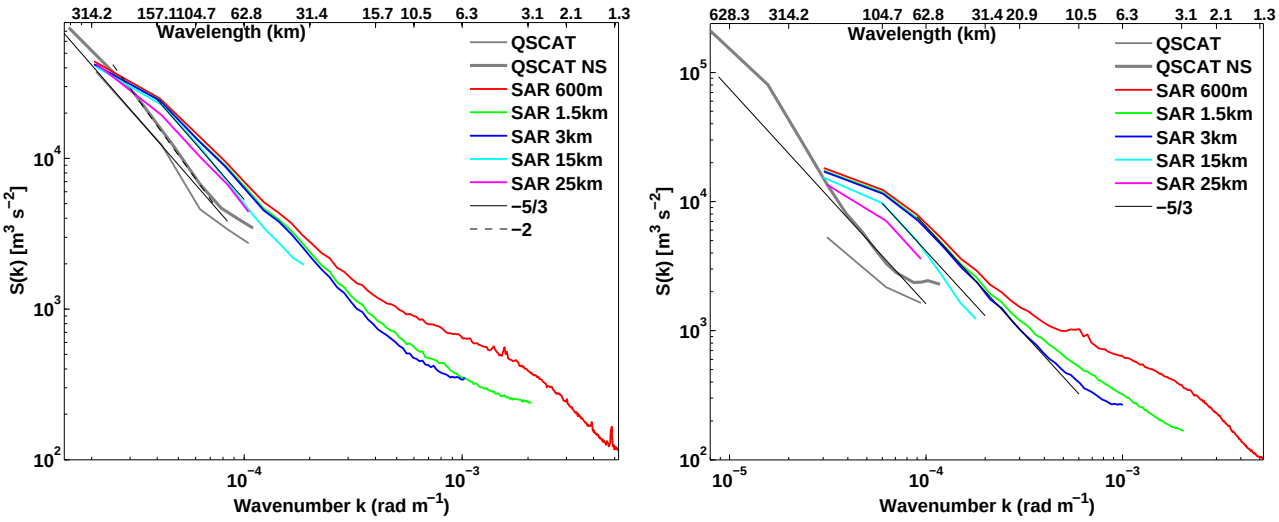

Figure 2. Averaged meridional (left) and zonal (right) spectra from SAR of various resolutions and QuikSCAT. Black lines show the -5/3 (solid) and -2 (dashed) slopes.

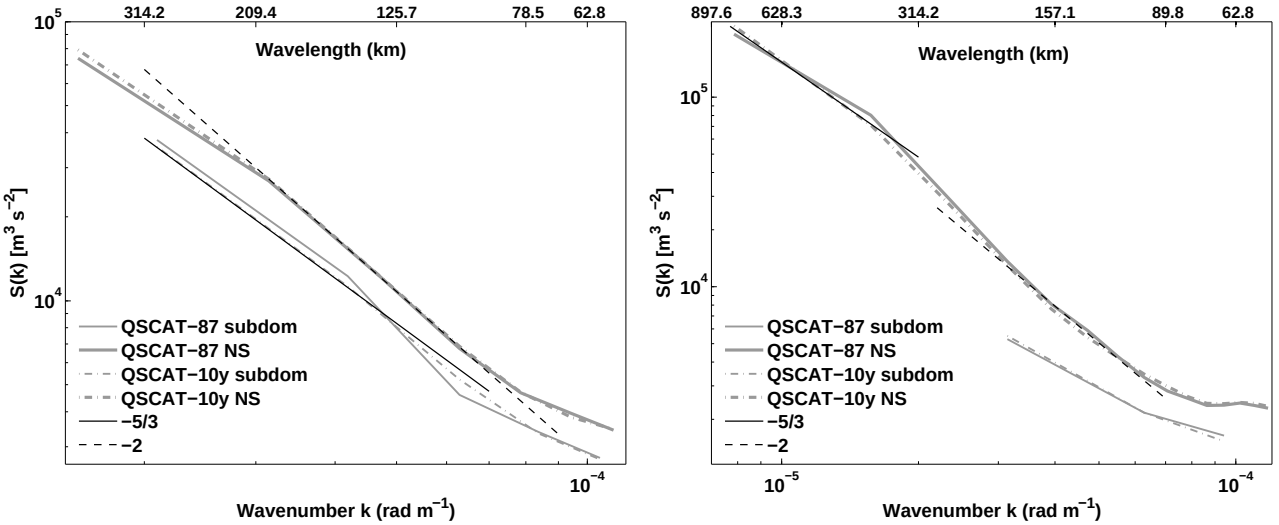

Figure 3. Averaged meridional (left) and zonal (right) spectra from QuikSCAT 87 scenes vs. QuikSCAT 10 years. Black lines show the -5/3 (solid) and -2 (dashed) slopes.

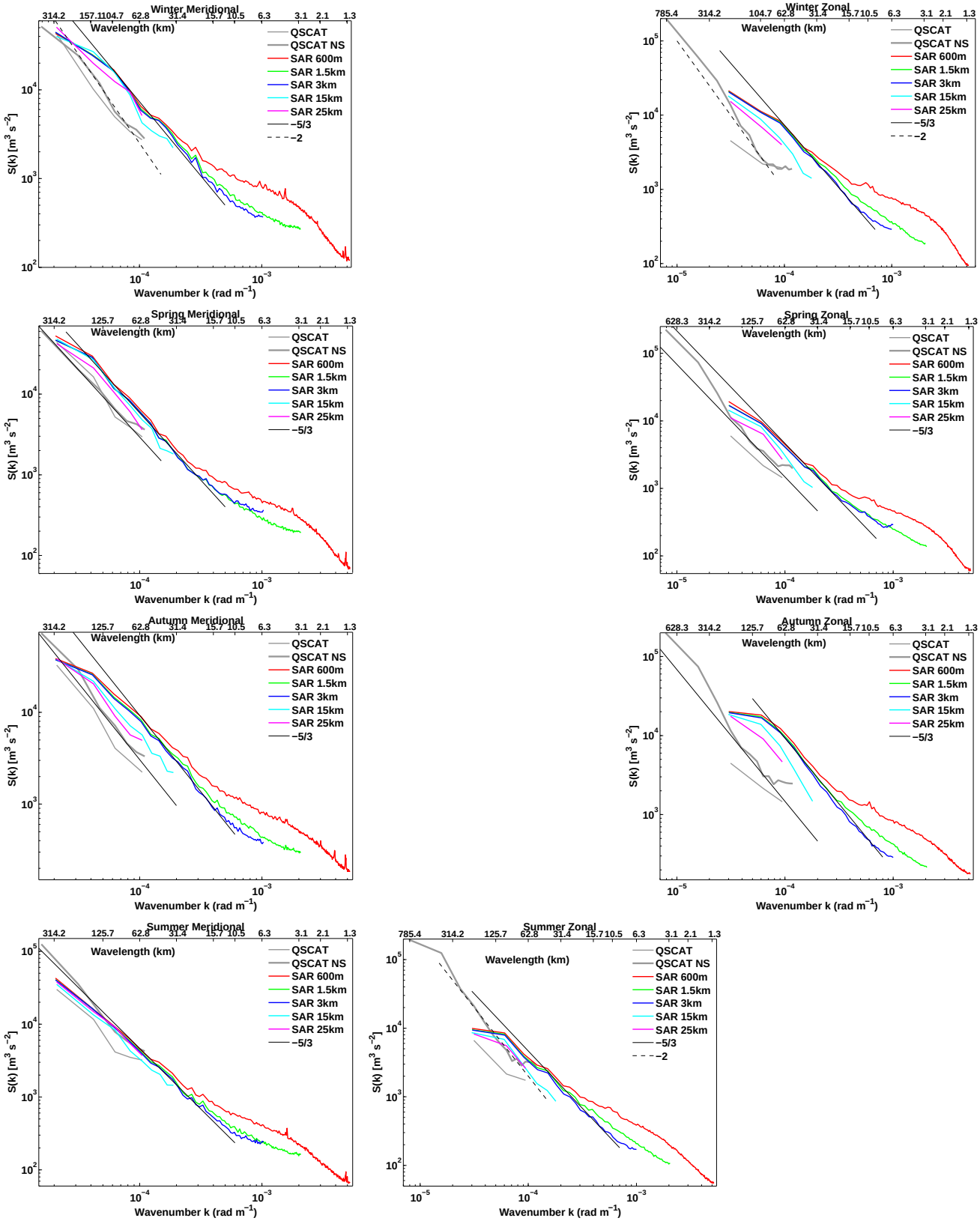

Figure 4. Seasonally averaged meridional (left) and zonal (right) spectra for i) winter, ii) spring, iii) summer, iv) autumn. Gray dashed curves show the -5/3 slope.

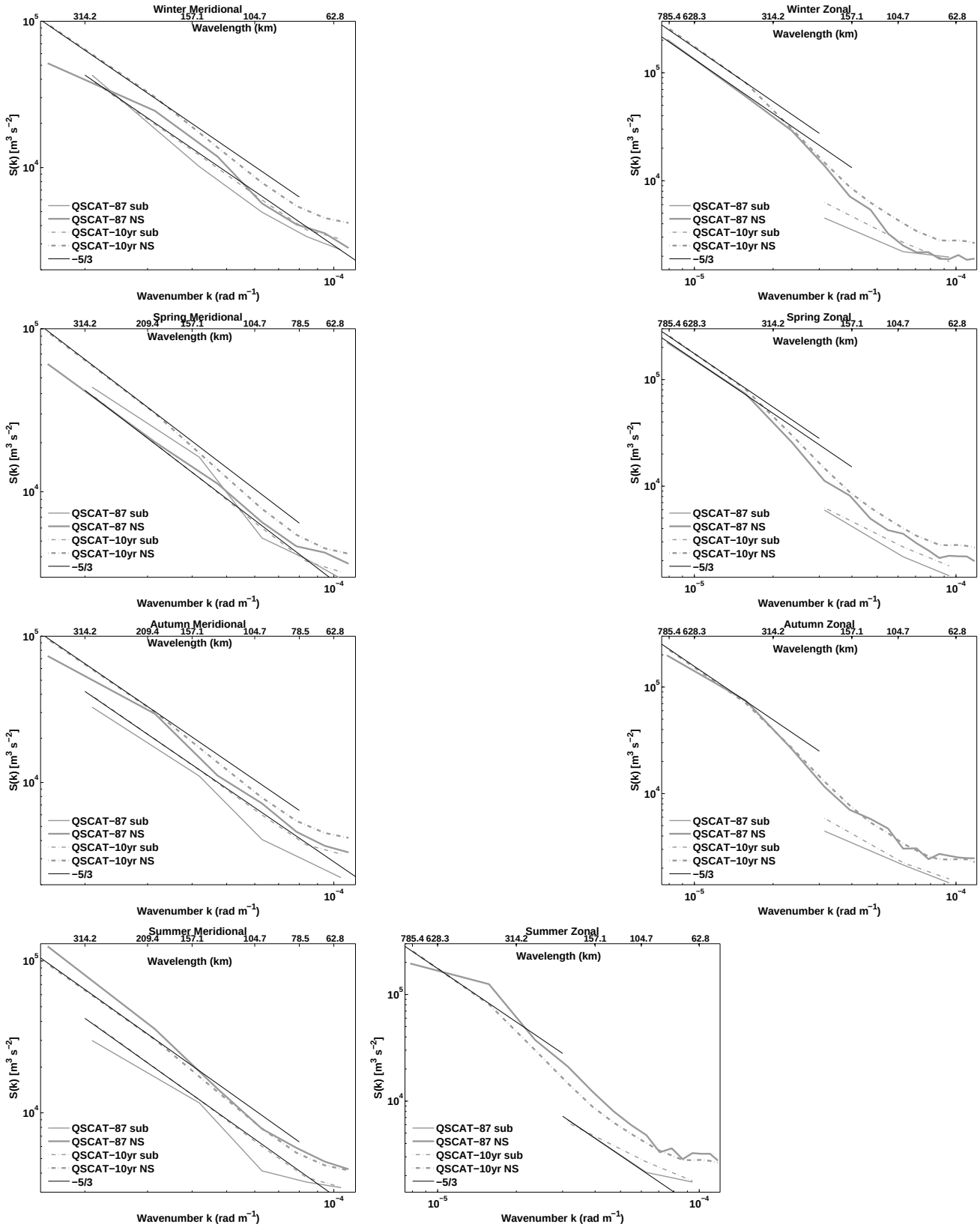

Figure 5. Seasonally averaged meridional (left) and zonal (right) spectra for i) winter, ii) spring, iii) summer, iv) autumn from QuikSCAT 87 scenes vs. 10 years.

Paper IV

SST diurnal variability in the North Sea and the Baltic Sea

SST diurnal variability in the North Sea and the Baltic Sea

Ioanna Karagali[a,b,*], Jacob L. Høyer[b], Charlotte B. Hasager[a]

[a] *Wind Energy Division, Risø National Laboratory for Sustainable Energy, Technical University of Denmark, Frederiksborgvej 399, Building 125, DK-4000, Roskilde, Denmark*
[b] *Polar Oceanography, Centre for Ocean and Ice (COI), Danish Meteorological Institute (DMI), Lyngbyvej 100,2100, Copenhagen Ø, Denmark*

Abstract

Five years of sea surface temperature (SST) retrievals from a geostationary platform are utilised to identify and characterise diurnal warming in the North and Baltic Seas. Observations from the Spinning Enhanced Visible Infrared Imager (SEVIRI) on board the Meteosat Second Generation satellite are proven valuable for quantifying the daily SST cycle in shallow and coastal waters at latitudes 48-60°N. Satellite minus in situ observations from moored buoys show biases ranging from -0.3 K to 0.1 K. A thorough analysis is carried out to obtain the optimal reference field used for calculating the daytime temperature anomalies. The best night-time reference field candidate is demonstrated to be an average of 3 days of satellite observations from local midnight to 0300. When compared against night-time in situ measurements from various locations, mean biases are found in the order of ±0.1 K and standard deviation (σ) between 0.4 K and 0.9 K. The 5 year record with daytime temperature anomalies is used to derive robust statistical description of duration, spatial extent, proximity to coast and water depth of the diurnal warming events. Seasonal and inter-annual variations in the diurnal warming are also quantified. Daytime anomalies exceeding 2 K are identified during the spring and summer months of every year, peaking at 1500 LT. Events with daily anomalies exceeding 5 K are observed. Areas where diurnal variability is often observed coincide with areas of frequently observed low winds and turbid waters (high $K_{d(490)}$ values).

Keywords: SST, diurnal warming, SEVIRI

1. Introduction

The temperature of the sea surface has been identified as an important parameter, governing processes that occur in the upper ocean. Biological activity, exchange of gas, heat and momentum with the atmosphere depend on this oceanic layer and its properties. Activities of scientific, commercial and social interest, such as weather forecasting, modelling of air-sea interactions, climate change studies, fisheries and coastal zone management, require information about the sea surface temperature (SST) in order to be more accurate and effective.

A significant percentage of the incoming solar radiation is absorbed by the top few meters of the ocean surface, increasing the temperature in a manner that depends on the daily solar cycle. Lack of wind prevents mixing of the water column, resulting in the formation of a surface thermal layer (Price et al., 1986).

The peak temperature difference between night and day may exceed three degrees (Gentemann et al., 2008; Merchant et al., 2008) depending on the location and environmental conditions. It may temporarily affect air-sea interactions by altering the heat and gas fluxes, atmospheric circulation and the height of the atmospheric boundary layer.

Diurnal warming of the surface layer was identified during early in situ studies, such as Stommel et al. (1969) and Kaiser (1978). It has been observed in different areas of the global ocean including the Mediterranean (Deschamps et al., 1984; Merchant et al., 2008), western North Atlantic (Cornillon et

*Corresponding author
Email addresses: ioka@risoe.dtu.dk (Ioanna Karagali), jlh@dmi.dk (Jacob L. Høyer), cbha@risoe.dtu.dk (Charlotte B. Hasager)

al., 1985; Stramma et al., 1986; Price et al., 1987), the Gulf of California (Flament et al., 1993; Ward, 2006) and various locations in the global ocean (Otobe et al., 1985; Stuart-Menteth et al., 2003, 2005; Gentemann and Minett, 2008) using combinations of in situ and satellite observations.

The first studies on diurnal warming were mainly focused on low latitude regions but recent studies have demonstrated diurnal warming at mid-latitudes (Gentemann et al., 2008). Recently, Eastwood et al. (2011) identified diurnal warming events in the Arctic on June and July of 2008. Merchant et al. (2008) stated that the magnitude and spatial distribution of diurnal warming events depend on local conditions and are affected by wind, cloud coverage and water turbidity.

The present paper aims at the long-term characterization and quantification of the daily SST variation in the North Sea and the Baltic Sea. The coastal areas surrounding the two basins are densely populated and the seas experience large spatial gradients in properties such as salinity and turbidity and are characterised by relatively small depths; on average 90 meters for the North Sea and 55 meters for the Baltic Sea. The North Sea has an area of approximately 750000 km^2, salinity varying between 34‰ and 35‰ and is connected to the south with the Atlantic Ocean through the English Channel.

The northern North Sea is open to the eastern part of the North Atlantic Ocean. On the east, it connects with the Baltic Sea through Skagerrak, Kattegat and the Danish straits. The circulation is tidally dominated with tidal amplitudes exceeding several meters in many areas. The Baltic Sea, with an area of 337000 km^2, is a semi-closed, brackish basin with salinity varying between 6‰ and 15‰, receiving the outflow of some of Europe's largest rivers. There are practically no tidal variations in the Baltic Sea, where the largest constituents have amplitudes smaller than 10 cm. Both the North Sea and Baltic Sea basins are located well within the North Hemisphere storm track and experience wind and pressure induced surges.

To study the daily SST variations in this region, 5 years of hourly satellite observations from the SEVIRI instrument, on-board a geostationary platform are utilised. Little has been done to quantify diurnal warming in these shallow waters but the high temporal resolution of SEVIRI provides a unique opportunity for a detailed investigation of diurnal warming events in coastal regions at latitudes up to 60°N. In addition, the long time series of SEVIRI now allows for detailed quantification of seasonal differences in diurnal warming events. The study will thus contribute to the understanding of the diurnal warming events in shallow and coastal seas and form the basis for incorporating these effects into atmospheric and hydrodynamic models.

This paper is organised as follows. A description of all data used in the present study can be found in Section 2 along with validation of satellite data against in situ observations. Section 3 presents the methodology used to generate the night-time reference fields that were used to estimate diurnal warming. All results regarding diurnal warming are presented in Section 4. The discussion can be found in Section 5, while conclusions derived from the present study are summarised in Section 6.

2. Data

2.1. In Situ Data

In situ temperature measurements are utilised for validation purposes. Temperature sensors at depths varying from 1 m to 10 m, from different platforms and buoys, exist at various locations in the North Sea and the Baltic Sea (Table 1).

MARNET Buoys. The German Marine Environmental Monitoring Network (MARNET) is a grid of monitoring buoys and platforms at various locations in the North Sea and the Baltic Sea (`http://www.bsh.de/en/Marine_data/Observations/MARNET_monitoring_network/`). For the purpose of the present study, temperature observations from nine stations are utilized. The locations of the platforms are shown in Figure 1.

Horns Rev Meteorological Mast. The meteorological mast (M2) operated by DONG Energy, was located north-west of the Horns Rev offshore wind farm, in the North Sea. A temperature sensor was located at 4 m below mean sea level. Observations were collected at 2 Hz and stored as 10 minute averages.

2.2. Satellite Data

SEVIRI (Spinning Enhanced Visible Infrared Imager), on board the MSG (Meteosat Second Generation) satellites, is an infra-red radiometer. The operating principle is to collect radiation from an

Table 1: Locations and description of platforms from where in situ observations were taken.

Name	Lat	Lon	Bathymetry	Sensor Depth	Period
Arkona Becken	54°53′ N	13°52′ E	45 m	2m, 5m, 7m	01/06/04 - 31/12/09
Darßer Schwelle	54°42′ N	12°42′ E	21 m	2 m, 5 m, 7 m	01/06/04 - 31/12/09
Fehmarn Belt	54°36′ N	11°09′ E	28 m	1 m, 3 m, 6 m	01/06/04 - 31/12/09
Kiel	54°30′ N	10°16′ E	13.5 m	0.5 m, 1 m, 2 m, 4 m, 8 m	01/01/05 - 25/12/09
Oder Bank	54°05′ N	14°10′ E	13.5 m	3 m	01/01/05 - 24/12/09
Nordseeboje II	55°00′ N	06°20′ E	42 m	4 m, 6m, 10m	01/01/05 - 27/12/09
Nordseeboje III	54°41′ N	06°47′ E	40 m	4 m, 6m, 10m	01/01/05 - 29/12/09
Deutsche Bucht	54°10′ N	07°27′ E	33 m	3 m, 6m, 10m	01/01/05 - 25/12/09
EMS	54°10′ N	06°21′ E	33 m	3 m, 6 m, 10 m	01/01/05 - 25/12/09
FINO-1	54°01′ N	06°35′ E	>26 m	3 m, 6 m, 10 m	01/01/05 - 25/12/09
M2	55°31′ N	07°47′ E		4 m	01/06/04 - 13/05/07

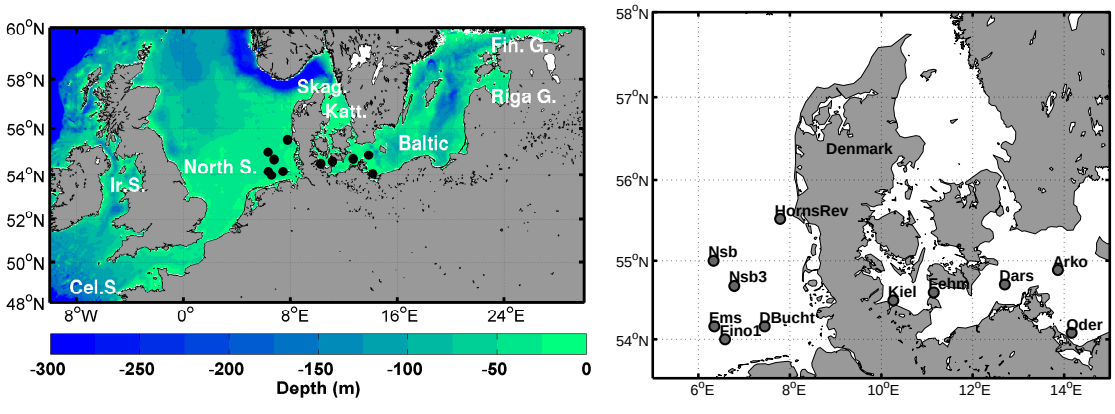

(a) (b)

Figure 1: a) Bathymetry of the area and b) locations of platforms and met. mast from where in situ measurements of SST are extracted. The area left of Denmark where most of the in-situ observing stations are, is also known as the German Bight.

Table 2: Validation of hourly SEVIRI observations with quality≥3, against in situ observations from the shallowest sensor of every location. Mean bias was defined as satellite minus in situ. N is the number of observations.

Name	Sensor Depth	Mean bias [K]	σ [K]	R^2	RMSE [K]	N
Arkona Becken	2 m	0.2385	0.7188	0.9832	0.7573	8675
Darßer Schwelle	2 m	0.2382	0.7888	0.9778	0.8239	8008
Fehmarn Belt	1 m	0.0259	0.7055	0.9806	0.7060	6515
Kiel	0.5 m	0.0886	1.1747	0.9540	1.1779	5771
Oder Bank	3 m	-0.0041	0.5985	0.9904	0.5984	2572
Nordseeboje II	4 m	0.0387	0.5035	0.9863	0.5048	1131
Nordseeboje III	4 m	0.0690	0.6291	0.9840	0.6327	1789
Deutsche Bucht	3 m	0.0031	0.5537	0.9860	0.5536	4002
EMS	3 m	-0.0718	0.5514	0.9852	0.5560	3924
FINO-1	3 m	0.2386	0.7197	0.9798	0.7580	1353
M2	4 m	0.1744	0.5951	0.9880	0.6200	2153

area using a telescope and focus it on detectors. These are sensitive to 12 bands of the electromagnetic spectrum (Aminou et al., 1997). The nadir sampling distance is 3 km for the near infra-red and infra-red channels. Due to the infra-red radiation's penetration depth, SEVIRI SST refers to the skin layer and retrievals are limited by cloud coverage. A flag ranging from 0 (unprocessed) to 5 (excellent) indicates the quality of the SST values, with 3 being acceptable.

The experimental SEVIRI product of CMS (Centre Météorologie Spatiale), Météo France is utilised from June 2004 to October 2009. This is different from the operational EUMETSAT OSI SAF product only in that it is hourly and mapped to a 0.05 degrees grid. Measurements are released hourly while the instrument scans from south to north every 15 minutes. The resolution in the area of interest, 48°S - 60°N and 10°W - 30°E, varies between 6 km and 8 km depending on latitude. For an average latitude of 50°, the grid cell dimensions are roughly estimated at 5.56 km∗3.2 km, covering an area of approximately 17.8 km^2 each.

To compare the spatial pattern of diurnal warming with occurrences of low winds, scatterometer measurements from QuikSCAT are used. Containing actual wind speed observations, the QuikSCAT product is considered appropriate for examining the spatial distribution of low winds. Modelled winds from global products may contain regional errors. At a height of approximately 800 km, completing each orbit in 100 minutes and observing a wide swath of 1800 km, QuikSCAT provided near-global coverage of the ocean surface, typically twice every day in the domain of interest. The mission description states that wind speed measurements in the range of 3-20 m s^{-1} have an accuracy of 2 m s^{-1} (`http://winds.jpl.nasa.gov/missions/quikscat/index.cfm`).

Daily gridded data from Remote Sensing Systems (RSS) are used, including two passes per day. Grid resolution is 0.25°, corresponding to a grid cell size of 16.83 km by 27.82 km for the domain of interest. Overpass time was approximately at 0600 and 1800 UTC, thus capturing early morning and evening conditions. Scatterometers are sensitive to rain because it changes the usual ocean surface and attenuates and scatters the radar energy at 13.4 GHz (Portabella & Stoffelen, 2001; Hoffman et al., 2005). RSS used contemporaneous microwave radiometer measurements for rain detection.

To evaluate the impact of the optical properties of water, a product from DMI is used. This is produced by an algorithm that was developed specifically for Case-II waters during the REgional VAlidation of Meris chlorophyll Product (REVAMP) project (Peters et al., 2005). Due to its regional character, it does not cover the entire domain, but extends only from 5°W to 26°E.

2.3. Validation of Satellite Data

To verify that SEVIRI SST is representative of the physical conditions in the area of interest, the hourly available observations with quality ≥ 3 are compared against in situ measurements from the shallowest sensors at various locations (Figure 1). Collocation criteria are set such that SEVIRI observations from the grid cell including the platform's location are used. Time collocation depends on the type of comparison; in situ measurements of the SEVIRI times are chosen when validating the satellite observations. For the night-time reference field comparisons, averaged in situ measurements corresponding to the averaged SEVIRI night-time measurements are used.

Biases do not exceed 0.24 K, while standard deviation (σ) ranges from 0.5 to 0.79 K (Table 2). An exception is found for the Kiel platform, where σ is 1.17 K. Correlation is high, with minimum R^2 values

Table 3: Description of parameters used for each one of the test reference fields.

Name	Averaged Days (Day±3days)	Night-time Temporal Window (LT)	Quality Flag
Ref1	7	0000-0300	3,4,5
Ref2a	7	0000-0400	3,4,5
Ref2b	7	0000-0400	5
Ref3	7	2200-0400	3,4,5
Ref4	7	0000-0600	3,4,5

of 0.954, for the Kiel platform, and maximum of 0.99.

Root mean square errors (RMSE) range from 0.5 to 1.18 K. The latter is a unique case for the Kiel sensor, that despite the very shallow depth (0 m) and the low mean bias (-0.08 K), has the highest σ (1.17 K) and lowest correlation (0.95). These comparisons are very good, considering the error from comparing spatially averaged to point measurements, depth sampling errors and biases introduced by the buoy locations (shallow, coastal areas).

When only anomalies between 0800 and 2100 local solar time (LST) are considered (not shown), mean biases increase in all cases but no more than 0.15 K. In general, biases do not exceed 0.38 K except for the Kiel platform (0.67 K). Nonetheless, correlation is high, with R^2 values ranging from a minimum of 0.947 to a maximum of 0.99.

3. Night-Time Reference Fields

3.1. Method

A representative night-time SST field is a requirement for determining diurnal variability. Various optimally interpolated fields from multiple sensors are easily available and frequently used. In the present study, we seek to generate night-time reference fields using SEVIRI observations to avoid errors introduced by multiple sensor biases. A sensitivity analysis was performed to conclude on the method applied to compose the daily reference fields.

To achieve minimum gaps in the composite fields, night-time observations from a certain number of days are aggregated. A preliminary analysis was performed, using 1, 2, 3, or 5 days. Other parameters that may influence data availability are the quality of observations and the night-time temporal window. A 3-day interval is the balanced choice between satisfactory data availability (not guaranteed with the 1 or 2 days intervals) and minimum averaging and blending of data. Thus, for every night-time reference field a total of 7 days of night-time observations are averaged in one single field.

For the night-time temporal window, different intervals are chosen considering the length of day during summer and winter. The quality of retrievals is allowed to vary between 3 (acceptable) and 5 (excellent). Five reference fields are composed for a test period from April to December 2006 with specifications shown in Table 3.

Validation fields are generated from the last pre-dawn values, where dawn is defined by computing the local sunrise time. The last SST value before local dawn is extracted in order to validate the different reference fields discussed above. Anomalies, defined as pre-dawn value minus reference fields, are estimated daily. Only the last pre-dawn quality 5 observation is utilised. The grid cell remains with no value in the case of lower quality retrieval. This criterion is set to ensure that anomalies are computed only utilising observations flagged as excellent.

Mean anomalies, shown in Figure 2a, range from a maximum of 0.8 K in favour of the reference field to 0.8 K in favour of the pre-dawn field. Most observed anomalies are between -0.2 and 0.1 K for all fields. Test reference fields utilising long night-time windows, i.e. 0000-0600 and 2200-0400 have most zero biases, as the pre-dawn value is included in the averaging for the reference field. Standard deviation (c), ranges between 0.2 K and 0.4 K with a peak at 0.3 K for most test fields.

The amount of valid observations used in the test reference fields is shown in Figure 2e, as the normalised percentage of maximum possible water pixels (74645), estimated as the number of grid cells covering water areas in the domain. Using only quality 5 observations for the night-time reference fields, significantly reduces data availability. Reference fields with six hours long night-time windows (2200-0400 or 0000-0600) show higher data availability more often than the ones with three (0000-0300) or four hours (0000-0400).

During the spring and summer months, more than half of the maximum water pixels are observed for all test reference fields except the one with only quality 5 retrievals. For these latitudes, daytime during summer may persist as late as 2200 and start as early as 0330. Thus, for every calendar day, observations with quality 3, 4 and 5 from 0000 to 0300 LST from that day, the previous and future 3 days are averaged in one single field.

3.2. Validation Against In Situ Data

Previously, SEVIRI observations were validated against in situ measurements, showing low biases and high correlation. Biases can be introduced by the night-time reference fields thus validation is required again. Night-time in situ observations concurrent with the SST observations used for the reference fields are averaged in one single value. Nonetheless, no averaging over 7-day long intervals is applied to the in-situ observations, as when composing the night-time reference fields.

Mean biases, defined as SEVIRI reference fields minus in situ observations, are shown in Figure 2b. In seven of the eleven locations, mean biases range from -0.1 to 0.1 K, for depths down to 4 meters. Biases do not exceed 0.4 K even when in situ measurements from depths down to 10 m are utilised. An exception is again observed for the Kiel platform (black line), where biases are negative down to 4 m with a maximum of 0.6 K and positive at 8 m (0.1 K). Also, for the Fehmarn Belt (light green line), biases are in favour of the buoy for all depths but do not exceed 0.25 K.

The standard deviation in Figure 2d, ranges between 0.4 K and 0.9 K for all depths, in eight of the eleven locations. Exceptions are the Kiel and Darßer Schwelle platform (light blue line) platforms. In Kiel, minimum σ (0.9 K) is observed for the 0 m and 2 m depths and maximum (1.4 K) for the 8 m sensor. In Darßer Schwelle, σ increases from 0.85 K to 1.15 K with depth.

The correlation coefficient r, shown in Figure 2f, is minimum (0.965) for the Kiel 8 m deep sensor and maximum (0.995) for the Fino-1 3 m deep sensor. For most locations correlation decreases drastically for depths below 6 m while being maximum for depths between 1-3 m. In nine locations, r values ranged between 0.98 and 0.995 for all depths, indicating a very good correlation between satellite and in situ averaged, night-time observations.

It is shown that only with extended night-time windows and extended averaging intervals, complete reference fields may be composed. Given the risk of including seasonal trends, we minimize both parameters as much as possible. The produced night-time reference fields are self consistent and representative of the night time temperatures observed by in situ instruments. Thus, they provide a proper foundation temperature, i.e. free of diurnal warming (Donlon et al., 2007), for investigating diurnal variability from SEVIRI daytime observations.

4. Diurnal Warming

Hourly satellite SST anomalies are defined as quality 5 day-time measurement minus night-time reference field. They are counted for every grid cell from 0800 to 2100 LST. To evaluate the threshold above which a temperature anomaly will be considered as diurnal warming, the amount of pixels showing SST variation larger than 1 K, 2 K and 3 K was counted on a daily basis. To evaluate the horizontal extent of warming, events are defined as occasions where more than five neighbouring grid cells show anomalies larger than the defined threshold. Only grid cells with at least 365 quality 5 observations were included in all analyses, corresponding to at least one daily, quality 5 observation for a year. This threshold was determined from trials, in order to mask out grid cells with spurious SST values.

4.1. Diurnal Warming Signals

The monthly distribution of anomalies larger than 1 K, 2 K and 3 K is shown in Figure 3a. The period with highest amount of anomalies, independent of threshold, is between April and August. Numbers of observed anomalies show a strong dependence on threshold. More than 25% of the available quality 5 observations exceed 1 K in June and July. Only 6% of the total available quality 5 observations exceeds 2 K and only 2% exceeds 3 K.

Considering the maximum biases and standard deviations from the SEVIRI validations discussed previously (Sections 2.3 and 3.2), the 2 K threshold is selected as a conservative threshold to define diurnal warming. By anomalies we refer to anomalies larger than this threshold for the rest of this study.

The temporal distribution of anomalies from June 2004 until October 2009 is shown in Figure 3b. The seasonal pattern is apparent, where most anomalies occur in the late spring (April and May) and early

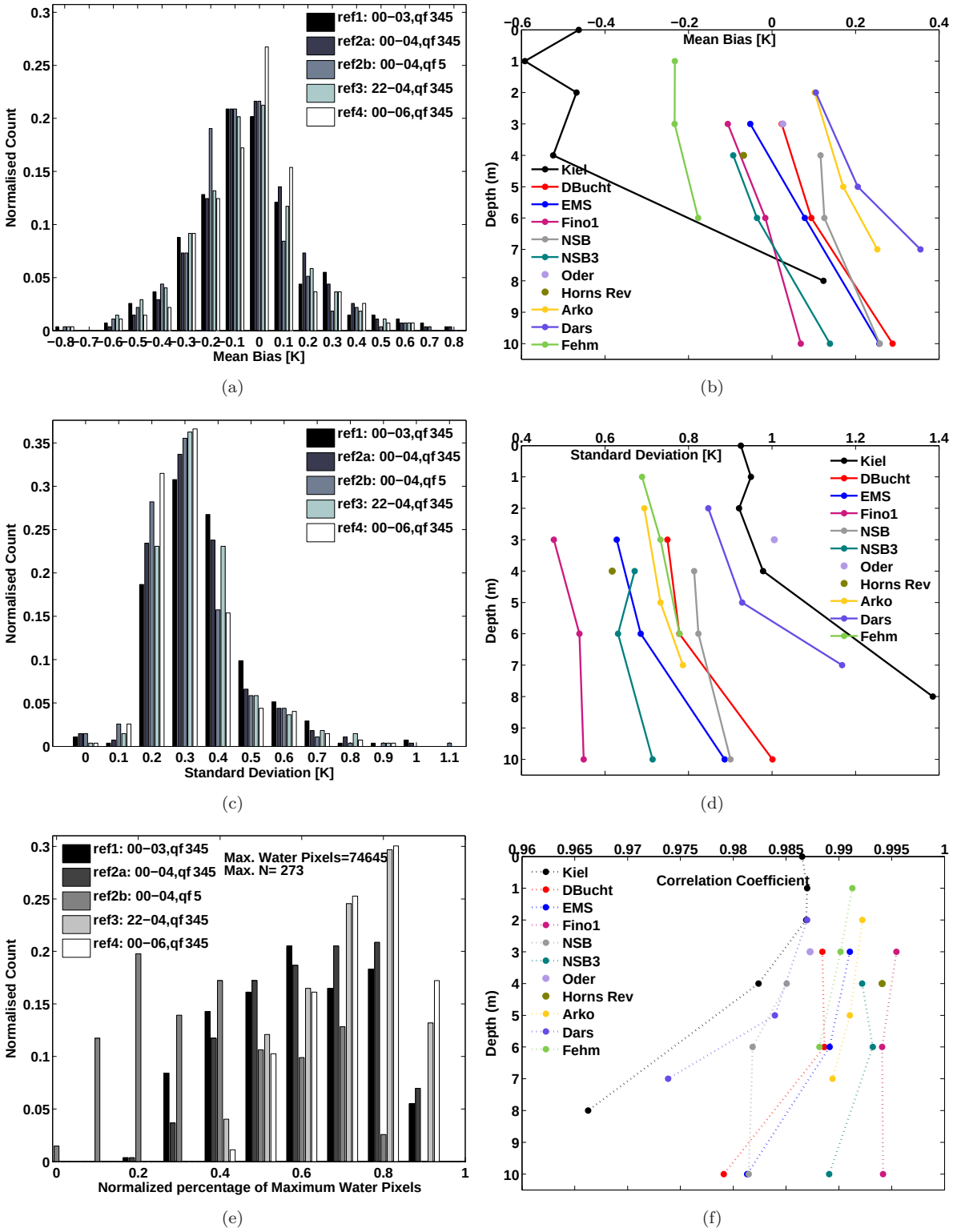

Figure 2: a, c) Mean bias and standard deviation of pre-dawn minus reference fields. e) Amount of valid grid cells in every reference field, all for the test period April-December 2006. b, d, f) Mean bias, standard deviation and correlation coefficient r for SEVIRI reference fields minus buoy temperatures from different depths.

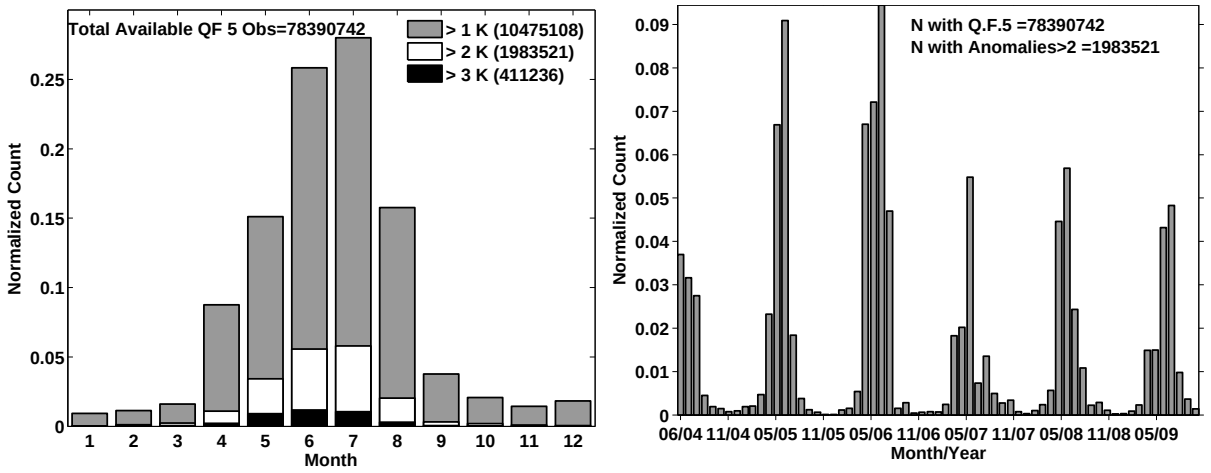

(a) (b)

Figure 3: a) Annual distribution of anomalies exceeding the threshold of 1, 2 and 3 K from June 2004 to October 2009 and b) temporal distribution of anomalies exceeding 2 K.

summer months (June and July) of every year. Significant inter-annual differences are also observed. In 2005, the majority of anomalies were observed as early as May and June, while in July of the same year observed anomalies were fewer even than in April. In particular, 2006 was a year with relatively high numbers of anomalies recorded consistently for 4 months, from April to July.

The averaged monthly variation of the diurnal cycle from March until August is shown in Figure 4, where dSST is the mean hourly difference from the night-time reference SST. The shape of the diurnal cycle is narrower in March, with a high, distinct peak occurring between 1200 and 1400 LST and a decrease starting from 1500 LST. Minimum values are observed around 0200 or 0300 while exceedances over 0.5 K are observed after 0700 LST.

During the transition from late winter to spring and early summer, the shape of the diurnal cycle becomes wider. Exceedances over 0.5 K start earlier; at 0500 LST in June. Maximum warming lasts until 1600 LST. Minimum values are observed earlier, around 0100, and are higher than earlier in the year. A decrease of maxima is observed during the transition from late winter to summer. Moreover, there is a difference of approximately 0.5 degrees between the start and end of the day, indicating that diurnal warming events are also associated with a general warming that persists to the following day.

4.2. Statistical Description

The duration of diurnal warming events is presented in Figure 5a. Warming lasts for a maximum of 3 hours for 75% of the observed cases. Nonetheless for 5% of them, warming lasts 7 hours or more. Short-lived anomalies of 1 hour occur for 41% of the observed cases. Examining the extend of warming, it is found that in 20% of the cases the grid cell showed an anomaly the next day also. Two days after only 10% persisted, while this level dropped to approximately 7.5% 3 days after and 5.5% 4 days after.

Figure 5b indicates that 99.9% of the observed maximum anomalies are below 6.4 K. For 25% of the cases, they exceed the 3 K threshold and approximately 5% of the cases exceed 4.1 K. The local time of maximum anomalies, shown in Figure 5c, is most frequently between 1400 and 1700, with a maximum at 1500. A 5% of the maximum anomalies occur later than 2000. These findings are consistent with results from Gentemann and Minett (2008), where daily maximum diurnal warming was found to peak between 1200 and 1600 LST.

The spatial extent of diurnal warming events, defined as the number of neighbouring grid cells showing anomalies, is shown in Figure 5d. A total amount of 7631 clusters of more than 5 grid cells is observed. The local extend of the DV events is evident from the figure where 75% of the events cover no more than 13 grid cells, corresponding to areas of approximately 231 km^2. For 5% of the observed warming events, the size is larger than 59 grid cells, approximately 1050 km^2. This corresponds to maximum length scales between 35 and 200 km. Merchant et al. (2008) identified diurnal warming events of length scales 40 km, routinely observable in SEVIRI SSTs. Gentemann et al. (2008) observed diurnal warming events with length scales approximately 1000 km.

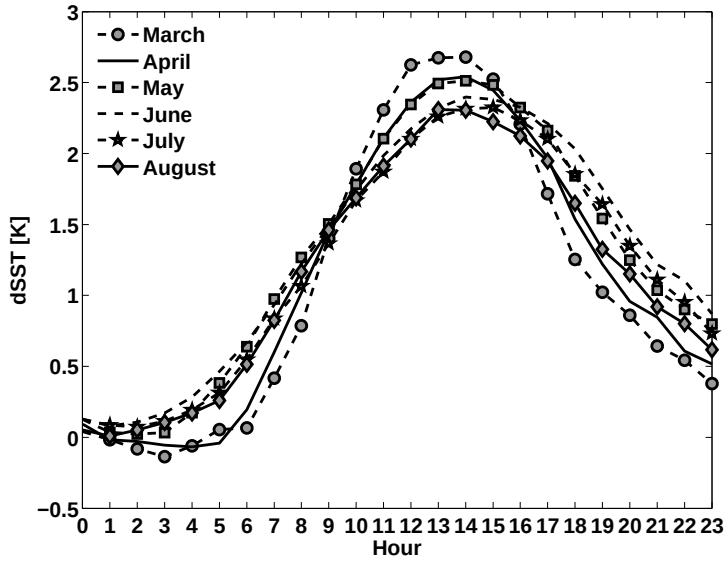

Figure 4: Inter annual monthly shape of the diurnal cycle, from 0000 to 2300 LST for the spring and summer months. Only grid cells showing anomaly > 2 K at least once a day are used. For those grid cells, all hourly values are used.

4.3. Spatial Distribution

The multi-year record of satellite observations provides solid statistics to investigate the spatial distributions of the diurnal warming events and their contributing factors. The spatial distribution of all quality 5 retrievals, from 0800 to 2100 LST is shown in Figure 6a. If all daytime hourly observations were of quality 5 every day, the maximum amount of observations in a given cell would be 25714. Recorded quality 5 retrievals reach a maximum between 2500 and 3000 for a small area of the Baltic Sea. Coastal areas and the North Atlantic, suffer from lack of excellent quality observations.

A significant reduction in data availability is observed below 50°N, due to the implementation of the Saharan Dust Index (SDI) flagging scheme applied from 2006 (LeBorgne, personal com., 2010). In general, the data availability is reduced in the North Sea compared to the Baltic Sea. The southern part of the English Channel also has a maximum of 2500 quality 5 retrievals. In the North Sea, the reduction in data availability has a strong South-East to North-West component.

The spatial distribution of diurnal warming exceeding 2 K (Figure 6b), indicates that high numbers of anomalies are mainly limited in semi-closed, shallow areas of the Baltic Sea; in the Gulfs of Riga and Finland, the south part of the basin and the Danish Straits where they may reach up to 3000 observations. In general, anomalies do not exceed 100 observations in the largest part of the domain. In most areas of the Baltic Sea, between 60 and 100 anomalies are observed.

In the North Sea, more anomalies are observed in the south-eastern corner of the basin and off the coast of Norway but the South-East to North-West data return pattern from Figure 6a is not recognised. The morphology of the German Bight area is characterized by shallow depths and lee-effects from adjacent land masses. More anomalies are recorded in the Irish and Celtic Seas and the central and eastern North Sea when compared to the North Atlantic.

Scatterometer observations of wind speeds lower than 5 m s^{-1} are shown in Figure 6c. Occurrences are high in the Baltic Sea, Kattegat, Skagerrak, the Irish Sea, the east coast of the British Isles, the south-eastern North Sea and the south-west coast of Norway. Areas close to coastlines are flagged due to the contamination of land in the backscattered signal, therefore information is not available for coastal areas of complex morphology, such as the Danish Straits. The very distinct feature with high values of low winds in the central part of the Baltic Sea is an artefact of the reduced data availability in the coastal areas of the basin. This is due to the winter sea ice mask provided by SSM/I, that only covers the central part of the Baltic Sea.

Some areas with frequent low wind observations coincide with areas of high numbers of observed SST anomalies. However, there are areas with high numbers of observed low winds, especially in the western North Sea, where almost no warming is observed. This discrepancy may reflect the complex nature of DV events where low winds are only one of the requirements for warming.

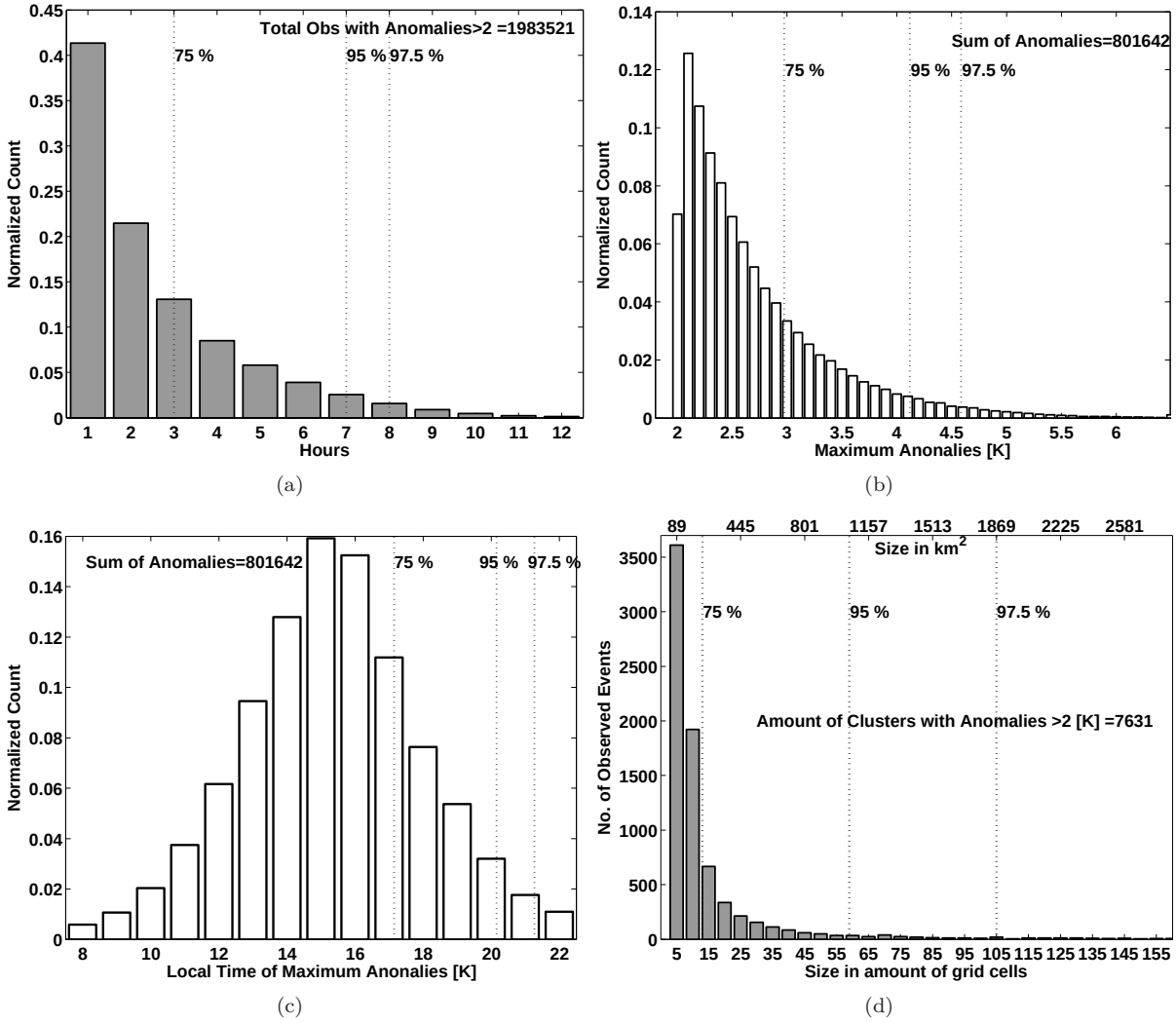

Figure 5: (a) Duration of DW, in hours from 0800 to 2100 LST. (b) Distribution of maximum anomalies scaled to 99.9 percentile and (c) local time of occurrence. (d) Distribution of warming events defined as clusters of 5 (or more) neighbouring grid cells.

It can also be an artefact of the QuikSCAT physical product; the equivalent neutral wind, referring to neutral atmospheric stratification. Due to the atmospheric stability scatterometer winds may be biased towards higher/lower wind speeds. Especially during spring and early summer, frequent stable conditions will lead to an underestimation of QuikSCAT winds.

Another parameter that has been speculated to have importance for DV events is the diffuse attenuation coefficient at 490 nm, $K_{d(490)}$, which is shown in Figure 6d. High values promote diurnal warming because of the increase in solar absorption in the upper layers. The mean $K_{d(490)}$ in the figure indicates very turbid waters in areas with increased diurnal warming observations. An exception is found at the South-East coast of the British Isles, where relatively high $K_{d(490)}$ are observed but no warming occurs.

Even though observations only cover 2009, the spatial extend of high $K_{d(490)}$ values in not expected to exhibit high inter annual variability. There is a difference between the average $K_{d(490)}$ values found in Merchant et al. (2008) and in the present study, of the order of 0.2 m^{-1}. In the former study, $K_{d(490)}$ has been estimated based on Case-I waters representative of open ocean, while in the present study the product used corresponds to Case-II waters.

Due to the shallow coastal nature of the study region, it is interesting to examine how the diurnal warming events are distributed in relation to the water depth and distance to the coast. These dependencies are estimated separately for the North and the Baltic Sea, with the meridian of 9°E as the divider. The separation is performed due to significant differences in observed anomalies, mean $K_{d(490)}$ values and lee effects. Figure 7a shows that in general, more anomalies are observed in the Baltic compared to the

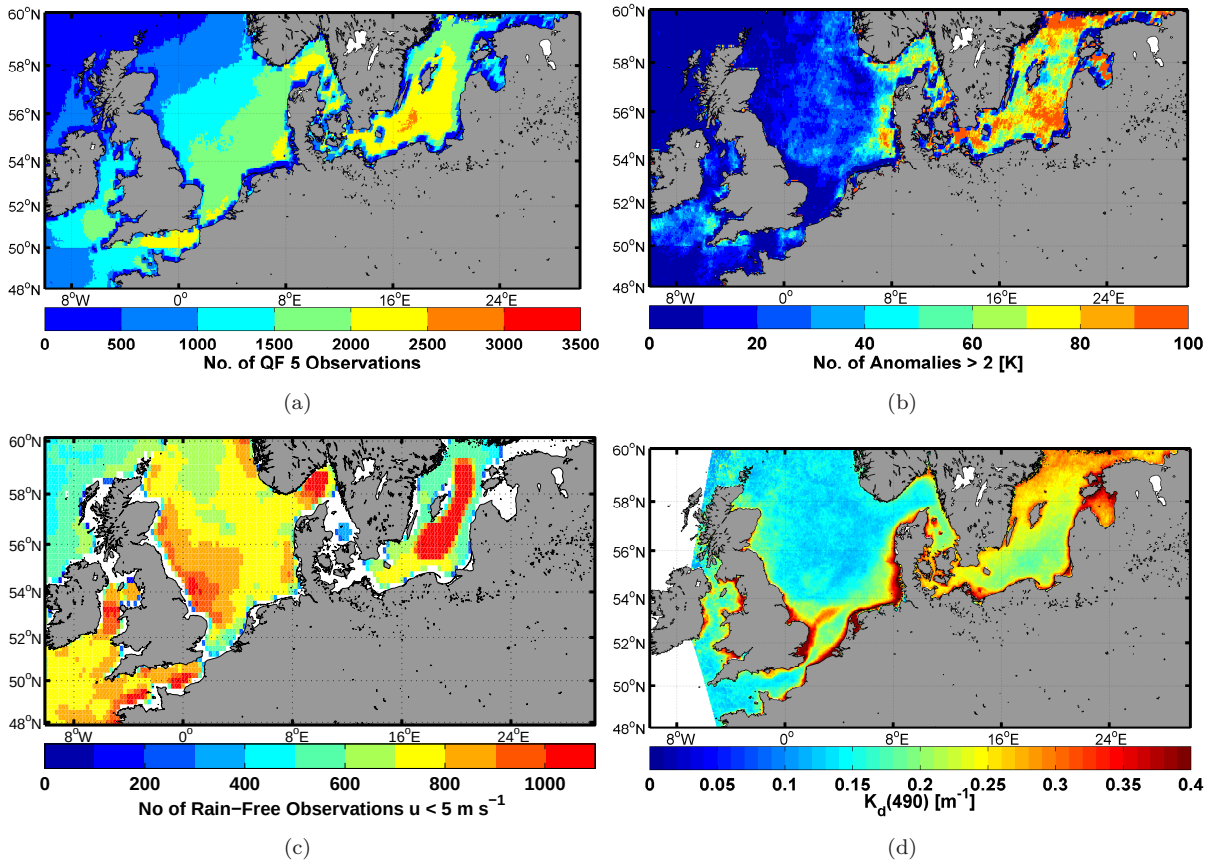

Figure 6: Spatial distribution of (a) quality 5 observations (SEVIRI), (b) anomalies greater than 2 K (SEVIRI), (c) wind speed < 5 m s^{-1} (QuikSCAT), all from 06/2004 to 10/2009. d) Mean diffuse attenuation coefficient at 490 nm (DMI) from 01/2009 to 12/2009.

North Sea. Most anomalies are observed for depths up to 200 m, similar with findings from Eastwood et al. (2011). The most typical depths for observed diurnal warming events are between 20 m and 40 m. Given the typical values of $K_{d(490)}$, shown in Figure 6d, light is not expected to reach down to depths of 20 m. Therefore, light reflection from the sea bed is not believed to contribute significantly to diurnal warming occurrences.

The occurrence of near-coastal diurnal warming events is shown in Figure 7b, which shows the number of anomalies as a function of distance to the nearest coast. In the North Sea (dark grey), most observations are recorded within the first 5 km from the coast, decreasing to zero observations 300 km offshore. In the Baltic Sea (light grey), most anomalies are observed within the first 10 km from the coast, while no anomalies are recorded further than 120 km offshore. In general both figures demonstrate the conditions of the coastal and shallow seas, where 75 % of the anomalies are from depths shallower than 90 m (80 m) in the North Sea (Baltic Sea) and within 125 km (45 km) from the coast.

Regarding the distribution of quality 5 observations depending on the bathymetry and distance to land (not shown), it is found that while the shape of the distributions is similar, anomalies are almost double for depths up to 20 m especially in the Baltic Sea. When the distance to coast is concerned, this feature is even more prominent with almost 10 times more anomalies being observed in the first 10 km in both basins. Moreover, within the first 5 km from land, the number of observed quality 5 retrievals is very low signifying a buffer zone along the coastlines where land contamination is important.

4.4. Vertical Extend

So far, we have attempted to quantify diurnal warming utilising SEVIRI observations and to examine the frequency of such events, their spatial and temporal distribution and dependence on other physical parameters and factors. Given the fact that diurnal warming does occur, it is also relevant to examine its vertical extend.

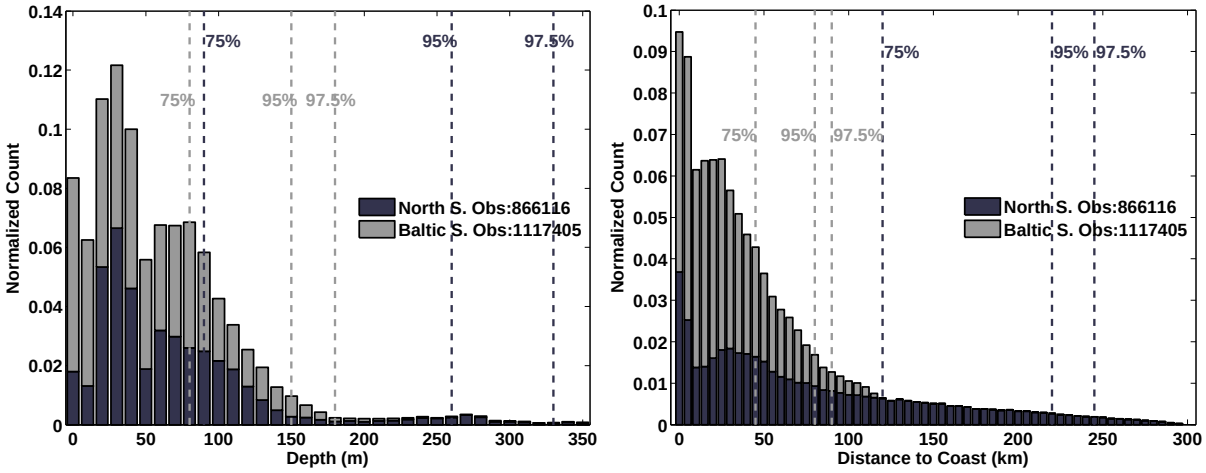

(a) (b)

Figure 7: Distribution of anomalies larger than 2 K according to (a) depth and (b) distance to the nearest coast, for the North Sea and the Baltic Sea.

To examine the relationship between diurnal warming, heat and momentum fluxes and the simplified vertical extend of diurnal warming, the period from March to August 2009 was selected. Numerical Weather Prediction model fields from The High Resolution Limited Area Model (HIRLAM) model are used to derive the hourly wind speed at 10 meters above the surface and estimate the net heat flux. The HIRLAM model is developed by several European meteorological institutes and has a spatial resolution of 3 km (Mahura et al., 2005).

The averaged monthly shape of the diurnal cycle from March to August of 2009 is calculated from days when SEVIRI observations indicate anomalies larger than 2 K. Hourly anomalies are averaged over the entire domain and then averaged to a daily value. Results are shown in Figure 8 for (a) net heat flux Q, (b) SST and (c) wind.

The distribution of Q during the day becomes wider from March to July, indicating increased heat input for longer periods of the day. Maximum values increase from 450 W m^{-2} to 750 W m^{-2}, observed in June. Moreover, Q becomes positive later in the day in March when compared to June, with approximately a phase shift of 3 hours. At the end of the day, when Q becomes negative again, the phase shift is almost half, 1.5 hours difference between March and June.

The diurnal shape of SST follows very closely the one of Q, peaking with a lag of 2 hours. Surprisingly, maximum temperature anomalies are observed in March (2.55 K) but in June they are only 0.16 K lower. The warm layer formed during daytime does not collapse until 2300. Warming persists even 5 hours after Q has turned negative and that is observed for all months.

The distribution of wind is variable; March has the highest values and the diurnal cycle shows variability during daytime of no more that 0.4 m s^{-1}. All other months indicate a more expected pattern with generally decreasing wind from early morning to mid-day and an increase towards the afternoon.

The hourly variation of cloudy grid cells with warming >2 K at least once per day and with no warming more than 1 K is presented in Figure 8d. The normalized counts are estimated based on the total number of grid cells with at least one hourly dSST<2 K and total number of grid cells with dSST less than 1 K, correspondingly. While the daily variation of cloudy conditions in the grid cells with no warming is relatively constant, this is not the case for the grid cells with warming. Cloudy conditions show a decrease after 10:00 or 11:00 depending on the month, a minimum around 16:00 and a relatively fast increase in the post-warming hours.

Based on the hourly temperature and net heat flux values, a simplified 1-D temperature equation can be applied in order to obtain a crude estimate for the penetration depth, as in Price et al. (1986).

$$D_P = \frac{Q}{\rho_0 c \partial T'_s / \partial t} \tag{1}$$

Q denotes the surface value of the heat flux, T' is the temperature anomaly, t is time, ρ_0 is the density and c the heat capacity of sea water. The equation assumes that the heat is evenly distributed in the upper layer, neglects the contributions from advection and assumes temporal collocation of Q and T'_s.

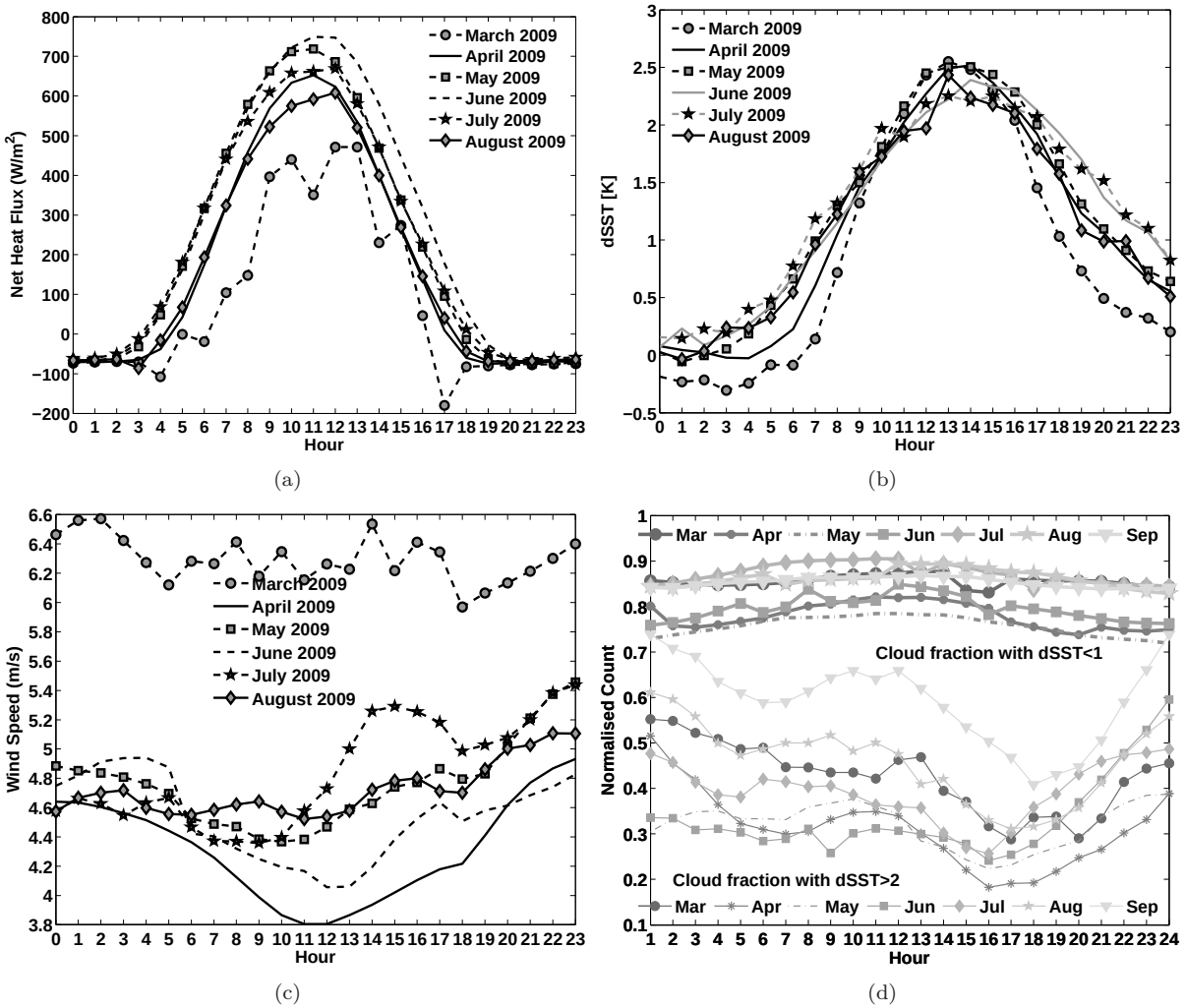

Figure 8: Average monthly shape of the diurnal cycle of (a) net heat flux from HIRLAM (b) SST from SEVIRI and (c) wind from HIRLAM from March to August 2009 (inclusive). Only grid cells that show anomaly > 2 at least once per day are used and all hours of the day are selected for those grid cells. (d) Cloud fraction for the grid cells with dSST>2 K at least once per day (thin lines) and with dSST<1 K (thick lines).

As the peak diurnal variability has a phase lag when compared to the net heat flux, Equation 1 can not be applied as such. Therefore, we estimate the daily penetration depth for the time when the maximum anomaly is observed, using the integrated heat flux from 0300 LST until the time of maximum anomaly.

Figure 9a shows the variation of monthly averaged D_P, from February to December 2009. D_P values almost double from March (0.6 m) to April (1.2 m) while they decrease almost to half from August (1.4 m) to September (0.8 m). The maximum penetration depth is observed for June, reaching down to 1.8 meters. For a change in Q of approximately 50 W m^{-2} and no practical change in dSST, D_P increases by 0.3 m from May to June.

The large seasonal change in the penetration depths can not be fully explained by seasonal variations in the heat flux, wind patterns or the turbidity of the water. If we assume that refracted light travels 2 m in the water column we can estimate the vertical distance it reaches for seasonally varying solar elevation angles. This depends on the location, thus we select a point in the centre of the domain, with co-ordinates 55°N, 4°E.

Figure 9b shows the estimated depth for the specific location as a function of the months. The variability is remarkably similar to the modelled D_p but there is a difference in the amplitude. Minimum values never drop below 1.3 m in December while maximum values exceed 1.6 m in June. These results indicate that the seasonal changes in solar elevation angles may play a role for the heat distribution in mid and high-latitude diurnal warming events.

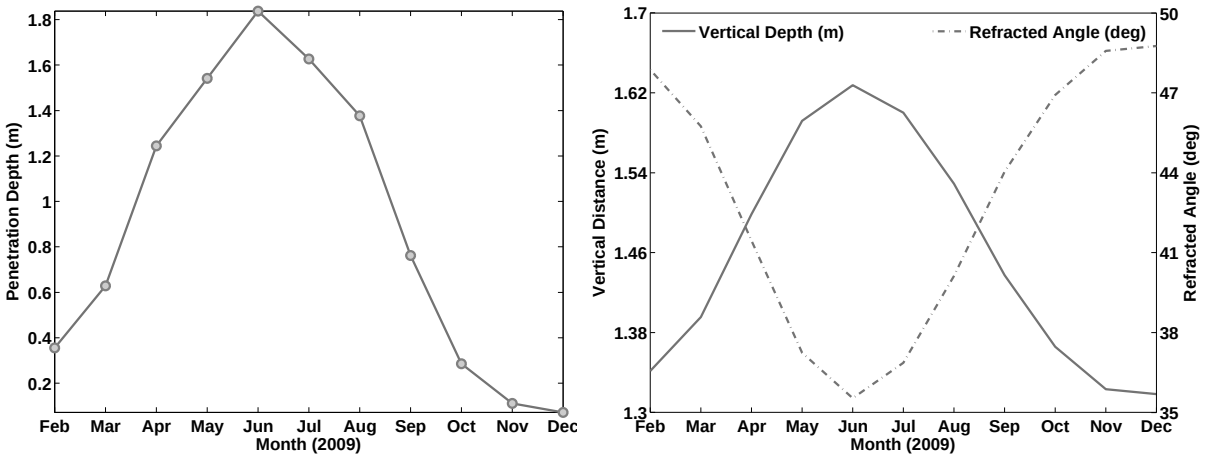

(a) (b)

Figure 9: a) Averaged monthly penetration depth from February to December 2009. b) Average monthly values of penetration depth of light (dashed), depending on solar elevation and accounting for defraction (dotted). Estimated for 55°N, 4°E assuming a constant distance of 2 m in the water column.

5. DISCUSSION

Current findings regarding the amplitude, peak timing, seasonality and spatial extend of diurnal warming are in very good agreement with results from previous studies (Deschamps et al., 1984; Cornillon et al., 1985; Flament et al., 1993; Stuart-Menteth et al., 2003; Gentemann et al., 2003; Gentemann and Minett, 2008; Gentemann et al., 2008; Merchant et al., 2008; Eastwood et al., 2011).

The observations from a geostationary satellite like MSG have a resolution that depends on latitude. The North Sea and the Baltic Sea are located relatively north, where the SEVIRI viewing angle is large and the resolution is severely demised. Despite that, it is shown that SEVIRI hourly observations can be valuable and very useful for studying the diurnal variability in detail at these latitudes.

Biases are generally low and correlation high, when hourly SEVIRI retrievals of quality 3-5 are compared against in situ observations from platforms and moored buoys. For the Kiel platform, the only one with a sensor at 0.5 meters, correlation against SEVIRI is lower than in all other cases, but it seems as a single case likely caused by its location in very shallow waters and very close to the coast. On average validation results of both the hourly SEVIRI fields and the night-time reference fields show a bias of 0.65 K when compared to in situ observations.

The good correlation between SEVIRI and in situ measurements is an encouraging result, considering the high latitudes and the moored buoys, which are generally considered to have higher errors than drifting buoys. Emery et al. (2001) found that in the extratropics moored SST buoys are 0.1°C colder than the drifting buoys. Brisson et al. (2002) reported a standard deviation of 0.5 K for SEVIRI. The results found here are in agreement with findings from Marullo et al. (2010), with reported annual biases between 0.4 and 0.9 K and σ of 0.4 $\pm$ 0.1 K.

Despite the positive validation results, the spatial distribution of in situ sensors available for comparison is limited to a small area of the North Sea and the Baltic Sea. Verification against Ferry Box data obtained by vessels sailing in larger parts of the domain, could prove valuable for the extended spatial validation required in such high latitudes. Unfortunately the low number of drifting buoys in this regions does not allow for comparisons.

Diurnal warming is defined given a known appropriate foundation temperature, representative of well mixed conditions. Foundation temperature fields from SEVIRI have been compared with night-time in situ observations and revealed biases around 0.1 K and σ that varies between 0.4 K and 0.9 K. These findings are in agreement with the low mean bias and σ of 0.5 K for night time conditions (LeBorgne et al., 2006). Small positive and negative biases are identified for depths down to 3 m, below which biases increase and become positive. This may be an indication for the existence of a near-surface layer where temperature is uniform. Marullo et al. (20007) find similar results in the Mediterranean Sea comparing Pathfinder SSTs and in situ of CTD and XBT measurements.

Constructing the optimal night-time reference field is a trade-off between accuracy and coverage.

Using retrievals with quality higher than 3 to compose the night-time fields may introduce biases but if only quality 5 retrievals are selected, there will be few information to compose the foundation fields. Averaging during night-time and for consecutive days to derive one foundation temperature field ensures some smoothing and elimination of such biases. Including more days in the averaging scheme may possibly give a more seasonal character to the night-time reference fields (see Knievel et al. (2010) for similar techniques and comparisons of composite MODIS fields with in situ observations).

On the other hand, the 3-day interval may be long enough, especially during summer in these latitudes, to preserve some residual warming in the reference fields thus biasing them towards daytime diurnal warming cases. The pre-dawn fields are generally colder than the reference fields, thus indicating that a small residual warming signal is included in the reference fields.

Diurnal warming is identified using quality 5 day-time observations, which may potentially reduce the number of observed anomalies. Moreover, erroneous cloud masking, as observed from the amount of available quality 5 retrievals and their spatial distribution, is present in coastal areas and that may also reduce significantly the number of anomalies.

There is also a significant dependence of the amount of anomalies on the threshold applied to define them, in particular a radical decrease for the 2 K threshold when compared to 1 K. Nonetheless, this threshold is selected considering the observed biases and standard deviations between satellite and in situ observations. A 2 K threshold thus gives a conservative number on the diurnal warming events and include very few erroneous DW identifications.

Stuart-Menteth et al. (2003) account for diurnal warming of more than 0.5°C. On the other hand Gentemann et al. (2008) observe events between 5 K and 7 K, Merchant et al. (2008) identify diurnal warming amplitudes greater than 4 K, routinely observable in SEVIRI SST. More recently, Eastwood et al. (2011) consider diurnal warming significant for peak amplitudes of 1 K or above. Considering the above, the authors believe that the 2 K threshold applied in the present study is reasonable and in context with current findings.

The duration of observed anomalies does not necessarily imply consecutive hours. Anomalies are counted for a relative extended day-time interval, from 0800 to 2100 LT, in order to accommodate for the length of daytime during boreal summer in these latitudes. However, essentially no anomalies last more than 8 hours. Similarly, Gentemann et al. (2003) report warming that starts at 0800, peaks around 1500 and decays until 2300 from TMI and AVHRR SSTs.

In the eastern North Sea, the increased number of anomalies can not be justified only by low winds. Other factors, such as water turbidity, may hold an important role (Dickey et al., 1982), in this region characterized by very turbid waters due to sediments from the large rivers outflowing in the German Bight. Merchant et al. (2008) found large diurnal variations in the North Sea related to increased chl-A concentrations and a strong influence of the optical attenuation coefficient, promoting diurnal warming. Moreover, Kahru et al. (1993) found that surface accumulations of cyanobacteria in the southern Baltic Sea caused a 1.5°C local increase of SST.

Areas of frequent low winds are larger and more abundant than areas with diurnal warming, especially in the North Sea. Moreover, relatively high $K_{d(490)}$ values are observed in areas with frequent low winds but no warming. Especially for the Western North Sea, quality 5 observations are also significant in numbers, therefore clear sky conditions are as often as in other areas where warming is observed. In such cases, it may be that coastal atmospheric circulations such as sea-land breeze systems occur in local scales and can not be captured by the scatterometer due to its spatial and temporal resolution. In addition, this is a region with very strong tidal currents, see eg. Davies and Furnes (1980), that may enhance the vertical mixing and prevent a diurnal warming layer to develop in the surface layer.

When evaluating the monthly shape of diurnal variability, all observed anomalies higher than 2 K are averaged, independent of location. Thus for months with few observations, the average diurnal variability curves has higher uncertainty. This may explain why the peak amplitude of diurnal variability is observed in March.

In addition, it is possible that the short life-time of conditions favourable for diurnal warming generates a very shallow layer within which heat is constrained, resulting in a sudden and dramatic increase of temperature. Moreover, the lower solar elevation angles lead to larger angles of refraction inside the water column. Thus the incoming light is absorbed in a shallower layer during winter and spring.

The residual warming observed from the monthly averaged diurnal variability cycles is a consistent feature, appearing at least from March to August. Its identification is important and highlights the need for such a feature to be included in diurnal variability models.

The assumption for synchronous increase of the net heat flux and temperature, required in order to

apply Equation 1 is not satisfied as seen from Figures 8a and 8b. The shape of the diurnal SST cycle is derived from observations while the one of net heat flux, from model outputs. These are not always expected to match, especially in the case where the NWP model does not include a scheme to account for diurnal warming. In addition, vertical diffusion of heat will introduce a lag between the surface heat flux and the upper ocean temperature.

Therefore, we chose to proceed with the estimation of a characteristic penetration depth by using the integrated heat flux from 0300 until the time of observed anomalies. One may argue that this is an oversimplified approach but it reveals a distinct seasonal pattern that may relate to the seasonal changes in solar elevation angles. The sensor depths for which the correlations between satellite and in situ observations are highest, range between 1 m and 3 m while maximum penetration depth is 1.8 m, when estimated from the 1-D heat equation and 1.65 m, when estimated from the solar elevation angle.

Stramma et al. (1986) state that under conditions that produce the largest surface warming, the trapping depth is about 1.5 m. A trapping depth of 0.68 m is reported in Flament et al. (1993), during a large event with amplitude of 6.6°C. Also, Kahru et al. (1993) stated that the vertical extension of the top diurnally heated layer was probably less than 1 m and definitely less than 5 m. Eastwood et al. (2011) used a constant value of 2 m for the depth of the warm layer. Considering the above, the authors believe that the present findings regarding penetration depth estimates are reasonable.

6. CONCLUSION

This study has shown that diurnal warming of the sea surface in latitudes above 48°N can be identified with the use of SEVIRI. It is found to occur in relatively high latitudes, up to 60°N, during the boreal spring and summer. Areas of most frequently observed warming events are characterized by generally shallow waters, complex coastal morphology and high water turbidity.

Night-time reference fields hold an important role in the definition of day-time warming. The performance of the reference fields is validated against in situ measured foundation temperatures in various locations, yielding very good results.

Diurnal warming exceeding 2 K was observed from April to August, mainly occurring from 1400 to 1600 local time. The maximum amplitude reached 6 degrees in a few cases. The horizontal extend of warming reaches 180 km^2 or more, and has a dependence on bathymetry and distance to coast.

The maximum amplitude of diurnal warming in this region is typically achieved with a phase shift of 2 hours, when compared to surface heat flux. The shape of the diurnal cycle varies seasonally, becoming wider from spring to summer. Estimation of corresponding penetration depths, showed maximum depths of 1.8 meters in June that rapidly decrease towards autumn.

The identification and quantification of diurnal warming events signifies their importance for relatively high latitudes and demonstrate that these effects should be included in regional high resolution hydrodynamic models.

SST diurnal variability can temporarily affect the stability of the lower atmospheric boundary layer. Such effects should be considered in applications ranging from operational weather forecasting to offshore wind energy, which is an important renewable energy resource for the European countries bordering with the North Sea and the Baltic Sea.

7. Acknowledgements

This study was partially funded by the EU NORSEWInD project (TREN-FP7EN-219048). SEVIRI data were processed by the Centre de Météorolgie Spatiale, Météo France for the EUMETSAT OSI-SAF project. Data from M2 are courtesy of Vattenfall and DONG Energy. QuikSCAT data obtained from Remote Sensing Systems (RSS). HIRLAM and $K_{d(490)}$ data obtained from the Danish Meteorological Institute (DMI). Data from the MARNET Monitoring Network are obtained from Bundesamt Für Seeschifffahrt und Hydrographie (BSH), Germany. The authors would like to thank the two anonymous reviewers for their valuable comments.

Aminou, D.M.A., Jacquet, B., & Pasternak, F. (1997). Characteristics of the Meteosat Second Generation (MSG) radiometerimager: SEVIRI. *Proc. SPIE 3221, 19*, 1997, doi:10.1117/12.298084

Brisson, A., Le Borgne, P., & Marsouin, A. (2002). Results of One Year of Preoperational Production of Sea Surface Temperatures from GOES-8. *Journal of Atmospheric and Oceanic Technology, 19*, 1638-1652.

Cornillon, P, & Stramma, L. (1985). The distribution of diurnal sea surface temperature events in the western Sargasso sea. *J. Geophysical Research, 90*, C6, 11811-11815

Davies, A. M., & Furnes, G. K. (1980). Observed and Computed M2 Tidal Currents in the North Sea. *Journal of Physical Oceanography, 10*, 237-257, doi: 10.1175/1520-0485(1980)010.

Deschamps, P. Y., & Frouin, R. (1984). Large Diurnal Heating of the Sea Surface Observed by the HCMR Experiment. *Journal of Physical Oceanography, 14*, 177-184

Dickey, T. D., & Simpson, J. J. (1983). The influence of optical water type on the diurnal response of the upper ocean. *Tellus B, 35B*, 142-154. doi: 10.1111j.1600-0889.1983.tb00018.x

Donlon C., Robinson, I., Casey, K.S., Vazquez-Cuervo, J., Armstrong, E., Arino, O., et al. (2007). The Global Ocean Data Assimilation Experiment High-resolution Sea Surface Temperature Pilot Project. *Bull. American Meteorological Society, 88(8)*, pp. 1197-1213.

Eastwood, S., LeBorgne, P., Préré, S., & Poulter, D. (2011). Diurnal variability in sea surface in the Arctic. *Remote Sensing of Environment, 115*, 2594-2602

Emery, W.J., Baldwin, D.J., Schlüssel, P., & Reynolds, R.W. (2001). Accuracy of in situ sea surface temperatures used to calibrate infrared satellite measurements. *Journal of Geophysical Research, 106 (C2)*, 2387-2405.

Flament, P., Firing, J., Sawyer, M., & Trefois, C. (1993). Amplitude and horizontal structure of a large diurnal sea surface warming event during the Coastal Ocean Dynamics Experiment. *Journal of Physical Oceanography, 24*, pp. 124-139, 199 (SOEST contr. 3275)

Gentemann, C. L., Donlon, C. J., Stuarth-Menteth, A. & Wentz F.J. (2003). Diurnal signals in satellite sea surface temperature measurements. *Geophysical Research Letters, 30(3)*, 1140.

Gentemann, C. L., Minnett, P. J., Le Borgne, P & Merchant C. (2008). Multi-satellite measurements of large diurnal warming events. *Geophysical Research Letters, 35*, L22602.

Gentemann, C. L., & Minnett, P.J. (2008). Radiometric measurements of ocean surface thermal variability. *Journal of Geophysical Research, 113*, C08017

Hoffman, R. N., & Leidner, S. M. (2005). An introduction to the near-real-time QuikSCAT data. *Weather and Forecasting, 20*, pp. 476-493.

Kahru, M., Leppänen, J-M, & Rud, O. (1993). Cyanobacterial blooms cause heating of the sea surface, *Marine Ecology Progress Series, 101*, 1-7.

Kaiser, J. A. C. (1978). Heat balance of the upper ocean under light winds. *Journal of Physical Oceanography, 8*, pp 1-12.

Knievel, J.C., Rife, D.L., Grim, J.A., Hahmann, A.N., Hacker, J.P., Ge, M., & Fisher, H. (2010). A simple technique for creating regional composites of sea surface temperature from MODIS for use in operational mesoscale NWP. *Journal of Applied Meteorology and Climatology, 49*, 2267-2284.

LeBorgne, P., Legendre, G., & Marsouin, A. (2006). Operational SST retrieval from MSG/SEVIRI data. paper presented at The 2006 EUMETSAT Meteorological Satellite Conference, Helsinki.

Mahura, A., Sattler, K., Petersen, C., Amstrup, B., & Baklanov A. (2005). DMI-HIRLAM Modelling with High Resolution Setup and Simulations for Areas of Denmark. *DMI Technical Report 05-12*, 44.

Marullo, R., Nardelli, B.B., Guarracino, M., & Santoleri (2007). Observing the Mediterranean Sea from space: 21 years of Pathfinder-AVHRR sea surface temperatures (1985 to 2005): re-analysis and validation. *Ocean Sci., 3*, 299-310.

Marullo, R., Santoleri, V., Banzon, R., Evans, H., & Guarracino, M. (2010). A diurnal-cycle resolving sea surface temperature product for the tropical Atlantic. *Journal of Geophysical Research, 115*, C05011, doi:10.1029/2009JC005466.

Merchant, C. J., Filipiak, M. J., Le Borgne, P., Roquet. H., Autret. E., et al. (2008). Diurnal warm-layer events in the western Mediterranean and European shelf seas. *Geophysical Research Letters, 35*, L04601.

Otobe, H., & Asai, T. (1985). Heat balance of the upper ocean under a land and sea breeze in Sagami Bay in summer. *Journal of Oceanography, 41(5)*, 299-306, Doi: 10.1007/BF02109237

Peters, S. W. M., Eleveld, M., Pasterkamp, R., Van der Woerd, H., Devolder, M., et al. (2005). Atlas of Chlorophyll-a concentration for the North Sea based on MERIS imagery of 2003. *Vrije Universiteit, Amsterdam, edition 3.0*

Portabella, M., & Stoffelen, A. (2001). Rain Detection and Quality Control of SeaWinds. *Journal of Atmospheric and Oceanic Technology, 18*, 1171-1183.

Price, J., Weller, R., & Pinkel, R. (1986). Diurnal Cycling: Observations and Models of the Upper Ocean Response to Diurnal Heating, Cooling and Wind Mixing. *Journal of Geophysical Research, 91(C7)*, 8411-8427.

Price, J., Weller, R. , Bowers, C. , & Briscoe, M. (1987). Diurnal Response of Sea Surface Temperature Observed at the LongTerm Upper Ocean Study (34° N, 70° W) in the Sargasso Sea. *Journal of Geophysical Research, 92(C13)*, 14480-14490.

Stramma, L., Cornillon, P., Weller, R.A., Price, J.F., & Briscoe, M. G. (1986). Large diurnal sea surface temperature variability: satellite and in situ measurements. *Journal of Physical Oceanography, 16*, 827-837

Stommel, H., et al. (1969). Observations of the diurnal thermocline. *Deep-Sea Research, 16*, 269-284

Stuart-Menteth, A. C., Robinson, I. S., & Challenor, P.G., (2003). A global study of diurnal warming using satellite-derived sea surface temperature. *Journal of Geophysical Research, 108*, C5, 3155.

Stuart-Menteth, A. C., Robinson, S. I., Weller, R. A., & Donlon, C. J. (2005). Sensitivity of the diurnal warm layer to meteorological fluctuations part 1: observations. *Journal of of Atmospheric and Oceanic Science, 10(3)*, 193-208.

Ward, B. (2006). Near-surface ocean temperature. *Journal of Geophysical Research, 111*, C02004.

Paper V

Observations and modelling of the diurnal SST cycle in the North and Baltic Seas

Observations and modeling of the diurnal SST cycle in the North and Baltic Seas

I. Karagali,[1], and J.L. Høyer[2]

I. Karagali, DTU Wind Energy, Technical University of Denmark, Risø Campus, Building 125, Roskilde, 4000, DK. (ioka@dtu.dk)

J.L. Høyer, Centre for Ocean and Ice (COI), Danish Meteorological Institute (DMI), Lyngbyvej 100, 2100, DK. (jlh@dmi.dk)

[1]DTU Wind Energy, Risø Campus,
Roskilde, 4000, DK.

[2]COI, DMI, Copenhagen Ø, 2100, DK.

Abstract. This paper discusses the evaluation of three parameterizations for the diurnal variability of SST during one year, from February 2009 to January 2010 (inclusive), using high resolution, regional NWP model outputs as input fields. Comparison of the spatial extend of diurnal warming in the Northern European Seas from SEVIRI and the models, indicates the ability of the models to reproduce the general patterns seen from the observations. Mean absolute biases between the SEVIRI observed peak warming and the modeled results do not exceed 0.25 K, with a maximum standard deviation of 0.76 and a 0.45 correlation. When random noise is added to the models, their ability to reproduce the statistical properties of the SEVIRI observations, improves significantly. The correlation between the observed and modeled anomalies and different parameters highlights the importance of wind as a driving field. A positive correlation is found between hourly SEVIRI anomalies and the daily mean diffuse attenuation coefficient $K_{d(490)}$.

1. Introduction

Properly resolving the daily cycle of sea surface temperature (SST) is of scientific interest due to its many implications. Accounting for the daily SST variability is considered a priority to be implemented in climate and numerical weather prediction (NWP) models as errors in the estimated fluxes can be large [*Webster et al.*, 1996; *Ward*, 2006]. Moreover, the diurnal variability must be known when composing SST fields from different satellite sensors with different overpass times. Such SST composite fields are representative of foundation temperatures, therefore it is of high relevance to include a diurnal variability field in the operationally available daily SST fields. Hourly satellite observations and in situ observations when available, are valuable for the quantitative and qualitative description of the daily SST cycle but their implementation in real time forecasting is complicated.

Many attempts to develop models for the diurnal variability of SST have been made and their complexity varies from empirical parameterizations to bulk mixed layer models and turbulent closure models. An extensive review is available from *Kawai & Wada* [2007]. *Price et al.* [1986] used a data set collected during the Long-Term Upper Ocean Study (LOTUS) to examine diurnal warming. A fully mixed layer model was developed, relating warming with the surface wind stress and surface heating. It was found to have some success in simulating the amplitude and day to day variability of the diurnal cycle.

Fairall et al. [1996] developed a warm layer model based on a single-layer scaled version of the *Price et al.* [1986] model. When combining this with their cool skin model and testing against data obtained from the Tropical Ocean-Global Atmosphere (TOGA)

Coupled Ocean-Atmosphere Response Experiment (COARE) program, they reported a model underestimation of 0.5 K for the observed 3-4 K warming amplitude and a phase lag of 1 hour.

Observations from the TOGA-COARE program were also used by *Webster et al.* [1996] to examine the amplitude of the peak daily warming and to develop a parameterization that used as input parameters the peak solar insolation, the 10-m wind speed and the daily averaged precipitation. They reported an overall bias lower than 0.05℃, maximized at 0.07℃ for very high wind speeds.

Kawai & Kawamura [2002] used a one dimensional model to simulate skin and 1-m depth temperatures. These were used for the derivation of a regression equation to evaluate the daily amplitude of SST from daily mean wind and daily peak solar radiation. They found greater skin SST values than in *Webster et al.* [1996] but not inconsistent with observations, as they stated.

Gentemann et al. [2003] calculated an empirical model using non-linear least squares regression, to relate the daily SST variability from Pathfinder and Tropical Microwave Imager (TMI) datasets to insolation and wind speed. The initial daytime minus nighttime differences were 0.22°C for the bias with a 0.68°C standard deviation. When the modeled diurnal warming was subtracted from the daytime PathFinder SSTs, the reported difference dropped to −0.04°C with a standard deviation of 0.63°C.

Clayson & Curry [1996] used the model results from *Webster et al.* [1996] to determine the amplitude of the diurnal cycle and developed a parameterization of peak daily warming dSST. Measured dSST was found 0.13 ℃ higher than the dSST modeled using ship-

measured input parameters, with a standard deviation of 0.31 ℃ and a correlation of 0.85.

Zeng & Beljaars [2005] derived a prognostic scheme for the computation of skin SST, required in applications such as weather forecasting and coupled ocean-atmosphere modeling. They compared modeled results with radiometric measurements from a ship over the Western Pacific warm pool region. The mean absolute deviation between computed and observed skin temperatures was 0.39 K and the correlation was 0.85. The observed amplitude of the averaged diurnal cycle over a 10-day period was 2.3 K and the modeled was 2 K.

Clayson & Weitlich [2007] used the parameterization of *Webster et al.* [1996] to produce modeled SST from satellite input fields. Comparisons with buoy data showed a mean bias of 0.0012 ℃, standard deviation of 0.26 ℃ and correlation of 0.74. *Gentemann et al.* [2009] developed the Profiles of Ocean Surface Heating (POSH) model, to determine the vertical profile of surface heating, based on the model described in *Fairall et al.* [1996] and additional measurements from the M-AERI and SkinDeEP instruments. Comparison of 72 days with measured diurnal warming showed a mean bias of -0.01 K and standard deviation of 0.28 for modeled minus measured warming.

Most of the models mentioned above were derived using in situ observations and are based on regression analysis. Lately, *Filipiak et al.* [2010] developed a model relating the diurnal variability of SST with modeled net surface heat flux and surface wind speed fields. They adopted an approach different than in previous studies, and attempted to ensure that the model predicts correctly the statistical distribution of diurnal warming.

Diurnal warming in the Northern European Shelf Seas from hourly SEVIRI observations has been formerly identified and characterized in *Karagali et al.* [2011]. Using five years of hourly SST retrievals (2004-2009), they showed that anomalies higher than 2 K occurred during the late spring and summer months of every year. *Merchant et al.* [2008] noted influential $K_{d(490)}$ variability in the North Sea and Baltic Sea that could explain up to 20% of the mean peak dSST spatial variance.

In the present paper, the ability of different parameterizations to predict diurnal warming is evaluated and compared to the SEVIRI observed anomalies in the Northern European Seas. Observations from this area of the world have not been generally considered when developing the diurnal warming models, therefore it is of interest to evaluate their performance in an area of the world where diurnal variability has only recently been characterized and quantified. As such, it is also sought to define the correlation between the observed warming with the modeled anomalies and the fields from a regional Numerical Weather Prediction (NWP) model. Finally, as the Northern European Seas are characterized by turbid waters due to the outflow of large rivers, the potential impact of the mean attenuation coefficient $K_{d(490)}$ on the development of diurnal warming cases is assessed.

The model from *Filipiak et al.* [2010], the prognostic scheme of *Zeng & Beljaars* [2005] and the parameterization from *Clayson & Curry* [1996] are implemented. The selection is based on their simple implementation, low computational cost and different modeling approaches. Observations from the Northern European Seas have been included in the *Filipiak et al.* [2010] model, therefore it is of interest to evaluate the model's performance when different input fields are used.

The data are presented in Section 2 and the models are briefly described in Section 3. Section 4 contains results separated in two parts. Initially, the SEVIRI and model dSSTs are compared in terms of spatial extend and statistics. The latter part describes sensitivity analyses and the correlation of observed anomalies to various physical parameters and the model dSSTs. A discussion can be found in Section 5 and the conclusions in Section 6.

2. Data

2.1. Satellite Data

The Spinning Enhanced Visible Infrared Imager (SEVIRI), on board the Meteosat Second Generation (MSG) satellites, is an infra-red radiometer. Radiation is collected from an area using a telescope and is focused on detectors sensitive to 12 bands of the electromagnetic spectrum [*Aminou et al.*, 1997]. The nadir sampling distance is 3 km for the near infra-red and infra-red channels.

The experimental SEVIRI product of CMS (Centre Météorologie Spatiale), Météo France is used from February 2009 to January 2010 (inclusive). It is different from the operational EUMETSAT OSI SAF product as it is released for every hour and is mapped to a 0.05 degrees grid. A flag ranging from 0 (unprocessed) to 5 (excellent) indicates the quality of the SST values, with 3 being acceptable. SEVIRI SSTs refer to subskin temperatures.

A Surface Solar Irradiance (SSI) experimental product is also available from CMS (Centre Météorologie Spatiale), Météo France for the O&SI SAF, EUMETSAT. It is calculated as the solar irradiance reaching the Earth's surface in the 0.3-4 μm band, with the irradiance being defined as the radiant flux per unit area (W m^{-2}). A full description of the algorithms and the processing chain is available in *O&SI SAF* [2005]. The product

used here is hourly, available on a grid of 0.1° resolution. For the present study, data are re-sampled to match the SEVIRI grid of 0.05°.

The diffuse attenuation coefficient at 490 nm is a measure of the optical properties of the water column. Higher $K_{d(490)}$ values indicate higher water turbidity and tend to promote diurnal warming [*Merchant et al.*, 2008]. For the purposes of the present study, fields from two different sources are obtained.

The GlobColour project (`http://www.globcolour.info/`) produces daily $K_{d(490)}$ fields based on the merged chlorophyll-A concentration for case I water. The $K_{d(490)}$ product from the Danish Meteorological Institute (DMI), is produced by an algorithm developed specifically for Case-II waters during the REgional VAlidation of Meris chlorophyll Product (REVAMP) project [*Peters et al.*, 2005]. Due to its regional character, it does not cover the entire domain, but extends only from 5°W to 26°E.

2.2. NWP fields

The NWP High Resolution Limited Area Model (HIRLAM) is developed by several European meteorological institutes and has a spatial resolution of 3 km [*Mahura et al.*, 2005]. HIRLAM outputs are used to obtain 10 m winds, the surface net heat flux, the solar and non-solar fractions of the surface fluxes and the averaged daily precipitation. All fields are re-sampled to match the SEVIRI grid.

3. DV Models

Filipiak et al. [2010] Model

This model, here referred as FMKLB, evaluates dSST from dawn to next dawn. It has been derived using 1 year of data over the Atlantic and the Mediterranean Sea from

SEVIRI SST observations and operational and analysis fields from the European Centre for Medium-Range Weather Forecasts (ECMWF). Diurnal warming (D) is described as a function of time (t), maximum wind speed (W) since the net heat flux (q) became positive and integrated net heat flux (Q) since the net heat flux (q) became positive. The warming part is described by

$$D\left(t\right) = Q\left(t\right)\frac{\alpha\left(t\right)}{1 + b\left(t\right){W_t}^2} + c\left(t\right), \tag{1}$$

where α, b, c are derived coefficients that depend on the hour of the day. Cooling periods are defined by negative integrated net heat flux (Q$<$ 0) and are described as

$$D\left(t\right) = f\left(t\right)\frac{Q\left(t\right)}{\rho c_p d}, \tag{2}$$

where ρ is the density and c_p, the specific heat of water, d is the climatological mixed layer depth and f is a coefficient that defines the fraction of d that undergoes cooling. For the climatological mixed layer depth d, the entire water column depth is used in this study, as both the North Sea and the Baltic Sea are characterized by very small depths.

Zeng & Beljaars [2005] Model

The prognostic scheme of *Zeng & Beljaars* [2005], referred as ZB, requires wind and surface fluxes, along with an a priori knowledge of foundation temperatures. In this case, the SEVIRI reference fields are used, as representative of night-time conditions (see [*Karagali et al.*, 2011] for validation results). The scheme, as described in *Zeng & Beljaars* [2005] consists of two parts. The sea surface skin temperature T_s is described as

$$T_s - T_{-\delta} = \frac{\delta}{\rho_w c_w k_w}\left(Q + R_s f_s\right), \tag{3}$$

where δ is the thickness of the skin layer, $T_{-\delta}$ is the sub-skin temperature, ρ_w is the density and c_w the volumetric heat capacity of sea water, k_w is the molecular thermal

conductivity of sea water, R_s is the net solar radiation at the surface of the ocean and f_s the fraction absorbed in the sub-layer. Q represents the sum of the surface sensible and latent heat fluxes and the net long-wave radiation. Below the skin layer the temperature is described by

$$\frac{\vartheta\left(T_{-\delta}-T_{-d}\right)}{\vartheta t}=\frac{Q+R_s-R\left(-d\right)}{d\rho_w c_w \nu/\left(\nu+1\right)}-\frac{\left(\nu+1\right)ku_{*w}}{d\varphi_t\left(d/L\right)}\left(T_{-\delta}-T_{-d}\right), \tag{4}$$

where d is the depth where no diurnal warming occurs, T_{-d} is the foundation temperature, φ_t is the stability function, u_{*w} is the friction velocity in the water and ν is an empirical parameter considered equal to 0.3 for a d=3 m. In the present study, two different thresholds are selected, d_1=3 m and d_2=6 m. In addition, as the scheme computes both the skin and sub-skin SST, we use the sub-skin to be comparable with SEVIRI.

Clayson & Curry [1996] Model

The parameterization, referred from hereafter as CC, was developed within the framework of the TOGA-COARE project and it is described originally in *Webster et al.* [1996]. This scheme uses a peak solar insolation, the averaged daily wind speed and the daily average precipitation through a regression equation of the form

$$DSST=\alpha+b\left(PS\right)+c\left(P\right)+dln\left(U\right)+e\left(PS\right)\left(U\right)+f\left(U\right). \tag{5}$$

PS is the peak solar insolation in W m^{-2}, U is the mean daily wind speed in m s^{-1}, P is the averaged daily precipitation in mm hr^{-1} and a, b, c, d, e, f are coefficients derived through regression and are determined separately for $U \geq$2 m s^{-1} and $U <$2 m s^{-1}.

In the present study, a Neural Network (NN) system, developed by Bogdanof & Clayson (personal communication), is used for the determination of coefficients and the dSST prediction. From the above, it follows that the CC scheme estimates the skin SST and

157 does not resolve the full daily cycle but only produces a peak dSST value. Therefore,
158 comparison with the other predicted dSSTs and the SEVIRI observed ones can be achieved
159 only through the distribution of the peak dSSTs and the mean peak dSST and it will
160 include the "cool skin" bias.

4. Observing and modeling the diurnal cycle

161 An example of the maximum dSST during a warming event on the 03/07/2009, as
162 estimated from SEVIRI and modeled by the different schemes, is shown in Figure 1. A
163 peak dSST of 5.5 K is observed from SEVIRI in an extended area of the west coast
164 of Denmark and smaller areas, where peak dSST is $\sim$4 K, are observed in the waters
165 around the country. Another area with a peak dSST of 5 K is observed in the Baltic
166 Sea. Each model shows a rather different behavior, with the FMKLB capturing warming
167 in the Danish inland waters and in the Baltic Sea but rather failing in the west coast of
168 Denmark. The ZB d_1 scheme predicts dSSTs of the correct amplitude but with a much
169 larger spatial extend while the d_2 version essentially reproduces the same spatial extend
170 but with a reduced amplitude. Finally, the CC scheme shows a much lower peak dSST, in
171 the order of 2 K; this scheme predicts the skin SST and thus, the potential large difference
172 between skin and sub-skin temperatures is highlighted.

4.1. Statistical Description

173 To evaluate the performance of the models, the statistical distributions are compared to
174 the results from SEVIRI. However, noise is inherent in the SEVIRI results, whereas DV
175 models estimate the "true" diurnal cycle without noise. The random noise component
176 can make a significant difference on the shape of the probability density function (PDF)

and for consistency, we thus also show the PDFs where white noise with zero mean and a standard deviation of 0.5 K has been added to each hourly model dSST. The results presented in this section, are with (white) and without (grey) the added noise. The percentiles and sums of data points are estimated only with the added noise.

The distribution of anomalies equal or larger than 2 K is shown in Figure 2, for SEVIRI and the different models. In particular, the FMKLB model reproduces remarkably the distribution shown from SEVIRI, especially without the added random noise. The model's behaviour does vary with the added noise; an increase of anomalies in the range 2-2.3 K and a decrease for the range 2.4-3.5 K when compared to results without random noise, is observed. In addition, the number of identified anomalies increases when the random noise is added. The FMKLB percentiles are $\sim$0.2 K lower than the SEVIRI ones. The FMKLB model has been developed using 1 year of SEVIRI observations, thus the noise inherent in SEVIRI is expected to be also inherent in the model. This explains why the distribution is more similar to SEVIRI without the added noise.

The distribution of the ZB d_1 version does not vary at all with the addition of the random noise, but the number of identified warming does increase. The distribution is similar to SEVIRI for dSST$\geq$2.5 K while the 95th and 97.5th percentiles are higher than the SEVIRI ones. Modeled anomalies do not exceed 5 K in amplitude while the 99.9th percentile from SEVIRI is at 6.25 K. The highest impact of adding random noise is seen for the ZB d_2 version. Without adding noise, no dSST higher than 3 K is identified. With the noise, the distribution resembles more the one from SEVIRI but the percentiles are significantly lower.

The time of occurrence of anomalies is shown in Figure 3. SEVIRI anomalies are evenly distributed during the day, with a peak at 15:00 LT and warming that persists until 22:00 LT. Adding random noise significantly improves all models. Especially, the FMKLB anomalies peak an hour earlier, at 14:00 and the noise adds warming until 22:00; originally no warming was observed after 20:00. The ZB scheme shows a time lag of 1 hour for the d_2 version. The random noise significantly improves the left part of the distributions as warming is identified earlier, which is also seen from SEVIRI. There is an overestimation of late warming from both ZB versions, which is slightly reduced when the random noise is added.

The duration of warming from the SEVIRI observations and the models is presented in Figure 4. All distributions are scaled on the highest 99.9 percentile; this is observed from SEVIRI and is estimated at 13 hours. The 99.9 percentiles for the models are 13 hours for FMKLB, 12 hours from ZB d_1 and 10 hours for ZB d_2. SEVIRI shows a decreasing trend for longer duration, with a 75th percentile at 3 hours. Once again, the noise significantly modifies the model distributions towards the SEVIRI one. The FMKLB and ZB d_2 have the same percentiles as SEVIRI. The ZB d_1 version has higher percentiles suggesting that warming is not sufficiently dissipated. This can be an artifact of the input fields, especially of the wind which may be biased too low, in combination with a shallow warm layer setting (d_1 =3 m).

Figure 5 shows the distribution of maximum anomalies, estimated as the daily maximum anomaly of every grid cell, independent of threshold. The CC model is also included for comparison as it can produce a daily peak dSST. Only anomalies with quality flag 5 are considered for SEVIRI. 75% of the SEVIRI daily maximum anomalies do not exceed 1.1 K

but 5% is higher than 2.4 K. Note the relatively few number of total observations, due to missing values either in the day-time SSTs or the night-time reference fields.

The distribution of peak anomalies from the FMKLB model has the 75th percentile higher by $\sim$ 0.2 K but the higher percentiles are lower than SEVIRI. The ZB d_1 scheme has the 75%, 95% and 97.5% of peak anomalies higher than SEVIRI; only the 99.9% is lower by $\sim$0.7 K. The d_2 version produces a distribution of peak dSSTs with percentiles following the behavior of the FMKLB model. Finally, the CC scheme has a much narrower distribution with no peak anomalies exceeding 2 K and 75% not exceeding 0.7 K. Adding the random noise modifies the distributions for all models, to resemble more the SEVIRI one.

The amount of peak dSSTs is different between the schemes and SEVIRI, especially between the FMKLB and the rest. This is because both the ZB and the CC require a foundation temperature field, for which the SEVIRI night-time reference fields are used. Thus, missing values in the reference fields will prevent the estimation of a dSST value while this is not the case for the FMKLB scheme; this only uses NWP fields that in principle do not have missing values. In addition, missing SST values from the daytime SEVIRI fields or the night-time reference fields will result in fewer identified anomalies for SEVIRI.

The averaged monthly diurnal cycle from the FMKLB, ZB schemes and the SEVIRI observations is presented for the period April-July 2009 in Figure 6. For every day, grid cells with warming are used to evaluate the mean hourly dSST, independent of threshold. No random noise is added to the models and the quality of the SEVIRI dSST must be 5. For every day, a diurnal cycle is estimated which is then aggregated to a monthly cycle.

This is estimated separately for SEVIRI and each of the schemes, therefore the monthly cycles represent the average dSSTs without any requirement of spatial and temporal collocation.

With the transition from spring to summer warming starts earlier; SEVIRI shows anomalies at 08:00 in April and at 07:00 in May while warming starts at 04:00 in June and July. Peak warming lasts longer in summer compared to spring. The FMKLB model reproduces the warming part of the cycle remarkably well, especially for June and July, while it also properly resolves the amplitude and the time of peak dSST (June). In April and May, the FMKLB scheme shows earlier warming and it does not dissipate at night-time. This residual warming of 0.3-0.4 K, depending on the month, in the FMKLB scheme is higher than what is seen from SEVIRI and the ZB scheme (0.1-0.2 K). The FMKLB model is computed from dawn to the next dawn, hence the timing of zero anomalies is at 04:00 LST. The persistence of the residual warm layer in both the FMKLB and the ZB schemes is a positive attribute as SEVIRI also demonstrates this feature.

The ZB scheme, independent of the d value, shows an early initiation of warming compared to SEVIRI in April and May. The peak amplitude is resolved (slightly underestimated) in April, but is overestimated for the remaining months by a maximum of 0.2 K. The warming part of the cycle is either fitting the SEVIRI warming especially for the early hours (June and July) or it is slightly overestimated (April and May). In the former case, SEVIRI and the ZB schemes match from midnight up to 9:00; after that the ZB schemes show more rapid warming. The d_2 version successfully captures the cooling part most of the months while the d_1 version slightly overestimates it. Adding random noise to the models does not modify the monthly shape of the diurnal cycle. We have also

evaluated the monthly averaged diurnal shape using only grid cells that show an anomaly higher or equal to 2 K. This has been performed by using the raw model outputs and by adding random noise. The monthly averaged diurnal cycle with the 2 K threshold is significantly different than the one shown previously. SEVIRI peak warming reaches up to 2.5 K in April and May, when none of the models exceeds 2.2 K. In June and July the peak dSST is similar between SEVIRI and the models. In general, warming is slower and cooling faster in all cases, with the exception of the ZB d_2 version in April and May, when its cooling part is slower than SEVIRI. All modeled diurnal cycles show a time lag of the peak dSST when compared to SEVIRI. Adding random noise reduces the peak amplitude of the models and improves the timing of the modeled peak dSST.

4.2. Spatial Distribution

The spatial distribution of anomalies of 2 K or more, for 1 year of SEVIRI observations and model runs is shown in Figure 7. Results are presented as hours of anomalies exceeding 2 degrees, for the test period. Note the different scaling to make the spatial differences visible. All models capture the difference in the spatial extend of warming between the North Sea and the Baltic Sea; more warming is identified in the Baltic Sea similar to the SEVIRI results. A good agreement between the modeled and observed anomalies is found for the Baltic Sea around 60°N, the North Sea around 58°N–4°E and the Danish Straits around 56°N–12°E. For an area west of Denmark (54°N–8°E), SEVIRI dSSTs are observed but the schemes do not succeed in resolving such warming.

When random noise is added to the models (not shown), the spatial distribution of warming exceeding 2 K is slightly extended. An increase of approximately 20 to 40 occurrences is observed in the areas where a significant number of warming is already

identified with no random noise. The FMKLB scheme shows the lowest increase, $\sim$ 20 observations, while the ZB d_2 version shows the highest increase, $\sim$ 40 observations. In most areas where no warming is observed without noise, adding noise produces some few occurrences of warming more than 2 K; nonetheless, their number ranges between 1 and 10 for all the models.

The input fields used for the modeling of the diurnal cycle influence the results. If low winds are predicted by HIRLAM more often than they actually occur, the models will have a tendency to overestimate warming. Figure 8 shows the number of cases for which u is equal to or lower than 5 m s^{-1} and at the same time the surface net heat flux q is higher than 300 W m^{-2}. In general, high coincidences of conditions favoring diurnal warming are found in areas where the models do predict most anomalies, i.e. the south part of the English Channel, the coastal areas of the Baltic Sea, the Irish Sea and the west coast of Norway. In addition, the area around 54°N–8°E where SEVIRI anomalies have been identified but the models do not perform accordingly, appears in Figure 8 as an area with generally low number of coincident low u and high q.

The averaged peak dSSTs are shown in Figure 9. They are computed as the maximum anomalies of the day for the SEVIRI observations and the FMKLB and ZB schemes, while the CC scheme provides only the peak skin dSST. The scaling is different for the FMKLB and CC models to highlight the spatial variability. Averaged peak dSST from SEVIRI is between 0.3 and 0.6 K for the largest part of the study area. Peak dSSTs higher than 0.6 K are observed in the west coast of Denmark, the Baltic Sea, the west coast of Norway and the Irish Sea. The models capture the peak dSST in some of these areas; the west coast of Norway (58°N–60°N, $\sim$6°E), the Baltic Sea (54°N–60°N, $\sim$20°E–30°E) and the

Irish Sea (52°N–54°N, ∼4°W). They also show a similar pattern as SEVIRI, where more warming is identified in the Baltic Sea compared to the North Sea. In general, higher peak dSST is observed from SEVIRI compared to the modeled peak dSSTs.

The statistics of peak dSSTs as observed and modeled are shown in Table 1, for the cases when a peak dSST value is available from SEVIRI and the models. These are estimated from all coincident peak dSSTs for each grid cell and every day, without adding any random noise. Mean biases are almost zero for the FMKLB and ZB schemes and ∼0.25 K for the CC scheme, highlighting the skin–subskin difference. From the tested hourly parameterizations, the FMKLB has the lowest bias and standard deviation.

4.3. Sensitivity Analyses

To investigate the relation between the observations, models and different forcing parameters, we compute the correlation between the input fields used in the diurnal warming schemes, the SEVIRI observed dSSTs and other physical parameters that are believed to promote warming. This is performed for SEVIRI anomalies exceeding the threshold of 0.5 K.

Daily values of the attenuation coefficient $K_{d(490)}$ and the sea surface solar irradiance from SEVIRI are used as the physical parameters not included in the modeling parameterizations, to evaluate possible correlation patterns. Ideally, one would expect a negative correlation between wind speed and warming and a positive correlation between $K_{d(490)}$, the integrated net heat flux Q, the SSI and integrated SSI' and dSST. Integration for the net heat flux and SSI is performed from 03:00 LST until the time of observed SEVIRI dSST.

SEVIRI anomalies of 0.5 K and above, occurring between 13:00 and 16:00 LT, are collocated with corresponding wind from HIRLAM, SSI from SEVIRI, $K_{d(490)}$ from DMI and the GlobColour project and dSST from the FMKLB and ZB models. Note that both $K_{d(490)}$ products are daily, thus only 1 value is available for every grid cell. To overcome this and proceed with the sensitivity analysis, the same value of the grid cell is used for all the collocations. Figure 10 shows the correlation matrix, with the numbers of the actual r values superimposed. On average, the correlation between SEVIRI dSSTs and all other included parameters shows the correct trends but weak signals.

Note the negative but low (-0.32) correlation with the wind speed U and the positive but very small correlation with the $K_{d(490)}$ products. The three schemes show a relatively high ($\sim$0.7) and negative correlation with U, which is one of their forcing fields. Their correlation with the integrated heat flux Q is positive but rather low ($\sim$0.3) while the one with $K_{d(490)}$, is negative but higher than the SEVIRI dSSTs. The two different $K_{d(490)}$ products are well correlated (0.7) despite the fact that they are for case I and II waters. The high correlation between Q and SSI' ($\sim$0.87) is considered a positive result for the validation of Q used in the models.

The time-lagged correlation of different parameters with the SEVIRI dSST is also estimated from 3 hours prior to 3 hours after the time of SEVIRI anomaly. Results not shown here indicated that the highest (negative) correlation with U is observed for the hours prior to the time of the anomaly. The same is the case for the SSI but for the integrated SSI' and net heat flux Q, highest correlation is found for the time of warming (and later). When the different parameterizations are considered, there is no time lag in the correlation and the ZB scheme is the one with the highest value ($\sim$0.42).

The correlation values found from this analysis are relatively low but the correct trends are captured. This can be related with the fact that for the relatively low value of 0.5 K set as the threshold, many SEVIRI dSSTs may be filtered that do not coincide with similar predictions from the models. When estimating the correlations but applying a threshold to warming more than 2 K (not shown), SEVIRI shows lower correlation with U, SSI, Q and the models but slightly higher correlation with the $K_{d(490)}$ products. In this case, the models are better correlated between them, their negative correlation with the $K_{d(490)}$ decreases while their correlation with U is lower for the FMKLB and ZB d_2 schemes but higher for the ZB d_1 version.

5. DISCUSSION

Of the three parameterization schemes applied, only two can resolve the daily cycle. Both tend to properly identify the different warming patterns between the Baltic Sea and the North Sea. They slightly overestimate the spatial extend of warming, with the ZB d_1 more than the rest. From a large number of coincident peak warming values the bias between SEVIRI and the models is not larger than 0.25 K and the highest standard deviation does not exceed 0.76 K.

Filipiak et al. [2010] compared their model with SEVIRI observations for a period that was not used during the model development and stated that the mean warming matched to 0.05 K. *Zeng & Beljaars* [2005] found a mean absolute deviation of 0.39 K and a correlation of 0.89 with in situ radiometric measurements for the skin SST. *Clayson & Curry* [1996] used ship measurements for the peak solar radiation, precipitation and wind to derive dSST and compared it with ship measured dSST, concluding that the derived dSST was lower by 0.13°C with a standard deviation of 0.31°C and a correlation of 0.85.

The mean biases shown in Table 1 are not far from their findings, especially for the FMKLB and ZB schemes. We have found higher standard deviations, than the ones reported in *Zeng & Beljaars* [2005]; *Clayson & Curry* [1996] while the correlation values reported here are almost half when compared to the ones reported above. It should be noted that the biases reported in *Zeng & Beljaars* [2005] are for the skin SST while in this study we compare the sub-skin SST. For the CC the bias found in this study is almost double but it is derived from a sub-skin minus skin comparison, while in *Clayson & Curry* [1996] the biases are estimated using skin measurements.

As such, the biases mentioned in the above studies and the ones given here are not directly comparable. Ideally, in situ observations from drifting buoys would be most suitable for the validation of the SEVIRI and modeled warming. Unfortunately, in the North Sea and Baltic Sea only moored buoys and platforms are available, with typically the shallowest sensor located no less than 1 m below the surface. Examination of such moored buoy observations showed that almost no diurnal cycle could be identified, thus eliminating the possibility for validation with in situ measurements.

Successful modeling of the diurnal cycle when using empirical parameterizations highly depends on the input fields and the representativity of the empirical relationships. The main contributing factors are the representativity of the parameterization's coefficients in respect to the local conditions and the accuracy of the input NWP model fields. When evaluating the number of observations where u <=5 m s^{-1} from HIRLAM and other available model outputs, it is found that for the same time period HIRLAM predicts low winds more often. In the case that HIRLAM is biased towards low winds, warming will be more often predicted by the parametrization schemes. As the correlation of the

modeled dSST with wind is much higher than with the integrated net heat flux Q, the parameterizations are sensitive to the input wind fields.

When examining the spatial extend of either individual warming cases (Fig. 1), or of the mean peak dSST (Fig.9) or of anomalies $\geq$2 K (Fig.7), a consistent feature is the lack of modeled warming in the west coast of Denmark in contrast to the SEVIRI observable warming. This area of the North Sea poses challenges due to its very shallow waters, intense tidal effects and high water turbidity. Low overall SEVIRI minus in situ biases from moored buoys and platforms in this area were reported in *Karagali et al.* [2011], slightly increasing during daytime. Such results lower the possibility of regional SEVIRI biases in this complex area but lack of drifting buoys does not allow for more accurate validation at shallow layers.

Especially for the CC scheme, its coefficients are evaluated through a Neural Network (NN) system that receives as an input multiple already derived coefficients and predicts the peak dSST based on the input fields. It is a very straightforward scheme, with a low computational cost but it predicts the skin dSST therefore it is expected to be lower than the SEVIRI observed dSST, especially since the cool skin effect can be large for low winds.

As stated in *Filipiak et al.* [2010], their model's coefficients should be re-fitted if NWP fields other than the ECMWF ones are used. In this study we used HIRLAM NWP fields without modifying the coefficients. The ECMWF wind fields used for the model derivation had a 6-hour time resolution, while HIRLAM winds are available every hour. These differences in the type of field, their time and spatial resolution may be a reason for the mismatch between modeled and observed warming. Despite this, the FMKLB model

425 can successfully reproduce the statistical distribution of anomalies and the averaged shape
426 of the diurnal cycle as seen from SEVIRI.

427 As the FMKLB scheme is based on the statistical distribution of warming, its behavior
428 is somewhat expected and very promising. For this, we attempted to modify the model
429 and tune it to the more local conditions of the North Sea and the Baltic Sea by examining
430 the possibility of including the mean attenuation coefficient at 490 nm as an additional
431 parameter. Results from regression analyses (not shown here) indicate that $K_{d(490)}$ does
432 contribute in the total variance of the dSST signal from the FMKLB model. Unfortu-
433 nately, the significance of this contribution is rather low. A long period of coincident
434 modeled anomalies and $K_{d(490)}$ values could possibly strengthen this signal and this is
435 something to look at in the future. In addition, the $K_{d(490)}$ values are daily and this is a
436 limitation when attempting to correlate it with the hourly model results.

437 In *Zeng & Beljaars* [2005], the shape exponent of the warm layer ν was set to a value of
438 0.3 for a warm layer depth of d =3 m. They also state that if the depth d is significantly
439 altered, the ν parameter has to be changed. In this study, the combination of parameters
440 described in *Zeng & Beljaars* [2005] has been found to overpredict warming. This may
441 be due to the biased HIRLAM winds towards lower winds and the different input fields
442 used for the foundation temperature. In addition, the ν parameter has not been altered
443 for d_2 =6 m. Future work on the sensitivity of this parameter in combination with the
444 depth d of the diurnal-free layer may provide a more appropriate combination of the two,
445 which nonetheless may be very local. Sensitivity tests were performed for point locations
446 of the buoys and platforms of the MARNET network in the North Sea and the Baltic Sea
447 (see *Karagali et al.* [2011], Figure 1b). The depth of the warm layer d was allowed to vary

between 2 m and 6 m and the shape exponent ν varied between 0.1 and 0.9. The results of the ZB model with various configurations were compared to the SEVIRI observed warming at these point locations; the collocation criteria were set such that the grid cell containing each location was selected. For the test period 03/01/2009 to 12/31/2009 it was found that most SEVIRI–ZB biases were minimized (0-0.2 K) for the d parameter equal to 6 m and the ν parameter between 0.1-0.3. Most standard deviations were lowest (0.2-0.9 K) for ν ranging between 0.2 and 0.6. Lowest rmse values (0.24-0.94 K) were found for different ν depending on the location, but mostly ranged between 0.2 and 0.5. The correlation was maximized (0.96-0.98) for almost all locations, for the combination d =6 3 and ν =0.1 and the number of match-ups ranged from 1000 to 1600.

Correlation between SEVIRI and U, Q, SSI, SSI' and $K_{d(490)}$ showed the correct sign but weak signal. Especially for the HIRLAM fields, such findings are positive especially under the assumption that the model can not exactly resolve the spatial location of low winds where the diurnal warming is observed. In addition, the correlation between Q and SSI' is very high, in the order of 0.9 which provides a positive validation of the HIRLAM fluxes and the computation of Q. A higher correlation of the SEVIRI dSST with $K_{d(490)}$ was expected. Given the fact that the temporal variability of $K_{d(490)}$ is expected to be lower than the one of SST, it is rather hard to associate hourly variations of temperature with variations in $K_{d(490)}$, that generally occur in longer time scales. Despite that, investigations on the dependence of observed dSST$\geq$2 K on Q and U from HIRLAM for different ranges of $K_{d(490)}$, showed that for high $K_{d(490)}$ values (¿0.37 m^{-1}, i.e. the upper 25th percentile) dSST was higher for the very low wind speeds and decreased faster for increasing wind speeds. When $K_{d(490)}$ was lower than 0.37 m^{-1}, dSST was lower for the very low wind

speeds and decreased slower for increasing winds. Such findings highlight the contribution of $K_{d(490)}$ to increased dSST values, given the sufficiently low wind and insolation values.

The modeled dSST negative correlations with $K_{d(490)}$ are somewhat difficult to interpret. It can be due to the time-lag between the observed and modeled dSST as the selection is controlled by the SEVIRI anomalies. This assumption can be somehow supported by the fact that the highest (negative) correlation is found for the ZB 6 m version, which also shows the greatest time lag. Independent sensitivity analyses on the dependence of modeled dSST on Q and U from HIRLAM for different ranges of $K_{d(490)}$ were performed similar as for the SEVIRI dSSTs. All schemes showed similar behaviour for $K_{d(490)}$ higher than 0.37 m^{-1} as the SEVIRI dSSTs. Especially the ZB d_1 version, showed very appropriate stratification and significant decrease of dSST with increasing U.

Another possible candidate for cross-comparisons would be the POSH model. This also provides vertical temperature profiles for which unfortunately no in situ data are available for the North and Baltic Seas. [*Filipiak et al.*, 2010] compared their model to the POSH and ZB models through an idealized case. They found that while their model and the ZB one had similar overall magnitudes, the POSH model slightly underestimated warming at higher wind speeds, compared to the proposed statistical model. In addition, they found that POSH predicted very large warming for the lowest wind speed and highest insolation. Such reported results are considered a good reason not to include the POSH model in this study. Future investigations amongst models that are able to resolve the vertical structure of the upper water temperature, will include the POSH model.

6. CONCLUSIONS

The aim of this study was to evaluate diurnal warming in the Northern European Seas through simple parameterizations using as input fields the outputs of a regional NWP model and compare the performance of the different parameterizations with observed anomalies from SEVIRI. In addition, to examine the correlation of observed warming with different physical parameters, such as the wind speed U and the integrated net heat flux Q from the regional NWP model, the SSI from SEVIRI and the diffuse attenuation coefficient $K_{d(490)}$ that describes the optical properties of water.

Three different models have been applied, described in *Filipiak et al.* [2010]; *Zeng & Beljaars* [2005] and *Clayson & Curry* [1996], due to their simple implementation and low computational cost. Of the three dSST models, only the first two resolve the full diurnal cycle and the third estimates peak skin dSST. Collocated peak dSSTs indicate almost zero biases for the *Zeng & Beljaars* [2005] and *Filipiak et al.* [2010] schemes while a 0.25 bias is found for the *Clayson & Curry* [1996] scheme. The overall correlation of peak dSSTs between the models and SEVIRI does not exceed 0.45.

The distribution of dSSTs$\geq$2 K from the *Filipiak et al.* [2010] scheme remarkably simulates the one of SEVIRI dSSTs, highlighting the very good ability of the model to capture the statistical distribution of warming. Both the *Filipiak et al.* [2010] and *Zeng & Beljaars* [2005] schemes identify more warming later in the day compared to SEVIRI, with the former scheme peaking 1 hour earlier and the latter peaking either at the same time or 1 hour later, depending on the version. Of the total SEVIRI dSSTs$\geq$2 K, 75% do not last more than 3 hours, as for the *Filipiak et al.* [2010] and *Zeng & Beljaars* [2005] d_2 version, while for the d_1 version this percentile is up to 6 hours. The mean monthly diurnal warming cycle from the FMKLB scheme is remarkably similar to SEVIRI.

The correlation between observed and modeled dSST and parameters such as U and Q from HIRLAM, SEVIRI SSI and $K_{d(490)}$ shows the correct trends. Negative correlation with U is found, low for SEVIRI and rather large for the models, as they are forced by the field. Positive correlation is found for Q, SSI and SSI', higher for the models ($\sim$0.1-0.4) than for SEVIRI dSSTs ($\sim$0-0.2). SEVIRI correlations with U and SSI are highest for the hours prior to the time of observed warming.

It is shown that the FMKLB model is representative of the distribution of warming cases as observed from SEVIRI. The ZB scheme is able to resolve the spatial extend of the observed warming also accounting for the depth of the warm layer. This is an important parameter to be included in the models, especially for the Northern European Seas where water turbidity is high due to shallow depths, tidal currents and outflow of major rivers. The CC scheme provides a quick estimation of the peak skin dSST which is useful for an estimation of potential warming but not representative enough, as the "cool skin" bias is expected to be rather large under very low wind conditions.

The test period of one year is not representative enough for solid conclusions regarding the performance of the models and the importance of $K_{d(490)}$ for the promotion of diurnal warming. A longer time period for the comparisons would eliminate the possibility of very particular conditions occurring for the test year that the NWP model failed to capture.

Acknowledgments. This study was partially funded by the EU NORSEWInD project (TREN-FP7EN-219048). SEVIRI data were processed by Centre de Météorolgie Spatiale, Mètèo France and the OSI-SAF project. HIRLAM and $K_{d(490)}$ data obtained from the Danish Meteorological Institute (DMI), MARCOAST project. $K_{d(490)}$ data are also obtained from the GlobColour Project, through ftp. The authors would like to thank Chris

Merchant for his help with the FMKLB model and his suggestions and guidance during the two months that Ioanna Karagali spend in the Department of Geosciences, University of Edinburgh. We are deeply grateful to Alec Bogdanof and Carol Anne Clayson for their collaboration and for providing the Neural Network code and the code of their model.

References

Aminou, D.M.A., B. Jacquet, and F. Pasternak (1997). Characteristics of the Meteosat Second Generation (MSG) radiometerimager: SEVIRI. *Proc. SPIE 3221, 19*, doi:10.1117/12.298084

Clayson, C.A., and J.A. Curry (1996). Determination of surface turbulent fluxes for the Tropical Ocean-Global Atmosphere Coupled Ocean-Atmosphere Response Experiment: Comparison of satellite retrievals and in situ measurements. *J. Geophys. Res., 101*, C12, 28,515–28,528.

Clayson, C.A., and D. Weitlich (2007). Variability of tropical diurnal sea surface temperature. *J. Climate, 20*, 334–352.

Fairall, C.W., E.F. Bradley, J.S. Godfrey, G.A. Wick, J.B. Edson, and G.S. Young (1996a). Cool-skin and warm-layer effects on sea surface temperature, *J. Geophys. Res., 101*, 1295–1308, doi:10.1029/95JC03190

Filipiak, M.J., C.J. Merchant, H. Kettle, and P. Le Borgne (2010). A statistical model for sea surface diurnal warming driven by numerical weather prediction fluxes and winds. *Ocean Sci. Discuss., 7*, 1497–1532.

Gentemann, C.L., C.J. Donlon, A. Stuart-Menteth, and F.J. Wentz (2003). Diurnal signals in satellite sea surface temperature measurements. *Geophys. Res. Let., 30(3)*, 1140,

559 doi:10.1029/2002GL016291.

560 Gentemann, C.L., P.J. Minett, and B. Ward (2009). Profiles of Ocean Surface Heat-
561 ing (POSH): A new model of upper ocean diurnal warming. *J. Geophys. Res., 114*,
562 doi:10.1029/2008JC004825.

563 Kawai, Y., and H. Kawamura (2002). Evaluation of the diurnal warming of sea surface
564 temperature using satellite-derived marine meteorological data. *J. Oceanography, 58*,
565 805–814.

566 Kawai, Y., and A. Wada (2007). Diurnal sea surface temperature variation and its impact
567 on the atmosphere and ocean: a review. *J. Oceanography, 63*, 721–744.

568 Karagali, I., J.L. Høyer, and C.B. Hasager (2011). SST diurnal variability in the North
569 Sea and the Baltic Sea. *Rem. Sens. Env., 121*, 159–170, 10.1016/j.rse.2012.01.016

570 Mahura, A., K. Sattler, C. Petersen, B. Amstrup, and A. Baklanov (2005). DMI-HIRLAM
571 Modelling with High Resolution Setup and Simulations for Areas of Denmark. *DMI*
572 *Technical Report 05-12*, 44.

573 Merchant, C. J., M.J. Filipiak, P. Le Borgne, H. Roquet., E. Autret, et al. (2008). Diurnal
574 warm-layer events in the western Mediterranean and European shelf seas. *Geophys. Res.*
575 *Let. 35*, L04601.

576 Météo France (2005). Surface Solar Irradiance Product Manual, Ocean & Sea Ice SAF,
577 Version 1.5, SAF/OSI/M-F/TEC/MA/123, November 2005.

578 Peters, S. W. M., M. Eleveld, R. Pasterkamp, H. Van der Woerd, M. Devolder, et al.
579 (2005). Atlas of Chlorophyll-a concentration for the North Sea based on MERIS imagery
580 of 2003. *Vrije Universiteit, Amsterdam, edition 3.0*

Table 1. Statistics of peak dSST as observed from SEVIRI and modeled by the different schemes. The bias, in K, is defined as peak SEVIRI dSST minus model dSST. σ is the standard deviation in K, RMSE the root mean squared error in K, r the correlation coefficient and N is the number of collocated dSSTs.

Model	FMKLB	ZB d_1	ZB d_2	CC
Mean Bias	0.01	-0.03	-0.05	0.25
σ	0.59	0.76	0.64	0.59
RMSE	0.59	0.76	0.64	0.64
r	0.45	0.42	0.45	0.43
N	2613317	2613317	2613317	2613317

Price, J., R. Weller, and R. & Pinkel (1986). Diurnal Cycling: Observations and Models of the Upper Ocean Response to Diurnal Heating, Cooling and Wind Mixing. *J. Geophys. Res., 91(C7)*, 8411–8427.

Webster, P.J., C.A. Clayson, and J.A. Curry (1996). Clouds, radiation, and the diurnal cycle of sea surface temperature in the Tropical Western Pacific. *J. Clim., 9*, 1712–1730.

Zeng, X., and A. Beljaars (2005). A prognostic scheme of sea surface skin temperature for modeling and data assimilation. *Geophys. Res. Let., 32*, L14605.

Ward, B. (2006). Near-surface ocean temperature. *J. Geophys. Res., 111(C02004)*.

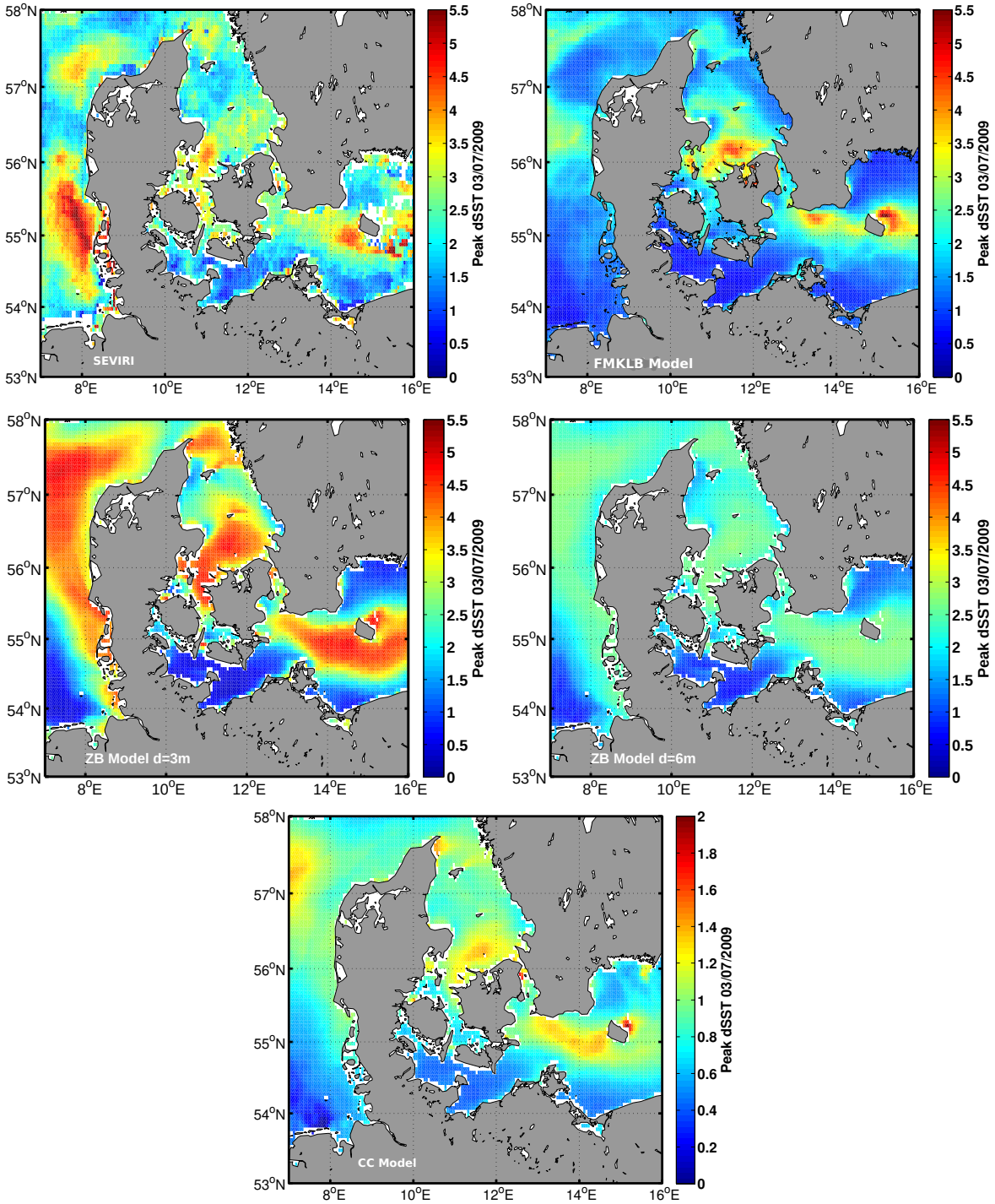

Figure 1. Spatial extend of peak dSST during a diurnal warming event (03/07/2009), observed from SEVIRI and reproduced by the models (no added noise). SEVIRI anomalies with quality $\geq$3 are used to avoid gaps in the field. The reduced range of the CC dSST is to make the spatial variability visible.

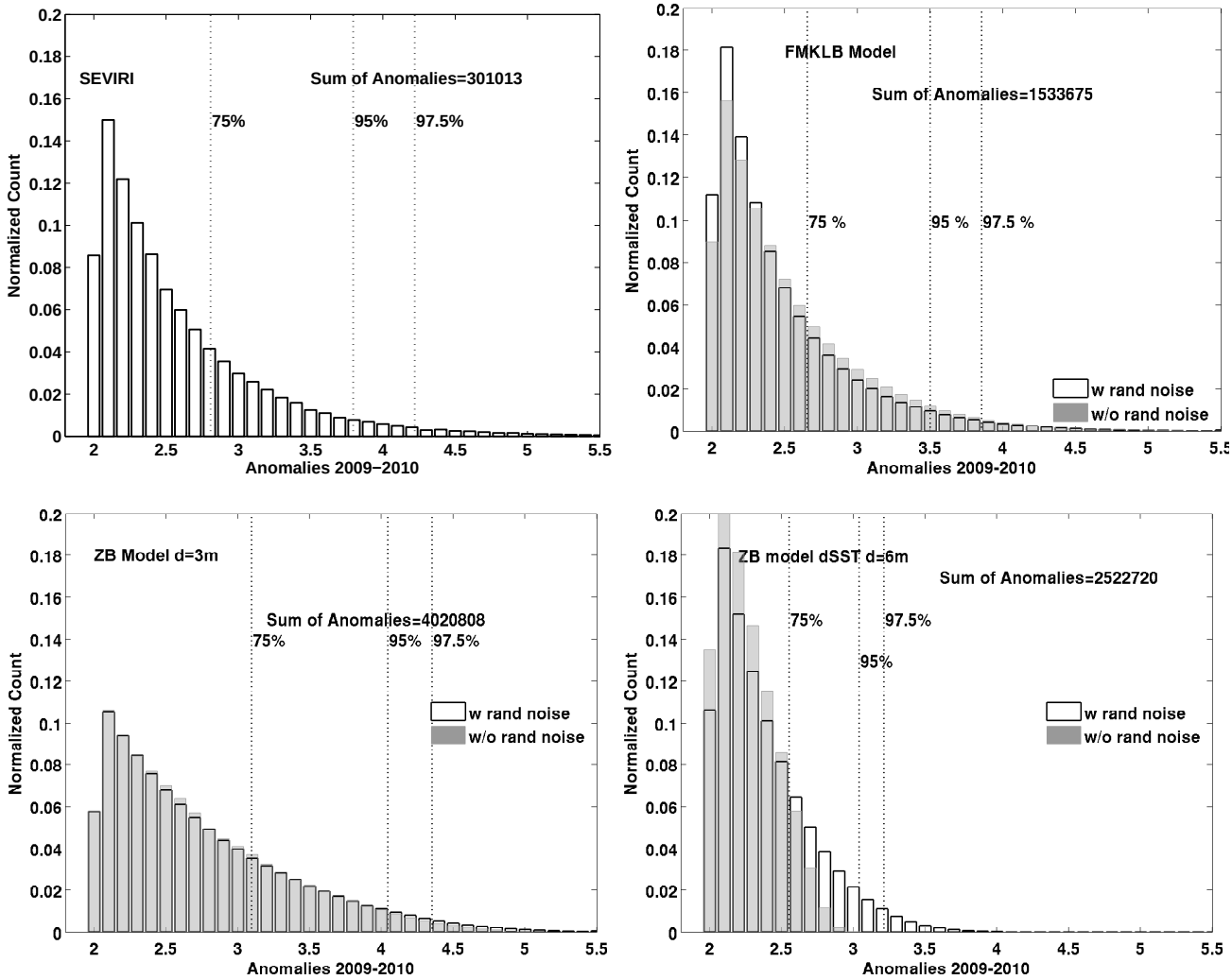

Figure 2. Distribution of anomalies>2 K from 02/2009 to 01/2010.The grey bars indicate the raw model outputs while the white bars show the results when random noise has been added to the hourly model dSST.

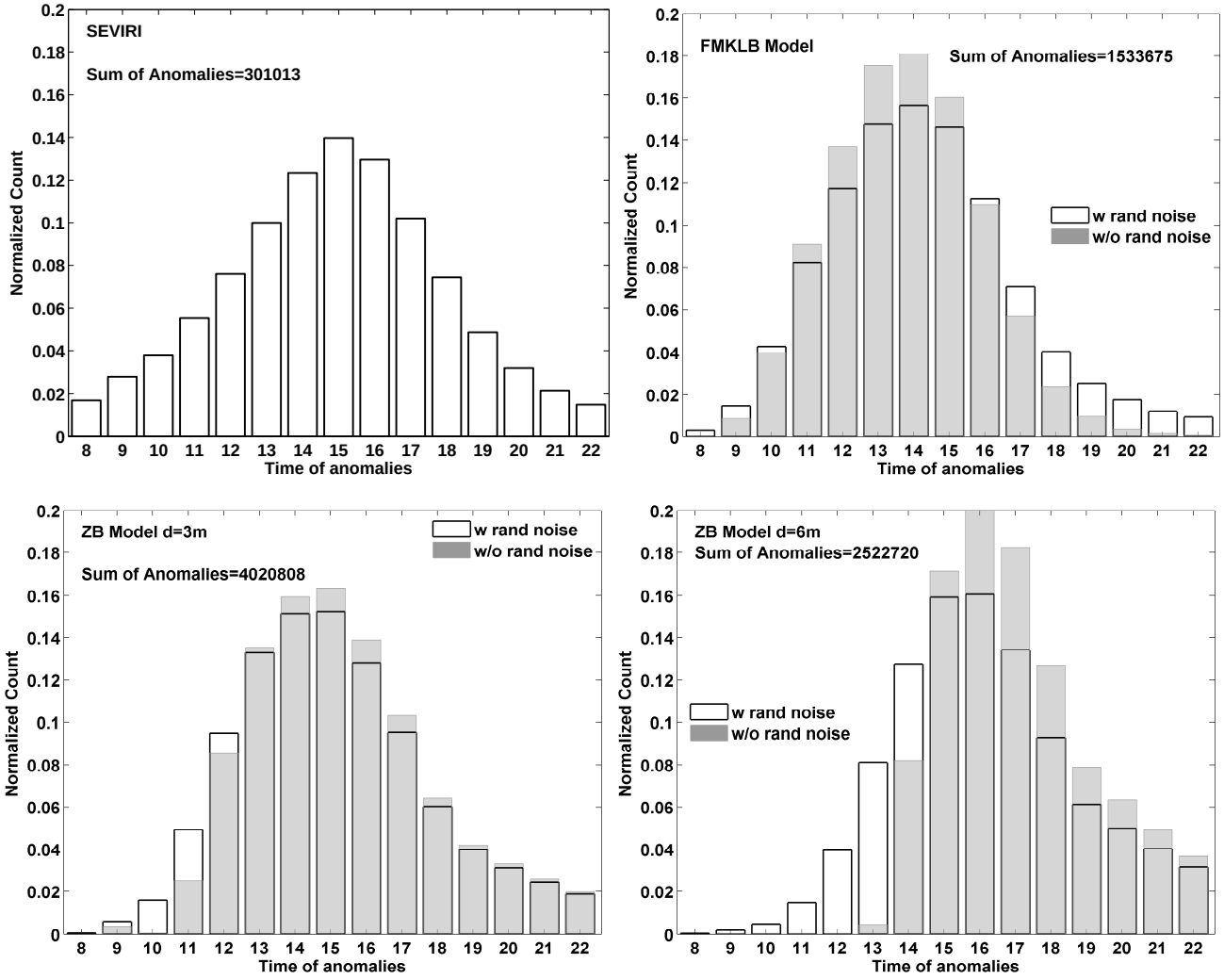

Figure 3. Distribution for the time of occurrence of anomalies from 02/2009 to 01/2010.The grey bars indicate the raw model outputs while the white bars show the results when random noise has been added to the hourly model dSST.

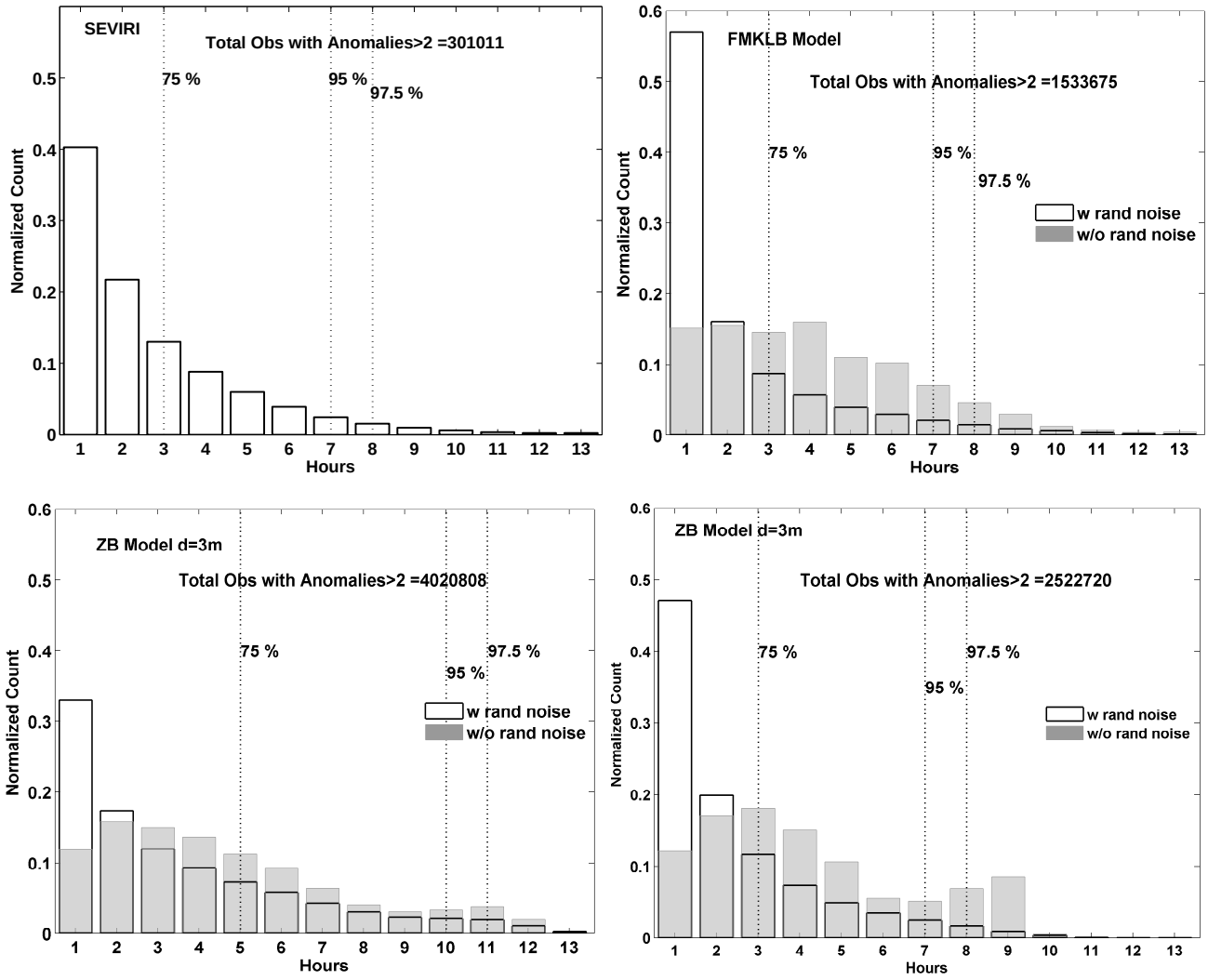

Figure 4. Duration of warming >2 K from 02/2009 to 01/2010.The grey bars indicate the raw model outputs while the white bars show the results when random noise has been added to the hourly model dSST. The dotted lines represent percentiles.

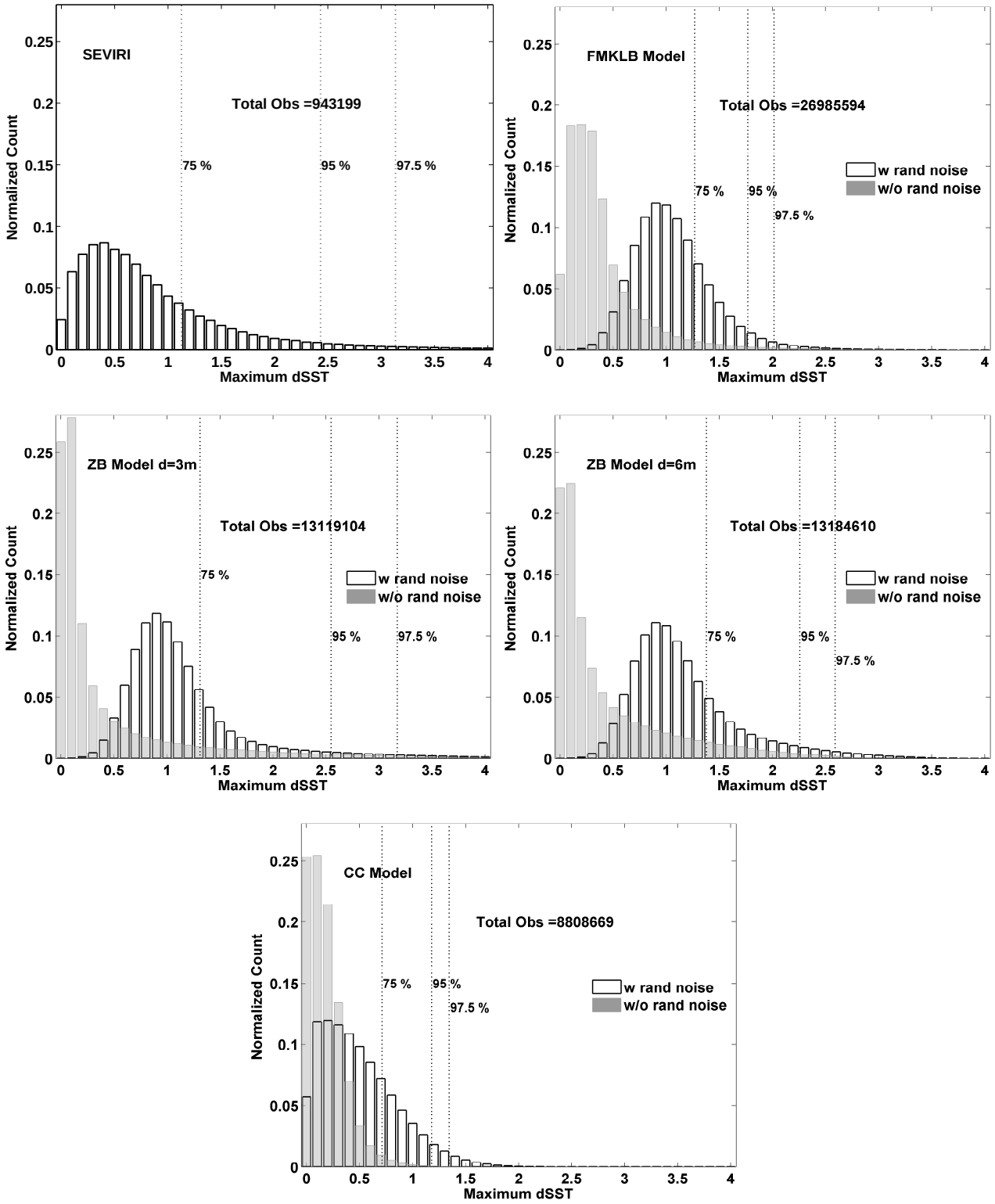

Figure 5. Distribution of maximum anomalies, counted for every grid cell, from 02/2009 to 01/2010.The grey bars indicate the raw model outputs while the white bars show the results when random noise has been added to the hourly model dSST.

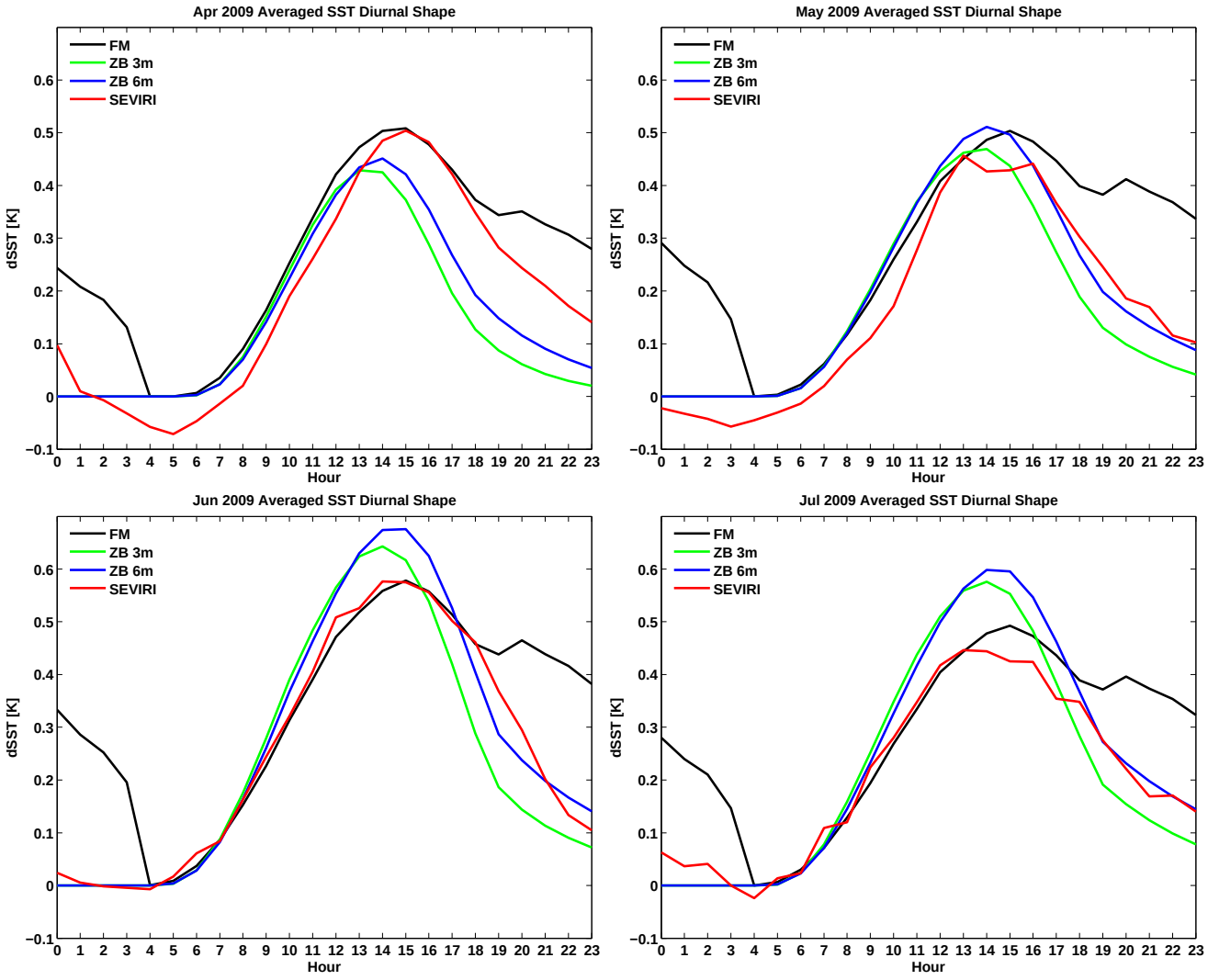

Figure 6. Monthly averaged diurnal cycle from SEVIRI (red), the FMKLB model (black), the ZB d_1 (green) and d_2 (blue). No anomaly threshold is applied, no time and space collocation criteria and no noise is added to the models.

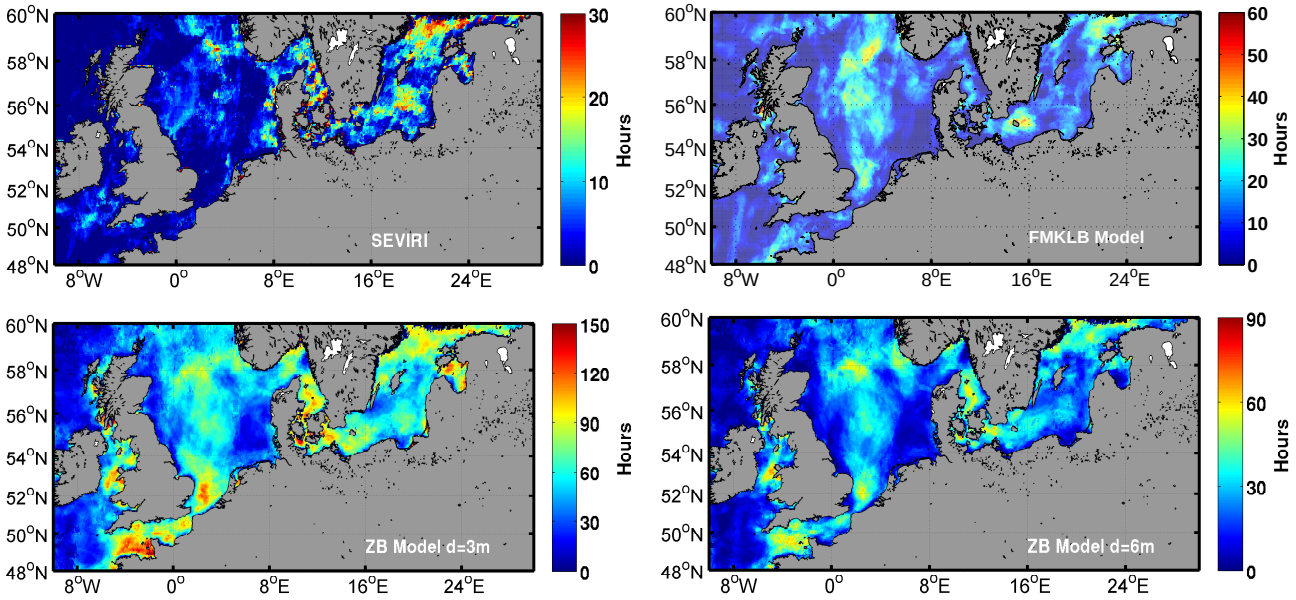

Figure 7. Spatial extend of anomalies≥2 K from 02/2009 to 01/2010. Note the different scaling, to make the spatial variability visible. Maximum for SEVIRI is 30 hours, all others are multiples. No random noise is added to the models.

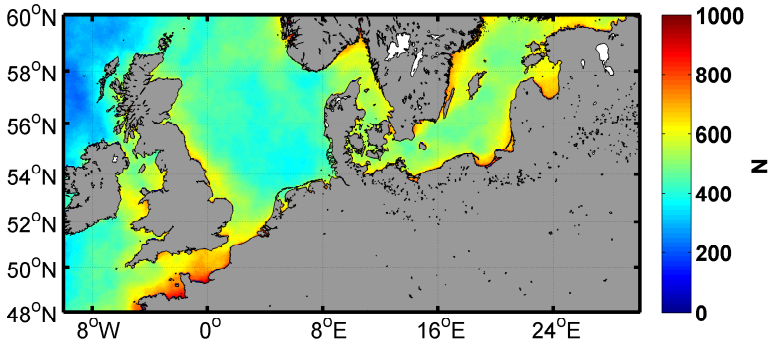

Figure 8. Number of occurrences for HIRLAM wind speed lower than 5 m s^{-1} and surface net heat flux higher than 300 W m^{-2}. From 02/2009 to 01/2010, a total of 8496 hourly fields are available.

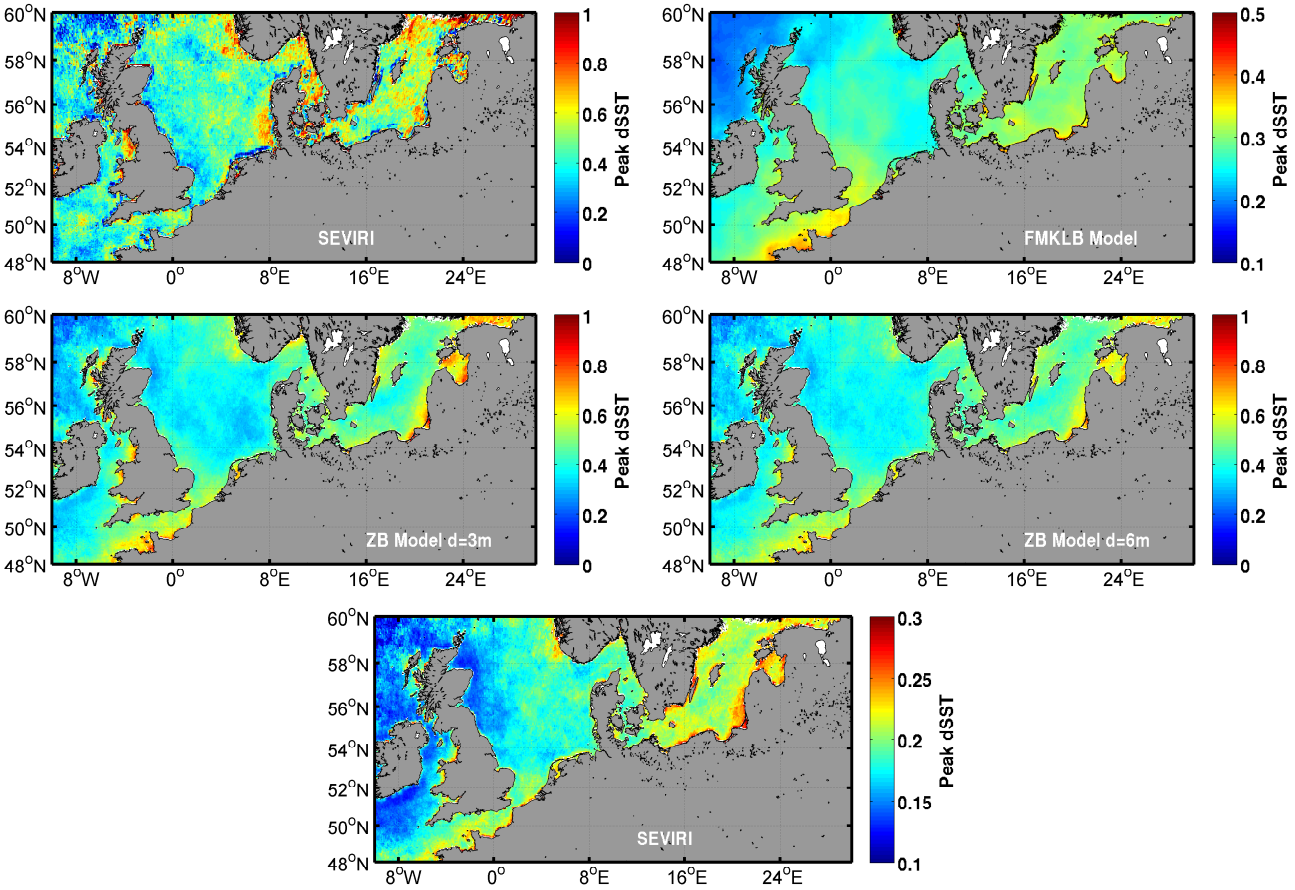

Figure 9. Spatial extend of averaged daily peak warming from 02/2009 to 01/2010. Note the reduced range of dSST for the FMKLB and CC schemes, to render spatial difference visible.

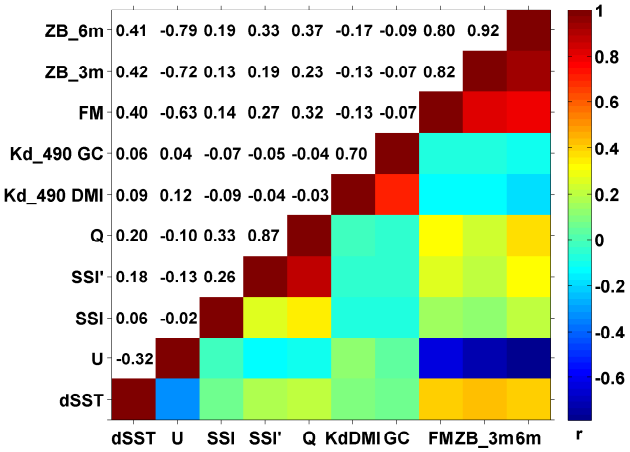

Figure 10. Correlation matrix of SEVIRI dSST, U, SSI, SSI′, Q and dSST from the FMKLB and ZB models (no random noise added).

This PhD thesis describes the use of remote sensing from satellites in order to obtain information for the near-surface ocean wind and the sea surface temperature over the North and Baltic Seas. The aim is to demonstrate the applicability of satellite observations and evaluate their potential use within the context of offshore wind energy. More specifically, wind retrievals from space-borne scatterometers are used for the quantification of the wind resources over large areas of the ocean where in situ measurements of the wind are rare. In addition, hourly retrievals from an infra-red sensor on board a geostationary platform are used for the identification of diurnal warming of the sea surface temperature. As such, the PhD thesis promotes the understanding of the physical interactions around the air-sea interface.

Meteorology, Risø Campus
Technical University of Denmark

Frederiksborgvej 399
4000 Roskilde
Tel. +45 4677 5700
Fax +45 4677 5758
www.vindenergi.dtu.dk

ISBN 978-87-92896-02-5
ISSN